Radiobiology of Normal Rat Lung in Boron Neutron Capture Therapy

by

Jingli Liu Kiger

B.S. Physics, Zhejiang University, China, 1999
M.S. Nuclear Engineering, Massachusetts Institute of Technology, 2002

Submitted to the Department of Nuclear Science and Engineering
in partial fulfillment of the requirements for the degree of

DOCTOR OF PHILOSOPHY IN NUCLEAR SCIENCE AND ENGINEERING

at the

MASSACHUSETTS INSTITUTE OF TECHNOLOGY

February 2006

Signature of Author: _____
Department of Nuclear Science and Engineering
September 30, 2005

Certified by: _____
Prof. Jeffrey A. Coderre
Associate Professor of Nuclear Science and Engineering
Thesis Supervisor

_____
Prof. Kathryn D. Held
Associate Professor of Radiation Oncology
Massachusetts General Hospital
Harvard Medical School
Thesis Reader

Accepted by: _____
Prof. Jeffrey A. Coderre
Associate Professor of Nuclear Science and Engineering
Chairman, Department Committee on Graduate Students

Radiobiology of Normal Rat Lung in Boron Neutron Capture Therapy

by

Jingli Liu Kiger

Submitted to the Department of Nuclear Science and Engineering
on September, 30, 2005 in Partial Fulfillment of the
Requirements for the Degree of Doctoral of Philosophy in
Nuclear Science and Engineering

Abstract

Boron Neutron Capture Therapy (BNCT) is a binary cancer radiation therapy that utilizes biochemical tumor cell targeting and provides a mixed field of high and low Linear Energy Transfer (LET) radiation with differing biological effectiveness. This project investigated the radiobiology of normal rat lung in BNCT and measured the relative biological effectiveness factors for the lung.

Rat thorax irradiations were carried out with x-rays and neutrons with or without the boron compound boronophenylalanine-fructose (BPA-F). Monte Carlo radiation transport simulations were used to design the rat lung neutron irradiations. Among the neutron beam facilities available for BNCT at the MIT Research Reactor, the thermal neutron beam facility was found to provide a suitable dose distribution for this project. A delimiter was designed and constructed for the rat lung irradiations as a lithiated-polyethylene plate of 1.5 cm thickness with an aperture tapered from 4 to 3 cm in width to expose the lung to the beam and shield adjacent radiosensitive organs. The simulation design was validated with in-phantom measurements using gold foil activation and the dual ion chamber technique. By using a two-field irradiation, a relatively uniform dose distribution could be delivered to the rat lung. The mean lung dose rate was 18.7 cGy/min for neutron beam only irradiation and 37.5 cGy/min with neutrons plus BPA and a blood boron concentration of 18 μg/g. The delimiter designed for rat lung irradiation, and another similar delimiter, along with the animal holding box, all designed in this project, also serve as the apparatus for other small animal irradiations and cell irradiations at the thermal neutron facility at the MIT Research Reactor.

An open-flow whole-body plethysmography system with fully automated signal processing programs was developed to non-invasively measure rat breathing rates and lung functional damage after lung irradiation. Noise reduction was carried out against high frequencies beyond the range of rat breathing frequency and large amplitude spikes due to abnormal animal movement. The denoised breathing signals were analyzed using the Fast Fourier Transform with

a circular moving block in combination with the bootstrap for noise suppression and to allow estimation of the statistical uncertainty (standard deviation) of frequency measurements. The major frequency of the mean frequency spectrum was determined as the breathing frequency. The mean control breathing rate was 176 ± 13 (7.4%) min^{-1} (mean ± SD), and breathing rates 20% (~ 3 SD) above the control average were considered to be abnormally elevated. The mean standard deviation of all measurements (n = 4269) was 2.4%. The dose responses of different irradiation groups with breathing rate elevation as the biological endpoint were evaluated with probit analysis. Two response phases of breathing rate elevation were observed as the early response phase (≤100 days) and the late response phase (>100 days). The ED_{50} values for x-rays, neutrons only, and neutrons plus BPA during the early response phase, and neutrons plus BPA during the late response phase, were 11.5 ± 0.4 Gy, 9.2 ± 0.5 Gy, 8.7 ± 0.6 Gy and 6.7 ± 0.4 Gy, respectively. The radiobiological weighting factors for the neutron beam (neutrons and photons), thermal neutrons only, ^{10}B dose component during the early response phase, and ^{10}B dose component during the late response phase were 1.24 ± 0.08, 2.2 ± 0.4, 1.4 ± 0.2, and 2.3 ± 0.3, respectively.

The histological damage to the lung during the late phase was also quantified with a histological scoring system. A set of linear dose response curves with histological damage as the endpoint was constructed. The radiobiological weighting factors for the different dose components were also determined at a degree of lung histological damage corresponding to a median histological score between the baseline (similar to the control) and the maximum. The weighting factors measured, 1.22 ± 0.09 for the thermal neutron beam and 1.9 ± 0.2 for the ^{10}B dose component, are consistent with the corresponding weighting factors measured using functional damage.

The knowledge gained in these radiobiological studies of the normal rat lung indicates that the lung complications experienced by two patients in the Harvard-MIT clinical trial of BNCT for brain tumors do not appear to be related to the BNCT irradiations. This project is also helpful for evaluating the feasibility of BNCT for lung cancer.

Thesis supervisor:	Jeffrey A. Coderre Associate Professor of Nuclear Science and Engineering Massachusetts Institute of Technology
Thesis reader:	Kathryn D. Held Associate Professor of Radiation Oncology Massachusetts General Hospital Harvard Medical School

Acknowledgements

The completion of my Ph.D. put a period on my formal education. If my life is a function determined by some unclear parameters, the last six years of my life as a Ph.D. student surely cast light on some of the parameters.

There are so many people whose presence in these six years of my life that I am deeply thankful for. I greatly appreciate the opportunity to work with my thesis advisor, Prof. Jeffrey Coderre. I am grateful for the opportunity he gave me to work hard on a very interesting and meaningful project, the trust he had for me that I would succeed in my work, and the help, enthusiasm, guidance and patience he readily provided throughout the work. I would like to thank Prof. Kathryn Held, the reader of my dissertation, for her insightful and critical suggestions and comments on this work, and carefully reviewing my dissertation. I am also thankful for the opportunity to work with Prof. Otto Harling and regard it as an honor. His devotion, attitude and persistence towards research inspire and encourage me to succeed in my research and career. Not only did I benefit from working with him, I also benefited from working with his former students, so much that I even married one. I am also very grateful to Dr. Kent Riley and Dr. Peter Binns, whose guidance and advice was essential to my understanding of radiation dosimetry and my success in the experimental work. Thanks to Dr. Riley also for reading and carefully reviewing my dissertation. I am grateful to Prof. Jacquelyn Yanch, also the reader for my Master's thesis, for serving on my thesis defense committee.

I am grateful to Dr. Huanmei Wu from Northeastern University for valuable discussions and for sharing her experience in human breathing signal analysis. I would like to thank Dr. Hemant Patel for his help with constructing the hardware for the rat breathing rate measurement instrument.

Special thanks also go to the Reactor Operations staff, especially Eddie Lau, Susan Tucker and Fred McWilliams, for their help in scheduling the irradiations at the MIT Research Reactor, contamination controls, and sometimes even shipping animals. I would also like to thank the staff of the Department of Comparative Medicine (DCM), especially Katie Madden and Christine Hewes, for their help and instruction in rat handling and surgery, and for allowing me to use their microscope for the histological scoring.

Dr. Prashant Nambiar at the Department of Comparative Medicine (DCM) at MIT patiently taught me histological scoring and examined and confirmed my scoring at every stage of the process. Prof. Jacqueline Williams from University of Rochester Medical Center carefully reviewed my histology scoring system and gave some important comments and suggestions; to both of them I am very grateful.

I would like to express my gratitude to Prof. Yip; I benefited greatly from his advice. I am also thankful for Dr. Bernard, for his kind and generous help and support in preparing for the general exam.

The friendship I gathered along the six years is very precious to me and makes the time more memorable. It is indeed a blessing to know so many wonderful people and be their friend, especially Julie, Rich, Ray, Jianmei, Paige and Maria.

I would also like to thank my teachers from middle school, Mr. Liu and Mr. Zhang, for the inspiration and virtue that they planted in my mind a long time ago.

I can never be thankful enough for the unconditional love and support from our parents and family. I would like to thank my brother as I realize more and more everyday how his love, support, and encouragement have contributed to the way I am.

I would like to dedicate this dissertation to my dear husband, Stead. It would have been a gloomy and unfruitful journey without his company and love. He is truly the best gift to me from God.

Finally, I would like to thank God, for the day he said, 'Let it be light'.

Table of Contents

List of Figures

List of Tables

CHAPTER ONE

Introduction

1.1 Introduction to BNCT

1.1.1 Principles of Boron Neutron Capture Therapy (BNCT)

Boron Neutron Capture Therapy (BNCT) is a binary cancer therapy with biochemical tumor-cell targeting (1). Theoretically, it delivers higher dose to the tumor cells, due to the higher concentration of the ^{10}B carrier in tumor cells and the significantly larger ^{10}B thermal neutron capture cross section than the other isotopes in normal tissues. The $^{10}B(n,\alpha)^{7}Li$ neutron capture reaction releases 2.79 Mev energy, of which 82.8% on average is deposited locally due to the short ranges (~7 μm and ~4 μm) of the heavy charged particles released, α and ^{7}Li. The BNCT theory was first proposed in 1936 by Locher (2). BNCT requires two elements: a ^{10}B-carrying drug that preferentially accumulates in tumor cells is first administered; then the target region (including some volume of surrounding normal tissue) is irradiated by a neutron beam of adequate intensity and appropriate energy range.

1.1.2 Clinical trials of BNCT

BNCT clinical trials were first carried out on human malignant tumors in the 1950s and 1960s at Brookhaven National Laboratory (BNL) and the Massachusetts Institute of Technology (MIT) Nuclear Reactor Laboratory (NRL) (1, 3). The results were discouraging due to lack of knowledge of the pharmacokinetic/biodistribution characteristics of the boron compound used and the poor penetration of the thermal neutron beam in tissue (3). Patients died from tumor

regrowth and, in many cases, developed serious radiation damage to their skin and brain. These results were attributed to two problems. The low energy neutron beams were attenuated exponentially in tissue, making it difficult to deliver adequate fluences to tumor at depth. The boron compounds used were not sufficiently selective for tumor; there were high concentrations of boron in the blood which led to damage to blood vessels in the skin and brain. Clinical trials of BNCT were therefore closed in the US after 1961. BNCT clinical trials continued in Japan in the 1970s, with anecdotal reports of long-term survivors following BNCT of brain tumors (4). Basic research on BNCT continued in the United States throughout this period. Investigations focused on finding more appropriate boron drugs and the development of higher energy neutron beams with improved tissue penetration characteristics, as well as developing adequate physical dosimetry and treatment planning methods. Two boron compounds, the amino acid p-boronophenylalanine (BPA) and the sulfhydryl borane ($Na_2B_{12}H_{11}SH$, or BSH) were evaluated and demonstrated higher accumulations in certain brain tumors (5-9), subcutaneous melanoma, and intracranial melanoma metastasis than surrounding normal tissues, and are currently used in BNCT clinical trials. Higher energy neutron beams composed of epithermal (0.4 eV $<E_{epi}<$ 10 keV) neutrons(10, 11), were developed to replace the thermal neutron beams previously used in BNCT clinical trials to achieve better penetration in tissues. The improvements in both boron carriers and neutron beams in BNCT irradiations led to the initiation of new BNCT clinical trials in the 1990s in the US. Several clinical trials were carried out in the 1990s for glioblastoma, melanoma metastatic to the brain, or subcutaneous melanoma of the extremities, at Harvard-MIT (12-14), and for glioblastoma multiforme at Brookhaven National Laboratory (15-17). Currently, BNCT is an experimental radiation therapy being evaluated mainly on brain tumors and melanoma in Japan, Europe and Argentina (18-23).

In the clinical trials at Harvard-MIT between 1994 and 1999, two patients out of thirteen receiving treatment for brain tumors developed a fatal acute respiratory distress syndrome (ARDS); one other patient developed acute pneumonitis, but recovered following intensive supportive care (14, 24). At the time dose estimates for scattered radiation to the lung were below the threshold for radiation induced ARDS. However the serious adverse events with ARDS raised the concern that the lung dose estimates might be too low. This indicated that studies of the radiobiology of the lung under BNCT conditions were needed. A project was therefore proposed to systematically study the effect of BNCT on normal lung and also examine the possibility of treating lung cancer using BNCT.

1.1.3 Dose components of BNCT radiation

The reaction used in BNCT is $^{10}B(n,\alpha)^{7}Li$, and is illustrated in Fig. 1.1, and the energy level diagram is illustrated in Fig. 1.2. When a thermal neutron ($E_n < 0.4$ eV) is captured by a ^{10}B nucleus, a temporary excited nuclear state of $^{11}B^*$ is formed which immediately breaks down into ^{4}He and $^{7}Li^*$ with 94% probability. The excited $^{7}Li^*$ then releases a photon of 479 keV in its decay to the ground state. With 6% probability the $^{11}B^*$ decays directly to the ground state of ^{4}He and ^{7}Li (Fig. 1.2). The initial linear energy transfer (LET) values in tissue for the heavy charged particles from the reaction, ^{4}He and ^{7}Li, are high, at 200 keV/μm and 300 keV/μm respectively. These heavy charged particles have very short ranges in tissue (5–9 μm), a scale comparable to a cell diameter, and deposit all their energy locally (1).

When energetic neutrons traverse tissue, they interact with the various nuclei present with different probabilities, being either scattered or captured, and at the same time creating secondary particles that eventually deposit energy. Epithermal (0.4 eV-10 keV) neutrons tend to be scattered and thermalized (mainly by collision with ^{1}H in tissue), with a certain amount of

kinetic energy transferred to the nuclei; thermal neutrons are more likely to be captured than epithermal neutrons with new energetic charged particles or photons released. The charged particles and photons typically released from the thermal neutron capture reactions have different mean free paths in tissue. The charged particles will deposit all their energy locally, and have high LET values. The photons have a much larger mean free path than the charged particles, will deposit only part of their energy in the target region, and have relatively lower LET.

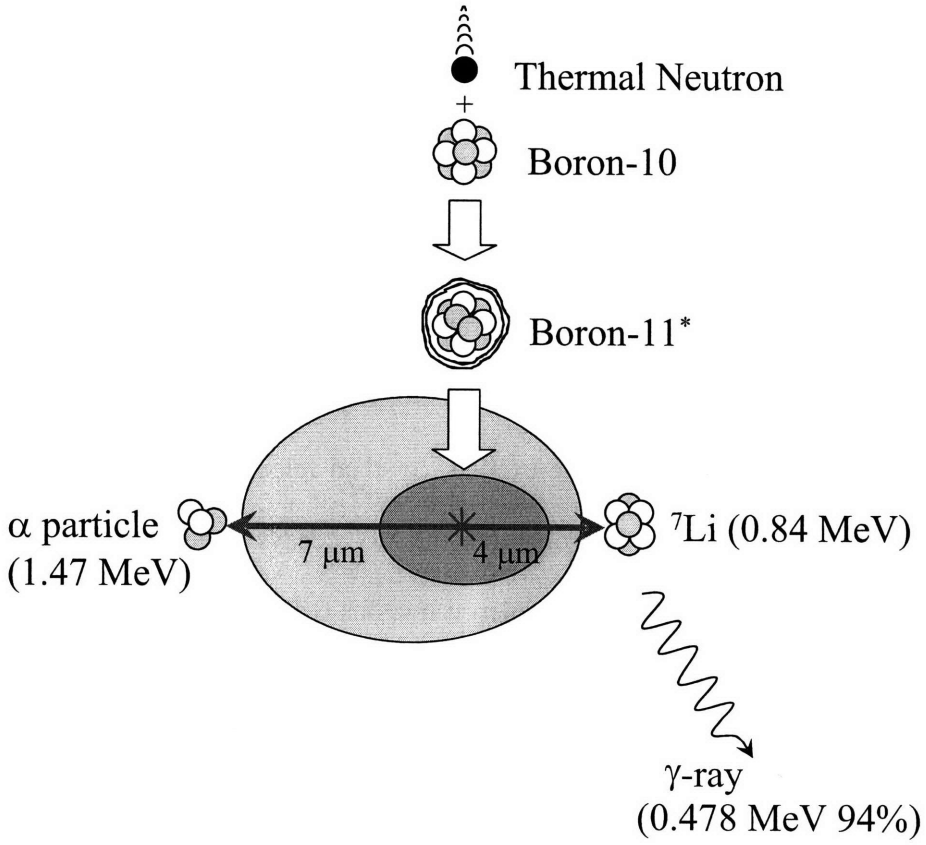

Fig. 1.1 Illustration of the reaction $^{10}B(n,\alpha)^{7}Li$. (Adapted from Ref. (27).)

The capture reactions of thermal neutrons with other nuclides are generally similar to the $^{10}B(n,\alpha)^{7}Li$ reaction, with a temporary nucleus formed from neutron capture which then decays.

Neutron capture is the primary mechanism for energy deposition by thermal neutrons in matter, with the reaction probability described by the thermal neutron absorption cross sections, which are often inversely proportional to neutron speed. The neutron cross sections for major elements in tissue at neutron speed of 2200 m/s (0.025 eV) are listed in Table 1.1 together with those of ^{10}B. The absorption cross sections of ^{1}H, ^{14}N, ^{16}O and ^{12}C are much lower than the absorption cross section of ^{10}B. Therefore, even though the boron accumulation in tumor cells is relatively small (usually tens of μg/g) (25), the dose from the $^{10}B(n,\alpha)^{7}Li$ reaction is generally larger than that from the reactions of neutrons with other elements in tissue. Under conditions with a boronated drug accumulation in tumor cells 3 or 4 times that of the normal cells (such as is the case with boronophenylalanine, BPA) (26), the tumor dose is significantly greater than the normal tissue dose within the treatment field, thus producing a therapeutic gain.

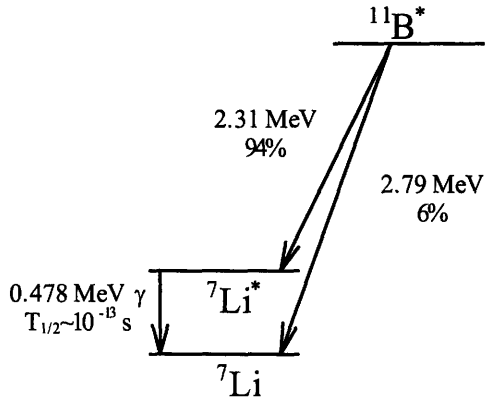

Fig. 1.2 Energy level diagram for the $^{10}B(n,\alpha)^{7}Li$ reaction. (Adapted from Ref. (27).)

Table 1.1 A summary of important thermal neutron capture reactions in normal brain tissue (28).

	Cross Section (barn)			N_T capture		Composition in
	Absorption	Scattering	Total	Reaction	Q value (MeV)	normal brain %
^{1}H	0.33	20.5	21.8	$^{1}H(n,\gamma)^{2}H$	2.22	10.7
^{12}C	0.004	4.8	4.8	-	-	14.5
^{16}O	2	3.8	5.8	-	-	71.2
^{14}N	1.7	10.0	11.7	$^{14}N(n,p)^{14}C$	0.626	2.2
^{10}B	3843	2.1	3845	$^{10}B(n, \alpha)^{7}Li$	2.79	-

In general, dose delivered to tissues in BNCT irradiations is compromised of:

D_γ: Photon dose (low LET). It mainly comprises the 2.22 MeV photon from $^{1}H(n,\gamma)^{2}H$ and contaminant photons from the neutron beam; with boron present, it also includes the 479 keV photon released by Li^* from $^{10}B(n,\alpha)^{7}Li^*$;

D_T: Thermal neutron dose (high LET). This dose component is mainly from 0.626 MeV protons produced by the $^{14}N(n,p)^{14}C$ reaction;

D_F: Fast neutron dose (high LET). This dose component is mainly due to recoil protons produced by epithermal and fast neutron collisions with hydrogen but also includes similar contributions from other nuclei;

D_B: ^{10}B dose component (high LET). This dose component is from ^{4}He and ^{7}Li from the $^{10}B(n,\alpha)^{7}Li$ reaction (Fig. 1.1).

1.1.4 Biological effectiveness of BNCT radiation

The BNCT dose components in tissue listed above have different biological effectiveness due to their differing LET. The biological effectiveness of ^{10}B dose is also influenced by the boron microdistribution from specific boron compounds. In order to express the total BNCT dose in photon-equivalent dose units, Relative Biological Effectiveness (RBE) factors determined experimentally were defined as the weighting factors for each of the high-LET dose components

(1). Analogous to the RBE, the compound biological effectiveness (CBE) factor is defined as the weighting factor for the ^{10}B dose component that accounts for the influence of both the $^{10}B(n,\alpha)^{7}Li$ radiation quality and the boron microdistribution on the radiobiological effectiveness (1, 29). For a given biological endpoint in a particular tissue, the RBE or CBE is defined as the ratio of the dose of a high LET radiation to an isoeffective dose of x-ray radiation. Thus, the total biologically weighted BNCT dose is the weighted sum of all dose components:

$$D_w = w_\gamma D_\gamma + w_T D_T + w_F D_F + w_B D_B, \qquad (1)$$

where w_γ, w_T, w_F and w_B are weighting factors (RBE or CBE factors) for the photon, thermal neutron, fast neutron and the ^{10}B absorbed doses, respectively. In BNCT, w_γ is usually regarded as unity and w_T and w_F are usually equal to each other (1). In lung, the biological effectiveness weighting factors are unknown. This information is critical for estimating the total biologically weighted dose to the lung.

1.1.5 BNCT radiobiology of normal tissues: skin, spinal cord, oral mucosa

Before the recent clinical trials of BNCT for brain tumor, normal tissue tolerance in BNCT was investigated for spinal cord (30), oral mucosa (31) and skin (32). Normal tissue dose responses with BNCT irradiations were established with animal models and certain biological endpoints, and compared to the irradiations with x-rays (1). The dose response curves are usually fitted to a smooth curve with probit analysis (33, 34). The weighting factors of the high LET dose components are usually determined at the ED_{50} (effective dose for 50% incidence) (29) of the dose response curves (1). The radiation responses of different normal tissues and the measured weighting factors of the high-LET dose components in BNCT are summarized in Table 1.2.

Table 1.2 Summary of radiation responses of different normal tissues in BNCT with rat as the animal model. The incidence/onset times recorded here are at the ED_{50} level of the dose response curves.

Tissue (Ref)	Biological Endpoint	ED_{50} (Gy_w)	Incidence time after irradiation (days)	CBE for BPA	RBE for neutron
Spinal cord/Brain (29)	paralysis	18.6 ± 0.1	163*	1.33	1.8
Oral mucosa (30)	tongue uleration	13.4 ± 0.2	6 - 10	4.9	3.8
Skin (31)	moist desquamation	42.2 ± 2.2	11 - 36	3.74	5.1
Skin (31)	dermal necrosis	56.6 ± 2.9	168 - 301	0.73	-

* onset time

1.2 Normal lung irradiation with conventional radiation

Lung is one of the dose limiting tissues in radiation therapy for bone marrow transplantation and thoracic malignancies including lung cancer and Hodgkin's disease (35-38). Significant work has been done in investigating lung radiation response and lung radiation damage mechanisms to improve the quality of clinical radiotherapy involving lung radiation.

1.2.1 Lung radiation response

Lung radiation damage in clinical radiotherapy was first reported in the 1920s and at the time the lung reaction was compared to the skin reaction (39). Two phases of the lung radiation response have been identified in the clinic and in animal models: the early inflammatory pneumonitis and the late pulmonary fibrosis (40-43). The pneumonitis phase usually occurs within 6 months after irradiation (44), with syndromes of shortness of breath and cough. Fine structural and histological changes occurring from hours to months after irradiation are well documented with animal models in the literature (40, 43, 45-49). Cellular changes due to radiation damage observed in this period include increased capillary permeability, Type I and II pneumocyte degeneration, increased vasculature permeability, fibrin and inflammatory infiltration into alveolar space, and other changes to lung structure. Pulmonary fibrosis due to

radiation damage can occur from months to years after irradiation, with the symptom of chronic dyspnea (shortness of breath). Histological observation in this stage shows that wounds are organized and that final scars are formed, mostly in the form of fibrosis. The exact onset time of the pneumonitis and fibrosis is dose-related and also varies with different animal species and strains (50-52). Experimental animals used in radiation lung studies are mostly rodents including rabbits (53), rats (43, 54, 55) and mice (46, 56), but also include dogs (57-59) and pigs (52).

1.2.2 Non-invasive assays of lung functions

Several techniques have been developed to non-invasively measure lung functional changes after irradiation of small animals, especially rats and mice. The most common technique is whole body plethysmography to measure the breathing rate, lung functional volume (tidal volume) and minute ventilation of the animal (60-63). The basic setup of the whole body plethysmography is to hold the animal in an air-tight chamber and to measure the breathing rate by measuring the temporal variation in air pressure inside the chamber. Carbon monoxide uptake has been used to measure the lung diffusion capacity (56, 64). Animals with irradiated lung usually have a smaller CO uptake than control animals primarily due to decreased lung ventilation and decreased diffusion between alveolar gas and blood as a result of a thickened alveolar wall. Other measurements of lung functional changes also show decreased compliance (ease of lung expansion) during radiation pneumonitis, increased vascular permeability, and decreased blood flow in the lung after irradiation (65). In addition to the functional assays listed above, Computed Tomography (CT) densitometry is another non-invasive assay to evaluate the increase in lung density after irradiation (51, 55, 66).

1.2.3 Lung radiation targets at the cellular level

There are more than 40 cell types in the lung, and the major cell types are Type I pneumocytes, Type II pneumocytes, endothelial cells, and interstitial cells (67, 68). In the rat lung, they compose 8.1%, 12.1%, 51.1%, and 24.4% of the total lung cells, respectively. Type I pneumocytes also cover 96.4% of the alveolar area in rat lung with the rest covered by Type II pneumocytes (67). Gas exchange in the lung takes place across the alveolar-capillary membrane, which consists of attenuated cytoplasm of type I pneumocytes, endothelial cell cytoplasm, and their cell membranes. The type II pneumocytes produce surfactant which reduces lung surface tension and prevents the lung from collapsing. They also serve as the 'stem cells' in the lung by degenerating into Type I cells and forming a new layer of epithelium upon lung injury (69, 70). Type II pneumocytes have been extensively studied due to their important function in the lung. The interstitial cells consist mostly of fibroblasts (50-60% in rat lung) and blood cells. Not much is known about the interstitial cells in the lung due to their low mitotic activity (67).

The mechanisms of radiation lung damage, especially for fibroblast synthesis and collagen deposition during the fibrosis stage, have been extensively studied. Damage targets at the cellular level, named 'target cells', were sought at the beginning. Endothelial cells and Type II pneumocytes, showing abnormal activities between hours and months after lung irradiation, were the two leading candidates for the target cells in lung radiation damage. Among the early changes in the lung tissue, edema, fibrin accumulation in alveolar space, and increased alveolar protein are all related to pulmonary vasculature permeability (71, 72), which supported the hypothesis that endothelia were the target. Similarly, other changes related to Type II pneumocytes, including dramatic increases in lung surfactant and phospholipids levels, attracted significant interest to Type II pneumocytes as the target cells for lung radiation damage (40, 73).

Various invasive techniques were developed to evaluate radiation lung damage both qualitatively and quantitatively. The most common and conventional technique is to examine the lung tissue changes directly under either a photomicroscope or electron microscope. Various stains are sometimes applied to highlight specific cells or cell types to enable easy recognition with the photomicroscope, e.g., Van Gieson is used specifically for fiber staining. The information and contents of the lung fluid, obtained with bronchioalveolar lavage (BAL) (74-76), are also valuable and were closely studied to detect the lung cellular activity after irradiation. The contents of the lung fluid from BAL, including hydroxyproline accumulation for collagenous protein synthesis (77), the amount of macrophages and protein as exudates from vasculature (78-80), phospholipids and surfactant released by Type II pneumocytes (40, 73), DNA accumulation for lung cellularity (81), and histamine released by mast cells related to fibrotic tissue turnover (82, 83), were all examined and quantified. Lung weight (wet and dry) has also been used to grossly estimate the amount of lung fluid and lung mass, respectively (81, 84, 85). Despite all the investigations of cellular activities after lung irradiation, the target cells have not been identified (50, 86, 87).

1.2.4 Lung radiation targets at the molecular level

Further investigation of the pathogenesis of lung radiation damage and the damage targets at the molecular level lead to a more fundamental understanding of lung radiation damage than the classical hypothesis as connective tissue replacement of the parenchymal cells. A new hypothesis proposed that genetic expression of radiation injury initiates synthesis and secretion of numerous growth and inhibitory factors that orchestrate multicellular interactions (88-93). With this theory, pneumonitis is considered as a stage for cells to prepare the growth factors and fibrosis is considered as the repair stage, both as a necessary component of the same process. A

most interesting growth factor and a target at the molecular level in mediating gene expression of extracelluar matrix proteins after lung irradiation is Transforming Growth Factor-β (TGF-β, 1-3) (80, 94-98). TGF-β holds a central role in normal wound healing, including inhibiting epithelial cell proliferation, promoting fibroblast proliferation (99), modulating the immune system and the inflammatory process (100), and controlling the homeostasis of the cellular matrix (101).

1.2.5 Alteration of lung radiation response

Two major approaches have been investigated to alter and relieve the radiation response process, especially fibrosis. Radioprotectors, mostly free radical scavengers, were tested with animals and were delivered to normal lung cells to protect them from radiation damage in lung irradiation (102-105). The other approach is pharmacological alteration of the gene expressions and pathways and cytokines responding to irradiation injuries. Captopril, one of the Angiotensin Converting Enzyme (ACE) inhibitors, has been proven in animals to reduce endothelial leakage from radiation damage (65, 106-109), and shows promise for clinical application.

1.2.6 The lung radiation response in clinical radiotherapy

Clinically, the incidence of radiation pneumonitis is related to the dose delivered and also to the fraction of the total lung volume irradiated. Therefore, dose volume histograms (DVH) of the lung and the mean lung dose are important in predicting the incidence of radiation induced pneumonitis (44, 110-112). A mean lung dose of 9.3 Gy in a single fraction was reported as the ED_{50} for radiation pneumonitis in patients (110). The fractionated dose-time relationship for the normal lung response is also well documented in both animal models (113, 114) and in humans (115). For 20 fractions, the TD_5 (tolerance dose at 5% incidence) is about 26 Gy mean lung dose and the TD_{50} is about 30 Gy mean lung dose in patients (112, 116). Higher doses are required to produce a similar incidence of radiation pneumonitis when the lung is partially irradiated. The

hypersensitivity of different parts of the lung volume to radiation damage is also currently being evaluated with experimental animals (117-119). The lung radiation response very likely depends on the individual patient. With similar radiation treatment to the lung, the lung radiation response among patients can vary significantly (38). The concentration of TGF-β in blood serum was found to be related to the lung radiosensitivity of individual patients (38).

1.3 Research goals and thesis organization

This thesis describes radiobiological studies of the normal rat lung which investigate the lung tolerance to BNCT radiation, and also measure the biological weighting factors required for the weighted lung dose calculation in BNCT. The knowledge of the normal lung tolerance in BNCT also provides information that will be helpful for evaluating the feasibility of BNCT for lung cancer (120) and for the BNCT irradiation of any organ near the lung.

1.3.1 Dosimetry of the rat lung irradiation

In this project, the whole rat lung is irradiated with x-rays and neutrons with or without BPA-F, the ^{10}B carrier. Since many radiosensitive organs are located close to the lung, including the spinal cord, skin, esophagus and small intestines, design studies using, e.g., Monte Carlo simulations, are necessary to ensure that adequate shielding is provided for these adjacent organs during lung irradiation with neutrons. Since the lung response may be influenced by a volume effect, that is, irradiating different fractions of lung volume may result in different responses, the design also needed to ensure a uniform dose delivery to the whole lung. Chapter 2 discusses in detail the design of the rat thorax irradiation, first carried out in simulations, then validated with measurement, describing the dosimetric aspects of this project.

1.3.2 Rat breathing rate measurement and the signal processing

After the lung irradiation, the lung damage is evaluated by measuring the lung response functionally and histologically. Among the non-invasive lung functional assays described above, whole body plethysmograph for breathing rate is the most convenient and commonly used assay. However, an automatic method for converting the raw pressure data into a breathing frequency was not fully developed; manual selection of the regular breathing signal was often used. The manual method is not only very laborious, especially when applied to a large number of animals, but the results are also prone to user bias. The plethysmograph, including both hardware for breathing signal collection, and software for signal processing and breathing rate determination, needed to be developed to reliably monitor the animal breathing rate changes after irradiation. Chapter 3 explains in detail both the hardware and software of the system constructed for this project.

1.3.3 Measurement of dose response

The breathing rate responses measured after irradiation of animals of different irradiation groups are reported in Chapter 4. The breathing rates along with the weight measured after irradiation of all animals are plotted in Appendix A. Lung histological changes of animals from different irradiation groups are also assessed at certain times after lung irradiation and the results are reported in Chapter 5. The weighting factors of different high-LET dose components in BNCT are determined by evaluating the dose response curves and comparing the doses of different radiations at the same biological effectiveness, usually ED_{50}. The endpoints used in this project are functional damage, measured with breathing rate elevation, and histological damage, scored with a histological system. The details of the weighting factor determination are reported in Chapters 4 and 5, with corresponding endpoints. The clinical implications for BNCT of the weighting factors measured in this project and possible future work are discussed in Chapter 6.

1.4 References

1. Coderre JA, Morris GM. The radiation biology of boron neutron capture therapy. *Radiation Research* 1999;151:1-18.
2. Locher GL. Biological effects and therapeutic possibilities of neutrons. *Am. J. Roentgenol.* 1936;36:1 - 13.
3. Slatkin DN. A history of boron neutron capture therapy of brain tumours. Postulation of a brain radiation dose tolerance limit. *Brain* 1991;114:1609-1629.
4. Hatanaka H, Nakagawa Y. Clinical results of long-surviving brain tumor patients who underwent boron neutron capture therapy. *Int*ernational Journal Radiation Oncology Biology Physics 1994;28:1215-1216.
5. Mishima Y, Ichihashi M, Tsuji M, *et al.* Treatment of malignant melanoma by selective thermal neutron capture therapy using melanoma-seeking compound. *Strahlenther Onkol* 1989;165:340-342.
6. Mishima Y, Ichihashi M, Nakanishi T, *et al.* Cure of malignant melanoma by single thermal neutron capture treatment using melanoma seeking compounds: ^{10}B/melanogenesis interaction to *in vitro/ in vivo* radiobiological analysis to preclinical studies. In: Fairchild RG, Brownell G, editors. Proceedings of the First International Symposium on Neutron Capture Therapy. Upton: Brookhaven National Laboratory; 1983. pp. 355 - 364.
7. Coderre JA, Button TM, Micca PL, *et al.* Neutron capture therapy of the 9L rat gliosarcoma using the p-boronophenylalanine-fructose complex. *Int J Radiat Oncol Biol Phys* 1994;30:643-652.
8. Barth RF, Yang WL, Rotaru JH, *et al.* Boron neutron-capture therapy of brain tumors: Enhanced survival following intracarotid injection of either sodium borocaptate or boronophenylalanine with or without blood-brain-barrier disruption. *Cancer Research* 1997;57:1129-1136.
9. Ceberg CP, Brun A, Kahl SB, *et al.* A comparative study on the pharmacokinetics and biodistribution of boronated porphyrin (BOPP) and sulfhydryl boron hydride (BSH) in the RG2 rat glioma model. *J Neurosurg* 1995;83:86-92.
10. Moss RL, Aizawa O, Beynon D, *et al.* The requirements and development of neutron beams for neutron capture therapy of brain cancer. *J Neurooncol* 1997;33:27-40.
11. Harling OK, Riley KJ, Newton TH, *et al.* The Fission Converter Based Epithermal Neutron Irradiation Facility at the MIT Reactor. *Nuclear Science and Engineering* 2002;140:223-240.
12. Palmer MR, Goorley JT, Kiger III WS, *et al.* Treatment planning and dosimetry for the Harvard-MIT Phase I clinical trial of cranial neutron capture therapy. *Int J Radiat Oncol Biol Phys* 2002;53:1361-1379.
13. Busse P, Zamenhof R, Madoc-Jones H, *et al.* Clinical follow-up of patients with melanoma of the extremity treated in a phase I boron neutron capture therapy protocol. In: B Larsson JC, R Weinreich, editor. Advances in Neutron Capture Therapy. Volume I, Medicine and Physics. Amsterdam: Elsevier Science B.V.; 1997. pp. 60-64.

14. Busse PM, Harling OK, Palmer MR, *et al.* A critical examination of the results from the Harvard-MIT NCT program phase I clinical trial of neutron capture therapy for intracranial disease. *Journal of Neuro-Oncology* 2003;62:111-121.

15. Chanana A, Capala J, Chadha M, *et al.* Boron neutron capture therapy for glioblastoma multiforme: interim results from the phase I/II dose-escalation studies. *Neurosurgery* 1999;44:1182-1192; discussion 1192-1183.

16. Chadha M, Capala J, Coderre JA, *et al.* Boron neutron-capture therapy (BNCT) for glioblastoma multiforme (GBM) using the epithermal neutron beam at the Brookhaven National Laboratory. *Int. J. Radiat. Oncol. Biol. Phys.* 1998;40:829-834.

17. Diaz AZ. Assessment of the results from the phase I/II boron neutron capture therapy trials at the Brookhaven National Laboratory from a clinician's point of view. *J Neurooncol* 2003;62:101-109.

18. Capala J, Stenstam BH, Skold K, *et al.* Boron neutron capture therapy for glioblastoma multiforme: clinical studies in Sweden. *J Neurooncol* 2003;62:135-144.

19. Joensuu H, Kankaanranta L, Seppala T, *et al.* Boron neutron capture therapy of brain tumors: clinical trials at the finnish facility using boronophenylalanine. *J Neurooncol* 2003;62:123-134.

20. Gonzalez SJ, Bonomi MR, Santa Cruz GA, *et al.* First BNCT treatment of a skin melanoma in Argentina: dosimetric analysis and clinical outcome. *Applied radiation and isotopes* 2004;61:1101-1105.

21. Kageji T, Nagahiro S, Kitamura K, *et al.* Optimal timing of neutron irradiation for boron neutron capture therapy after intravenous infusion of sodium borocaptate in patients with glioblastoma. *International Journal Radiation Oncology Biology Physics* 2001;51:120-130.

22. Nakagawa Y, Pooh K, Kobayashi T, *et al.* Clinical review of the Japanese experience with boron neutron capture therapy and a proposed strategy using epithermal neutron beams. *J Neurooncol* 2003;62:87-99.

23. Kageji T, Nagahiro S, Uyama S, *et al.* Histopathological findings in autopsied glioblastoma patients treated by mixed neutron beam BNCT. *J Neurooncol* 2004;68:25-32.

24. Kabalka GW, Nichols TL, Smith GT, *et al.* The use of positron emission tomography to develop boron neutron capture therapy treatment plans for metastatic malignant melanoma. *J Neurooncol* 2003;62:187-195.

25. Wazer D, Zamenhof R, Madoc-Jones H, *et al.* Boron Neutron Capture Therapy. In: Mauch P, Loeffler J, editors. Radiation Oncology: Technology and Biology. New York: Saunders; 1994.

26. Madoc-Jones H, Zamenhof, R., Solares, G., Harling, O., Yam, C.-S., Riley, K., Kiger, S., Wazer, D., Rogers, G., and Atkins, M. A Phase-I dose escalation trial of boron neutron capture therapy for subjects with metastatic subcutaneous melanoma of the extremities. In: Mishima Y, editor. Cancer Neutron Capture Therapy. New York: Plenum Press; 1996. pp. 707-716.

27. Kiger III WS. Developments in micro- and macro dosimetry of Boron Neutron Capture Therapy. Department of Nuclear Engineering. Cambridge, Massachusetts: Massachusetts Institute of Technology; 2000.

28. Mughabghab SF, Kinsey RR, Dunford CL. Neutron cross sections series. New York: Academic Press; 1981.

29. Hall EJ. Radiobiology for the Radiologist. Vol 1988. Philadelphia: J.B. Lippincott Company; 1988.

30. Morris GM, Coderre JA, Hopewell JW, *et al.* Response of the central nervous system to boron neutron capture irradiation: evaluation using rat spinal cord model. *Radiother Oncol* 1994;32:249-255.

31. Morris GM, Coderre JA, Smith DR, *et al.* A rat model of oral mucosal response to boron neutron capture irradiation. In: Hawthorne MF, Shelly K, Wiersema RJ, editors. Frontiers in Neutron Capture Therapy. New York: Kluwer Academic/Plenum Publishers; 2001. pp. 1273-1277.

32. Morris GM, Coderre JA, Hopewell JW, *et al.* Response of rat skin to boron neutron capture therapy with *p*-boronophenylalanine or borocaptate sodium. *Radiother. Oncol.* 1994;32:144 - 153.

33. MuCullagh P, Nelder JA. Generalized linear models. Second ed. London: Chapman and Hall; 1990.

34. Dobson AJ. An introduction to generalized linear models. Second ed. London: Chapman and Hall; 2001.

35. Cardozo BL, H. Z, van Bekkum DW, *et* al. Lung damage following bone marrow transplantation: I. the contribution of irradiation. *International Journal of Radiation Oncology Biology Physics* 1985;11:907-914.

36. Torres PY, Bross DS, Lam WC, *et al.* Risk factors in interstitial pneumonitis following bone marrow transplantation. *International Journal of Radiation Oncology Biology Physics* 1982;8:1301-1307.

37. Abratt RP, Morgan GW, Silvestri G, *et al.* Pulmonary complications of radiation therapy. *Clinics in chest medicine* 2004;25:167-177.

38. Anscher MS, Kong F, Marks LB, *et al.* Changes in plasma transforming growth factor beta during radiotherapy and the risk of symptomatic radiation-induced pneumonitis. *International Journal of Radiation Oncology Biology Physics* 1997;37:253-258.

39. Groover TA, Christie AC, Merritt EA. Intrathoracic changes following roentgen treatment of breast carcinoma. *American Journal of Roentgenology* 1923;10:471.

40. Rubin P, Casarett GW, editors. Respiratory system. Philadelphia: W. B. Saunders Company; 1968.

41. Gross NJ. Pulmonary Effects of Radiation-Therapy. *Annals of Internal Medicine* 1977;86:81-92.

42. Coggle JE, Lambert BE, Moores SR. Radiation effects in the lung. *Environmental health perspectives* 1986;70:261-291.

43. Phillips TL. An ultrastructural study of the development of radiation injury in the lung. *Radiology* 1966;87:49-54.

44. Perez CA, Brady LW. Thoracic radiotherapy: complications and injury to normal tissue. In: Principles and practice of radiation oncology. New York: Lippincott Williams & Wilkins; 2002.

45. Maisin JR. The ultrastructure of the lung of mice exposed to a supra-lethal dose of ionizing radiation on the thorax. *Radiation Research* 1970;44:545-564.

46. Travis EL. The sequence of histological-changes in mouse lungs after single doses of X-rays. *Inter*national Journal of Radiation Oncology Biology Physics 1980;6:345-347.

47. Murray JC. Radiation-Induced Fibrosis - the Structure/Function Relationship. *Scanning Microscopy* 1994;8:79-87.

48. Moosavi H, McDonald S, Rubin P, *et al.* Early radiation dose-response in lung: an ultrastructural study. *International Journal of Radiation Oncology Biology Physics* 1977;2:921-931.

49. Siemann DW, Hill RP, Penney DP. Early and Late Pulmonary Toxicity in Mice Evaluated 180 and 420 Days Following Localized Lung Irradiation. *Radiation Research* 1982;89:396-407.

50. Down JD. The nature and relevance of late lung pathology following localized irradiation of the thorax in mice and rats. *Br J Cancer Suppl* 1986;7:330-332.

51. Down JD, Nicholas D, Steel GG. Lung damage after hemithoracic irradiation: dependence on mouse strain. *Radiother Oncol* 1986;6:43-50.

52. Hopewell JW, Rezvani M, Moustafa HF. The pig as a model for the study of radiation effects on the lung. *Int J Radiat Biol* 2000;76:447-452.

53. Engelstad RB. Pulmonary lesions after roentgen and radium irradiation. *American Journal of Roentgenology* 1940;43:676.

54. Giri PGS, Kimler BF, Giri UP, *et al.* Comparison of single, fractionated and hyperfractionated irradiation on the development of normal tissue damage in rat lung. *Inter*national Journal of Radiation Oncology Biology Physics 1985;11:527-534.

55. Lehnert S, el-Khatib E. The use of CT densitometry in the assessment of radiation-induced damage to the rat lung: a comparison with other endpoints. *International Journal of Radiat*ion Oncology Biology Physics 1989;16:117-124.

56. Franko AJ, Sharplin J. Development of fibrosis after lung irradiation in relation to inflammatoin and lung function in a mouse strain prone to fibrosis. *Radiation Research* 1994;140:347-355.

57. Teates CD. Effects of unilateral thoracic irradiation on lung function. *Journal of Applied Physiology* 1965;20:628-636.

58. McChesney SL, Gillette EL, Powers BE. Response of the canine lung to fractionated irradiation: pathologic changes and isoeffect curves. *Internat*ional Journal of Radiation Oncology Biology Physics 1989;16:125-132.

59. Poulson JM, Vujaskovic Z, Gillette SM, *et al.* Volume and dose-response effects for severe symptomatic pneumonitis after fractionated irradiation of canine lung. *International Journal* of Radiation Biology 2000;76:463-468.

60. Travis EL, Brightwell D, Aiken M, *et al.* Whole-Body Plethysmography as a Non-Invasive Assay of Toxic Lung Injury in Mice - Studies with the Pulmonary Alkylating Agent and Cyto-Toxin, 4-Ipomeanol. *Toxicology and Appl*ied Pharmacology 1982;66:193-200.

61. Feaster GR, Kimler BF, Henderson SD, *et al.* Simple Plethysmograph for Measuring Respiration Rates in Rats with Lung Damage. *Review of Scientific Instruments* 1984;55:1058-1060.

62. Haston CK, Newcomb CH, Grant K, *et al.* Ultrasonic Measurements of Breathing Rate in Rats and Computer-Assisted Analysis. *International Journal of Radiation Oncology Biology Physics* 1993;27:651-657.

63. Travis EL, Down JD, Holmes SJ, *et al.* Radiation pneumonitis and fibrosis in mouse lung assayed by respiratory frequency and histology. *Radiat Res* 1980;84:133-143.

64. Franko AJ, Sharplin J. Assessment of radiation-induced lung injury in mice using carbon-monoxide uptake - correlation with histologically visible damage. *Radiation Research* 1993;133:245-251.

65. Peterson LM, Evans ML, Graham MM, *et al.* Vascular response to radiation injury in the rat lung. *Radiation Research* 1992;129:139-148.

66. Vujaskovic Z, Down JD, van t' Veld AA, *et al.* Radiological and functional assessment of radiation-induced lung injury in the rat. *Exp Lung Res* 1998;24:137-148.

67. Travis EL, Tucker SL. The relationship between functional assays of radiation response in the lung and target cell depletion. *Br J Cancer Suppl* 1986;7:304-319.

68. Crapo JD, Young SL, Fram EK, *et* al. Morphometric characteristics of cells in the alveolar region of mammalian lungs. *Am Rev Respir Dis* 1983;128:S42-46.

69. Adamson TYR, Bowden DH. The type II cell as progenitor of alveolar epithelial regeneration, a cytodynamic study in mice after exposure to oxygen. *Lab Invest* 1974;30:35.

70. Ballard PL. Hormonal aspects of fetal lung development. In: Farrell PM, editor. Lung Development: Biological and Clinical Perspectives. Vol 2. New York: Academic; 1982. pp. 205-253.

71. Sharplin J, Franko AJ. Irradiation of mouse lungs causes a dose-dependent increase in lung weight. *International Journal of Radiation Oncology Biology Physics* 1982;8:1065-1069.

72. Evans ML, Graham MM, Mahler PA, *et al.* Changes in vascular permeability following thorax irradiation in the rat. *Radiation Research* 1986;107:262-271.

73. Ahier RG, Anderson RL, Coultas PG. Response of mouse lung to irradiation 1. Alterations in alveolar surfactant after neutrons and X-rays. *Radiotherapy and oncology* 1985;3:61-68.

74. McDonald S, Rubin P, Phillips TL, *et al.* Injury to the lung from cancer therapy: Clinical syndromes, measurable endpoints, and potential scoring systems. *Int. J. Radiat. Oncol. Biol. Phys.* 1995;31:1187-1203.

75. Pauluhn J, Baumann M, Hirth-Dietrich C, *et al.* Rat model of lung fibrosis: comparison of functional, biochemical, and histopathological changes 4 months after single irradiation of the right hemithorax. *Toxicology* 2001;161:153-163.

76. Rubin P, Siemann DW, Shapiro DL, *et al.* Surfactant release as an early measure of radiation pneumonitis. *International Journal of Radiation Oncology Biology Physics* 1983;9:1669-1673.

77. Stratford MRL, Watfa RR, Murray JC, *et al.* Determination of collagen and protein turnover by HPLC. *J Chromat (Biomed Appl)* 1990;526:383-395.

78. Lehnert BE, Dethloff LA, Finkelstein JN, *et al.* Temporal Sequence of Early Alterations in Rat Lung Following Thoracic X-Irradiation. *Int. J. Radiat. Biol.* 1991;60:657 - 675.

79. Meistrich ML, Williams MV, Soranson J, *et al.* Increased collagen and fluid content of mouse kidneys at 9 months after single or fractionated X irradiation. *Radiation Research* 1984;99:185-201.

80. Buttner C, Skupin A, Reimann T, *et al.* Local production of Interleukin-4 during radiation-induced pneumonitis and pulmonary fibrosis in rats: macrophages as prominent source of Interleukin-r. *Am. J. Respir. Cell Mol. Biol.* 1997;17:315-325.

81. Travis EL, Parkins CS, Holmes SJ, *et al.* WR-2721 protection of pneumonitis and fibrosis in mouse lung after single doses of x rays. *Int J Radiat Oncol Biol Phys* 1984;10:243-251.

82. Bienenstock J, Tomioka M, Stead R, *et al.* Mast cell involvement in various inflammatory processes. *Am Rev Respir Dis* 1987;135:S5-S8.

83. Choi KL, Claman HN. Mast cells, fibroblasts, and fibrosis. *Immunology Research* 1987;6:145-152.

84. Law MP, Hornsey S. Collagen content in lungs of mice after X-ray irradiation. *Radiation Research* 1976;65:60-70.

85. Ward WF, Shin-Hoellwarth A, Tuttle RD. Collagen accumulation in the irradiated rat lung: modification by D-penicillamine. *Radiology* 1983;146:533-537.

86. Watanabe S, Watanabe K, Oishi T, *et al.* Mast cells in the rat alveolar septa undergoing fibrosis after ionizing irradiation. Ultrastructural and histochemical studies. *Lab Invest* 1974;31:555-567.

87. Nisson K, Henriksson R, Hellstrom S, *et al.* Hyaluronan reflects the pre-fibrotic inflammation in irradiated rat lung: cocomitant analysis of parenchymal tissues and bronchoalveolar lavage. *International Journal of Radiation Biology* 1990;58:519-530.

88. Rubin P, Finkelstein J, McDonald S, *et al.* The identification of new early molecular mechanisms in the pathogenesis of radiation induced pulmonary fibrosis. *International Journal of Radiation Oncology Biology Physics* 1991;21:163.

89. Datta R, Rubin E, Sukhatme V, *et al.* Ionizing radiation activates transcription of the EGR1 gene via CArG elements. *Proc. Natl. Acad. Sci. USA* 1992;89:10149-10153.

90. Rubin P, Johnston CJ, Williams JP, *et al.* A perpetual cascade of cytokines postirradiation leads to pulmonary fibrosis. *International Journal of Radiation* Oncology Biology Physics 1995;33:99-109.

91. Franko AJ, Sharplin J, Ward WF, *et al.* Evidence of two patterns of inheritance of sensitivity to induction of lung fibrosis in mice by radiation, one of which involves two genes. *Radiation Research* 1996;146:68-74.

92. Haston CK, Travis EL. Murine susceptibility to radiation-induced pulmonary fibrosis is influenced by a genetic factor implicated in susceptibility to bleomycin-induced pulmonary fibrosis. *Cancer Res* 1997;57:5286-5291.

93. Williams JP, Hernady E, Johnston CJ, *et al.* Effect of administration of lovastatin on the development of late pulmonary effects after whole-lung irradiation in murine model. *Radiation Research* 2004;161:560-567.

94. Maity A, Kao GD, Muschel RJ, *et al.* Potential molecular targets for manipulating the radiation response. *International Journal of Radiation Oncology Biology Physics* 1997;37:639-653.

95. Moses HL, Branum EL, Proper JA, *et al.* Transforming growth factor production by chemically transformed cells. *Cancer Research* 1981;41:2842.

96. Roberts AB, Anzano MA, Lamb LC, *et al.* New class of transforming growth factors potentiated by epithermal growth factor: isolation from non neoplastic tissues. *Proc. Natl. Acad. Sci. USA* 1981;78:5339.

97. Jordana M, Ohno I, Xing Z, *et al.* Cytokines in lung and airwarys fibrosis. *Regional Immunology* 1993;5:201-206.

98. Burger A, Loffler H, Bamberg M, *et al.* Molecular and cellular basis of radiation fibrosis. *International Journal of Radiation Biology* 1998;73:401-408.

99. Martin M, Lefaix JL, Delanian S. TGF-beta1 and radiation fibrosis: A master switch and a specific therapeutic target? *International Journal of Radiation Oncology Biology Physics* 2000;47:277-290.

100. Vodovotz Y, Bogdan C, Paik J. Mechanisms of suppression of macrophage nitric oxide release by TGF-beta. *J Exp Med* 1993;178:6005-6013.

101. Roberts AB, Sporn MB. The transforming growth factor-betas. In: Sporn MB, Roberts AB, editors. Peptide growth factors and their receptors. Vol 1. Berlin: Springer-Verlag; 1990. pp. 419-472.

102. Travis EL, Meistrich ML, Finchneimeyer MV, *et al.* Late Functional and Biochemical-Changes in Mouse Lung after Irradiation - Differential-Effects of WR-2721. *Radiation Research* 1985;103:219-231.

103. Vujaskovic Z, Batinic-Haberle I, Rabbani ZN, *et al.* A small molecular weight catalytic metalloporphyrin antioxidant with superoxide dismutase (SOD) mimetic properties protects lung from radiation-induced injur. *Free Radical Biology and Medicine* 2002;33:857-863.

104. Kang SK, Rabbani ZN, Folz RJ, *et al.* Overexpression of extracellular superoxide dismutase protects mice from radiation-induced lung injury. *International Journal of Radiation Oncology Biology Physics* 2003;57:1056-1066.

105. Khan MA, Van Dyk J, Yeung IWT, *et al.* Partial volume rat lung irradiation; assessment of early DNA damage in different lung regions and effect of radical scavengers. *Radiotherapy and oncology* 2003;66:95-102.

106. Graham MM, Evans ML, Dahlen DD, *et al.* Pharmacological alteration of the lung vascular response to radiation. *Int J Radiat Oncol Biol* Phys 1990;19:329-339.

107. Ward WF, Molteni A, Tsao CH, *et al.* Radiation pneumotoxicity in rats: modification by inhibitors of angiotensin converting enzyme. *International Journal of Radiation Oncology Biology Physics* 1992;22:623-625.

108. Ward WF, Molteni A, Tsao CH, *et al.* Captopril reduces collagen and mast cell accumulation in irradiated rat lung. *International Journal of Radiation Oncology Biology Physics* 1990;19:1405-1409.

109. Molteni A, Moulder JE, Cohen EF, *et al.* Control of radiation-induced pneumopathy and lung fibrosis by angiotensin-converting enzyme inhibitors and an angiotensin II type 1 receptor blocker. *Int J Radiat Biol* 2000;76:523-532.

110. Van Dyk J, Keane TJ, Kan S, *et al.* Radiation pneumonitis following large single dose irradiation: a re-evaluation based on absolute dose to lung. *International Journal of Radiation Oncology Biology Physics* 1981;7:461-467.

111. Kwa SLS, Lebesque JV, Theuws JCM, *et al.* Radiation pneumonitis as a function of mean lung dose: an analysis of pooled data of 540 patients. *International Journal of Radiation Oncology Biology Physics* 1998;42:1-9.

112. Seppenwoolde Y, Lebesque JV, Jaeger K, *et al.* Comparing different NTCP models that predict the incidence of radiation pneumonitis. *International Journal of Radiation* Oncology Biology Physics 2003;55:724-735.

113. Travis EL, Down JD. Repair in mouse lung after split doses of X rays. *Radiat Res* 1981;87:166-174.

114. Travis EL, Harley RA, Fenn JO, *et al.* Pathologic-Changes in Lung Following Single and Multi-Fraction Irradiation. *International Journal of Radiation Oncology Biology Physics* 1977;2:475-490.

115. Littman P, Meadows AT, Polgar G, *et al.* Pulmonary function in survivors of Wilms' tumor: patterns of impairment. *Cancer* 1976;37:2773-2776.

116. Wohl ME, Griscom NT, Traggis DG, *et al.* Effects of therapeutic irradiation delivered in early childhood upon subsequent lung function. *Pediatrics* 1975;55:507-514.

117. Travis EL, Liao ZX, Tucker SL. Spatial heterogeneity of the volume effect for radiation pneumonitis in mouse lung. *International Journal of Radiation Oncology Biology Physics* 1997;38:1045-1054.

118. Tucker SL, Liao ZX, Travis EL. Estimation of the spatial distribution of target cells for radiation pneumonitis in mouse lung. *International Journal of Radiation Onco*logy Biology Physics 1997;38:1055-1066.

119. Novakova-Jiresova A, van Luijk P, van Goor H, *et al.* Pulmonary radiation injury: Identification of risk factors associated with regional hypersensitivity. *Cancer Research* 2005;65:3568-3576.

120. Imahori Y, Mineura K, Fujii R, *et al.* Simulation studies of BNCT for lung cancer [abstract]. The 11th World Congress on Neutron Capture Therapy (ISNCT-11). Waltham, MA; 2004.

CHAPTER TWO

Design of a Delimiter for Rat Lung Irradiations in the MITR-II Thermal Neutron Beam

2.1 Introduction

Boron neutron capture therapy (BNCT) is a binary therapy that has the potential to selectively target high linear energy transfer (LET) radiation to tumors while sparing normal tissue (1). BNCT requires the selective delivery of a boron-labeled compound to tumor tissue to attain therapeutic advantage. The tumor region, is then irradiated with low-energy neutrons. When a nucleus of the minor stable isotope of boron, ^{10}B, captures a thermal neutron, it immediately undergoes a fission reaction producing highly-energetic, short-range disintegration products (2). The short track lengths of the alpha (9 μm) and lithium (5 μm) particles produced by the boron neutron capture reaction essentially limit their radiation damage to cells containing ^{10}B or the nearest neighbors. Concurrently, a non-specific background from the neutron beam delivers dose to both tumor and the normal tissues. Thus the dose to tumor and normal tissues is composed of the boron and background beam components, with the boron component in tumor considerably higher due to the selective uptake of boron from presently available boron compounds. Several reviews on BNCT have recently been published (3-7).

In tissue, the boron neutron capture irradiation produces a complex mixture of radiation types that differ in their LET characteristics and, hence, in their relative biological effectiveness. The dose components comprise (8): a) thermal neutron dose, mainly delivered by the protons produced by the thermal neutron capture reaction $^{14}N(n,p)^{14}C$; b) fast neutron dose (neutron energies above 0.4 eV), primarily from energy released by elastic collisions of fast neutrons on hydrogen $^{1}H(n,n')^{1}H$; c) photon dose, comprised of incident photons in the neutron beam incident on the target, and induced photons arising in tissue primarily from the capture of thermal neutrons by hydrogen: $^{1}H(n,\gamma)^{2}H$; and d) ^{10}B dose, arising from the heavy charged particles released by thermal neutron capture reaction $^{10}B(n,\alpha)^{7}Li$. The biological weighting factors, relative biological effectiveness (RBE) (7) for each of the high-LET components, are employed to express total BNCT radiation doses in photon-equivalent terms. An analogous terminology, compound biological effectiveness (CBE) factor, is implemented since the weighting factor for ^{10}B dose is strongly influenced by the characteristics, primarily the microdistribution, of the specific boron compound (7). The convention recommended for the description of the total biologically weighted BNCT dose is (9):

$$D_w = w_\gamma D_\gamma + w_F D_F + w_T D_T + w_B D_B, \qquad (1)$$

where w_γ, w_F, w_T and w_B are weighting factors for photon dose, fast neutron dose, thermal neutron dose and ^{10}B dose, respectively.

BNCT clinical trials are underway at a number of sites worldwide (9-14). In the period between 1994 and 1999, researchers at Harvard and MIT carried out clinical trials for patients with glioblastoma and melanoma metastatic to the brain (9, 11), or subcutaneous melanoma of the extremities (15). Two patients treated for brain tumors in the initial Harvard-MIT BNCT clinical trial developed an acute respiratory distress syndrome (ARDS) that proved fatal; one

other patient developed an acute pneumonitis, but recovered following intensive supportive care. The physical dose at several points of the lung was measured afterwards in an Anderson/Rando (ART) head, neck and chest phantom, with the phantom repeating various patient positions during the cranial BNCT irradiations (16). At the time, the BNCT dosimetry and radiobiology of the lung during brain irradiations was not well defined and so it was not clear whether the ARDS was due to the radiation dose to the lung either from beam leakage around the irradiation port or from a dose scattered from the head or a result of completely different causes unrelated to the BNCT treatments.

The normal lung dose response to BNCT irradiation must be established to calculate the corresponding RBE and CBE factors and to determine the total weighted tolerance dose of the normal lung in BNCT. Rat was chosen as the experimental subjects since rat lung responses to photon irradiations have been reported in the literature (17-19). Shielding of the adjacent radiosensitive normal tissues during the lung irradiations is essential to avoid death from acute radiation responses of the normal tissues other than lung during the long follow up period required for lung irradiation endpoints ($\geq$ 6 months). With neutrons, the relatively small size of the rat complicates the shielding design in BNCT, since low energy neutrons are far more difficult to efficiently collimate than photons.

This Chapter describes an approach using Monte Carlo radiation transport simulations to design a rat lung neutron irradiation experiment. The specific goals include selecting a suitable beam from the two NCT neutron beam facilities at the MITR-II and, designing and optimizing a beam delimiter for the rat lung irradiations. The simulation design was validated with measurements in two cylindrical water-filled rat phantoms.

2.2 Materials and Methods

2.2.1 Neutron beam facilities

The MITR-II Research Reactor has a maximum operating power of 5 MW with neutron facilities for multiple research purposes (20). The core burns highly enriched ^{235}U fuel and is cooled by light water and moderated by heavy water. Neutrons from the core are reflected and moderated by a heavy water tank and further reflected by the surrounding graphite reflector. The maximum thermal neutron flux of 10^{14} n/cm^{2}s is produced below the core in the D_2O reflector tank (21).

One neutron facility at the MITR-II currently available for human or animal BNCT irradiations is the vertical M011 thermal neutron beam port (22). The M011 beam line extends from below the D_2O reflector tank to the beam port in the medical room located in the basement of the reactor facility. It measures about 2.3m long, including in series, a D_2O blister tank embedded in the D_2O reflector tank, an H_2O shutter tank, a tapered graphite collimator, a movable boral shutter, a movable lead shutter, a bismuth plug fit into a tapered bismuth collimator. A recently constructed borated polyethylene delimiter is fixed beneath the lead shutter and contains four fission counters to monitor the neutron beam. The D_2O filter tank efficiently moderates and thermalizes the fast fission neutrons from the core to produce an intense, high purity thermal neutron beam (E_{th}<0.4 eV) with a negligible fast neutron dose component. The graphite collimator improves the directionality of the neutron beam and conducts the neutrons to the beam port. The bismuth plug and bismuth collimator close to the end of the beam line provide photon filtration for the neutron beam. The borated polyethylene plate delimiter reduces the ambient dose in the medical room away from the beam port. A cross section of the M011 beam is plotted in Fig. 2.1. The M011 beam is suitable for small animal irradiations and superficial human tumors such as melanoma with its low energy spectrum and

high intensity (~10^{10}n/cm^{2}s) (23, 24). The circular beam aperture of the M011 is 12 cm in diameter and is able to irradiate two rats simultaneously.

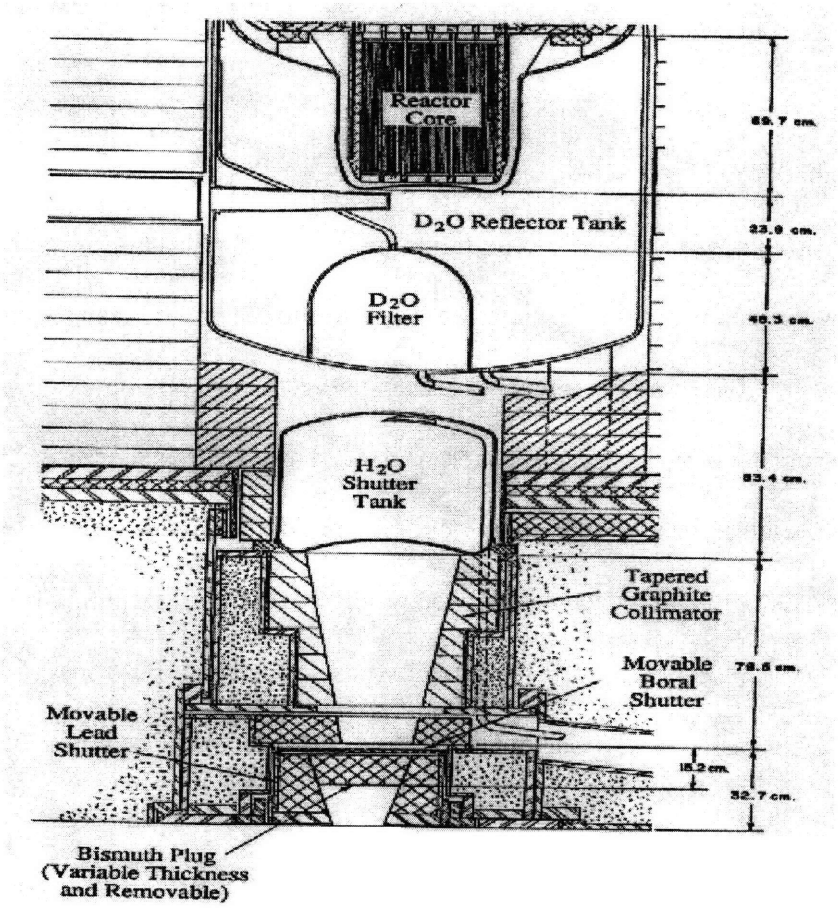

Fig. 2.1 The cross-section of the M011 beam at the MITR-II (23).

The M011 beam line was previously occupied by the M067 epithermal neutron beam that was used for the Phase I clinical trials of BNCT at the MITR-II in the 1990s (9, 11, 25). In the M067 beam, the D_2O blister tank was emptied to reduce the thermalization. Additional aluminum and sulfur filters were installed in the graphite collimator to filter out fast neutrons (25, 26). After the advanced fission converter epithermal neutron beam was constructed and

commissioned, the M067 beam was decommissioned and converted back to the M011 thermal beam. More detailed descriptions of the two beam lines is available in the literature (23, 24).

The other neutron facility at the MITR-II eligible for BNCT radiobiology experiments is the horizontal fission converter beam (FCB) (21, 27, 28). The FCB is a high-intensity epithermal neutron beam (0.4 eV<E_{epi}<10 KeV) with very low, essentially negligible, fast neutron and photon contamination designed for deep-seated tumors (21, 27, 29). The fission converter is located outside the graphite reflector surrounding the D_2O reflector tank of the reactor core. A 14-inch window through the graphite allows neutrons from the core to reach the fission converter after moderation by H_2O, graphite and D_2O. The subcritical fission converter, contained in an aluminum tank and cooled by heavy water, is driven by the reactor core. In the current configuration of converter fuel, the maximum power of the fission converter is 83.5 kW, controlled by a cadmium shutter located between the core and the fission converter. The beam line measures about 2m long from the fission converter to the beam port, including in series: an Al and Teflon (PTFE) moderator surrounded by a lead reflector, a cadmium thermal neutron filter, a lead photon filter, a lead collimator surrounded by high density concrete and, a set of leaded-lithiated-epoxy patient collimators with inner diameters varying from 16 to 8 cm. The FCB is further controlled with two in line shutters, the water shutter and the mechanical shutter. Detailed descriptions of the FCB are available elsewhere (21, 27, 29, 30). Since the beam aperture diameter of the FCB varies from 12 to 16 cm, 2 to 3 rats can be irradiated at once.

2.2.2 Computational methods

Monte Carlo N-Particle (MCNP) is a well-benchmarked simulation code commonly used in neutron, photon and electron transport calculations (31). A computational model of the reactor core, as well as the M067 beam (32), were previously constructed in MCNP, and provided the

beam source description for the treatment planning computations in clinical trials during the 1990s (9). This MCNP model was benchmarked against experiments at various positions, including the reactor core (32, 33) and the beam port (34), and became the basis of the MCNP model of the reconstructed M011 facility. The MCNP model of the MITR-II core was also used in design studies for the FCB. This model was later validated against measurements at both the fission converter position (21, 35) and the beam port (27, 36, 37), and was similarly used for treatment planning.

Since the primary disadvantage of the Monte Carlo simulations of large structures, such as the reactor neutron beams, is the lengthy computer time required to achieve good statistics, the MCNP code offers several techniques to improve computational efficiency (31). Surface source generation, which allows separating large transport calculations into smaller segments, was used in the MITR-II MCNP model. The model was segmented into several divisions and a surface source file at the boundary of each segment was written, recording every particle passing that surface. The surface source then served as the neutron source in calculations of the next segment. A variance reduction technique, the energy dependent weight window, was also used in each simulation segment to improve computational efficiency. The weight window values were calculated manually (33) or calculated using MCNP weight window generator. This technique shifts computational emphasis to the particles coming from the source with higher probabilities to reach the regions of interest and produces improved statistics within the same computer time.

In the MCNP simulations of the FCB, the model and particle transport calculations was separated into three parts and two surface sources files were written at the corresponding planes. The first part encompasses the reactor core, and a source file was written at the edge of the

graphite reflector, 10 cm before the fission converter. A criticality calculation of the core was performed and an energy-independent weight window for neutrons only (32) was applied to enhance the number of neutrons reaching the source plane. The surface source, with records of all neutrons passing through the plane, was fit in the upstream region of the second segment, which includes the region from the fission converter to the end of the mechanical lead shutter, where a second surface source was written. In the simulations of the second segment, energy-dependent weight windows for both neutrons and photons were used to enhance the number of particles reaching the plane at the shutter. The second surface source was set at the upstream portion of the third segment, in which the simulation optimization of the FCB suitability for the rat lung irradiations was carried out.

In the M011 MCNP model, a similar calculation scheme was applied, and the simulations were split into four segments with three neutron source planes. The first segment was the criticality calculation in the core and to construct a fission volume neutron source. No weight windows were used in this stage. The volume source then was read into the second stage, and neutrons were transported through the beam line to the core reflector boundary in the middle of the light water shutter, where the second neutron source was written. In the third stage, neutrons transport from the water shutter to the end of the bismuth collimator at the beam port, where the third neutron source plane was written. The last segment, with the third source plane as the neutron source, was used in the simulation design of the delimiter for the rat lung irradiations. Weight windows for neutrons only were applied in the last three stages; thus no photon particles were recorded in any of the three sources. A uniform importance was assigned to all photons in the last simulation segment in the M011 beam where the delimiter was designed, to tally induced photon dose rate in the rat phantoms.

Fig. 2.2 illustrates the general simulation setup in the last segment of the FCB and M011 MCNP model, with the neutron source planes serving as the beam source. Two rat models, positioned in the shielding box with the delimiter mounted on the top, were located next to the beam port. Neutron transport from the source through the objects was simulated and dose rates and neutron fluxes were tallied in the rat models, to select a neutron beam and optimize the delimiter geometry.

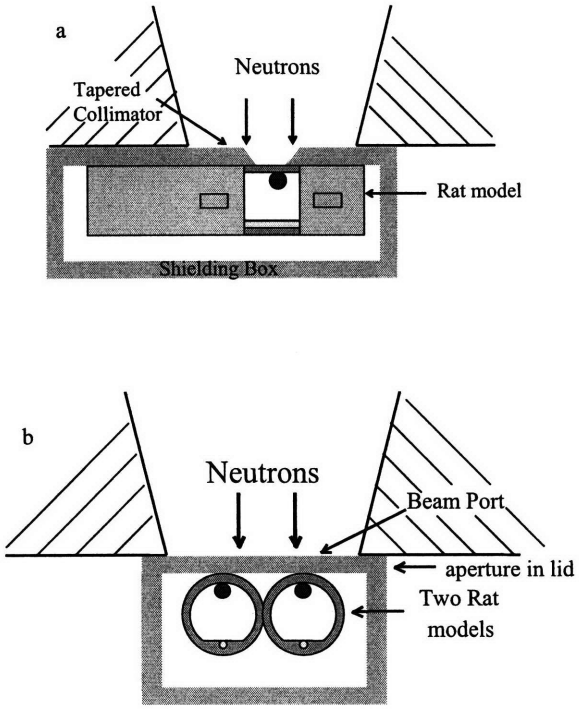

Fig. 2.2 The sagittal (a) and transverse (b) cross-section of the rat lung irradiation configuration used in simulations.

2.2.3 Detailed rat computational model

A detailed rat model was constructed in the MCNP simulations that included the critical anatomical features. The cross-sections are illustrated in Fig. 2.3. The rat model was defined as a cylinder 5 cm in diameter and 20 cm long. The lung region was approximated as a 4 cm

diameter cylinder, 4 cm long, located at 4.7 cm from the top of the rat phantom, filled with ICRU 46 (38) lung tissue of low density (0.26 g/cm^3). A cylindrical spinal cord of 0.5 cm in diameter and spherical heart of 1.2 cm in diameter were embedded in this region to approximate the true anatomy. Adult brain composition and adult healthy heart (38) composition were used for spinal cord and heart tissue, respectively. A concentric layer, 0.5 cm-thick, and of adult skin (38) composition, surrounds the lung region, designating the rat skin. The rest of the rat cylinder other than the lung region was filled with average soft tissue (38). Two radiosensitive regions representing intestines and esophagus were defined as cylinders 1-cm in diameter and 2-cm long, located along the central axis of the rat cylinder and 1 cm from the lung.

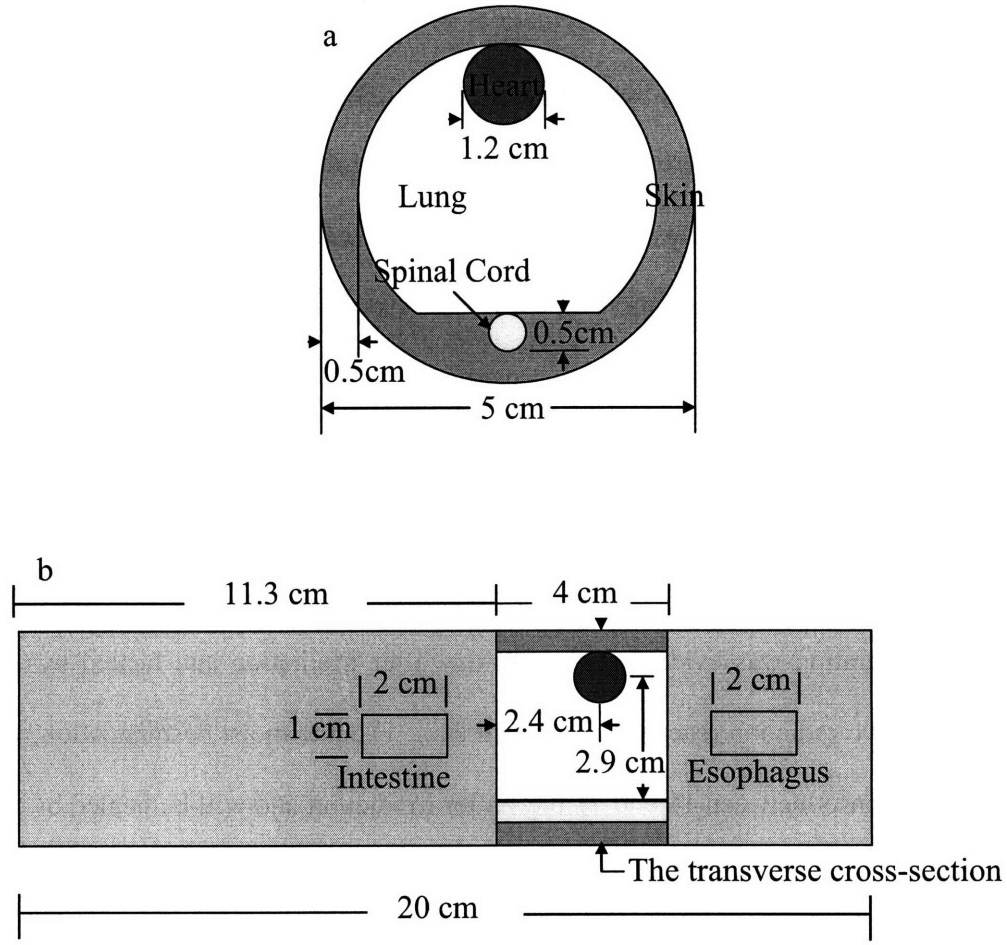

Fig. 2.3 The transverse (a) and sagittal (b) cross-sections of the rat model in MCNP. The location of the cross section plane in panel a is labeled in panel b.

With the rat model specified in MCNP, upper dose limits were set for the lung volume and other radiosensitive tissues according to the normal tissue tolerance data in the literature. An average lung dose of 12 Gy with X-rays has been reported to produce 100% response in lung irradiations using the breathing rate assay (17-19, 39). A 10 Gy mean lung dose from a neutron beam in the absence of boron was assumed to have the equivalent effect and chosen as the target dose for simulating lung irradiation. This neutron beam physical dose was chosen with the assumption that the RBE of the neutron beam alone would be approximately 1.2. This is the

value that was previously reported for the thermal neutron beam of the Brookhaven Medical Research Reactor using other radiobiological endpoints of other tissues (7, 40).

Upper weighted dose limits were also set for the radiosensitive tissues. An effective dose of 20% (ED_{20}) of a biological endpoint was selected as the upper limit for each normal tissue. The upper limits of single fraction irradiation for the acute response of specific tissues are listed in Table 2.1. The dose delivered to the radiosensitive tissues should be lower than the limits prescribed, attained by shielding from the delimiter or irradiation field arrangement. For the throat region, a dose response curve for ulceration of the rat tongue was used as the biological endpoint (40). From the published data, the dose for ED_{20} was 13 Gy_w. With 13 Gy delivered to the rat tongue, ulceration was evident at the 5th day after irradiation and healed by 13 days. There are mainly two radiation reactions for the rat skin: 1) acute moist desquamation, which is less severe, shows onset between 11 and 21 days after irradiation and will be healed by 36 days; 2) late dermal necrosis, which is evident at 24-25 weeks and the healing is usually finished by 42-43 weeks after irradiation (41). The physical dose adequate for moist desquamation is smaller than that for dermal necrosis, in irradiations with thermal neutrons only and thermal neutrons with BPA. Therefore moist desquamation was selected as the endpoint and the RBE dose for ED_{20} (~ 42 Gy_w), was chosen as the upper limit for skin irradiations. With this much dose delivered to the skin, the late response from dermal necrosis is negligible. In deciding spinal cord upper dose limit, paralysis was used as the biological endpoint (42). The ED_{20} for this effect is 17 Gy_w (42), and was chosen as the upper dose limit delivered to the spinal cord in the rat lung irradiations. The intestinal complications of enterocutaneous fistula formation and intestinal obstruction were used as the biological endpoint for the intestine irradiations. The ED_{20}

for these effects is 18 Gy_w (43, 44) and was chosen as the upper limit for the dose delivered to the intestines.

Table 2.1 RBE factors and weighted dose limits of the radiosensitive normal tissues.

Tissue (ref)	Dose Gy_w	Neutron RBE
Skin (40)	42	5.1
Thorax (tongue) (39)	13	3.8
Intestine (43)	18	5*
Spinal Cord (41)	17	1.8

*Because intestine irradiations in low energy neutron beams were not found in the literature, a conservative neutron RBE for the intestines of 5 was chosen.

2.2.4 The Beam optimization

There are advantages and disadvantages to both the FCB and the M011 beam for this rat lung irradiation. The FCB has better penetration and would deliver a more uniform dose distribution at a greater depth over the irradiated field. At the same time, epithermal neutrons are more difficult to shield and the scattering can produce unfavorably high dose in shielded regions. The M011 beam, on the other hand, is easier to shield and produces less scattering, but the dose decreases exponentially with depth in tissue. Parallel-opposed radiation fields would have to be used to address this problem. An optimization study was performed to determine which beam is best suited for the rat lung irradiations. The figure of merit of the FCB and the M011 beam in the rat lung irradiation were explored using MCNP simulations.

The optimum situations for the rat lung irradiations were investigated in MCNP with four neutron beams: two epithermal neutron beams, including a unidirectional ideal epithermal neutron beam (8), the actual FCB, and two thermal neutron beams, including an ideal unidirectional monoenergetic (0.0253 eV) beam and the actual M011 beam. Ideal shielding of neutrons and photons were applied in the two real neutron beams (FCB and M011) outside the

lung region, on the two collateral regions 2 cm from the lung center. Similar boundary conditions were applied to the two ideal neutron beams with no photon contaminations. The two ideal beams were of 4 cm x 15 cm rectangular geometry, comparable in size to the real beams, and placed right above the 4 cm rat lung. Thus in these simulations, almost all neutrons and photons entering the collateral regions outside the incident beam in the rat model were scattered from the lung region. The setup in the simulations was to compare and investigate the maximum performance of the epithermal and thermal neutron beams without impact from the delimiters and the suitability for the rat lung irradiations.

In-phantom thermal neutron fluxes and photon dose rates were tallied along the central axis at 0, 1.5, 2.5, 3.5 and 4.5 cm from the lung center. Published photon kerma factors were used to calculate the dose rates in tissues (8). Relative thermal neutron fluxes and photon dose rates to the lung center were calculated to investigate shielding under extreme situations with different neutron beams. The two ideal-source simulations were run with enough particles that the uncertainties for the relevant tallies were less than 1%. The uncertainties for the tallies with the FCB and M011 beams were around 2% and 1%, respectively.

2.2.5 The delimiter and its design and optimization criteria

After the beam was optimized and selected, a delimiter was designed for the rat lung irradiation in this beam. Two optimization criteria were considered for the delimiter design. The dose rate in the lung center was one criterion and a larger dose rate in the lung would ensure comparatively shorter irradiation. To quantify the delimiter shielding quality, the second criterion was defined, as the thermal neutron dose rate ratios in the lung center relative to those in the collateral regions especially the intestines and esophagus. While in reality too much shielding would block the beam and decrease the dose rate and dose distribution uniformity in

the lung region, the thermal neutron dose rate ratios were optimized below an upper limit. The delimiter with ideal shielding, described in the last section, was set as the goal and upper limit for the delimiter design. That was, a delimiter producing similar thermal neutron dose rate ratios as the one with ideal shielding, and with adequately large lung dose rates, was deemed optimum.

The range of the thermal neutron dose rate ratio also had a lower limit, to ensure the doses to collateral radiosensitive tissues below the dose limits listed in Table 2.1, with 10 Gy mean lung dose. For the rat lung irradiation in the M011 beam, the neutron component of total in-phantom dose was approximately 20% with negligible fast neutron contamination (22), indicating 2 Gy thermal neutron dose delivered to the lung. The thermal doses to the collateral regions could be estimated with the thermal neutron dose rate ratio. The photon doses to these regions were estimated as 8 Gy, similar to the photon dose delivered to the lung. In order to keep the biologically weighted dose to the esophagus and intestines below 13 Gy_w and 18 Gy_w, respectively (Table 2.1), the minimum thermal neutron dose rate ratio was determined as 1.5, using reported or estimated neutron RBE values of gastrointestinal death and Eq. 1. This simple estimation was theoretical and based on a rigid rat phantom. The thermal neutron dose rate ratio in the actual design needed to be significantly larger than this lower limit.

A delimiter of thin plate geometry with a rectangular opening exposing the rat lung region to the neutron beam was the basic idea of the design. Li-poly was selected as the delimiter material, due to the high concentration of Li-6 (7% by weight), which has high thermal neutron capture cross-section with almost no photons produced from the capture reaction. The simulation goal was a delimiter geometry that would reach the design criteria described above, to have close to ideal thermal neutron dose rate ratios and dose rates in the lung as large as possible. Photon dose rates, thermal neutron dose rates and total neutron dose rates were tallied in the lung

and along the central axis including the esophagus and intestines, for this purpose. The parameters of the geometry to be optimized are thickness, aperture width and the taper angle of the aperture edges. The optimization of the delimiter was initially in two dimensions, the thickness and the aperture width, with the third parameter, the aperture taper angle, fixed at 90°. After the thickness and the width were decided, the taper angle was fine-tuned in search of some advantages of larger neutron dose rate ratios or larger physical dose rates in the lung. The detailed calculations for each beam are discussed later.

2.2.6 Experimental validation

Two Lucite phantoms filled with light water were built for the validation of the MCNP beam model. Lucite was selected for the phantom material because it has a density close to that of tissue and it has a low activity induced by neutrons. The phantoms are 20 cm long cylinders, 5 cm in diameter, a much simplified version of the MCNP rat model. One cylindrical phantom has a 1-cm inner diameter concentric channel for dosimeters positioned along the horizontal dimension to check the shielding effect of the delimiter. Another phantom has a 1-cm channel to measure the dose/flux depth profiles in the lung location. Dose and flux profiles along these two orthogonal dimensions were measured to benchmark the simulation design against the experiment.

The measurements were done with the Lucite phantoms positioned inside the Li-poly shielding box with the Li-poly delimiter mounted on the top and placed below the M011 beam port. The dual ion chamber technique (25) was used to measure the photon and the neutron dose rates in the mixed radiation field at various horizontal locations along the cylinder axis. An A-150 muscle tissue-equivalent (25, 38) ionization chamber flushed with tissue equivalent gas and a carbon graphite ionization chamber flushed with CO_2 gas were used. The gas flow rate for

both chambers was 20 ml/min. The two chambers have different sensitivities to photons and neutrons, thus providing two simultaneous equations from which the photon and neutron dose rates are readily solved (25).

Bare gold foils (12-18 mg, 0.005 cm thick) and gold foils with cadmium covers (0.050 cm thick) were used to measure total neutron and epi-cadmium neutron flux (E>0.4eV), respectively, along the horizontal and vertical dimensions in the two Lucite rat dosimetry phantoms. The gold reaction induced by neutrons is $^{197}Au(n, \gamma)^{198}Au$. Cadmium covers served as thermal neutron barriers to allow only fast neutrons to pass through and interact with the gold foils. A high purity germanium detector was used to count the emission rate of the 411 keV photons from the gold foils after the irradiation. To determine the neutron flux in the vertical dimension of the phantom, bare gold foils were positioned every 1 cm from the surface of the phantom at 0, 1, 2, 3, 4 cm depth along the central beam line. The foils with cadmium covers were positioned at every 2 cm (0, 2, 4 cm from the surface) to avoid perturbation of the neutron field at the location of the next foil (24). In the phantom to determine the flux distribution along the horizontal dimension, bare foils were positioned at the center of the lung (0 cm), and 1.0, 2.5, 3.5, 4.5 cm from the center towards the 'body' end of the phantom, and 1.0, 2.0, 3.5 cm towards the 'head' end of the phantom. Cadmium-covered foils were placed 2.5, 4.5 cm and 2, 3.5 cm from the center of the lung region to each end of the phantom. The techniques for mixed field dosimetry, including the dual chamber technique and gold foil measurement, have been described in detail (25). The simplified cross-section of the phantom irradiation underneath the beam and the Li-Poly delimiter, the phantoms, and the dual ion chambers and the foils are displayed in Fig. 2.4.

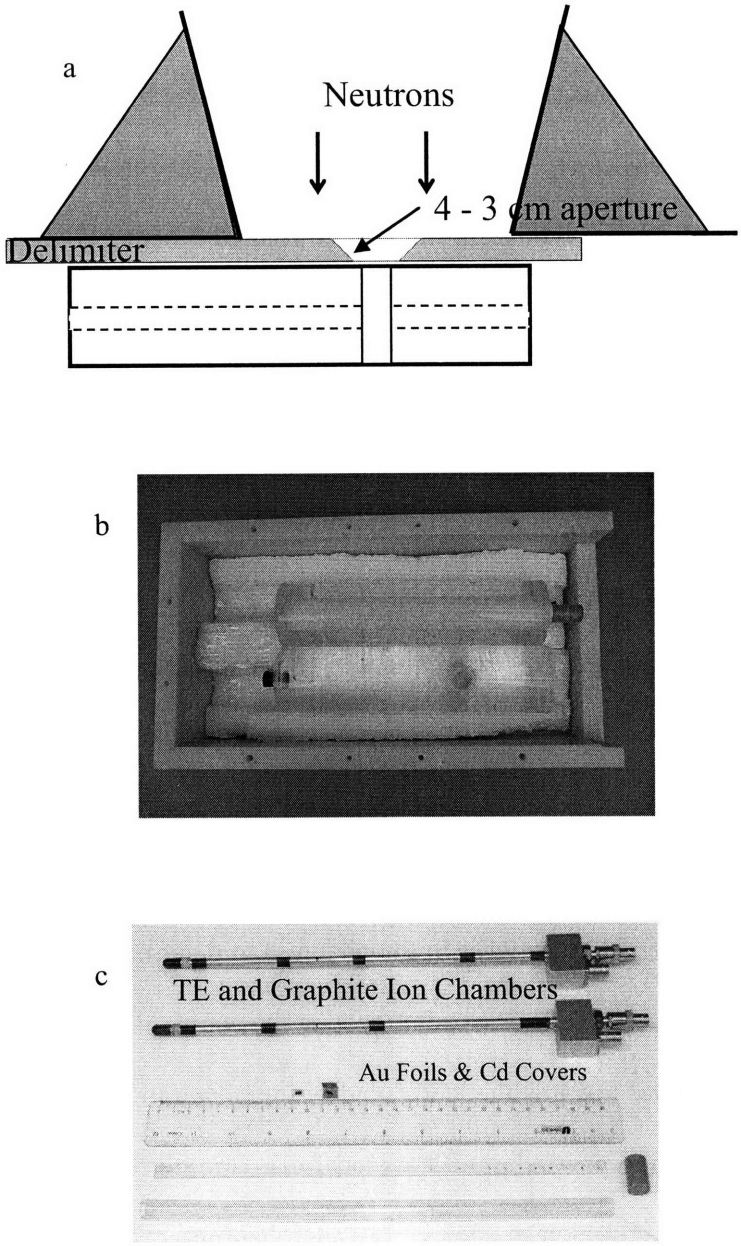

Fig. 2.4 Experimental validation of irradiation simulations: a) a simplified cross-section of the simulated irradiation geometry with the dosimetry phantom in place; b) the two lucite water-filled phantoms positioned inside the Li-Poly shielding box; and c) the dual ion chambers and gold foils used to measure the dose rate and neutron flux in the irradiation field.

These simplified dosimetry phantoms were modeled in MCNP to obtain scale factors between simulations and measurements. The geometries of the water filled lucite phantoms, the Li-poly delimiter, and the Li-poly shielding box were constructed below the MCNP model of the M011 beam. The dose rates were tallied at various locations matching the real ion chamber measurements. Cadmium-covered and bare gold foils were also included in the simulations to tally the fast neutron (E>0.4eV) flux and thermal neutron flux. The scale factors were then applied to the calculations of lung and other tissue dose rates in the sophisticated MCNP models, to obtain the dose rates delivered in the real irradiations. The dose contribution from the $^{10}B(n,\alpha)^{7}Li$ reaction was calculated from the simulation data multiplied with scale factors, with reported Boron-10 kerma factors (8).

2.3 Results

2.3.1 Comparison of the FCB and the M011 beams

Simulations with four idealized neutron beams were performed to investigate the suitability of actual epithermal and thermal neutron beams available for the rat lung irradiations, including the FCB and the M011 beam. With ideal shielding or unidirectional beams in simulations, doses delivered to the collateral region were mostly due to scattered neutrons and induced photons from the exposed lung region, with minimum neutrons and photons directly from the beam. Distributions of relative neutron fluxes and photon dose rates along the central axis, including the esophagus and intestines, compared to those at the lung center, were calculated and plotted in Fig. 2.5.

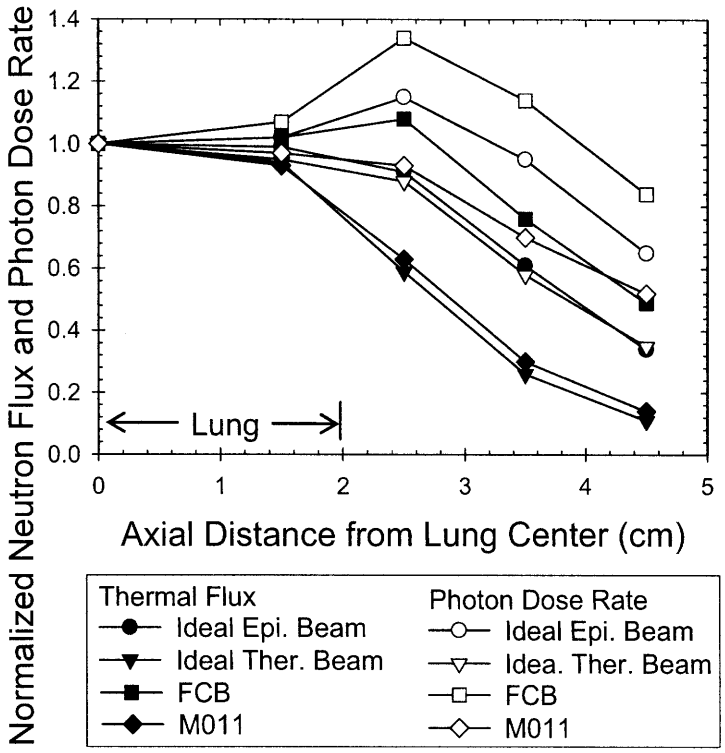

Fig. 2.5 Normalized neutron flux and photon dose rate distribution along the central axis of the rat cylinder from the calculations with MCNP. Lung region extends from 0-2 cm, which is exposed to the beams. 'Ideal shielding' is applied beyond 2 cm from the lung center, with all neutrons and photons entering the shielded regions terminated in MCNP. The size of the two ideal epithermal and thermal neutron beams is 4 x 15 cm, and the two neutron sources are unidirectional (fully collimated).

For the irradiations with the epithermal neutron beams, both relative thermal neutron flux and photon dose rates at 0.5 cm outside the beam were close to or above 1. With the ideal unidirectional epithermal neutron beam, photon dose rate at 0.5 cm outside the beam is about 15% higher than that in the lung center and then decreases to about 95% at 2.5 cm outside the beam opening. The thermal neutron flux at 0.5 cm outside the beam in this situation is about 91% of the flux at the lung center and decreases to 61% at the locations of the intestines and esophagus. Similarly, in the simulation with the FCB and ideal collateral shielding, both off-

central thermal neutron flux peaks and off-central photon dose peaks were accumulated due to neutron scatterings. The thermal neutron flux at 0.5 cm beyond the opening is 8% higher than that in the center of the lung, and decreases to 76% at the locations of intestines and esophagus. The photon dose at 0.5 cm outside the beam is 34% higher than the lung center, and remains 14% higher at the intestines and esophagus locations. A simple estimation showed that with 10 Gy mean lung dose in the irradiations with the FCB, the dose at the esophagus and intestines would be much higher than the weighted dose limits listed in Table 2.1. These distributions of thermal neutron fluxes and photon dose rates in the collateral regions demonstrate the significantly unfavorable scattering characteristic of the epithermal neutron beams. This problem is not relievable since ideal conditions have already been applied to the irradiation simulations with epithermal neutron beams.

More simulations were done with real collateral shielding (a 0.8 cm thick and 4 cm aperture Li-Poly delimiter) in the irradiation of FCB. Not surprisingly, the off-central dose peak problem was more severe with less idealization. Both relative thermal neutron flux and photon dose rate were greater than 1 at up to 1.5 cm beyond beam opening. Though the epithermal beams have advantages of greater penetration and more uniform distribution in the lung, the unfavorably high dose delivered to the shielded radiosensitive regions cannot be compromised. Therefore, the FCB is determined as unsuitable for the rat lung irradiations.

In contrast, the irradiations with the two thermal neutron beams have much less problems from neutron scattering. Fig. 2.5 shows that, with the unidirectional and monoenergetic thermal neutron beam, the thermal neutron flux decreases significantly faster along the central axis, dropping to 59% of the flux at the lung center at 0.5 cm outside the beam, and 26% at 1.5 cm beyond, where the esophagus and intestines are located. The relative induced photon dose rates

are also smaller, being 88% and 58% of the photon dose rate at the lung center, at 0.5 cm and 1.5 cm beyond the beam, respectively. The relative thermal neutron flux distribution along the central axis of the rat phantom with the M011 beam and ideal collateral shielding is similar to that with the ideal thermal neutron beam. The relative photon dose rate distribution along the central axis with the M011 beam is slightly larger at 1.5 cm and beyond outside the beam than that with the ideal thermal beam. This indicates that the M011 beam is composed of almost pure thermal neutrons and is much easier to shield for the rat lung irradiations. A calculation with the neutron kerma factors (8) applied showed that the thermal neutron dose rate ratio at the intestines and esophagus is 4 in this M011 irradiation, significantly larger than the minimum required ratio of 1.5, as discussed above.

From the calculations and comparisons above, thermal neutron beams proved to be more suitable for the rat lung irradiations, due to the neutron scattering problem resulted in irradiations with epithermal neutron beams. Thus the M011 beam was chosen over the FCB for the rat lung irradiations. From the comparison between the ideal thermal neutron beam and the M011, the M011 beam has characteristics similar to a unidirectional and monoenergetic thermal neutron beam. The performance along the central axis of the rat cylinder in the irradiations with the M011 beam and ideal collateral shielding, was set as the goal for delimiter design in the rat lung irradiations in the M011 beam, in the following stage of this project.

2.3.2 Delimiter design for irradiations in the M011 thermal neutron beam

A delimiter was designed and optimized for the rat lung irradiations in the M011 thermal neutron beam. As described in the method section, two criteria were used to evaluate the delimiter design: the thermal neutron dose rate in the lung center; the ratios of the thermal neutron dose rate in the lung center to those in the collateral regions along the central axis,

especially the intestines and esophagus. Also as discussed above, the delimiter with ideal shielding was set as the goal for the real delimiter design for the rat lung irradiations in the M011 beam. In the simulations, the delimiter was optimized by comparing the thermal neutron dose rate ratios to the idealized situation of the M011 irradiations. The geometry of the Li-poly delimiter was optimized with the thickness and aperture width determined first and then the aperture edge fined tuned.

In the previous section, ideal shielding of neutrons and photons was applied to the collateral sides above the cylinder rat phantom with a 4 cm aperture in the M011 beam irradiation. According to a simple hand-calculation, 1 cm Li-poly plate can absorb up to 99.9% of the thermal neutron flux (0.0253 eV) (33). The initial geometric parameters of the delimiter were therefore approximated as 1-2 cm thick, with an aperture tapered from 4-3 cm, comparable to the lung length of 4 cm. The calculated data in the rat models from the simulations of the M011 beam irradiations, with various real delimiters and the ideal delimiter, are plotted in Fig. 2.6. From this figure, the thermal neutron dose rate ratios varied more with the delimiter width opening than the thickness, between the thickness of 1 - 2 cm. The ratios of the Li-poly delimiter group of 3 cm aperture width were closer to the ratios with ideal shielding of 4 cm aperture width. This indicates that a close to ideal thermal neutron dose rate ratio was achieved by decreasing the aperture width, or the beam exposing area. Among delimiters of the same aperture (4 cm or 3 cm) but different thickness, the delimiters of 1.5 cm thick seemed to provide a better shielding effect than delimiters of 1.2 cm and 1.8 cm thick, though there is no statistical difference between the ratios. Therefore, the initial delimiter geometry was chosen to be 1.5 cm thick with a 3 cm aperture width. Fig. 2.7 also lists the relative thermal neutron dose rate at the lung center of the irradiations with different delimiters compared to that of ideal shielding,

assuming the latter as the standard. The thermal neutron dose rates at the lung center were lower for 3 cm aperture and compromised for a better shielding.

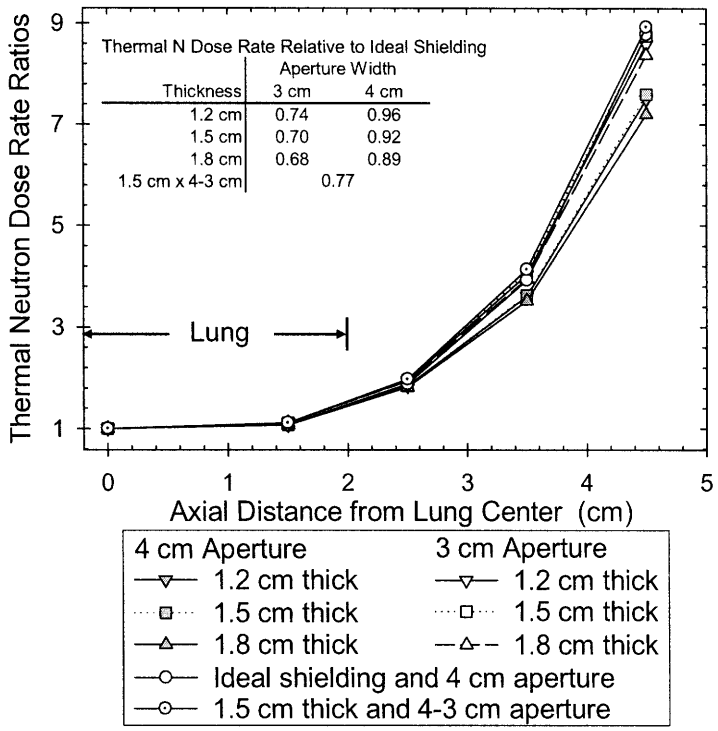

Fig. 2.6 Simulations of thermal neutron dose rate ratios in the M011 thermal beam, of the lung center to the collateral regions on the central axis, with Li-poly delimiters of various combinations of thickness and aperture width. A larger ratio indicates better shielding. The results were compared with ideal shielding of a 4 cm aperture. The relative thermal neutron dose rates at the lung center of different delimiters were compared to the case of ideal shielding, listed in the panel. The uncertainties for all the thermal neutron dose tallies are within 1.5% in simulations.

After the parameters of thickness and aperture width of the delimiter were optimized, the aperture tapering angles were fine tuned from 90° to 72°. That is, the original straight delimiter aperture was altered to a tapered opening 4-3 cm with the smaller aperture close to the rat phantoms, with the 1.5 cm thickness unchanged. The thermal neutron dose rate ratios were also

plotted in Fig. 2.6. Similar shielding ratios were obtained for this altered geometry but the average thermal neutron dose rate in the lung center increased by about 10%. This is desirable for both a shorter irradiation time and a more distinguishable boron physical dose when boron compound is added in the lung irradiations. Therefore, the final design of the plate Li-poly delimiter was 1.5 cm thickness and 3 cm wide aperture tapered 72° to 4 cm at the beam entry surface, to produce a thermal neutron dose rate ratio of 4 at the esophagus and intestines locations. A total physical lung dose rate of 19.2 cGy/min/5MW with single field was obtained and about 50 minutes beam time is required to deliver 10 Gy dose with two-field. Table 2.2 lists the mean lung dose rates in the M011 beam irradiations with single field shielded by the optimized delimiter.

The final design of the shielding box (rat holder) for the thermal beam irradiation is a Li-poly box of 7 × 15 × 30 cm inner dimensions, which can hold 2 rats. The optimized 1.5 cm thick delimiter with a 3 x 14 cm aperture, tapered 72 degrees, is mounted on the top of the box. The delimiter/holder is attached to the beam port in the ceiling of the medical room for irradiation in the vertical M011 neutron beam.

Table 2.2 Mean lung dose rates calculated for the lung in the M011 beam irradiations for single and with the delimiter of 1.5 cm thickness and 4-3 cm wide aperture. Only calculation uncertainties are included.

Physical Dose Rate for the Lung Volume (cGy/min)			
Thermal N	Total N	Photon	Total Physical
3.29 ± 0.04	3.50 ± 0.04	15.71 ± 0.14	19.21 ± 0.29

2.3.3 Validation measurements

Validation measurements were carried out following the simulation design of the rat lung irradiation delimiter as described in previous sections. In-phantom photon dose rates and total thermal neutron dose rates were measured along the horizontal axis: at the centre of the 'lung' of

the phantom, and 3.5 cm away from this point, which is 2 cm from the bottom edge of the Li-poly delimiter aperture. Total neutron flux was measured along the horizontal axis: at the center lung, 1.0, 2.0, 3.5 cm away towards the 'head' end, and 1.0, 2.5, 3.5, 4.5 cm away towards the 'body' end. Cadmium covered gold foils were placed at the 'lung' center, 2.0, 3.5 cm and 2.5, 4.5 cm away correspondingly on each end. Only neutron fluxes were measured on the vertical direction of the phantom. Bare gold foils were positioned every 1 cm from the phantom surface to 4 cm depth. Cadmium covered gold foils were placed at 0, 2 and 4 cm from the surface.

Figs. 2.7 - 9 plot the measured and calculated thermal neutron flux and photon dose rates along the vertical and horizontal directions of the phantom. Both the measurements and calculations demonstrate that the M011 beam has a very small fast neutron contamination. The simulations show that the in-phantom fast neutron component is less than 1% of the total neutron flux, with the uncertainties for fast neutron flux around 5% or less. In the measurements, the counting rates for bare gold foils is 20 times or more higher than that of the cadmium covered gold foils, while both sets of foils had similar beam exposure time and counting start time after irradiations. A gross calculation demonstrates that the M011 beam has a cadmium ratio of approximate ~150 in the central 'lung' of the rat phantom. Therefore, the beam was considered as a pure thermal neutron beam and only total/thermal neutron flux was plotted in Figures 5 and 6 for clarity.

From Fig. 2.7, the thermal neutron flux at the surface of the phantom was 8.4 x 10^9 n/cm^2 s. This flux decreased to 6.1, 3.4, 1.8 and 0.9 x 10^9 n/cm^2 s at depths of 1, 2, 3 and 4 cm in the phantom, respectively. Along the central axis of the rat phantom (2.5 cm from the surface) the thermal neutron flux directly under the delimiter aperture was 2.2 x 10^9 n /cm^2 s. This dropped to 0.6 x 10^9 n/cm^2 s in the region of the shielded collateral regions 3.5 cm from the center of the

aperture opening. The measured photon dose rate in the central axis of the phantom, directly under the aperture, was 19.5 cGy/min. All MCNP simulations were scaled to match these physical dosimetry measurements. The scaling factors connecting the simulation and the experiment for the rat lung irradiations were determined to be 0.56 for neutrons and 0.75 for photons. After this scaling, the discrepancies between measured and calculated neutron flux and photon dose rate depth profiles along the beam axis, as well as the profiles along the central axis of the phantom, were mostly within 5%.

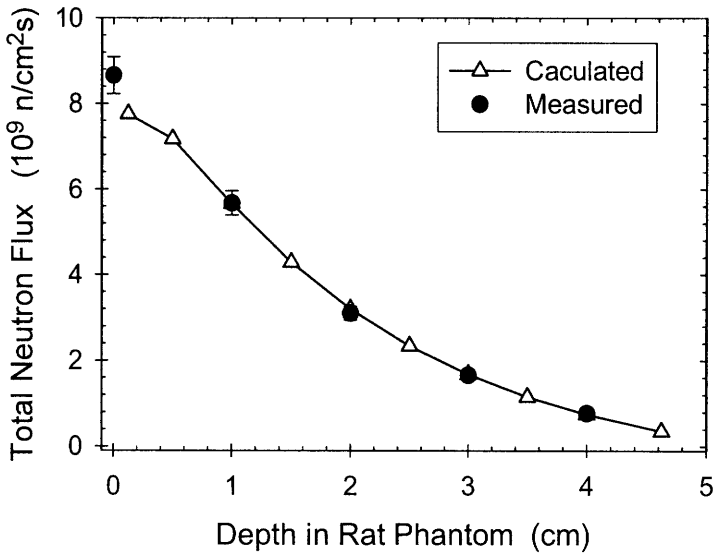

Fig. 2.7 Neutron flux versus depth profile in the rat phantom along the central beam axis. In the M011 thermal neutron beam, calculations were normalized to measurements by applying a factor of 0.56.

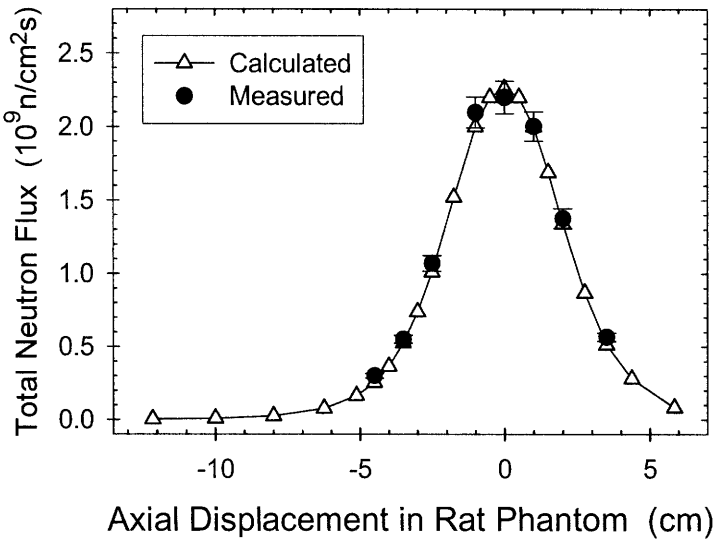

Fig. 2.8 Profile of neutron flux versus displacement along the axis of the rat cylinder. Calculations were normalized to measurements by applying a factor of 0.56.

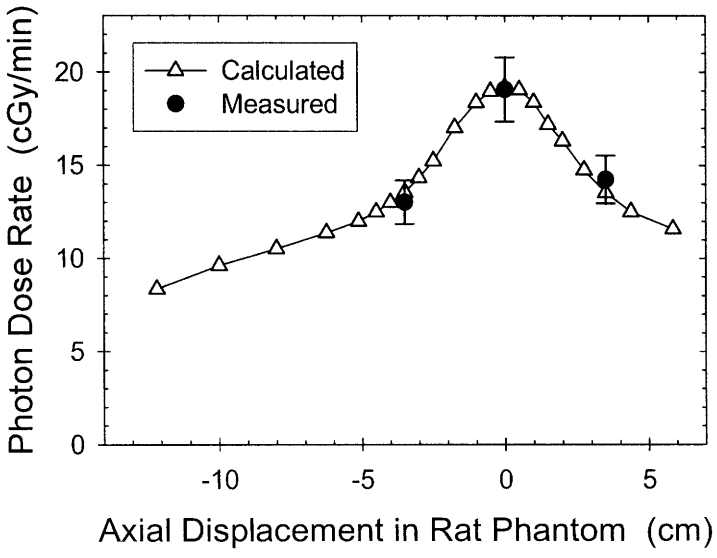

Fig. 2.9 Photon dose rates versus axial displacement profile. Calculations were normalized to measurements by applying a factor of 0.75.

2.3.4 Dose Volume Histogram (DVH) and the irradiation fields

After the delimiter was designed, the irradiation procedure was further optimized to produce a uniform dose distribution in the lung volume and avoid over exposure of surrounding tissues including skin and spinal cord. Due to the significant attenuation of thermal neutrons with depth in tissue, irradiation of the lung with a single field will produce a large dose gradient as a function of depth. A two-field irradiation from ventral and dorsal surfaces of the phantom was superior to the one-field irradiation in terms of dose uniformity in the lung volume. The dose distribution in the total lung volume was calculated by constructing dose volume histograms (DVHs) from the MCNP simulation data. To calculate the DVH, the 4 cm diameter, 4 cm long lung cylinder was segmented into voxels by first dividing the lung cylinder into three segments (1, 2 and 1 cm-thick) along the body axis, and then subdividing these cylinders further by superimposing a grid of ~ 0.5 cm squares on each segment. The heart and spinal cord volumes were excluded. Thus, voxels along the outer edge and adjacent to the heart or spinal cord, had irregular geometries. Voxel volumes ranged from 0.6 cm^3 to 0.02 cm^3. The calculation uncertainties for the thermal neutron and photon doses were less than 2.5% for each voxel. The DVHs was constructed from the dose rates tallied in each voxel in MCNP.

The calculated dose volume histograms (DVHs) for one-field and two-field irradiation were compared and are shown in Fig. 2.10. The two-field irradiation showed more uniform dose distribution (approx. 9.5 -11.5 Gy) than the one-field irradiation (approx. 7-15 Gy) with the mean lung dose fixed at 10 Gy in both cases. This is due to the compensation of the two-field irradiation for the exponential attenuation of the thermal neutron beam in tissue. The DVHs for thermal and total neutron dose components for the two-field irradiation are also shown in Fig. 2.10. Additionally, the dose delivered to the ventral skin in the two-field irradiation was significantly lower than in the one-field irradiation. This protected the ventral skin from

receiving overdose during irradiations especially when B-10 carrying drug were introduced in the irradiations.

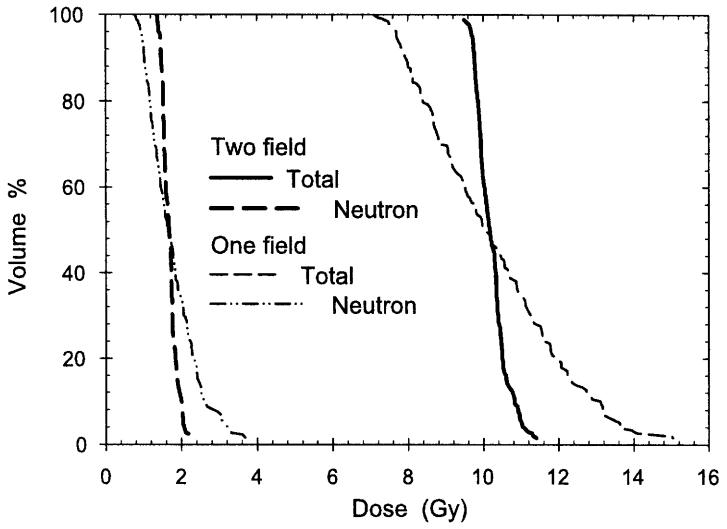

Fig. 2.10 Physical dose volume histograms for the lung with mean lung dose fixed at 10 Gy for both one- and two-field irradiations.

2.3.5 Final calculation results

Table 2.3 lists the simulation results of the physical dose delivered to different tissues with 10 Gy mean lung dose, with the delimiter of 1.5 cm thickness and 4-3 cm aperture width. The calculated total physical dose rate in the lung volume was 18.7 cGy/min for a 2-field irradiation in the absence of boron, including thermal neutron and photon components of 3.3 cGy/min and 15.4 cGy/min, respectively. A beam only 10 Gy mean lung dose could be delivered to the rat in a total irradiation time of about 54 minutes using two fields (~ 27 min/field) at 5 MW reactor power. With ^{10}B present, the calculated dose rate for the boron neutron capture dose component was 1.04 cGy/min for every μg ^{10}B present in 1 gram blood. Assuming the average boron concentration in the rat blood is 18ppm at the irradiation time (2.5-3.5 hours after Intraperitioneal

Injection) (45), the total irradiation time required to deliver 10 Gy physical dose is about 26.7 minutes (13.4 min/field), approximately half of the time for beam only irradiations.

Table 2.3 Physical radiation doses in Gy delivered to the surrounding tissues with 10 Gy mean lung dose. The calculation uncertainties are within 5% and are omitted for clarity.

	1-field (ventral) (Gy)			2-field (ventral and dorsal) (Gy)		
Tissue	Neutron	Gamma	Total	Neutron	Gamma	Total
Skin	7.0	13.0	20.0	3.9	9.5	13.4
Spinal cord	0.7	6.5	7.2	1.9	9.8	11.7
Heart	4.1	15.2	19.3	2.8	12.4	15.2
Intestines	0.4	6.8	7.2	0.4	7.0	7.4
Esophagus	0.4	6.8	7.2	0.4	7.0	7.4
Lung	1.8	8.2	10	1.8	8.2	10

2.4 Conclusions and Discussion

The simulations indicated that 10 Gy mean lung dose can be delivered within 54 min beam time using two-field irradiations (27 min per field). The DVH for the rat lung region indicated a relatively uniform dose distribution in the lung for two-field irradiations. With a thermal neutron dose rate ratio of 4 at the esophagus and intestines relative to the lung center, acceptable doses (about 9 Gy_w) to these critical normal tissues can be delivered, which are well below the tolerance limits listed in Table 2.1. The doses delivered to the surrounding skin and spinal cord in the two-field irradiations are about 30 Gy_w and 13 Gy_w, respectively, again below the tolerance limits.

The irradiation of the whole lung volume in rats is significantly different than the small animal BNCT radiation studies reported to date, where the exponential attenuation of thermal neutrons as a function of depth in tissue was not a limiting factor for irradiation of brain tumors, skin, spinal cord or tongue of rats. All of these tissues were $\leq$ 1 cm from the skin surface and

generally represent treated volumes of much less than 1 cm^3 (8). Irradiations of the rat lung require the delivery of uniform thermal neutron fluences to tissue depths of 3-4 cm for a target volume of approximately 50 cm^3. In addition, the sensitive normal tissues outside the field, such as the esophagus and intestine, must be adequately shielded so that the rats will survive long enough to express the late pneumonitis and fibrosis changes to the lung. Thermal neutrons are attenuated exponentially in tissue, which with a single-field irradiation produces a steep dose gradient across the lung volume as a function of depth. Simulations with the MITR-II thermal neutron beam showed that the collateral regions could be shielded effectively, and the approach of using parallel apposed field can deliver a more uniform thermal neutron fluence to the lung volume (~ 50 cm^3). This approach delivers the specified dose to the lung volume with a dose variation of approximately ± 10%, based on the calculations. An additional advantage of the two-field approach is the relative sparing of the skin.

The thermal neutron facility of the MITR-II is being prepared for both clinical applications and for small animal radiation biology experiments. Most small animal irradiations in the M011 medical beam, similar to the rat lung irradiations, require shielding of the neutrons to confine the irradiations to small target areas. With additional calculations and dosimetry, the same holder and delimiter or with some simple adaptation, should also be adequate for irradiations of subcutaneous or intracranial tumors in small animals in the M011 beam. So far a Li-poly delimiter of the same thickness but an aperture tapered from 3 to 2 cm aperture and the Li-poly rat holder have served in mice leg irradiations and rat brain irradiations. The holder also serves as the container for other irradiations, such as the cell irradiations.

2.5 References

1. Locher GL. Biological effects and therapeutic possibilities of neutrons. American Journal of Roentgenology 1936;36:1-13.
2. Taylor HJ, Goldhaber M. Detection of nuclear disintegration in a photographic emulsion. Nature, London 1935;135:341.
3. Coderre JA, Turcotte JC, Riley KJ, Binns PJ, Harling OK, Kiger III WS. Boron Neutron Capture Therapy: Cellular targeting of high linear energy transfer radiation. Technology in Cancer Research and Treatment 2003;2:355-375.
4. Zamenhof RG, Harling OK, Busse PM, Goorley JT. Boron Neutron Capture Therapy. In: Van Dyke J, editor. The Modern Technology of Radiation Oncology. Madison Wisconsin: Medical Physics Publishing; 1999. pp. 981-1020.
5. Barth RF. A critical assessment of boron neutron capture therapy: an overview. J Neurooncol 2003;62:1-5.
6. Barth RF, Soloway AH, Goodman JH, Gahbauer RA, Gupta N, Blue TE, Yang W, Tjarks W. Boron neutron capture therapy of brain tumors: an emerging therapeutic modality. Neurosurgery 1999;44:433-450.
7. Coderre JA, Morris GM. The radiation biology of boron neutron capture therapy. Radiat. Res. 1999;151:1-18.
8. Goorley JT, Kiger III WS, Zamenhof RG. Reference dosimetry calculations for neutron capture therapy with comparison of analytical and voxel models. Med Phys 2002;29:145-156.
9. Palmer MR, Goorley JT, Kiger III WS, Busse PM, Riley KJ, Harling OK, Zamenhof RG. Treatment planning and dosimetry for the Harvard-MIT Phase I clinical trial of cranial neutron capture therapy. Int J Radiat Oncol Biol Phys 2002;53:1361-1379.
10. Kiger III WS, Lu XQ, Harling OK, Riley KJ, Binns PJ, Kaplan J, Patel H, Zamenhof RG, Shibata Y, Kaplan ID, Busse PM, Palmer MR. Preliminary Treatment Planning and Dosimetry for a Clinical Trial of Neutron Capture Therapy using a Fission Converter Epithermal Neutron Beam. Appl Radiat Isot 2004;61:1075-1081.
11. Busse PM, Harling OK, Palmer MR, Kiger III WS, Kaplan J, Kaplan I, Chuang CF, Goorley JT, Riley KJ, Newton TH, Santa Cruz GA, Lu XQ, Zamenhof RG. A critical examination of the results from the Harvard-MIT NCT program phase I clinical trial of neutron capture therapy for intracranial disease. J Neurooncol 2003;62:111-121.
12. Capala J, Stenstam BH, Skold K, af Rosenschold PM, Giusti V, Persson C, Wallin E, Brun A, Franzen L, Carlsson J, Salford L, Ceberg C, Persson B, Pellettieri L, Henriksson R. Boron neutron capture therapy for glioblastoma multiforme: clinical studies in Sweden. J Neurooncol 2003;62:135-144.
13. Nakagawa Y, Pooh K, Kobayashi T, Kageji T, Uyama S, Matsumura A, Kumada H. Clinical review of the Japanese experience with boron neutron capture therapy and a proposed strategy using epithermal neutron beams. J Neurooncol 2003;62:87-99.

14. Joensuu H, Kankaanranta L, Seppala T, Auterinen I, Kallio M, Kulvik M, Laakso J, Vahatalo J, Kortesniemi M, Kotiluoto P, Seren T, Karila J, Brander A, Jarviluoma E, Ryynanen P, Paetau A, Ruokonen I, Minn H, Tenhunen M, Jaaskelainen J, Farkkila M, Savolainen S. Boron neutron capture therapy of brain tumors: clinical trials at the finnish facility using boronophenylalanine. J Neurooncol 2003;62:123-134.

15. Busse P, Zamenhof R, Madoc-Jones H, Solares G, Kiger S, Riley K, Chuang C, Rogers G, Harling O. Clinical follow-up of patients with melanoma of the extremity treated in a phase I boron neutron capture therapy protocol. In: B Larsson JC, R Weinreich, editor. Advances in Neutron Capture Therapy. Volume I, Medicine and Physics. Amsterdam: Elsevier Science B.V.; 1997. pp. 60-64.

16. Palmer MR. Harvard/MIT BNCT program technical report; 1999.

17. Lehnert BE, Dethloff LA, Finkelstein JN, Vanderkogel AJ. Temporal Sequence of Early Alterations in Rat Lung Following Thoracic X-Irradiation. Int. J. Radiat. Biol. 1991;60:657 - 675.

18. Kimler BF, Giri PGS, Giri UP, Cox GG. Effect of single dose, fractionated, and hyperfractionated trunk irradiation on weight gain, respiration frequency, and survival in rats. Br J. Cancer 1986;53:360-362.

19. Rongen EV, Tan CHT, Durham SK. Late functional, biochemical and histological changes in the rat lung after fractionated irradiation to the whole thorax. Radiotherapy and oncology 1987;10:231-246.

20. Reactor system manual, MITNRL-004, Massachusetts Institute of Technology; 1980.

21. Kiger III WS, Sakamoto S, Harling OK. Neutronic design of a fission converter-based epithermal neutron beam for neutron capture therapy. Nuclear Science and Engineering. 1999;131:1-22.

22. Harling OK, Riley KJ, Binns PJ, Patel H, Coderre JA. The MIT user center for neutron capture therapy research. Radiation Research 2005;165:221-229.

23. Choi J-HR, Clement SD, Harling OH. Neutron capture therapy beams at the MIT Research Reactor. Basic Life Sci 1990;54:201-218.

24. Choi J-HR. Development and characterization of an epithermal beam for boron neutron capture therapy at the MITR-II Reseacrh Reactor. Nuclear Engineering Department: Massachusetts Institute of Technology; 1991.

25. Rogus RD, Harling OK, Yanch JC. Mixed field dosimetry of epithermal neutron beams for boron neutron capture therapy at the MITR-II research reactor. Med Phys 1994;21:1611-1625.

26. Rogus RD. Design and dosimetry of epithermal neutron beams for clinical trials of boron neutron capture therapy at the MITR-II reactor. Nuclear Engineering. Cambridge, MA: Massachusetts Institute of Technology; 1994.

27. Riley KJ, Binns PJ, Harling OK. Performance characteristics of the MIT fission converter based epithermal neutron beam. Phys Med Biol 2003;48:943-958.

28. Riley KJ. Construction and characterization of a fission converter based epithermal neutron beam for BNCT. Nuclear Engineering Department. Cambridge: Massachusetts Institute of Technology; 2001.

29. Sakamoto S, Kiger III WS, Harling OK. Sensitivity Studies of Beam Directionality, Beam Size and Neutron Spectrum for a Fission Converter-Based Epithermal Neutron Beam for Boron Neutron Capture Therapy. Medical Physics 1999;26:1979-1988.

30. Harling OK, Riley KJ, Newton TH, Wilson BA, Bernard JA, Hu L-W, Fonteneau EJ, Menadier PT, Ali SJ, Sutharshan B, Kohse GE, Ostrovsky Y, Stahle PH, Binns PJ, Kiger III WS, Busse PM. The Fission Converter Based Epithermal Neutron Irradiation Facility at the MIT Reactor. Nuclear Science and Engineering 2002;140:223-240.

31. Briesmeister JF. MCNP- A general Monte Carlo N-Particle Transport Code (Version 4B). Los Alamos: Los Alamos National Laboratory; 1998.

32. Redmond II EL, Yanch JC, Harling OK. Monte Carlo Simulation of the MIT Research Reactor. Nuclear Technology 1994;106:1-14.

33. Kiger III WS. Neutronic Design of a Fission Converter-Based Epithermal Neutron Beam for Neutron Capture Therapy. Nuclear Engineering. Cambridge: Massachusetts Institute of Technology; 1996.

34. Zamenhof R, Redmond E, Solares G, Katz D, Riley K, Kiger S, Harling O. Monte Carlo-based treatment planning for boron neutron capture therapy using custom designed models automatically generated from CT data. International Journal Radiation Oncology Biology Physics 1996;35:383-397.

35. Newton Jr. TH, Riley KJ, Binns PJ, Kohse GE, Hu L-W, Harling OH. Startup of the Fission Converter Epithermal Neutron Irradiation Facility at the MIT Reactor. Nuclear Technology 2002;139:175-183.

36. Kiger III WS, Santa Cruz GA, González SJ, Hsu F-Y, Riley KJ, Binns PJ, Harling OK, Palmer MR, Busse PM, Zamenhof RG. Verification and Validation of the NCTPlan Treatment Planning Program. In: Sauerwein W, Moss RL, Wittig A, editors. Research and Development in Neutron Capture Therapy. Bologna, Italy: Monduzzi Editore; 2002. pp. 613-616.

37. Riley KJ, Binns PJ, Kiger III WS, Harling OK. Clinical Dosimetry of the MIT FCB. In: Sauerwein W, Moss RL, Wittig A, editors. Research and Development in Neutron Capture Therapy. Bologna, Italy: Monduzzi Editore; 2002. pp. 347-351.

38. ICRU 46. Photon, Electron, Proton, and Neutron Interaction Data for Body Tissues. Bethesda, MD: International Commission on Radiation Units and Measurements; 1992.

39. Gregoire V, Beauduin M, Gueulette J, Decoster BM, Octaveprignot M, Vynckier S, Wambersie A. Radiobiological Intercomparison of p(45)+Be and p(65)+Be Neutron Beams for Lung Tolerance in Mice After Single and Fractionated Irradiation. Radiat. Res. 1993;133:27 - 32.

40. Coderre JA, Morris GM, Kalef-Ezra J, Micca PL, Ma R, Youngs K, Gordon CR. The effects of boron neutron capture irradiation on oral mucosa: evaluation using a rat tongue model. Radiat Res 1999;152:113-118.

41. Morris GM, Coderre JA, Hopewell JW, Micca PL, Rezvani M. Response of rat skin to boron neutron capture therapy with p-boronophenylalanine or borocaptate sodium. Radiother. Oncol. 1994;32:144 - 153.

42. Morris GM, Coderre JA, Hopewell JW, et al. Response of the central nervous system to boron neutron capture irradiation: evaluation using rat spinal cord model. Radiother Oncol 1994;32:249-255.

43. Withers HR, Mason KA, Taylor JMG, Kim DK, Smathers JB. Dose Survival Curves, Alpha-Beta Ratios, RBE Values, and Equal Effect Per Fraction for Neutron-Irradiation of Jejunal Crypt Cells. Radiation Research 1993;134:295-300.

44. Withers HR, Elkind MM. Radiosensitivity and Fractionation Response of Crypt Cells of Mouse Jejunum. Radiation Research 1969;38:598-613.

45. Morris GM, Coderre JA, Micca PL, Fisher CD, Capala J, Hopewell JW. Central nervous system tolerance to boron neutron capture therapy with p-boronophenylalanine. Br. J. Cancer. 1997;76:1623-1629.

CHAPTER THREE

An Automated Method for Breathing Frequency Determination in Rat Whole-body Plethysmography

3.1 Introduction

Whole-body plethysmography for small animal breathing frequency measurement has been widely used to non-invasively assess lung damage after irradiation or toxic exposures. The apparatus and hardware for plethysmography of small animals, especially rats and mice, have been well established (1-6). The basic principle is to confine the animal in an air-tight chamber and measure the pressure changes inside the chamber due to the respiration-related movement. Potential problems have been reported related to inadequate measurement time due to the limited air supply and possibly increased temperature inside the sealed chamber (1, 3). These problems were addressed by purging the chamber with a constant or low-frequency air flow during measurement, an approach known as open-flow plethysmography (4, 5).

The method for converting the raw pressure data into a breathing frequency continues to evolve. Breathing frequencies were originally counted manually or reported by a frequency counter, based on a few breath cycles during regular breathing. Regular breathing, as opposed to animal movement or sniffing, which caused irregular pressure signal changes, was observed and

accepted manually by the operator. These methods were not only very laborious, especially when applied to a large number of animals; but the results were also prone to user bias due to the need for manual selection of regular breathing regions of the data set. Additionally, it has been reported that breathing frequencies calculated from short evaluation intervals (< 15 s) have significantly larger variations than the frequencies calculated from longer intervals (≥ 15 s) (6). It is possible that some of the considerable differences in breathing frequencies reported for control animals of the same strain, sex, and similar age could be due to variations in evaluation intervals or to differences in identification of the breathing cycle endpoints and evaluation procedures (7-12). Significant variations in the pattern of the resting breathing signal for a group of control WAG/Rij rats have been reported to produce a three-fold difference in the calculated breathing frequency (6). This problem could be more severe, if breathing pattern variations become more pronounced due to lung damage.

Two computer-aided analysis methods for breathing frequency measurement in small animals have been reported (2, 13) which eliminate some of the potential user bias. In one report, the consistency of the breath cycles was used to discriminate against animal movement. Regular breathing was empirically defined as when the difference between the periods of two consecutive breath cycles was less than 4% (13). The computer results were reported to correlate well with manual counting (13). In another report, the standard deviation of the breathing cycle period during the measurement interval was used to discriminate against aberrant data related to animal movement. Regular breathing was defined as when the standard deviation of the period varied by less than 5% of the average baseline period, measured for each animal prior to irradiation (2). Though these two computer-aided methods could better discriminate against movement than manual labor and possibly bias, they still calculated the breathing frequencies

based on mostly short evaluation intervals (< 15 s). Additionally, assessing quiet breathing using signal segment lengths of multiple breath periods unfavorably discarded quiet breathing cycles along with adjacent aberrant cycles. After identifying periods of quiet breathing, these approaches counted breathing cycles using either a zero-crossing counter approach (2) or, similarly, by calculating the mean amplitude of the signal and then using a mean-crossing counter technique (13). In the zero-crossing approach, a pressure reference was set either using the zero pressure or the local mean pressure, and the points where the breathing signal crossing the pressure reference were regarded as the beginnings or ends of the breath cycles.

An open-flow whole-body plethysmography approach with an automatic data analysis system is reported here, and will be applied for measuring rat breathing frequencies after irradiations to noninvasively quantify radiation-induced lung damage. This chapter describes both the hardware and software of this system and uses data from sham-irradiated control rats and one group of 8 rats that received a whole-lung dose of 11.75 Gy of x-rays; the BNCT radiation biology in the lung will be reported in Chapter 4. The apparatus was adapted from a commercially available system for rat breathing signal collection (Respiromax, Columbus Instruments, Columbus, OH). Customized Matlab programs were written for noise reduction and breathing frequency calculations. Fourier transform analysis was used to extract the breathing frequency from the breathing signal pressure data. The results of this Fourier transform-based analysis were compared to a method based on breath cycle counting, also programmed in Matlab, and to the results from the commercial software. The goals of the signal processing approach described here were to preserve long segments of breathing rate pressure change data after the automated noise filtering. The algorithms described here also allow estimation of the uncertainty (standard deviation) on each individual measurement using the

bootstrap method (14-16). The Fourier transform approach described here does not rely on a zero-crossing count as a measure of breath cycles and has allowed us to detect a fine structure in the breathing rate signal that is present in some control animals at a very low amplitude, but increases dramatically in the x-ray irradiated group, for example. The irregular shape of the individual breath cycles described here and analyzed by the signal processing algorithm could contain significant information about the nature of the lung damage.

3.2 MATERIALS AND METHODS

3.2.1 Animal irradiations

Male Fisher 344 rats, approximately 12 weeks old, were used for these studies. Rats were anesthetized with an i.p. injection of ketamine (80 mg/kg) and xylazine (10 mg/kg). Two rats were positioned, side-by side, under a 0.64 cm-thick lead delimiter with 4 cm wide aperture and immobilized with 5-cm wide clear adhesive tape. The lung region was positioned in the beam aperture (12 cm in diameter) using the bony protuberance of the T2 vertebra and the xyphoid sternum as reference points. Irradiations with x-rays were carried out using a Phillips RT250 unit operating at 250 kV and 12 mA with 0.4 mm Sn plus 0.25 mm Cu added filtration and a focus-to-skin distance of 32 cm. The x-ray dose rate in the lung volume was 1.0 Gy/min. These experiments were conducted with approval from the Committee on Animal Care at the Massachusetts Institute of Technology.

3.2.2 Breathing measurement apparatus

The apparatus for breathing frequency measurement was adapted from a commercially available breathing rate measurement system (Respiromax, Columbus Instruments, Columbus, OH). The commercial design confined the animal in a chamber and sealed the chamber by

cuffing the animal at the neck with an air-filled collar. The chamber was connected to a pressure transducer (SenSym, SCXL004DN, Columbus Instruments, Columbus, OH) and pressure changes inside the chamber were converted to electrical voltage signals, at data sampling rates of up to a maximum of 200 Hz, then sent to a laptop computer. The signal was displayed and stored on the computer. Four animals could be measured simultaneously on independent channels, each with one transducer and one chamber to hold one animal, provided by the system. Mean pressure during 8 breath cycles was calculated by the commercial software and 'zero-crossing' was applied to define the start and end of each breath cycle. The commercial software calculated breathing frequency as the mean of the 8 breath cycles and the results were recorded every 5 seconds during the measurement. No noise reduction was available in the commercial software.

The commercial chamber design for rat immobilization and breathing rate measurement did not work well with the male Fisher 344 rats in this experiment. The animals confined in the commercial chambers constantly struggled, sometimes were able to escape and occasionally died from asphyxiation. To resolve these issues, new chambers were designed, constructed and integrated into the commercial system. Four cylindrical Lucite chambers, each of 7.6 cm inner diameter and 20 cm long, with plugs and with expandable gaskets on each end to obtain an air-tight seal, were built to contain the animals. The chamber volume is adequate for rats weighing between 200 g and 500 g and the pressure changes inside the chamber due to animal respiration were easily detectable. Two holes were drilled in each chamber near each end and fitted with brass tubing connection ports (2 mm inner diameter). One port was connected to an air pump to provide fresh airflow through the chamber. Four chambers were connected to the airflow using

T-connections in the air-supply tubing. The second port on each chamber was connected to the pressure transducer and also served as the airflow outlet.

The breathing rates were measured for each animal every 1-2 weeks until 180 days after irradiation. During the measurement, animals were placed in the chambers with the head close to the air inlet. The airflow was maintained constant at 110 cm^3/min using a pressure meter. The chambers were covered with a cloth to calm the animals, and the four breathing signals were monitored simultaneously on the computer using the commercial software (Columbus Instruments). Breathing signals were collected continuously for 3 minutes with a sampling rate of 200 Hz.

3.2.3 Breathing Rate Analysis

Noise Reduction. The stored 3-minute breathing signals were analyzed offline using custom-developed programs in Matlab (The Mathworks, Natick, MA). Noise reduction was carried out in three stages. In the first stage, the sign of the first derivative of the pressure signal was computed and transition points from positive to negative or vice versa were marked, determining all local maxima and minima in the pressure signal. With the transition points, the signal was divided into individual segments of monotonic pressure changes. These segments were comprised of mainly regular animal inhalations and exhalations, a small portion of high-frequency noise, and, occasionally, large-amplitude noise related to animal movement. The noise was filtered in the next two stages.

In the second stage, high-frequency noise were removed by comparing the time intervals between the transition points. If any two transition points occurred within 0.04 s of each other, one was removed. This amounts to a 12.5 Hz high frequency cut-off on the raw pressure signal data. Maxima or minima with intervals of 0.04 s or less would correspond to $\geq$ 750 breaths per

minute (min^{-1}), and were considered to be beyond the breathing frequency range of a male F344 rat. Also, the amplitude of this noise was small compared to the usual amplitude for a regular breath cycle. It should be emphasized that the breathing signal pressure data remained unchanged; only the very high frequency transition point markers were discarded.

In the third stage, large-amplitude peaks, due to irregular animal movement (e.g., struggling against the chamber), were eliminated from the breathing signal data. Absolute values of the differences in amplitude between adjacent transition points were calculated. A histogram was plotted for this distribution of peak to valley (and valley to peak) amplitudes and the median value of this amplitude distribution was calculated. A limit was defined from the distribution as 2.5 times the median value, to differentiate animal movement from regular breathing. Segments with amplitudes larger than the limit were eliminated from the breathing signal. The remaining breathing signal, free of large-amplitude segments, was joined together. Once the breathing pressure signal was processed to remove the high-frequency noise and the large-amplitude noise from spurious movement to produce a continuous breathing pressure signal, the breathing frequency was then calculated using two independent algorithms and the results were compared.

Fast Fourier Transform and Bootstrap (FFT+BS). The algorithm to calculate breathing frequency used the Fast Fourier Transform to nonparametrically calculate the frequency spectrum of the pressure breathing signal. The input was the original pressure signal after the large-amplitude, movement-related peaks had been removed as described above. The FFT+BS method does not rely on peak counting, therefore no high frequency (>12.5 Hz) data was removed from the signal prior to the FFT analysis.

Rather than Fast Fourier transforming the entire 3 min breathing signal into the frequency domain all at once, the signal was analyzed using the FFT in combination with a circular moving

block bootstrap (14-17). This approach has advantages of noise suppression in the frequency domain and permits estimation of the uncertainty (standard deviation or confidence interval) of the frequency spectrum parameter of interest. In the time domain, the 3-min breathing signal was evenly segmented into 12 consecutive, overlapping blocks. Each block was 1 minute in length and the time between the start of two consecutive overlapping blocks was ~15 seconds. Some times between the start of two consecutive blocks are slightly shorter than 15 seconds, depending on the length of large-amplitude noise removed, as described above. Thus, there was 75% (45 seconds) or slightly larger overlap between two consecutive blocks. In the circular blocking technique, the last few blocks (three in this case) are wrapped around from the end of the signal to the beginning and encompass both the end and the beginning section of the breathing signal. This circular blocking technique ensures that all segments of the signal are equally sampled and weighted.

The frequency spectrum of each of the 12 blocks was calculated using FFT and a mean spectrum was calculated from the 12 frequency spectra. The maximum peak location in the mean frequency spectrum of the 12 blocks was defined to be the breathing frequency for the 3-min measurement. The starts of the overlapping breathing signal blocks were ~15 seconds apart, which is much longer than one breath cycle. The signal blocks were therefore regarded as only weakly dependent on each other. Also, after the large amplitude noise reduction described above, the statistical character of the rat breathing was assumed not to change significantly over the 3-min measurement period. Thus, the 12 overlapping blocks of breathing signal data were considered as "identical distributions" and the 12 frequency spectra from the 12 signal blocks were treated as Identical Independently Distributed (i.i.d.) random variables. The standard deviation of the breathing frequency derived from the mean frequency spectrum was estimated

using the bootstrap, a nonparametric re-sampling method with replacement (15, 16). The 12 frequency spectra served as a data set for bootstrap re-sampling. In each bootstrap calculation, 12 bootstrap samples (frequency spectra) were randomly selected, with replacement, from the data set. The location of the peak frequency computed from the mean of the 12 resampled bootstrap spectra was defined as the bootstrap breathing frequency for that calculation. To generate adequate statistical power, the bootstrap calculation of the breathing frequency was repeated 200 times. The 200 bootstrapped breathing frequencies formed an estimated distribution of the breathing frequency for the one original 3-min pressure change breathing signal. The standard deviation of this distribution estimates the standard deviation of the breathing frequency of this particular breathing signal, obtained previously from the mean of the 12 original frequency spectra (15). In summary, for each 3-min breathing signal measurement, the breathing frequency was the maximum value in the mean frequency spectrum of the 12 signal blocks. The standard deviation of the breathing frequency was estimated using the bootstrap from the 12 i.i.d. signal blocks. The process of mean breathing frequency determination and the uncertainty estimation with bootstrap is displayed in Fig. 3.1.

Based on a survey of the rat breathing rate literature, it was assumed that a breathing rate range of 100 to 600 min^{-1} would cover all situations for the male F344 rats. The frequency spectra were only analyzed within this range. The control Fisher 344 rats showed a regular and symmetrical pattern of breath cycles, and the FFT frequency spectra usually had one major peak, but occasionally one or two very low amplitude peaks appeared at higher frequencies. In this situation, the frequency of the major peak maximum was defined as the breathing frequency of the breathing signal data, and the standard deviation was estimated with the bootstrap method described above. For animals with radiation-induced lung damage, considerably larger variation

of the breath cycle pattern was observed. Up to three peaks of comparable amplitude appeared in the FFT frequency spectra calculated from the breathing signal data. In this situation, frequencies of each peak maximum were recorded and the standard deviations of the frequencies were estimated within subranges of about 100 min^{-1} centered on each peak. Since only one value of breathing frequency was to be derived from the breathing signal, if the relative amplitude of the higher frequency peak in the FFT spectrum was greater than 0.5, the higher value was used as the breathing frequency and served to demonstrate the severity of the lung damage.

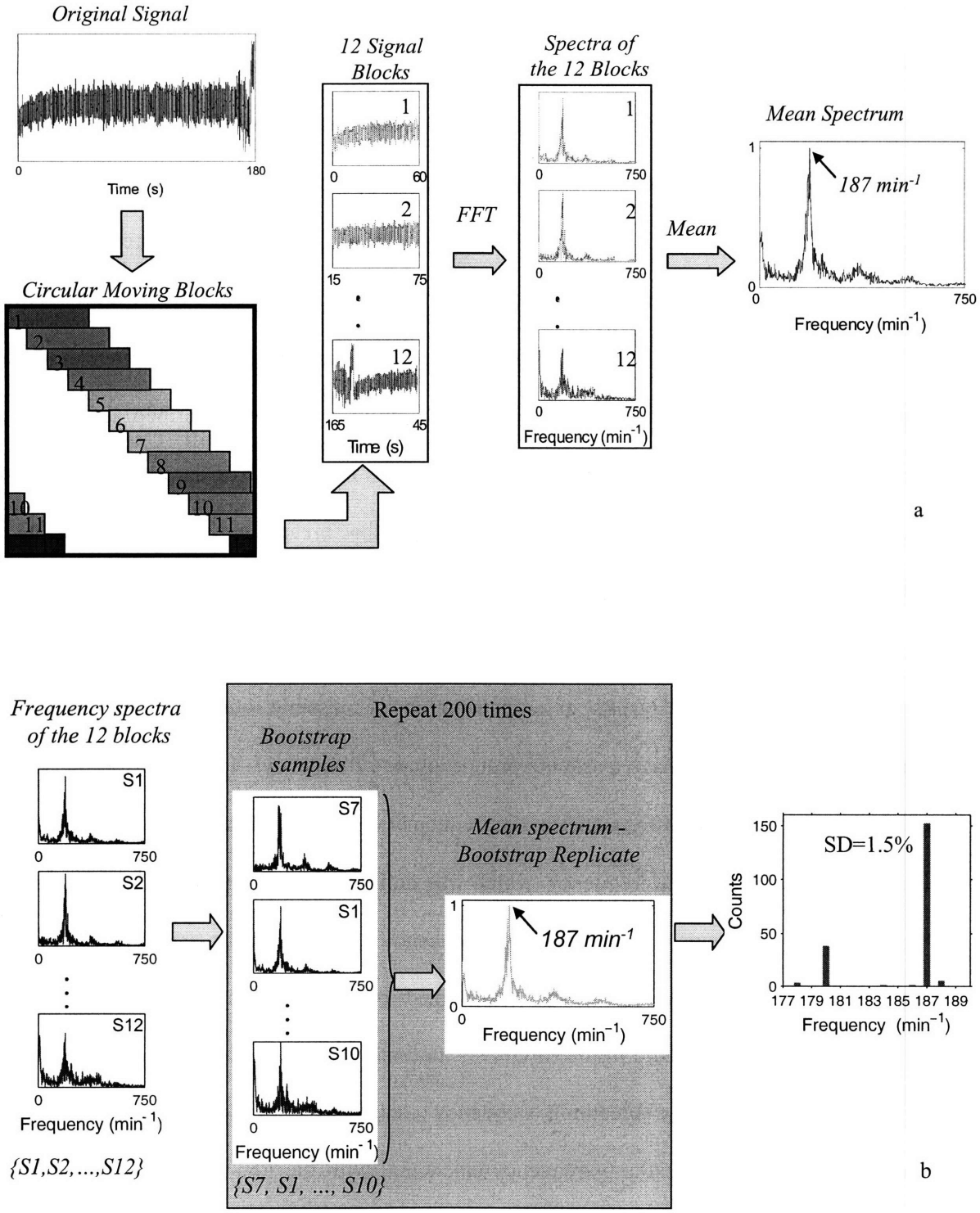

Fig. 3.1 The process of the FFT+BS method: breathing frequency determination (panel a) and the uncertainty estimation with bootstrap (panel b).

Breathing Frequency Density Function. The Breathing Frequency Density Function (BFDF) method is an approach for estimating the distribution of breathing frequencies based on peak counting. The input is the original pressure signal after the noise reduction algorithm has removed both the large-amplitude, movement-related noise, as well as components greater than 12.5 Hz, as described above. The BFDF method uses the transition points of the pressure signal, where the derivative changes sign, to calculate the periods of individual breath cycles. Time intervals were calculated for each breath cycle, defined as two consecutive monotonic segments of opposite sign in the breathing signal data, after the noise reduction described above. The breathing frequency of each breath cycle was calculated as the inverse of the time interval. A histogram of the distribution of breathing frequency of this breathing signal was calculated. Because the breathing signal is sampled at 200 Hz, the distribution of the time intervals of the breathing periods is discretized in increments of 0.005 s. Inverting the discrete time intervals to obtain breathing frequencies results in a distribution of possible frequencies that are not uniformly spaced but, rather, have a spacing proportional to frequency. To properly compensate for this nonuniform spacing of frequencies, the frequency distribution histogram was divided by the band width of each discrete frequency, which was defined as the sum of half the distance to the upper and lower frequencies. The breathing frequency density function (BFDF) was defined as this frequency distribution histogram, normalized by the frequency bandwidths. The frequency with maximum density in the BFDF was defined to be the breathing frequency of the particular measurement. The breathing frequency calculated with BFDF was used as an independent check on the breathing frequency calculated with the FFT+BS method described above.

3.3 RESULTS

Fig. 3.2 shows an example of a 30 s segment from a 3-minute long breathing signal acquired from a control animal 35 days after sham irradiation. Calm regular breathing is evident with a few periods of large amplitude movement-related noise near the end of the signal.

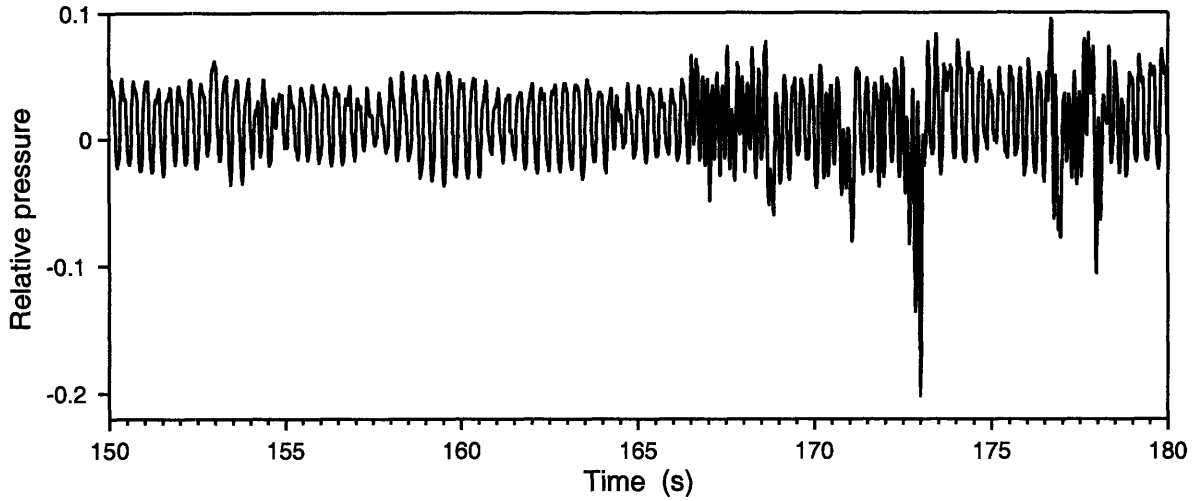

Fig. 3.2 A 30 s segment from a 3-minute long breathing signal from a control animal acquired 35 days after sham irradiation. After a period of relatively regular breathing, high amplitude movement-related noise is evident in the latter third of this signal segment.

3.3.1 Noise Reduction

The procedure for noise reduction is demonstrated with a breathing signal example from a control animal with large-amplitude movement-related noise observed at the end of the 3-minute measurement. In the first stage of noise reduction, pressure signal sign change transition points were identified, and the high-frequency noise (>12.5 Hz) filtered out by removing transition points with periods < 0.04 s. The absolute values of the amplitudes of the segments from this signal, after high-frequency filtering, were calculated and the histogram is shown in Fig. 3.3 with the x-axis (amplitude) normalized to the median value of the distribution. The main distribution

of the pressure amplitude histogram was approximately bell-shaped. The main distribution decreased to almost zero at about 2 times the median with a low-occurrence tail out to 2.5 times the median. Beyond 2.5 times the median, the segments were sparse and did not appear to be relevant to the main distribution. Therefore, a value of 2.5 times the median pressure amplitude of the segments was defined to be the limit for large-amplitude noise elimination for this breathing signal. With the limit defined, breath cycles with individual monotonic pressure change sign segments having an amplitude greater than the limit were eliminated from the signal and the remaining signal was joined together. Fig. 3.4 shows the detail of this stage of noise reduction with this breathing signal as an example. The dark black section of the original signal (dashed black line) was determined to be large amplitude noise and then removed from the signal. The remaining signal was then joined together as the processed signal (the solid grey line). The derivative sign change transitions of the pressure signal at the start and end of each inhalation and exhalation are also highlighted with circles on the processed signal.

The value of 2.5 times the median pressure segment amplitude was found to be a universal threshold between segments of regular breathing and irregular animal movement in each individual breathing signal. Therefore, this value was calculated and defined as the limit for large amplitude noise elimination during processing of each breathing signal. Using this limit, among more than 4000 breathing signals processed, 92% of the signals had more than 98% of the original 3-minute breathing signal remaining. Only 0.6% of the signals had less than 90% of the original signal remaining and none lost more than 30% of the original signal. The signals processed for noise reduction were then used in the two independent calculations of breathing frequencies.

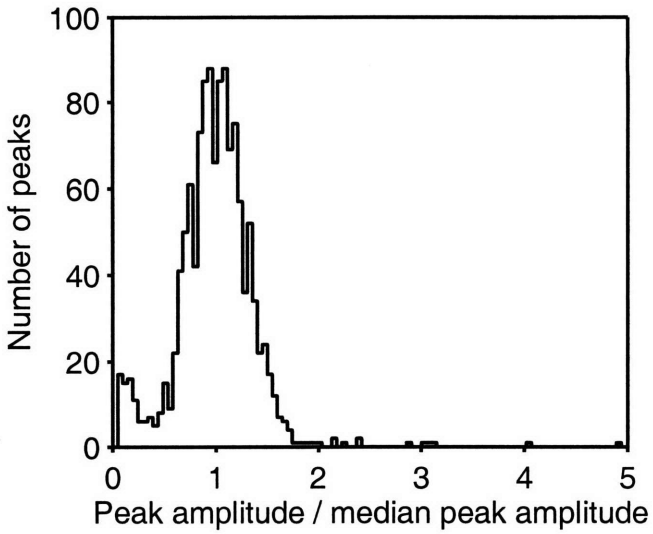

Fig. 3.3 An example pressure amplitude distribution histogram for a 3-minute breathing signal from a control animal.

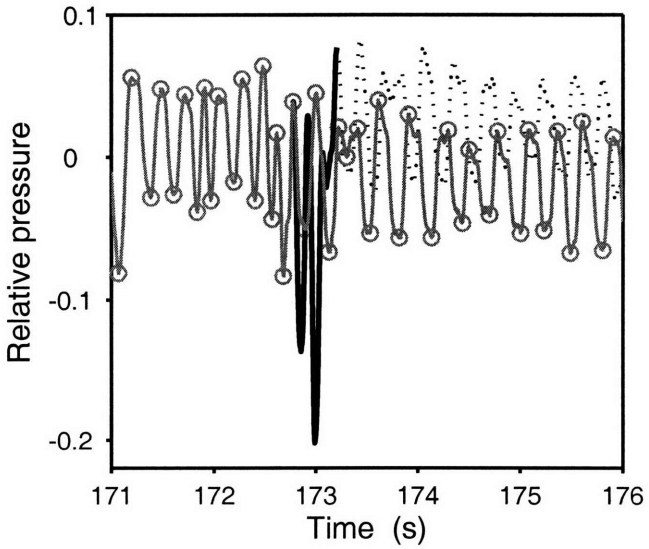

Fig. 3.4 The elimination of segments of large amplitude in noise reduction after discrimination against ripple noise. The dotted line is the signal before noise reduction. The black solid line is the highlighted noise due to irregular animal movement and was eliminated from the original signal. The signal after noise reduction is demonstrated with the grey line, with the circles marking the pressure transition points (after elimination of ripple noise).

3.3.2 Comparison of different methods for determining of breathing frequency using control animals

An example of the mean frequency spectrum calculated with the FFT from the 12 blocks of a 3-minute breathing signal of a control animal is shown in Fig. 3.5. In the example, the spectrum has been normalized to its maximum amplitude and shows one major peak located at a frequency of 177 ± 1.4 min^{-1}, and two small peaks located at higher frequencies of about 350 and 530 min^{-1}, respectively. The relative amplitudes of the two higher frequency peaks were less than 0.1. The BFDF of this signal is also plotted in Fig. 3.5 and normalized to its maximum amplitude. The peak of the BFDF is located at 171 min^{-1}. The difference between breathing frequencies determined by these two methods is 3.4%.

The two methods of breathing frequency calculation, FFT+BS and BFDF, were compared to each other by using both methods to analyze the breathing signal data from a group of 8 control rats. The data set consisted of 136 signals from 8 sham-irradiated control animals measured over a period of about 180 days after the sham irradiations. Among the total 136 pairs (FFT+BS and BFDF) of results, 81% had less than 5% difference; 15% had differences between 5% and 10%; and the rest had differences of more than 10%, but none of the differences exceeded 20%. For this group of 8 control rats, the breathing frequency calculated with the FFT+BS was 176 ± 13 (7.4%) min^{-1} (mean ± SD), with a mean standard deviation for each individual breathing frequency of 2.3%. For the same data from the same group, the value calculated with the BFDF was 177 ± 11 min^{-1} (mean ± SD).

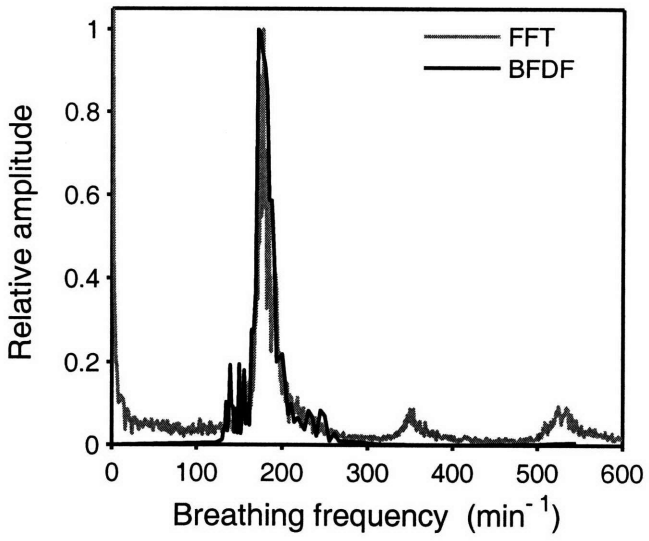

Fig. 3.5 The spectrum calculated with FFT compared to BFDF of a 3-minute breathing signal from a control animal. The major peak values from the FFT and BFDF analyses are 177 min^{-1} and 171 min^{-1}, respectively. Both the FFT spectrum and the BFDF are normalized to a major peak amplitude of unity. The presence of peaks in the FFT spectrum, at about 2 and 3 times the frequency of the principal peak, is notable.

After the FFT+BS method was compared to the BFDF method, the results with FFT+BS were compared to the results calculated by the commercial software which used short evaluation intervals, no noise reduction, and a zero-crossing approach for breath cycles counting. Using the commercial software, during one 3-minute measurement of control rat breathing rate, the breathing frequency based on 8-breath cycles was recorded every 5 seconds and the mean and standard deviation of the these 36 values were calculated. As an example, the breathing frequencies calculated with this commercial software are compared to results with FFT+BS using data from one individual sham-irradiated control animal (Fig. 3.6). Since the commercial software does not employ noise reduction, the data used to determine the 36 breathing rates from each 3-minute breathing signal sometimes included large-amplitude noise which was otherwise eliminated in the customized software described in this thesis. In Fig. 3.6, the number of the 36

subsamples calculated by the commercial software that contained large-amplitude noise was determined manually for this example and the values are indicated above each breathing frequency value. The frequency measurements with no numerical labels above the points had no large-amplitude noise involved in the measurements and agree reasonably with the breathing frequencies calculated by the FFT + BS method. The standard deviation of individual breathing frequency measurements from the commercial software is significantly larger than with FFT+BS, in all situations, including the points with no large-amplitude noise. In this example, the mean of the standard deviation from the 17 measurements taken over 180 days with this animal was 17% with the commercial method compared to 2% with the FFT+BS. For the control group, both the mean breathing frequency and the standard deviation calculated with the commercial software were larger than with FFT+BS, as 213 ± 28 min^{-1} compared to 176 ± 13 min^{-1}. The average standard deviation of the 136 measurements from this particular control animal with the commercial software was 16%, much larger than the corresponding value of 2.3% with the FFT+BS method. This is perhaps not a fair comparison due to the serious limitations in the commercial software: short (8 breath cycle) evaluation intervals and no noise reduction. This software would only produce data as accurate if there were manual observation to identify periods of quiet breathing and data acquisition only during these quiet periods.

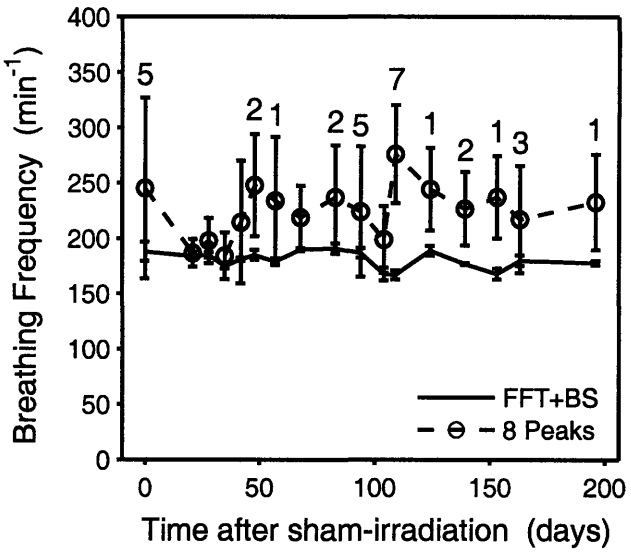

Fig. 3.6 The breathing frequencies of a control rat versus time after sham irradiation calculated with 8-peak method from the commercial software compared to the FFT+BS method. The number labeled above each frequency of 8-peak method is the number of the 36 subsamples recorded during the 3-minute measurement calculated from 8 breath cycles involving large amplitude noise. The measurements with no labels above them had no large amplitude noise involved in the data.

3.3.3 Analysis of radiation-damaged rat breathing signal data with the method of FFT+BS

As shown in Fig. 3.5, small peaks at frequencies higher than the main breathing frequency peak sometimes appeared in the frequency spectrum of the control animals. This phenomenon occurred in about 70% of the control signals collected. This feature of the breathing signal frequency spectrum is presumably due to the natural variations and fine structure of the breathing pattern. In the control group breathing frequency spectra, the amplitudes of these peaks at high frequencies were small compared to those of the primary peak. About 80% of these smaller, higher frequency peaks had a relative amplitude of 0.2 or smaller and none of them had a relative amplitude larger than 0.5. However, when the lung became damaged from radiation, the pattern of breathing varied considerably and this fine structure phenomenon became more significant. More than one peak was often observed in the breathing frequency spectrum, and the amplitude

of the high-frequency peaks became comparable to or larger than the primary breathing frequency peak. A relative amplitude of 0.5 was used as a threshold to define peaks at high frequency as 'normal' ($\leq$0.5) and due to the fine structure of the normal breathing pattern variation or as 'responding' (>0.5) and due to lung damage. Peaks in the frequency spectra larger than the 0.5 relative amplitude threshold were automatically located and their frequencies were recorded. The frequency of the highest frequency significant peak in the spectrum was defined as the breathing frequency for the measurement, although, the frequencies of all significant peaks were recorded. The standard deviation of the frequency of each significant peak of the spectrum was estimated using the bootstrap within a 100 min^{-1} range centered around the maximum value. The BFDF method also detected more than one peak, but the frequency of the maximum value of the BFDF was used directly as the breathing frequency with the BFDF for irradiated animals. For breathing signal from control animals, the high frequency peaks were barely detectable with the BFDF, because most of this fine structure of the breath cycles fell into the range of ripple noise (< 25 Hz) and their transition markers were discarded before frequency calculation in the BFDF.

Breathing signal pressure change data from a rat with radiation-induced lung damage is shown in Fig. 3.7 and compared to data from a control animal. The animal with lung damage received an X-ray dose of 11.75 Gy to the whole lung region and the breathing measurement was at 68 days after irradiation. The breath cycles of the responding animal showed significantly larger variations and more fine structure compared to the control animal (Fig. 3.7). The frequency spectrum of the breathing signal of the control animal is shown in Fig. 3.5. The frequency spectrum of the responding animal is shown in Fig. 3.8. Two peaks were observed in the responding animal frequency spectrum, located at 200 $\pm$ 1 min^{-1} and 381 $\pm$ 2 min^{-1} with

relative amplitudes of 1 and 0.8, respectively. Also shown in Fig. 3.9 is the BFDF of the same breathing signal from this positively-responding, irradiated rat. Two corresponding peaks were also observed located at 203 and 375 min^{-1}, which are within 3% and 2% of the respective values obtained via FFT.

Of the more than 4000 breathing signals processed with this software using the two independent methods of FFT+BS and BFDF, about 70% of the pairs of breathing frequency values calculated with the two methods from the same pressure signal (after noise reduction) had agreement better than ±5%; about 90% had agreement better than ±10%; 98% of the results had agreement better than ±20%. The mean of standard deviation of all the breathing frequencies estimated with the FFT+BS method was 2.4%, with 75% of the values smaller than 3% and 99% smaller than 10%.

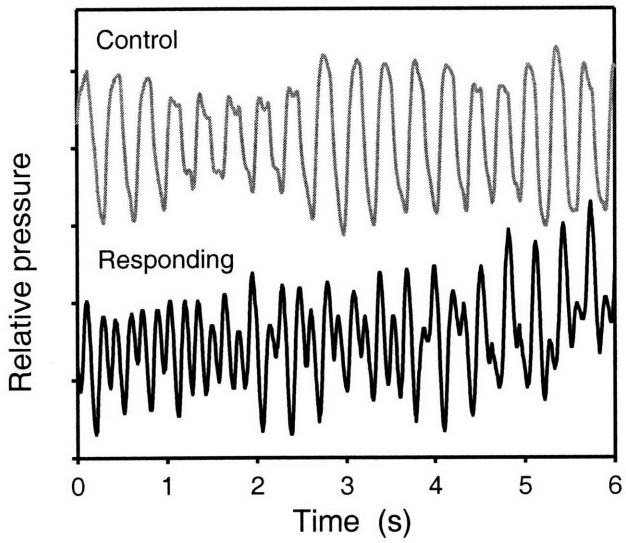

Fig. 3.7 The comparison of breath cycle patterns from a responding animal to the patterns of a control animal. The frequency spectrum of this control signal is shown in Fig. 3.5. The frequency spectrum of the responding signal is shown in Fig. 3.8.

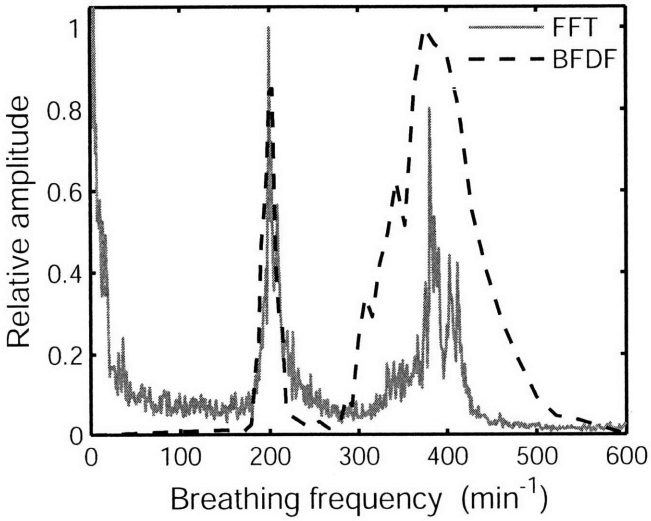

Fig. 3.8 The spectrum with the method of FFT+BS comparing to the BFDF of a breathing signal from a responding animal. Peaks of relative amplitude larger than 0.5 were automatically located and the corresponding frequencies calculated. The peak location for the second peak of the FFT spectrum was used as the breathing frequency of this signal. The breathing frequency in this case is 381 ± 2 min^{-1} with FFT+BS and 375 min^{-1} with BFDF.

3.4 DISCUSSION

The FFT+BS and BFDF methods produce similar but subtly different results related to the distribution of breathing frequencies. The BFDF method constructs a histogram of breathing frequencies for a signal by determining the frequency of each breathing cycle in a signal (as determined by the inverse of the period between peaks) and counting the number of occurrences of each of the resulting discrete frequencies. The FFT plus bootstrap method resolves a breathing signal into its constituent frequencies. The values contained in FFT frequency spectrum at each frequency are proportional to the signal amplitude at that frequency. The BFDF is proportional to the incidence of breathing cycles at a particular frequency in a signal.

The differences in the nature of these two techniques, the analysis of discrete breathing cycles in the BFDF and the continuous analysis of the breathing signal with the FFT, can lead to differences in results. One might consider this as a difference in how the breathing cycles are weighted in the two techniques. In the BFDF, all breathing cycles are weighted uniformly and their contributions to the distribution are equal, where as in the FFT spectrum, each frequency is weighted by its amplitude in the time domain. Thus, differences in the amplitudes of breathing peaks will be reflected in the FFT spectrum. Moreover, quick changes (<0.04 s) or irregularities in the shapes of the peaks and valleys of the breathing cycle will be detected by the FFT spectrum, but not by the BFDF. In spite of the differences between these two techniques, they produced very similar results in this study and their comparison serves as a useful consistency check on these results.

The use of breathing rate as a functional endpoint in studies of the radiation biology of the lung is well established (1-6). A serial functional assay has many advantages over an invasive one-time assay. The analysis of breathing signal pressure data has always involved the

complications due to animal movement producing spurious noise in the data. Early investigations relied on manual observation to identify time periods when the animal was resting quietly and breathing "normally." Some investigations preferably selected minimum recordings of the breathing frequency as quiet breathing data to avoid large variations in the determined breathing frequency (11). Two semi-automated approaches have been previously reported that use computer algorithms to identify periods of quiet resting breathing and analyze only this part of the signal (2, 13). These approaches have taken the approach of sequentially analyzing short segments of breath cycle data and rejecting as noise segments containing a calculated breathing frequency difference greater than an arbitrarily chosen limit. One effective improvement of the customized breathing frequency analysis software reported here from the previous approaches is noise reduction. Since there seemed to be no universal threshold with the period or frequency covering all situations in noise discrimination without having prior knowledge of the breathing signal, the noise discrimination was carried out on the basis of peak amplitude. The peak amplitude distribution histogram of the 3-minute breathing signal was used to discriminate against large-amplitude noise. It is a more direct and efficient way to differentiate irregular animal movement. In the FFT+BS method, random noise suppression was further carried out in the frequency domain through a circular blocking technique.

Another advance of this breathing frequency analysis approach is that the breathing frequency is derived from a distribution of frequencies in the 3-minute breathing signal, yielded either with the BFDF or FFT, as compared to the conventional method, where breathing frequency is defined as the number of breath cycles during a period divided by the time (1-3, 13). Most conventional frequency measurements counted breath cycles with a zero-crossing approach or an exactly analogous mean amplitude crossing approach. For example, Haston et al.

calculated breathing frequency by first determining the mean signal amplitude for a region of quiet breathing and then counting the number of times the breathing signal crossed this mean value divided by twice the duration of the counted region (2). Thus, the zero-crossing approach yields the mean value of the breathing frequency during the selected period (or periods). The definition of each individual breath cycle with a zero-crossing approach can be problematic and can influence the frequency measured, especially with a small number of breath cycles, due to the locally changing baseline of the breathing pressure trace. A defined or calculated mean pressure drawn through the breathing pressure trace (mean-crossing) does not necessarily segment the breath cycles consistently or uniformly. Additionally, it can overlook some fine structures in the valleys or peaks of the breath cycles. Defining the breath cycles with transition points at their local maxima or minima, as in BFDF, in contrast, more consistently segments the breath cycles and is a more accurate approach especially with a small number of breath cycles.

The conventional peak counting approach results in a single mean value for the breathing rate while the FFT and BFDF yield distributions of frequencies, with the standard deviation of the mean breathing frequency with FFT estimated with the bootstrap. The differential analysis of the breathing frequency components in the signal make the FFT and BFDF more robust than conventional approaches, and more readily capture irregularities in the breathing patterns. Fourier transform analysis is especially well suited to extract the underlying frequency information by decomposing the signal into its constituent frequencies. Nevertheless, it is still necessary to determine a single value from the FFT and BFDF spectra to represent the breathing rate. For the BFDF, this value is the most probable (most frequently occurring) frequency while for the FFT, it is the most powerful frequency.

Using the Fourier transform to analyze the breathing signal and decompose the frequency information has detected and quantified interesting information and fine structure of the animal breathing pattern, which would be overlooked by a conventional zero-crossing approach. For example, consider the lower (responding) data trace in Fig. 3.7. The irregularities of the breathing pattern of this trace were transformed into two major peaks in the frequency domain obtained with FFT in Fig. 3.8. On the other hand, a conventional zero-crossing counting method with a horizontal line drawn through this trace at the mean amplitude would miss many of the fine structure peaks that occur near the peaks or valleys of the primary signal. Additionally, as a result of the averaging in the conventional approach, it is possible to calculate a breathing frequency that does not actually exist in the frequency spectrum obtained with FFT, due to the irregularity of the breathing signal from radiation damage. This might have contributed to the variation that has been reported by different groups in the literature for the breathing rates of similarly-treated animals of the same strain (7, 8, 10, 18). The possibility of breathing frequency measurements being influenced by variations in breathing pattern was also reported by Raabe and Beck-Bornholdt (6) with a group of control WAG/Rij rats that had not been subjected to any lung insult. The breathing patterns of these control animals fell into three distinct shapes: regular sinusoidal; an elongated inhalation phase followed by a short exhalation; and a third example that was a more extreme version of the second. The breathing frequencies determined for these three distinct patterns, by manual counting of the breath cycles from printed strip chart records, varied by a factor of three and were reported as 150 ± 3 , 104 ± 3, and 44 ± 1 min^{-1}, respectively. The authors pointed out that breathing pattern should be considered when breathing rate data were evaluated.

The phenomenon that we have detected in the breathing signal from irradiated rats indicates that this may indeed be a case of the breath cycle pattern changing as a function of the physiology due to the damage in the lung. The data shown in Fig. 3.7 as a typical example of breathing signals of irradiated animals suggest that the breath cycles are mostly primary regular breath cycles with secondary, higher frequency damaged-breathing activities superimposed on top of it. It is interesting to note that the positions of these peaks are at about 2-times and 3-times the primary frequency. Moreover, in some control animals these peaks are also visible, albeit at a very low amplitude (see Fig. 3.5). This observation suggests that even in the control animals, a small percentage of the individual breath cycles had a fine structure, i.e., a secondary smaller peak (see the upper trace in Fig. 3.7). The changing of the breathing patterns can be explained as the lung physiological change due to radiation damage, which is often observed in human with radiation lung damage (19). During the pneumonitis stage after the lung radiation, the lung alveoli are partially obstructed by lung fluid, and the surface tension of the lung increased due to lack of surfactant. Both contributed to the decreased lung compliance (the ease to inflate a lung) (20). Under this condition, with the same pressure change applied to the lung by the chest wall, the volume change of the lung with radiation pneumonitis is smaller that of a normal lung. Not only does the lung have problem inflating during inspiration, it also has problem to exhale the air inside and decrease its volume. Most often, the first breath cycle is not totally completed and the lung has not returned to the status at the beginning of the inhalation, when the beginning of the next breath cycle takes place. Similarly, during the lung radiation response of fibrosis, the compliance is also decreased due to the thickened alveolar wall, which initiates the irregularity of the breath cycles. In general, the breathing signals with radiation lung damage are composed of irregular and nonsymmetrical breath cycles (Fig. 3.7).

Breathing frequency dose response data are often quantized, fit with a probit function, and analyzed by comparing 50% effective doses (ED_{50}). Converting the dose response data into a quantal response is carried out by establishing a threshold based on the control breathing frequency and by defining a positive response as any breathing rate that exceeds this threshold. For this approach, the standard deviation of the control data defines the threshold that can be used. The difference between the threshold and the controls must be statistically significant; the threshold should be at least 2 standard deviations above the control group mean value. Response threshold values used in the literature have ranged from 20% to 40% above the control group mean (2, 11, 21, 22). The improved accuracy and small standard deviation of the measured breathing frequencies of the control group with this custom developed software resulted in significant improvements in sensitivity for detecting the occurrence of lung damage. The FFT+BS mean for the 8 control animals was 176 ± 13 min^{-1} and a positive response threshold 20% higher would be 212 min^{-1}, which is 2.8 standard deviations above the control group mean. No breathing frequency was measured above the positive response threshold (mean +20%) for control animals using this customized system. Variability is dramatically higher with the commercial software, making correct assessment of the breathing rate data very difficult. With the breathing rates determined by the commercial software, 1 of the 8 control animals would be categorized as responding if the response threshold were set at 40% above the mean value. Using a threshold 30% above the mean, 2 of the 8 controls would be categorized by the commercial software as responding and, with the threshold used with the FFT+bootstrap method, 20% above the mean, 6 of 8 controls would be categorized as responding.

In summary, a new and improved approach to the analysis of digital breathing signal data is reported here. The method includes an automated program for removal of movement-related

noise in the signal, followed by a Fourier transform analysis to extract all breathing frequency information from the raw data. A fine structure in the breathing rate data is detected that is infrequently present in the controls at very low amplitude, but that increases dramatically in amplitude in the irradiated group of rats. This fine structure in the breathing pressure change signal will require further study to fully understand the origin and implications of this phenomenon.

3.5 REFERENCES

1. Travis EL, Vojnovic B, Davies EE, Hirst DG. Plethysmographic Method for Measuring Function in Locally Irradiated Mouse Lung. British Journal of Radiology 1979;52:67-74.
2. Haston CK, Newcomb CH, Grant K, Hill RP, Vandyk J. Ultrasonic Measurements of Breathing Rate in Rats and Computer-Assisted Analysis. International Journal of Radiation Oncology Biology Physics 1993;27:651-657.
3. Feaster GR, Kimler BF, Henderson SD, Mansfield CM. Simple Plethysmograph for Measuring Respiration Rates in Rats with Lung Damage. Review of Scientific Instruments 1984;55:1058-1060.
4. Landry TD, Ramsey JC, McKenna MJ. Pulmonary Physiology and Inhalation Dosimetry in Rats - Development of a Method and 2 Examples. Toxicology and Applied Pharmacology 1983;71:72-83.
5. Jacky JP. Plethysmograph for Long-Term Measurements of Ventilation in Unrestrained Animals. Journal of Applied Physiology 1978;45:644-647.
6. Raabe A, BeckBornholdt HP. The possible influence of breathing patterns on the measurements of breathing frequency. Radiation Research 1996;145:236-238.
7. Pauluhn J, Baumann M, Hirth-Dietrich C, Rosenbruch M. Rat model of lung fibrosis: comparison of functional, biochemical, and histopathological changes 4 months after single irradiation of the right hemithorax. Toxicology 2001;161:153-163.
8. Mauderly JL. Respiration of F344 Rats in Nose-Only Inhalation Exposure Tubes. Journal of Applied Toxicology 1986;6:25-30.
9. Chen LG, Brizel DM, Rabbani ZN, Samulski TV, Farrell CL, Larrier N, Anscher MS, Vujaskovic Z. The protective effect of recombinant human keratinocyte growth factor on radiation-induced pulmonary toxicity in rats. International Journal of Radiation Oncology Biology Physics 2004;60:1520-1529.

10. van Eerde MR, Kampinga HH, Szabo BG, Vujaskovic Z. Comparison of three rat strains for development of radiation-induced lung injury after hemithoracic irradiation. Radiotherapy and Oncology 2001;58:313-316.

11. Van Rongen E, Tan CHT, Durham SK. Late Functional, Biochemical and Histological-Changes in the Rat Lung after Fractionated-Irradiation to the Whole Thorax. Radiotherapy and Oncology 1987;10:231-246.

12. Travis EL, Down JD, Hall L, Vojnovic B, Holmes SJ. Factors affecting the breathing rate of mice as used for studies of radiation damage to lungs. Brithish Journal of Radiology 1981;54:50-53.

13. Lockhart SP, Hill D, King S, Down JD. A Semiautomated Method for Breathing Rate Measurement in the Mouse. Radiotherapy and Oncology 1991;22:68-70.

14. Zoubir AM, Iskander DR. Boostrap techniques for signal processing. New York: Cambridge University Press; 2004.

15. Efron B, Tibshirani RJ. An introduction to the Bootstrap. Boston: Chapman & Hall; 1993.

16. Politis DN, Romano JP. A circular block-resampling procedure for stationary data. In: R. L, L. B, editors. Exploring the limits of Bootstrap. New York: John Wiley & Sons; 1992. pp. 263-271.

17. Stearns SD. Digital signal processing with examples in Matlab. New York: CRC Press; 2003.

18. Wiegman EM, Meertens H, Konings AWT, Kampinga HH, Coppes RP. Loco-regional differences in pulmonary function and density after partial rat lung irradiation. Radiotherapy and Oncology 2003;69:11-19.

19. Abratt RP, Morgan GW. Lung toxicity following chest irradiation in patients with lung cancer. Lung Cancer 2002;35:103-109.

20. Gross NJ. Experimental radiation pneumonitis: changes in physiology of the alveolar surface. J of Lab Clin Med 1978;92:991-1001.

21. Parkins CS, Fowler JF, Maughan RL, Roper MJ. Repair in Mouse Lung for up to 20 Fractions of X-Rays or Neutrons. British Journal of Radiology 1985;58:225-241.

22. Travis EL, Parkins CS, Holmes SJ, Down JD, Fowler JF. WR-2721 protection of pneumonitis and fibrosis in mouse lung after single doses of x rays. Int J Radiat Oncol Biol Phys 1984;10:243-251.

CHAPTER FOUR

Radiobiology of Normal Rat Lung in Boron Neutron Capture Therapy Evaluated with Breathing Frequency

4.1 Introduction

Lung is one of the dose limiting tissues in radiation therapy for bone marrow transplantation and thoracic malignancies including lung cancer and Hodgkin's disease (1-4). Two phases of the lung radiation response have been identified both in the clinic and in experimental animal models of lung radiation response: the early inflammatory pneumonitis and the late pulmonary fibrosis (5-8). In clinical radiotherapy, the early phase usually occurs within 6 months after irradiation (9). The late fibrosis can develop from months to years after the irradiation. The incidence of radiation pneumonitis is related to the dose delivered and also to the volume of the lung irradiated. Dose volume histograms (DVH) of the lung are calculated, and the mean lung dose is used as a simple parameter to predict the incidence of radiation induced pneumonitis (9-11). A single mean lung dose of 9.3 Gy was reported as the ED_{50} for radiation pneumonitis in patients (12). Higher doses are required to produce a similar incidence of radiation pneumonitis when the lung is partially irradiated or dose is fractionated.

Boron Neutron Capture Therapy (BNCT) is a binary cancer therapy with biochemical tumor-cell targeting (13). The neutron capture reaction in ^{10}B releases 2.79 Mev energy, 82.8% on average of which is deposited within the targeted cell due to the short ranges (7 μm and 4 μm) of the heavy charged particles released, α and ^{7}Li. In the period between 1994 and 1999, researchers at Harvard-MIT carried out BNCT clinical studies involving patients with glioblastoma, melanoma metastatic to the brain, or subcutaneous melanoma of the extremities (14, 15). Two patients receiving treatment for brain tumors developed a fatal acute respiratory distress syndrome (ARDS); one other patient developed an acute pneumonitis, but recovered following intensive supportive care. At the time dose estimates for scattered radiation to the lung were below the threshold for radiation induced ARDS. However the serious adverse events with ARDS raised the concern that the lung might be more radiosensitive to BNCT irradiation than presumed and the weighting factors might be unexpectedly high. The boronated amino acid, boronophenylalanine-fructose (BPA-F), was used in this clinical trial (16).

BNCT produces a mixture of radiations in tissue that have different Linear Energy Transfer (LET) and hence have varying biological effectiveness. Our approach to express the total BNCT dose in photon-equivalent units utilizes the experimental determination of Relative Biological Effectiveness (RBE) factors, weighting factors for each of the high-LET dose components (13). Analogous to the RBE, the compound biological effectiveness (CBE) factor is defined the weighting factor for the ^{10}B dose component that accounts for the influence of both the $^{10}B(n,\alpha)^{7}Li$ radiation quality and the boron microdistribution (from a specific boron compound) on the radiobiological effectiveness. (13, 14). For a given biological endpoint, the RBE or CBE is defined as the ratio of the dose of a high LET radiation to an isoeffective dose of x-ray

radiation. Thus, the total biologically weighted BNCT dose is the weighted sum of all dose components:

$$D_w = w_\gamma D_\gamma + w_T D_T + w_F D_F + w_B D_B, \quad (1)$$

where w_γ, w_T, w_F and w_B are weighting factors (RBE or CBE factors) for the photon, thermal neutron, fast neutron and the ^{10}B absorbed doses, respectively. In BNCT, w_γ is usually regarded as unity and w_T and w_F are usually equal to each other (13). In lung, the biological effectiveness weighting factors are unknown. This information is critical to estimation of the total biologically weighted dose to the lung. From the normal lung clinical tolerance reported in the literature (12), if the lung complications in the three patients treated with BNCT were indeed due to radiation dose, it would imply that the maximum (single fraction) dose to the lung was at least 8 Gy_w.

Dosimetry measurements in an Alderson-RANDO anthropomorphic phantom indicated that the weighting factors for the high LET (Linear Energy Transfer) dose components of neutron and ^{10}B in BNCT would have to be at least 3.2 and 4, respectively, to bring the dose to the apex of the lung to 8 Gy_w (17). The ^{10}B concentration in the lung was estimated to be twice the blood ^{10}B concentration in this report. In this chapter, radiobiological studies in the normal lung of rats are described which measure the weighting factors required for the weighted lung dose calculation in BNCT. Rat whole-thorax irradiations were carried out with x-rays, thermal neutrons, and thermal neutrons with BPA. The rat lung functional morbidity measured with a breathing rate assay was used as the biological endpoint to quantify lung radiation damage in BNCT. Dose response curves were established and the RBE and CBE factors were determined from these curves.

4.2 Materials and methods

The vertical M011 thermal neutron beam (18, 19) of the MIT Research Reactor (20) was used for neutron irradiations in these studies. This neutron beam is suitable for small animal irradiations and for treating superficial human tumors such as melanoma. It has a clean thermal neutron energy spectrum (fast neutron component of total neutron flux is ~ 1%) and high intensity (~10^{10}n/cm^{2}s) (19). Irradiations with x-rays were carried out using a Phillips RT250 unit operating at 250 kV and 12 mA with 0.4 mm Sn plus 0.25 mm Cu added filtration.

4.2.1 The MCNP rat model for BNCT irradiations

The computational tool used in the design of the experimental rat lung irradiation in BNCT was MCNP-4B (21). The rat model was defined as a cylinder, 5 cm in diameter and 20 cm long. The lung region was approximated as a 4 cm diameter cylinder, 4 cm long, located 4.7 cm from the superior of the model, composed of ICRU 46 lung tissue with a density of 0.26 g/cm^3 (22). A cylindrical spinal cord and spherical heart were embedded in the lung region, and skin was simulated as a 0.5 cm-thick concentric shell. Elemental compositions for brain, heart, skin and average soft tissue were obtained from ICRU 46. Two radiosensitive regions, representing the intestines and esophagus, were defined as cylinders 1 cm in diameter and 2 cm long, located on the central axis of the model, 1 cm from the lung volume. An average physical dose of 10 Gy to the entire lung volume with the neutron beam irradiation in the absence of ^{10}B was chosen as the planned maximum dose for simulating lung irradiation. This dose was assumed to be the highest dose required to obtain a full thermal neutron dose response curve (in the absence of ^{10}B) for breathing rate increase, assuming that the Relative Biological Effectiveness (RBE) of the thermal neutron beam alone would be approximately 1.2. Similar value has been reported for the thermal neutron beam of the Brookhaven Medical Research Reactor using myeloparesis in rat spinal cord

irradiations with single dose (13). X-ray doses of 12 Gy to the whole rat lung have been reported to produce a 100% response using the breathing rate assay (23).

4.2.2 The delimiter for the rat lung irradiations in BNCT

In the rat lung irradiations with the M011 neutron beam, a delimiter was designed to allow an adequate thermal neutron flux delivered to the lung region, while shielding the nearby radiosensitive tissues (24, 25). The shielding material used for thermal neutron beam irradiation was lithiated-polyethylene (Li-Poly; 93% ^{6}Li-enriched Li_2CO_3 dispersed in polyethylene; 7.5% total Li by weight; Reactor Experiments, Sunnyvale, CA). A shielding box was constructed of 1.5 cm-thick Li-poly plates, with inner dimensions of $7 \times 15 \times 30$ cm^3. The lid includes a 3 x 14 cm rectangular aperture that serves as the beam delimiter for the simultaneous irradiation of two rats. The aperture opening was tapered 72° from 3 cm on the inside to 4 cm on the outside facing the reactor.

4.2.3 Two simplified phantoms for Monte Carlo model validation

Two simplified phantoms consisting of water-filled cylinders with 3 mm-thick Lucite walls (overall dimensions 20 cm long and 5 cm in diameter) were built for dose measurements to validate the MCNP models. Dose and neutron flux profiles along two axes were measured to compare the simulation results with experimental measurements. The phantoms had 1 cm-diameter, air-filled channels, along either the horizontal central axis, which would be perpendicular to the beam axis when the phantom was placed in the shielding box under the delimiter, or perpendicular to the rat body axis to provide depth-dose data along the beam axis. The photon and the neutron dose rates in the mixed radiation field at various locations in the phantom were measured with the dual ion chamber technique (26). Total neutron flux, along the horizontal and the vertical dimensions of the two rat dosimetry phantoms, were measured using

bare gold foil activation (12-18 mg, 0.005 cm thick) (27). The validation experiments with two simplified phantoms were duplicated in MCNP simulations and scaling factors were obtained between the calculations and measurements. The scaling factors were then applied to the calculations of lung and other tissue doses in the more detailed MCNP model. The photon, neutron and boron dose rates were calculated in MCNP by integrating the neutron and photon flux spectra against the appropriate energy dependent kerma factors (28).

4.2.4 Dose Volume Histograms of 2-field irradiation and the validation

The dose distribution in the total lung volume was calculated by constructing dose volume histograms (DVHs) from the MCNP simulation data. To calculate the DVH, the 4 cm diameter, 4 cm long lung cylinder was segmented into voxels by first dividing the lung cylinder into three segments (1, 2 and 1 cm-thick) along the body axis, and then subdividing these cylinders further by superimposing a grid of ~ 0.5 cm squares on each segment. The heart and spinal cord volumes were excluded. Thus, voxels along the outer edge and adjacent to the heart or spinal cord, had irregular geometries. Voxel volumes ranged from 0.6 cm^3 to 0.02 cm^3. The statistical uncertainties for the thermal neutron and photon doses were less than 2.5% for each voxel. The DVH was constructed from the dose tallied in each voxel in MCNP. A 2-field (ventral and dorsal) irradiation procedure was employed for these experiments. Different mean lung doses were delivered to the lung with neutron beam irradiations, including 4.7, 7.1, 8.2, 9.1, 9.4 and 9.7 Gy.

4.2.5 X-ray dosimetry

A 6 mm thick lead plate with an opening of 4 x12 cm exposing the lung region was used as the beam delimiter in x-ray irradiations. The two simplified cylindrical rat phantoms used in the neutron dosimetry validations were used in the x-ray dosimetry measurements. The dose rate in

the center of the 'lung' position in the phantom was measured with a graphite ion chamber. A focus-to-skin distance of 32.6 cm was used and the dose rate in the center of the 'lung' was 1 Gy/min. Single field irradiations were used for the x-ray irradiations, with dose groups of 11, 11.5, 11.75 and 12 Gy.

4.2.6 Animal irradiation procedures

Male Fisher 344 rats, approximately 12 weeks old (200-250 g) at the time of irradiation, were used for these studies. Rats were anesthetized with an intraperitoneal (i.p.) injection of ketamine (80 mg/kg) and xylazine (10 mg/kg). During the irradiations, two rats were positioned side-by side on the beam delimiter and attached to the delimiter with 5-cm wide clear adhesive tape. The lung region was positioned in the beam aperture with the bony protuberance of the T2 vertebra and the xyphoid sternum as reference points which were aligned with the delimiter aperture. Approximately 10 rats were irradiated at each dose level.

In the groups irradiated with neutrons plus BPA-F, BPA-F was administered as an i.p. injection of the BPA-fructose complex (900 mg BPA/kg body weight), approximately 2.5 hours prior to irradiation, for a relatively stable blood ^{10}B concentration during the time of irradiation. At the time of irradiation, a blood sample of about 0.5 ml was taken from each rat via the retro-orbital sinus for boron analysis. The ^{10}B concentration of each blood sample was measured using Prompt Gamma Neutron Activation Analysis (PGNAA)(29). As previously reported (30, 31), the blood B-10 concentration at this BPA dose can be regarded as constant with time during the period 2.5-3.5 hrs after injection. Therefore, the ^{10}B concentration measured at one time point during irradiation was used directly to calculate the boron dose delivered to the lung, assuming that the lung ^{10}B concentration is the same as blood at about 3 hrs after BPA injection.

For the irradiations with neutrons plus BPA, 90 rats were irradiated with mean lung doses ranging from 4 to 12 Gy and approximately 10 animals were irradiated per dose level.

4.2.7 Breathing rate measurement

Rat breathing rates were measured using whole-body plethysmography at one to two-week intervals from one or two weeks before the irradiation until the euthanasia or death of the animals. The apparatus for breathing frequency measurement was adapted from the commercially available rat breathing rate measurement system (Respiromax, Columbus Instruments, Columbus, OH). Four cylindrical Lucite chambers, 7.6 in diameter and 20 cm long, with plugs on each end with expandable gaskets to obtain an air-tight seal, were built for the rat whole-body plethysmography. A constant airflow of 110 ml/min was provided to the animals during the measurement via two ports on each chamber. Up to four animals were measured at once and the chambers were covered during the measurement to ease the animals. The pressure inside each chamber was recorded digitally during the measurement at a sampling rate of 200 Hz. If any animal showed significant movement during the 3-minute data collection, the measurement was repeated. Before measurements, rats were acclimated to being inside the chambers for measurements.

Breathing rate analysis is described in detail in Chapter 3. Briefly, the digitized breathing signals were analyzed automatically offline using custom designed programs written in Matlab. Noise discrimination was employed in the time domain against ripple noise (< 0.04 s), and large amplitude noise from animal movement. The median of the peak amplitudes of the 3-minute sample was calculated and peaks larger than 2.5 times the median were discriminated against as large-amplitude noise and removed from the signal. In general, less than 10% of any 3-minute signal was removed and usually there were only a few, if any, peaks deleted. After noise

reduction, the signal was segmented into 12 circular, consecutive and overlapping blocks, with each block approximately 1 minute in length. The time between the start of two consecutive blocks was ~15 s, and the overlap was ~75% of the block length (~45 s). The frequency spectrum of each block was calculated with Fast Fourier Transform (FFT), and the mean of the 12 spectra was calculated as the mean frequency spectrum (32) of each breathing pressure signal. The frequency of the primary peak of the mean frequency spectrum was determined as the breathing frequency of the breathing signal. The standard deviation of the breathing frequency, the location of the primary peak in the mean frequency spectrum, was estimated with the bootstrap (32-35), assuming that the spectra of the 12 blocks are Identically Independently Distributed (i.i.d.) random variables (34). The number of bootstrap repetitions (33) was 200. The circular blocking technique with the bootstrap and FFT provides noise suppression and a direct means of estimating the uncertainty in the measured breathing frequency for individual measurements.

4.2.8 Dose response analysis and the determination of weighting factors for rat lung irradiation in BNCT with BPA

Animals with breathing frequencies greater than the threshold, 20% (~ 3 standard deviations) above the mean of the control group, occurring after 20 days post irradiation, were considered as responding to radiation lung damage. The binary response data (0 no response or 1 for response) and the dose delivered to the lung of individual rats were analyzed with probit analysis (13, 36-38). ED_{50} values of the dose response curves were calculated to determine RBE or CBE factors for the rat lung in the BNCT irradiation (13, 14).

With x-ray and neutron beam irradiation, the absorbed dose deviated only a few percent from the planned dose and the variation in delivered dose is mainly due to the inherent minor fluctuations of the x-ray or neutron beam. The relative proportions of the neutron and photon

dose components in the doses delivered by the neutron beam were also fixed and invariant from animal to animal. This was not the case with the neutron irradiations with BPA. The blood boron concentration varied from animal to animal and consequently, for the same neutron fluence, the boron dose component and the total dose varied, even for animals irradiated simultaneously. On the other hand, for animals that received the same absorbed doses to the lung, the proportions of different dose (beam and ^{10}B) components were not necessarily uniform. In the neutron-only irradiations, the total dose value and the total weighted dose value are directly proportional because the high and low LET dose components are fixed relative to the total dose. However, in the irradiations with BPA, this one-to-one relationship no longer holds. Instead, for the same total dose delivered to the lung with neutrons plus BPA, different weighted doses could result due to the changing proportion of boron dose component of the total dose. This problem makes it difficult and perhaps inaccurate to calculate the biological group response in the conventional way, where the animals are grouped according to their previously planned dose, or according to their final delivered physical dose (13, 39, 40).

To solve the problem of variability in total absorbed dose and inconstant ^{10}B dose in neutron irradiations with BPA, a new computer algorithm was developed to more accurately assess the CBE of the boron dose. The CBE is defined as the ratio of the dose of a test radiation to an isoeffective dose of reference photon radiation, usually at ED_{50}. In the new algorithm, a range of potential CBE values were evaluated to determine the one that provided the best match between the ED_{50} of the weighted dose response of the neutron beam plus BPA and the ED_{50} of the x-ray dose response. Each value in the range of CBE being evaluated was used to calculate the weighted dose using Eq. 1, using the measured RBE for the thermal neutron beam for normal rat lung. The binary response data of the individual animals and the weighted dose were fitted using

probit analysis and the ED_{50} value was derived for the potential CBE being tested. The CBE value that produced minimum difference between the ED_{50} of the weighted dose response of neutrons plus BPA, and the ED_{50} of the x-ray dose response was selected as the CBE at ED_{50}. Using an analogous approach, the CBEs for BPA at the ED_{10} and ED_{90} levels of the breathing rate dose response were also derived.

4.3 Results

4.3.1 Dosimetry of the rat lung irradiations in the M011 beam and the DVH

In the validation of the Li-poly delimiter of 1.5 cm thick and with a 14 x 3 cm aperture designed in MCNP, the two simplified lucite phantoms were positioned side by side in the Li-poly rat box underneath the delimiter. The box was then positioned in the M011 neutron beam with the center of the delimiter aperture aligned along the central axis of the beam.

The neutron flux measured at the surface of the phantom under the delimiter aperture and 2.5 cm displacement from the beam central axis, after scaled to match the full operation power of the reactor at 5 MW, was 8.4 x 10^9 n/cm^2 s. This flux decreased to 6.1, 3.4, 1.8 and 0.9 x 10^9 n/cm^2 s at depths of 1, 2, 3 and 4 cm in the phantom, respectively. Along the longitudinal axis of the rat phantom (2.5 cm from the surface) the thermal neutron flux directly under the delimiter aperture was 2.2 x 10^9 n /cm^2 s. This dropped to 0.6 x 10^9 n/cm^2 s in the shielded collateral regions 3.5 cm from the center of the aperture opening. The measured photon dose rate in the longitudinal axis of the phantom, directly under the aperture, was 19.5 cGy/min. The validation experiment simulated with MCNP and the calculation results were compared to the measurements. The scaling factors connecting the simulation and the experiment for the rat lung irradiations were determined to be 0.56 for neutrons and 0.75 for photons. After applying this scaling, the

difference between measured and calculated neutron flux and photon dose rate depth profiles along the beam axis, as well as the profiles along the central axis of the phantom were within 5% except for the flux measured at the phantom surface. Since both calculations and measurements indicated that the M011 beam has a fast neutron component less than 1% of the total neutron flux, it was taken to be a pure thermal neutron beam and the total neutron flux and thermal neutron flux were assumed to be the same.

The photon scaling factor being larger than the neutron scaling factor can be due to two major factors. In the MCNP model of the M011 beam, photons were not represented and therefore no incident photons from the beam were included in the photon dose rate calculation in the rat models. Additionally, MCNP does not calculate delayed photons which compose a large portion of the photon dose in the neutron irradiation field. The scaling factors obtained in this rat irradiation are similar to 0.64, the factors measured and used in the clinical trial with the M067 epithermal neutron beam, which the M011 beam was adapted from.

Two-field (anterior and posterior) irradiations were used in the rat lung neutron irradiations with or without BPA. Scaled to full power (5 MW), the calculated mean lung dose rate was 18.7 cGy/min for a 2-field irradiation of the neutron beam only. The thermal neutron component was 3.3 cGy/min, approximately 20% of the total beam dose rate. With this dose rate, a mean lung dose of 10 Gy could be administered in two fields of approximately 25 min each. The DVH of the rat lung in the neutron-only irradiations is shown in Fig. 4.1. With the mean lung dose of 10 Gy, a relatively uniform dose distribution (range: 9-11.5 Gy) was achieved with the two-field irradiation.

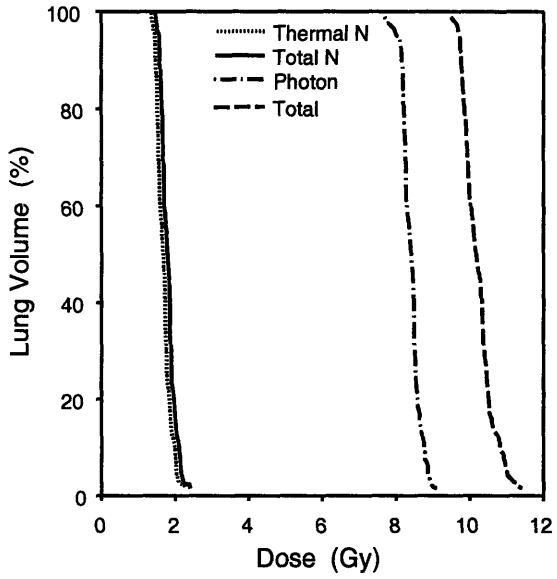

Fig. 4.1 The dose volume histogram (DVH) for a two-field neutron-only lung irradiation, with a mean lung dose of 10 Gy.

4.3.2 Boron biodistribution

A simple biodistribution study with 6 rats was done at 3 hrs after BPA injection and the ^{10}B concentration in blood and different tissues were measured with ~0.5 ml samples with PGNAA (29). The measured concentrations in different tissues are listed in Table 4.1. No statistically significant difference between ^{10}B concentration in blood and lung was detected. The measured concentrations were consistent with reports in the literature (30, 31). In the neutron irradiations with BPA, a blood sample was taken from each rat at the time of irradiation, approximately 3 hrs after i.p. injection of BPA. The lung tissue ^{10}B concentration of the rat was assumed equal to the ^{10}B concentration of its blood. The mean blood ^{10}B concentration for all 90 rats was 17.7 ± 3.4 μg/g, ranging between 6.3 – 29.1 μg/g.

In neutron irradiations with BPA, the calculated mean lung dose rate for the ^{10}B dose component was 1.04 cGy/min for every μg ^{10}B present per gram of tissue. With blood and lung ^{10}B concentrations of approximately 20 μg/g, the total mean lung physical dose rate was about

0.4 Gy/min, of which approximately 50% was due to ^{10}B reactions. In this case, delivering a mean lung dose of 10 Gy with BPA requires approximately 26 minutes or 13 min for each field.

Table 4.1 The ^{10}B concentrations measured with PGNAA in different tissues at 3 hrs after i.p. injection of BPA-F (900 mg BPA/kg body weight) with 6 animals.

Tissue	^{10}B concentration (μg/g)
Blood	19.9 ± 3.2
Lung	21.9 ± 1.7
Heart	21.2 ± 1.3
Skin	21.5 ± 6.5
Liver	21.6 ± 1.3
Spinal Cord	8.9 ± 1.4
Brain	11.2 ± 0.5
Intestine	32.4 ± 10.8
Kidney	108.5 ± 3.3

4.3.3 Dose responses of radiosensitive tissues

The estimated total weighted doses and the dose components to the surrounding radiosensitive tissues with 10 Gy mean lung dose in neutron irradiations with or without BPA, are reported in Table 4.2. Esophagus and intestines are shielded by the Li-Poly delimiter and the weighted doses were well below the ED_{50} of 13 Gy_w for tongue ulceration (39), or the LD_{50} of 22 Gy_w for gastrointestinal death after local intestine irradiation (41-44). No gastrointestinal death or severe tongue ulceration was observed among the rats with lung neutron irradiations with or without BPA. Complications were observed for tissues exposed in the delimiter aperture, with skin reactions the most serious aside from the lung. For the irradiations with neutrons-only, the acute skin response of epilation and mild moist desquamation were observed from several weeks to two months after irradiation at doses close to 10 Gy mean lung dose. For the neutron irradiations with BPA, similar skin responses were observed with a mean lung dose of about 6-7 Gy. At higher doses, more severe skin responses (erythema and ulceration) were observed with

a shorter latent time and persisting up to three months post irradiations, especially with a mean lung dose at about 10 Gy. At these dose levels, the skin was treated with antibiotic ointment. No dermal necrosis was observed before euthanasia. The highest dose delivered to the skin in the lung irradiations was about 50 Gy_w, close to the dose threshold for dermal necrosis (45). If the rats had been kept long enough, dermal necrosis might have occurred with low frequency (45). The skin responses of the early phase observed here are generally consistent to what has been reported in the literature with BNCT radiation (45). For the rats receiving neutron radiation with or without BPA, no animal died at about 100 days after irradiation, when pericarditis death occurred due to radiation heart damage (46, 47). For the lung x-ray irradiations up to 12 Gy, no signs of radiation damage were observed to any of the in-field or out-of-field tissues except the lung.

Table 4.2 Calculated maximum local absorbed doses in surrounding tissues with a mean lung dose of 10 Gy, with or without BPA present. The ^{10}B concentrations are assumed at 20 μg/g for skin, heart, and esophagus (the same as blood), 9 μg/g for spinal cord, and 32 μg/g for intestines, based on the biodistribution data 3 hr after BPA i.p. injection (Table 4.1). The RBEs and CBEs used for skin (45), spinal cord (48) and esophagus (39) are reported in the literature. The weighting factors for intestines (41-43) are estimated from the literature. The statistical uncertainties in the calculated dose are within 5% and omitted for clarity.

	RBE/CBE		Thermal neutron beam only			Thermal neutron beam with BPA			
Tissue	Thermal N	BPA	Neutron (Gy)	Photon (Gy)	Total (Gy_w)	Neutron (Gy)	Photon (Gy)	^{10}B (Gy)	Total (Gy_w)
Skin	5.1	3.74	4.1	9.5	30.4	1.9	4.7	9.6	50.3
Spinal cord	1.8	1.33	1.9	9.8	13.2	0.9	4.8	3.5	11.1
Heart	-	-	2.8	12.4	-	1.3	5.9	8.9	-
Intestine	5	5	0.4	7.0	9.0	0.2	3.3	1.9	13.8
Esophagus	3.8	4.9	0.4	6.9	8.4	0.2	3.3	1.1	9.5

4.3.4 Breathing Rate Measurement and Computer Analysis

Two examples of breathing signals are shown with their mean normalized frequency spectra after noise reduction in Fig. 4.2. One animal (a control) was measured 48 days after sham irradiation and the other at 37 days after irradiation to a mean lung dose of 10.5 Gy of neutrons

with BPA. Sham-irradiated control breathing signals acquired in this experiment demonstrated mostly a symmetrical breathing pattern and some irregularity mainly in the peaks and valleys of the breathing cycles. The symmetrical breathing patterns in the time domain transformed into a primary frequency peak with the Fast Fourier Transform (FFT). In this control animal breathing signal, the maximum value of the normalized mean spectrum from the 12 blocks of the 3-minute signal was 179 ± 1 min^{-1}. The mean spectrum of the control signal also captures the irregularities of the breathing signal from the time domain, demonstrated as small secondary peaks at higher frequencies, located approximately at 350 min^{-1} and 530 min^{-1} in this example.

In the example of the segment from a 3-minute breathing signal from a positively responding irradiated rat (Fig. 4.2c), the breathing pattern shows more significant irregularity and more fine structure compared to the control animal signal. Three major peaks were present in the mean frequency spectrum (Fig. 4.2d), located at 185 ± 5 min^{-1}, 291 ± 8 min^{-1} and 439 ± 10 min^{-1}. The FFT spectrum was normalized to its maximum value at 439 min^{-1} and the relative amplitudes of the three peaks in the frequency domain were about 0.8, 0.6 and 1, respectively. The peak value in the frequency domain with the highest frequency (439 ± 10 min^{-1}) was taken as the breathing frequency of the breathing signal.

For the male Fisher 344 rats with radiation-induced lung damage, considerable irregularity of the breathing pattern was observed in this experiment, indicating functional lung damage. Up to three peaks were observed in the breathing frequency spectra from the responding rats. The relative amplitudes of the significant peaks in the frequency domain were usually comparable to each other and greater than the threshold of significance previously defined as a relative amplitude of 0.5. Frequency peaks with relative amplitudes larger than 0.5 were located and the highest frequency among the peaks larger than 0.5 was selected as the breathing frequency of the

measurement. For breathing signals from control animals, the phenomenon of breathing pattern irregularity, in addition to the dominant regular and symmetrical breath cycles, was also observed, but at a much smaller scale. The secondary higher frequency peaks in the breathing frequency spectra for control animals were usually significantly smaller than 0.5 and mostly around 0.2 in normalized amplitude. Using this breathing rate measurement method, the breathing rate for the control group of 8 animals and 136 measurements altogether, up to 180 days after sham irradiations was determined to be 176 ± 13 min^{-1} (mean ± SD).

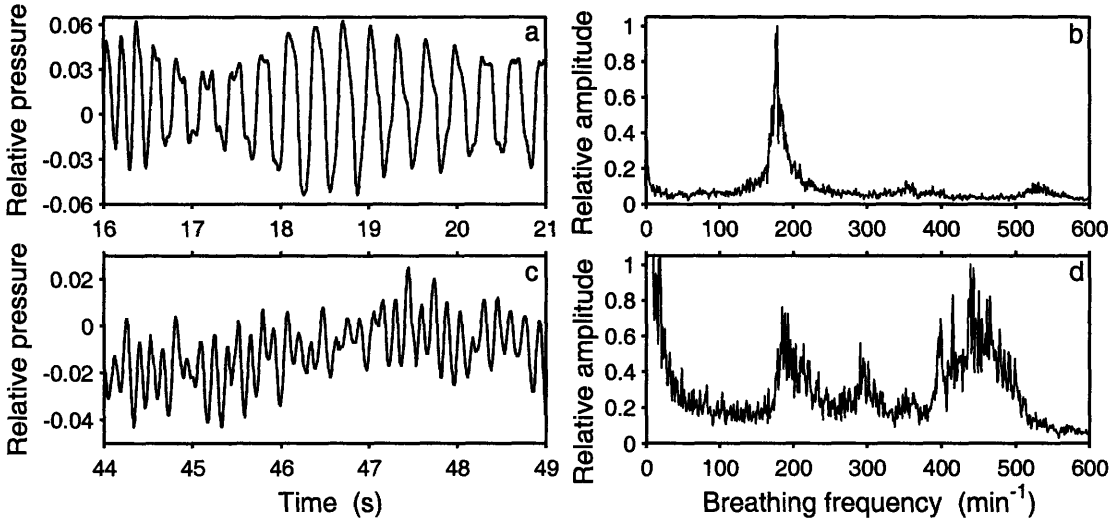

Fig. 4.2 Breathing pressure signals and their FFT spectra of a control animal (panels a and b) and responding animal (panels c and d). The signal of the control animal was acquired 48 days after sham irradiation. The signal of the responding animal was acquired 37 days after irradiation with neutrons plus BPA.

4.3.5 Breathing frequency and body weight responses

The group means and percent responses of breathing rate measured up to about 180 days post irradiation at various dose levels for the different radiations are shown in Fig. 4.3. Two responding phases with elevated breathing rate were observed, as shown in Fig. 4.3. The early phase occurred before about 100 days post irradiation with the maximum elevation occurring

between 40 to 80 days. At lower doses, the elevation from the early response phase often decreased to the normal range by about 100 days. The late phase was observed after 100 days, and usually elevation started at about 120 days and sometimes persisted until euthanasia or death of the animal. For some animals that received relatively high doses (e.g., 9.7 Gy of neutron or 9.5 Gy of neutrons plus BPA), the breathing rate elevation started in the early phase would extend until the death or euthanasia of the animal. The onset time for the early and late phases of breathing rate response observed with the high-LET radiations of neutrons-only or neutrons plus BPA is consistent with the fact that reported for x-rays with F344 rats in the literature (49-51).

For the responding rats that received neutrons-only or x-ray radiation, most rats showed a biphasic response of breathing rate increase, the early phase and the late phase. However, the response changed significantly for neutrons plus BPA. With relatively low doses (~ 5-9 Gy), 25 out of 47 animals showed only the late phase, and the early phase was asymptomatic. As an example of this situation, the percent responses of breathing frequency for the 7.5 Gy and 8.6 Gy dose groups for neutrons plus BPA are larger after 100 days post irradiation than before, as shown in Fig. 4.3f.

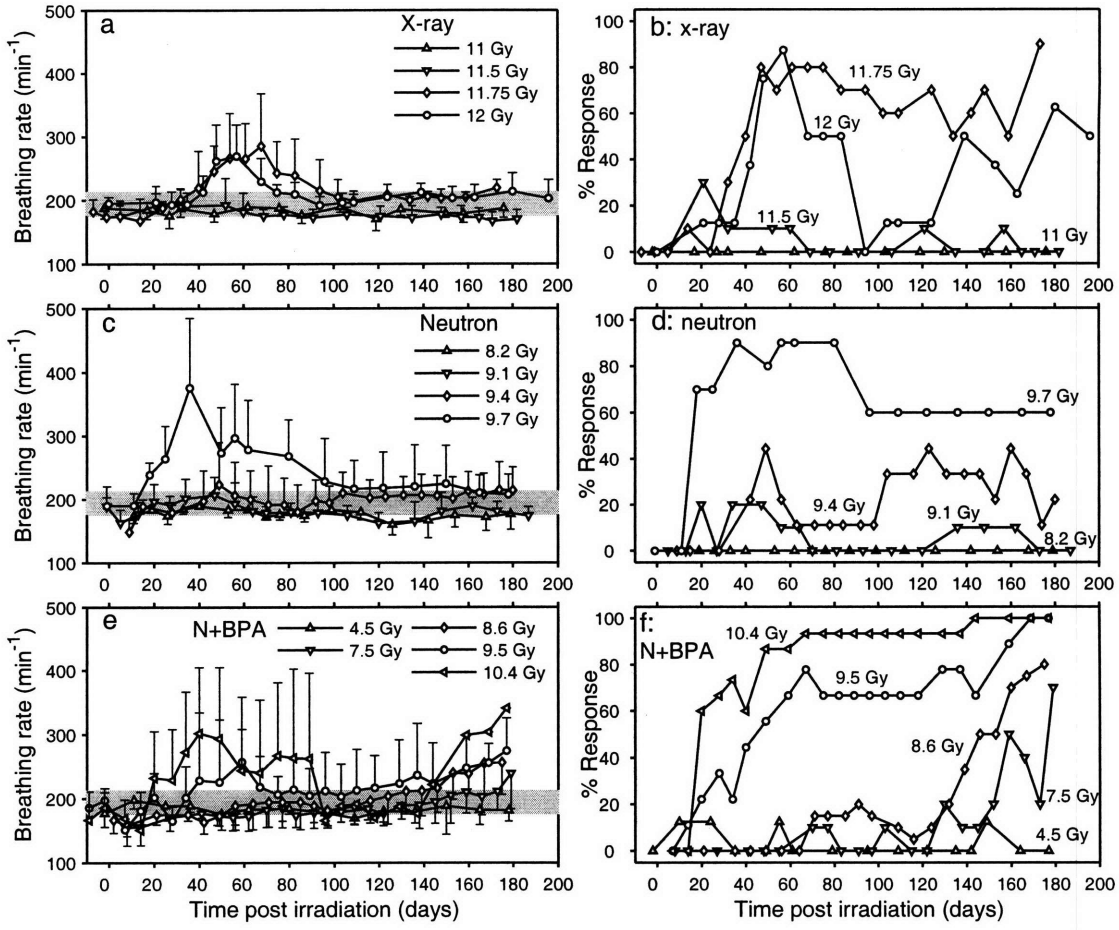

Fig. 4.3 The group mean breathing frequency and percentage response of breathing frequency elevation measured up to ~ 180 days after irradiation with x-rays (a, b), neutrons-only (c, d) and neutrons with BPA (e, f). The range of control values is represented by the grey shaded areas with the mean breathing frequency and 20% (~ 3 SD) above the mean, and plotted in panels a, c and e. The error bars for the percentage response data (b, d and f) are generally about 10% since 10 animals were usually in each dose group, and are omitted for clarity. For animals that died before 180 days due to lung damage, a positive response was counted until 180 days. In the neutron-only response data (panels c and d), the responses for the 4.7 and 7.1 Gy dose groups are omitted for clarity since they are similar to the control. In the neutrons with BPA response data (panels e and f), dose groups of 5.5 and 6.5 Gy have similar response to 4.5 Gy, and are also omitted for clarity.

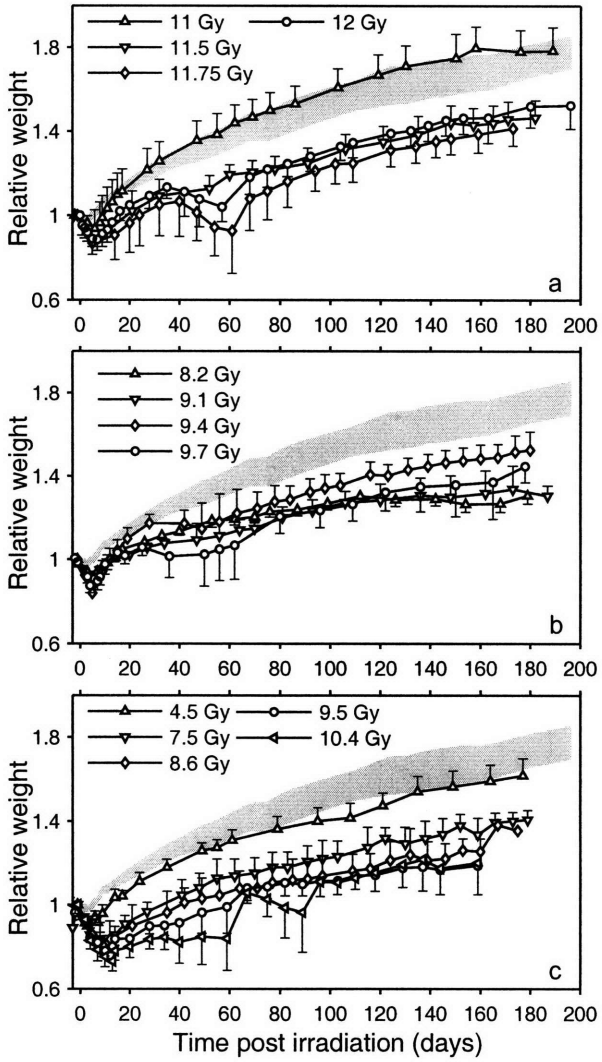

Fig. 4.4 Group mean of normalized weight for animals irradiated with x-ray (a), neutrons-only (b), and neutrons with BPA (c). The weight was normalized to the weight measured one day before irradiation for each animal. The range of control values (mean ± SD of the normalized weight of the control group) is represented by the shaded area in each panel.

Body weight was also monitored from several days before the irradiations until euthanasia or death. The group means of normalized weight from different dose groups are shown in Fig. 4.4. Groups with higher doses had larger mean weight losses right after irradiations for the same radiation type. For groups that received relatively high doses, a growth delay or weight loss was

observed at about 60 days, demonstrated by the 12 Gy and the 11.75 Gy x-ray group, the 9.7 Gy group in neutrons-only and the 10.4 Gy group in neutrons plus BPA. The onset of the weight loss at about 60 days is consistent with the onset of breathing rate elevation (Fig. 4.3) in the same dose groups. Among the irradiations with neutrons-only or neutrons with BPA, some dose groups showed no breathing rate response but did show a growth delay compared to the control group. An example of this is the 8.2 Gy neutrons-only group.

4.3.6 Dose responses with breathing frequency and the RBEs and CBEs

The dose response curves of the x-ray and neutron-only radiation fitted with probit analysis are shown in Fig. 4.5a. Since the response curves for the late phase of x-ray and neutrons-only had no statistically significant difference from their corresponding early phases, only one curve was plotted for each radiation in Fig. 4.5a. X-ray and neutron-only irradiations produced similarly steep dose-response relationships and the difference between ED_5 and ED_{95} were less than 2 Gy. The ED_{50} for x-rays was 11.5 ± 0.2 Gy and the ED_{50} for the neutron-only irradiation was 9.2 ± 0.6 Gy. Comparison of these ED_{50} values determined that the RBE of the MITR-II thermal neutron beam was 1.2 ± 0.1 and the RBE for thermal neutrons was 2.2 ± 0.3 with a 50% incidence of breathing rate increase as the biological endpoint in rat lung.

For the irradiation with neutrons plus BPA, the dose ranges for the early phase (≤100 days) and late phase (>100 days) of breathing rate elevation were different. The dose response curves were determined separately for these two phases, using probit analysis of the lung physical dose and binary response of individual animals. The dose responses for neutrons plus BPA are shown in Fig. 4.5a. The ED_{50} values are 8.7 ± 0.5 Gy and 6.7 ± 0.4 Gy for the early and late phases, respectively. With these ED_{50} values, the CBE factors were determined with this conventional method as 1.4 ± 0.1 and 2.2 ± 0.2 for early and late responses, respectively. The ^{10}B dose

component of the ED_{50}s were calculated with the mean blood ^{10}B concentration for the 90 irradiated rats, 17.7 ± 3.4 μg/g.

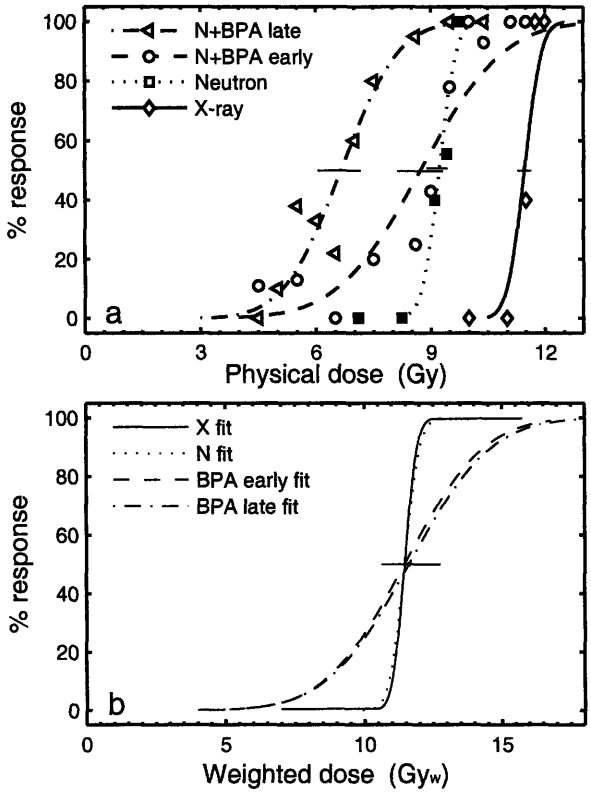

Fig. 4.5 Dose responses and their probit analysis for animals irradiated with x-ray, neutrons, and neutrons with BPA. a) group response and probit analysis (using the binary responses and doses of individual animals) with absorbed dose; b) analysis using weighted dose.

The CBE factors were also evaluated with the new minimization algorithm described above. The CBE values at ED_{50} were determined to be 1.4 ± 0.1 for the early phase breathing rate response and 2.3 ± 0.2 for the late phase. The probit analysis response curves for weighted dose are plotted in Fig. 4.5b for the early and late phases.

The biologically weighted dose responses of the x-ray and neutrons-only irradiations are also plotted in Fig. 4.5b. The two biologically weighted dose response curves of the x-ray and neutrons-only irradiations are consistent, having similar steepness. The weighted dose response curves for neutrons plus BPA, however, are not parallel to the response curves for x-rays and neutrons-only. The CBE factors for BPA, correspondingly, varied depending on the response level. The CBEs at ED_{10} and ED_{90} approximately represent the maximum and minimum of the CBE range. Determined with similar method for the CBE factors at ED_{50}, the factors at ED_{10} for the early phase and late phase breathing rate response were 2.2 ± 0.2 and 3.6 ± 0.3, respectively, defining the upper limit of the CBE range. The CBE factors for BPA at ED_{90} for the early and late breathing rate response phases were 1.0 ± 0.1 and 1.7 ± 0.1, respectively, defining the lower limit of the CBE range.

4.4 Discussion

One of the major motivations of this experiment was to investigate whether the lung complications that the patients developed during the Harvard-MIT BNCT clinical trial in the period between 1994 and 1999 was due to the unexpectedly high radiosensitivity of the lung.in BNCT irradiation. With the lung dosimetry measured in an anthropomorphic phantom positioned for cranial irradiation, the minimum weighting factors for neutron and ^{10}B dose needed to elicit the lung damage in the patients were estimated to be at least 3.2 and 4, respectively (17). In this experiment, the RBE measured for thermal neutrons was 2.2 ± 0.3, and the range of the CBE for BPA with the early breathing rate response was 1.0 - 2.2, both below the estimated requirements for weighting factors. This suggests that the lung complications

developed by the three patients after BNCT treatment for brain tumors most likely did not result from BNCT irradiation.

In this report, the similar onset times of the early and late breathing rate responses for the high-LET neutron radiation with or without BPA are comparable to the onset times for low-LET x-ray radiation, and are similar to what has been reported in the literature (49, 50). However, the different steepness of the dose response curves observed for neutrons plus BPA compared to x-rays and neutrons-only, suggests different damage mechanisms with the radiation of neutrons plus BPA. For the early breathing rate dose response curve for neutrons plus BPA, two different situations seem to occur for lower (<8 Gy) and higher (>8 Gy) doses (Fig. 4.5). In the 4.0-8.0 Gy dose range, only 4 out of 36 rats developed an early breathing rate response. The dose response within this range is therefore much shallower than the x-ray response curve at similar percent responses. With neutrons plus BPA in the dose range 8.0-12 Gy, the response of the early phase almost overlaps the neutrons-only response curve, except for at about 10.4 Gy, where one rat out of 15 failed to show early phase response. The biphasic early response curve for neutrons plus BPA suggests that there maybe different damage mechanisms for the lower and higher dose ranges.

One reason for the increased variability in the lower end of the dose response curve for neutrons with BPA may be the inhomogeniety of the BPA distribution in the lung. With the neutron and x-ray irradiations, the dose delivered mainly depends on the spatial distribution of neutron or x-ray fluence. With the neutron irradiations with BPA, however, the spatial distribution of ^{10}B is also an important factor in the dose delivered to lung tissue. If the spatial distribution of BPA in the lung is non-uniform, different lung volumes or populations of functional units (52, 53) will receive different doses when irradiated with neutrons, resulting in a

different overall radiation response distinct from the response from a uniform dose to the lung. A volume effect due to BPA inhomogeneity in the lung may contribute to the less steep dose response curves of neutrons plus BPA as compared to x-rays and neutrons alone. Unfortunately, there is no information on the BPA distribution in the lung available in the literature to address this question. The simple biodistribution at 3hr after BPA injection in this report and a lung BPA biodistribution in mice (51), both analyzed with PGNAA(29), can only give a gross boron concentration in the entire lung sample analyzed, including blood within the sample. These measurements were statistically nondiscernible from the BPA concentration measured in blood. Microscopic techniques such as High Resolution Quantitative Autoradiography (HRQAR) (16) or Secondary Ion Mass Spectroscopy (SIMS) (54), more advanced than PGNAA, are required to provide information on BPA concentration inhomogeniety within the lung and to measure the BPA concentration of the lung tissue only, without blood.

In this report, another interesting phenomenon occurred in the neutrons plus BPA groups, where 28 animals, with 25 within dose range of 5-9 Gy and 3 larger than 9 Gy, showed no early response but did develop a late response. The spared early phase has been reported in lung in radiations of mice or rats, with either hyper-fractionated dose delivery to allow repair between fractions for the first phase (55-57), or partial lung volume irradiation (53). There are possibly two interpretations for this observation in this report.

The first interpretation is that there are separate target cells (9, 36) responsible for early and late radiation lung responses, or cells that have different significance for developing early and late responses, and BPA has a different boron microdistribution in them. The two leading target cell candidates for radiation lung response are endothelium (58-62) and type II pneumocytes (63, 64), based on their important function in lung tissue and the cellular changes of lung tissue after

irradiation (58-60, 63, 64). One could hypothesize that BPA has a higher concentration in cells that are more important in the late response phase, which reduces the ED_{50} dose of the late response for neutrons with BPA. The fact that BPA concentrations are different in blood and other cells was reported in rat skin and tongue (65), where the concentration was reported to be 25% higher in lamina propria than that in the blood (65). However, this hypothesis of different target cells and different BPA micro-distribution can not explain the different steepness of the late response curve for neutrons plus BPA as compared to those of x-ray and neutrons-only. Additionally, the hypothesis of different target cells is not consistent with the finding that the response curves for the early phase and the late phase are statistically the same for x-rays and neutrons-only.

The second interpretation of the decreased doses for late lung radiation response compared to the early response for neutrons plus BPA is that complications from heart irradiation enhanced loss of the lung function during the late response period. In terms of radiation damage, heart and lung are reported to be closely correlated and interacting with each other such that a functional loss in one organ would aggravate the functional loss in the other in both humans (66) and experimental animals (67, 68). Pulmonary hypertension from radiation lung damage can lead to a right ventricular hypertrophy and on the other hand, decreased cardiac output and oxygen supply would result in a breathing rate increase (67, 68). Therefore in the whole thorax irradiation, breathing rate increase could be a synergistic response to multiple organ damage. That this combined radiation effect seems to affect the late lung response more than the early response has been reported in the literature for the hypersensitivity testing of different lung volumes (53). The authors suggested that the reasons were related to a lower sensitivity of the mediastinum and also the possible repair of the heart radiation damage during the intermediate

lung response phase (53). In this report, this could be explained by the relatively lower dose (5-9 Gy) of neutrons plus BPA which resulted in damage to the lung that was not significant enough to induce immediate or early abnormal breathing rate elevation and also repair may have occurred in the lung and heart during the intermediate phase. The hypothesis that the late breathing rate response for neutrons plus BPA is due to combined heart and lung organ damage, could also explain the different steepness of this dose response curve compared to those of the neutrons-only or x-rays.

If this hypothesis of cardiac involvement in the functional lung response holds, the weighing factors for the high LET dose components in BNCT heart irradiations can also be estimated. In heart only x-ray irradiation excluding the lung in rats, a single fraction dose of 15-20 Gy was reported to produce up to 100% reversible pericarditis at about 100 days post irradiation (46, 69). At a single fraction dose of 17.5 Gy, cardiomyopathy with various onset time after irradiation were elicited (70). With single fraction doses larger than 20 Gy, the rats were sacrificed for pericarditis at 100-120 days post irradiation (46) . From the lung dose response with neutrons-only (Fig. 4.5), the response curves for early phase and late phase are not distinguishable and have the same steepness as those of x-rays. It seems that the responses here are not due to combined heart and lung organ damage but rather lung damage only. This would indicate that with a mean lung dose of 9.7 Gy, the ED_{100} for the lung response, the weighted dose delivered to the heart is smaller than 15 Gy, the minimum dose for any heart radiation response. Using Table 4.2 and a simple proportional calculation, the physical dose delivered to the heart in this case is 14.7 Gy (15.2 Gy /10 Gy × 9.7 Gy = 14.7 Gy), with 2.7 Gy high-LET dose components from thermal neutrons. Assuming that the heart dose of 14.7 Gy in neutron irradiation and 15 Gy in x-ray irradiation are isoeffective, a weighting factor for thermal neutrons-only close to unity is

obtained. Similarly, assuming the late breathing rate responses of neutrons plus BPA are also due to heart damage in addition to lung damage, and at ED_5 of the response and mean lung dose of 5 Gy, the dose to the heart is the isoeffective dose to 15 Gy x-ray to the heart. Using the weighting factor of one for the thermal neutron component, the CBE for BPA for heart irradiation in BNCT should be approximately 2.5.

4.5 References

1. Cardozo BL, H. Z, van Bekkum DW, Zurcher C, Hagenbeek A. Lung damage following bone marrow transplantation: I. the contribution of irradiation. *International Journal of* Radiation *Oncology Biology Physics* 1985;11:907-914.
2. Torres PY, Bross DS, Lam WC, Wharam MD, Snatos GW, Order SE. Risk factors in interstitial pneumonitis following bone marrow transplantation. *International Journal of Radiation Oncology Biology Physics* 1982;8:1301-1307.
3. Abratt RP, Morgan GW, Silvestri G, Willcox P. Pulmonary complications of radiation therapy. *Clinics in chest medicine* 2004;25:167-177.
4. Anscher MS, Kong F, Marks LB, Bentel GC, Jirtle RL. Changes in plasma transforming growth factor beta during radiotherapy and the risk of symptomatic radiation-induced pneumonitis. *International Journal of Radiation Oncology Biology Physics* 1997;37:253-258.
5. Rubin P, Casarett GW, editors. Respiratory system. Philadelphia: W. B. Saunders Company; 1968.
6. Gross NJ. Pulmonary Effects of Radiation-Therapy. *Annals of Internal Medicine* 1977;86:81-92.
7. Coggle JE, Lambert BE, Moores SR. Radiation effects in the lung. *Environmental health perspectives* 1986;70:261-291.
8. Phillips TL. An ultrastructural study of the development of radiation injury in the lung. *Radiology* 1966;87:49-54.
9. Perez CA, Brady LW. Thoracic radiotherapy: complications and injury to normal tissue. In: Principles and practice of radiation oncology. New York: Lippincott Williams & Wilkins; 2002.
10. Kwa SLS, Lebesque JV, Theuws JCM, Marks LB, T. MM, Bentel GC, Oetzel D, Spahn U, Graham MV, Drzmala RE, Purdy JA, Lichter AS, Martel MK, Haken RKT. Radiation pneumonitis as a function of mean lung dose: an analysis of pooled data of 540 patients. *International Journal of Radiation Oncology Biology Physics* 1998;42:1-9.

11. Seppenwoolde Y, Lebesque JV, Jaeger K, Belderbos JSA, Boersma LJ, Schilstra C, Henning GT, Hayman JA, Martel MK, Haken RKT. Comparing different NTCP models that predict the incidence of radiation pneumonitis. *International Journal of Radiation Oncology Biology Physics* 2003;55:724-735.

12. Van Dyk J, Keane TJ, Kan S, Rider WD, Fryer CJ. Radiation pneumonitis following large single dose irradiation: a re-evaluation based on absolute dose to lung. *International Journal of Radiation Oncology Biology Physics* 1981;7:461-467.

13. Coderre JA, Morris GM. The radiation biology of boron neutron capture therapy. *Radiation Research* 1999;151:1-18.

14. Palmer MR, Goorley JT, Kiger III WS, Busse PM, Riley KJ, Harling OK, Zamenhof RG. Treatment Planning and Dosimetry for the Harvard-MIT Phase I Clinical Trial of Cranial Neutron Capture Therapy. *International Journal of Radiation Oncology Biology Physics* 2002;53:1361-1379.

15. Busse PM, Harling OK, Palmer MR, Kiger III WS, Kaplan J, Kaplan I, Chuang CF, Goorley JT, Riley KJ, Newton TH, Santa Cruz GA, Lu XQ, Zamenhof RG. A critical examination of the results from the Harvard-MIT NCT program phase I clinical trial of neutron capture therapy for intracranial disease. *Journal of Neuro-Oncology* 2003;62:111-121.

16. Kiger WS, 3rd, Palmer MR, Riley KJ, Zamenhof RG, Busse PM. A pharmacokinetic model for the concentration of 10B in blood after boronophenylalanine-fructose administration in humans. *Radiat Res* 2001;155:611-618.

17. Palmer MR. Measurements and estimates of dose to the lungs during cranial BNCT with the MIT M67 beam. Cambridge: Harvard/MIT BNCT program; 1999.

18. Choi J-HR. Development and characterization of an epithermal beam for boron neutron capture therapy at the MITR-II Research Reactor. Nuclear Engineering Department: Massachusetts Institute of Technology; 1991.

19. Choi JR, Clement SD, Harling OK, Zamenhof RG. Neutron capture therapy beams at the MIT Research Reactor. In: J. A. Bernard, Harling OK, Zamenhof RG, editors. Neutron Beam Design, Development, and Performance for Neutron Capture Therapy. Vol 54. New York and London: Plenum Press; 1990. pp. 201-218.

20. Redmond II EL, Yanch JC, Harling OK. Monte Carlo Simulation of the MIT Research Reactor. *Nuclear Technology* 1994;106:1-14.

21. Briemeister JF. MCNP- A general Monte Carlo N-Particle Transport Code (Version 4B). Los Alamos: Los Alamos National Laboratory; 1998.

22. ICRU 46. Photon, Electron, Proton, and Neutron Interaction Data for Body Tissues. Bethesda, MD: International Commission on Radiation Units and Measurements; 1992.

23. Lehnert S, el-Khatib E. The use of CT densitometry in the assessment of radiation-induced damage to the rat lung: a comparison with other endpoints. *International Journal of Radiation Oncology Biology Physics* 1989;16:117-124.

24. Liu J, Kiger III WS, Harling OK, Binns P, Riley K, Coderre JA. Design of Shielding and Collimation for Small Animal Irradiations in the MITR-II Thermal Neutron Beam. In:

Sauerwein W, Moss RL, Wittig A, editors. Research and Development in Neutron Capture Therapy. Bologna, Italy: Monduzzi Editore; 2002. pp. 523-527.

25. Kiger JL, Kiger III WS, Patel H, Binns PJ, Riley KJ, Hopewell JW, Harling OK, Coderre JA. Effects of boron neutron capture irradiation on the normal lung of rats. *Applied Radiation and Isotopes* 2004;61:969-973.
26. Rogus RD, Harling OK, Yanch JC. Mixed field dosimetry of epithermal neutron beams for boron neutron capture therapy at the MITR-II research reactor. *Med Phys* 1994;21:1611-1625.
27. ASTM. Standard Method for Measuring Thermal Flux by Radioactivation Techniques; 1977.
28. Goorley JT, Kiger III WS, Zamenhof RG. Reference dosimetry calculations for neutron capture therapy with comparison of analytical and voxel models. *Med Phys* 2002;29:145-156.
29. Riley KJ, Harling OK. An improved prompt gamma neutron activation analysis facility using a focused diffracted neutron beam. *Nuclear Instruments and Methods in Physics Research B* 1998;143:414-421.
30. Morris GM, Micca PL, Nawrocky MM, Weissfloch LE, Coderre JA. Long-term infusions of p-boronophenylalanine for boron neutron capture therapy: evaluation using rat brain tumor and spinal cord models. *Radiat Res* 2002;158:743-752.
31. Morris GM, Coderre JA, Micca PL, Fisher CD, Capala J, Hopewell JW. Central nervous system tolerance to boron neutron capture therapy with p-boronophenylalanine. *Br. J. Cancer.* 1997;76:1623-1629.
32. Stearns SD. Random signals and spectral estimation. In: Digital signal processing with examples in Matlab. New York: CRC Press; 2003. pp. 167-198.
33. Efron B, Tibshirani RJ. An introduction to the Bootstrap. Boston: Chapman & Hall; 1993.
34. Politis DN, Romano JP. A circular block-resampling procedure for stationary data. In: R. L, L. B, editors. Exploring the limits of Bootstrap. New York: John Wiley & Sons; 1992. pp. 263-271.
35. Zoubir AM, Iskander DR. Boostrap techniques for signal processing. New York: Cambridge University Press; 2004.
36. Travis EL, Tucker SL. The relationship between functional assays of radiation response in the lung and target cell depletion. *Br J Cancer Suppl* 1986;7:304-319.
37. MuCullagh P, Nelder JA. Generalized linear models. Second ed. London: Chapman and Hall; 1990.
38. Dobson AJ. An introduction to generalized linear models. Second ed. London: Chapman and Hall; 2001.
39. Coderre JA, Morris GM, Kalef-Ezra J, Micca PL, Ma R, Youngs K, Gordon CR. The effects of boron neutron capture irradiation on oral mucosa: evaluation using a rat tongue model. *Radiat Res* 1999;152:113-118.

40. Morris GM, Coderre JA, Bywaters A, Whitehouse E, Hopewell JW. Boron neutron capture irradiation of the rat spinal cord: histopathological evidence of a vascular-mediated pathogenesis. *Radiat Res* 1996;146:313-320.

41. Langberg CW, Sauer T, Reitan JB, Hauerjensen M. Tolerance of Rat Small-Intestine to Localized Single Dose and Fractionated-Irradiation. *Acta Oncologica* 1992;31:781-787.

42. Withers HR, Mason KA, Taylor JMG, Kim DK, Smathers JB. Dose Survival Curves, Alpha-Beta Ratios, RBE Values, and Equal Effect Per Fraction for Neutron-Irradiation of Jejunal Crypt Cells. *Radiation Research* 1993;134:295-300.

43. Withers HR, Elkind MM. Radiosensitivity and Fractionation Response of Crypt Cells of Mouse Jejunum. *Radiation Research* 1969;38:598-&.

44. Hendry JH, Potten CS, Roberts NP. The Gastrointestinal Syndrome and Mucosal Clonogenic Cells - Relationships between Target-Cell Sensitivities, LD50 and Cell-Survival, and Their Modification by Antibiotics. *Radiation Research* 1983;96:100-112.

45. Morris GM, Coderre JA, Hopewell JW, Micca PL, Rezvani M. Response of rat skin to boron neutron capture therapy with *p*-boronophenylalanine or borocaptate sodium. *Radiother. Oncol.* 1994;32:144 - 153.

46. Lauk S, Kiszel Z, Buschmann J, Trott KR. Radiation induced heart disease in rats. *International Journal Of Radiation Oncology Biology Physics* 1985;11:801-808.

47. Schultz-Hector S. Radiation-induced heart disease: review of experimental data on dose response and pathogenesis. *Int. J. Radiat. Biol.* 1992;61:149-160.

48. Morris GM, Coderre JA, Hopewell JW, Micca PL, Nawrocky MM, Liu HB, Bywaters A. Response of the central nervous system to boron neutron capture irradiation: evaluation using rat spinal cord model. *Radiother Oncol* 1994;32:249-255.

49. Pauluhn J, Baumann M, Hirth-Dietrich C, Rosenbruch M. Rat model of lung fibrosis: comparison of functional, biochemical, and histopathological changes 4 months after single irradiation of the right hemithorax. *Toxicology* 2001;161:153-163.

50. Lehnert BE, Dethloff LA, Finkelstein JN, Vanderkogel AJ. Temporal Sequence of Early Alterations in Rat Lung Following Thoracic X-Irradiation. *Int. J. Radiat. Biol.* 1991;60:657 - 675.

51. Shibata Y, Lin H, Busse P, Patel H. Normal lung uptake of BPA-f after intra-peritoneal injection in mice. In: Sauerwein W, Moss R, Wittig A, editors. Research and development in Neutron Capture Therapy: proceedings of the 10th international congress on Neutron Capture Therapy. Essen, Germany: Monduzzi Editore; 2002. pp. 791-795.

52. Travis EL, Liao ZX, Tucker SL. Spatial heterogeneity of the volume effect for radiation pneumonitis in mouse lung. *International Journal of Radiation Oncology Biology Physics* 1997;38:1045-1054.

53. Novakova-Jiresova A, van Luijk P, van Goor H, Kampinga HH, Coppes RP. Pulmonary radiation injury: Identification of risk factors associated with regional hypersensitivity. *Cancer Research* 2005;65:3568-3576.

54. Chandra S, Lorey ID, Smith DR. Quantitative subcellular secondary ion mass spectrometry (SIMS) imaging of boron-10 and boron-11 isotopes in the same cell delivered by two combined BNCT drugs: in vitro studies on human glioblastoma T98G cells. *Radiat Res* 2002;157:700-710.

55. Fowler JF. Review: Total doses in fractionated radiotherapy - implications of new radiobiological data. *International Journal of Radiation Biology* 1984;46:103-120.

56. Withers HR, Peters LJ, Thames HD, Fletcher GH. Hyperfractionation. *International Journal of Radiation Oncology Biology Physics* 1982;8:1807-1809.

57. Travis EL, Parkins CS, Down JD, Fowler JF, Thames HD, Jr. Repair in mouse lung between multiple small doses of X rays. *Radiat Res* 1983;94:326-339.

58. Peterson LM, Evans ML, Graham MM, Eary JF, Dahlen DD. Vascular response to radiation injury in the rat lung. *Radiation Research* 1992;129:139-148.

59. Law MP, Ahier RG. Vascular and epithelial damage in the lung of the mouse after x-rays or neutrons. *Radiation Research* 1989;117:128-144.

60. Law MP, Ahier RG, Coultas PG. The Role of Vascular Injury in the Radiation Response of Mouse Lung. *British Journal of Cancer* 1986;53:327-329.

61. Rubin P, Johnston CJ, Williams JP, McDonald S, Finkelstein JN. A perpetual cascade of cytokines postirradiation leads to pulmonary fibrosis. *International Journal of Radiation Oncology Biology Physics* 1995;33:99-109.

62. Williams JP, Hernady E, Johnston CJ, Reed CM, Fenton B, Okunieff P, Finkelstein JN. Effect of administration of lovastatin on the development of late pulmonary effects after whole-lung irradiation in murine model. *Radiation Research* 2004;161:560-567.

63. Rubin P, Shapiro D, Finklestien J, Penney DP. The early release of surfactant following lung irradiation of alveolar type II cells. *International Journal of Radiation Oncology Biology Physics* 1980;6:75-77.

64. Shapiro DL, Finkelstein JN, Penney DP, Seimann DW, Rubin P. Sequential effects of irradiation on the pulmonary surfactant system. *International Journal of Radiation Oncology Biology Physics* 1982;8:879-882.

65. Kiger WS, 3rd, Micca PL, Morris GM, Coderre JA. Boron microquantification in oral muscosa and skin following administration of a neutron capture therapy agent. *Radiat Prot Dosimetry* 2002;99:409-412.

66. McDonald S, Rubin P, Phillips TL, Marks LB. Injury to the lung from cancer therapy: Clinical syndromes, measurable endpoints, and potential scoring systems. *Int. J. Radiat. Oncol. Biol. Phys.* 1995;31:1187-1203.

67. Geist BJ, Trott KR, Lauk S. Physiologic consequences of local heart irradiation in rats. *International Journal Of Radiation Oncology Biology Physics* 1990;18:1107-1113.

68. van Luijk P, Novakova-Jiresova A, Faber H, Schippers JM, Kampinga HH, Meertens H, Coppes RP. Radiation damage to the heart enhances early radiation-induced lung function loss. *Cancer Research* 2005;65:6509-6511.

69. Lauk S. Stain differences in the radiation response of the rat heart. *Radiotherapy and Oncology* 1986;5:333-335.

70. Yeung TK, Hopewell JW. Effects of single doses of irradiation on cardiac function in the rat. *Radiotherapy and Oncology* 1985;3:339-345.

CHAPTER FIVE

Pathological Changes of the Rat Lung in Boron Neutron Capture Therapy Irradiation

5.1 Introduction

Lung is one of the dose limiting organs in radiation therapy for bone marrow transplantation and thoracic malignancies including lung cancer and Hodgkin's disease (1-4). Three phases have been categorized for radiation lung changes as follows: the early phase, including the latent period before radiation pneumonitis and the pneumonitis itself; the intermediate phase between pneumonitis and fibrosis, when healing of damage from the early phase occurs to some extent; and the late fibrosis phase (5-9). Ultrastructural and histological changes occurring from hours to months after irradiation are well documented with experimental animals in the literature (5, 8, 10-14). Cellular changes due to radiation damage, occurring as early as hours after irradiation during the early phase are observed, including increased capillary permeability, Type I and II pneumocyte degeneration, edematous basement membrane, fibrin and inflammatory cell infiltration into alveolar space, and other changes to lung structure. During the intermediate phase, healing is activated. Increased cellularity and hyperplasia is generally observed for Type II pneumocytes and septal membranes, and large foamy cells appear in the alveolar space in this stage. In the fibrosis stage, radiation wounds are organized and final scars are formed, mostly in

the form of fibrosis. The exact onset time of the pneumonitis and fibrosis is dose-related and also varies with different animal species and strains (15-17). The lesions of the three stages may also exist simultaneously in the lung after irradiations.

Functional damage to the lung, measured with the breathing rate assay, for irradiations with x-rays, neutrons, and neutrons plus BPA, is reported in detail in Chapter 4. Animals with breathing rate 20% higher than the control mean after irradiations, set as the threshold for abnormal breathing rate, were defined as positive responses. The fractional response of each dose group was calculated and dose response curves determined for the three radiation groups. Weighting factors for the high-LET dose components in BNCT rat lung irradiation were derived from the dose response curves at the ED_{50} level of response. The weighting factors were 1.24 ± 0.08 for the M011 thermal neutron beam RBE, and 1.4 ± 0.2 and 2.3 ± 0.3 for the CBE factors for the ^{10}B dose from neutron plus BPA for early and late responses, respectively.

In this chapter, the lung damage in the irradiated rats was evaluated histologically and quantified with a histological scoring system. The lung damage from different radiations and dose levels were compared in severity and development in time. The weighting factors of the high LET dose components in BNCT rat lung irradiation were also determined from the histological assessment of lung damage. Functional damage assessed with breathing rate measurement and the histological damage was compared to demonstrate the correlation between these two methods.

5.2 Materials and Methods

Male Fisher 344 rats, approximately 12 weeks old, were used for these studies. The vertical M011 thermal neutron beam (18, 19) of the MITR-II was used for neutron irradiations. The

irradiations and dosimetry are described in detail in Chapters 2 and 4. Irradiations with x-rays were carried out using a Phillips RT250 unit operating at 250 kV and 12 mA with 0.4 mm Sn plus 0.25 mm Cu added filtration. Different doses were delivered to the lung, including 11, 11.5, 11.75 and 12 Gy of x-rays, 4.7, 7.1, 8.2, 9.1, 9.4 and 9.7 Gy of neutrons-only radiation. For the irradiations with neutrons plus BPA, the doses delivered to the lung were distributed between 4-12 Gy. Precise delivery of certain doses with BPA was not possible because of the variability in blood boron concentration. 90 animals were irradiated within this dose range with approximately 10 rats irradiated for each dose level. During irradiations, rats were anesthetized with intraperitoneal (i.p.) injections of ketamine (80 mg/kg) and xylazine (10 mg/kg). Two rats were positioned, side-by side, under the delimiter and immobilized with 5-cm wide clear adhesive tape. The lung region was positioned in the beam aperture using the bony protuberance of the T2 vertebra and the xyphoid sternum as reference points, with the reference points lined up with the edge of the delimiter aperture. These experiments were conducted with approval from the Committee on Animal Care at the Massachusetts Institute of Technology.

The rats were euthanized for lung histological changes during early and late phases at various times after different radiations. For the early phase of the rat lung radiation response, rats were euthanized 60 days after irradiations with 9.7 Gy neutrons only or 10.5 Gy neutrons plus BPA, and 20, 40, 60, 80 and 100 days after irradiation with 12 Gy X-rays. The dose levels of the three radiations selected for the early phase lung radiation damage produced a 100% response for breathing rate increase. Some representative histological changes were specifically examined during the early response phase. For the late phase of rat lung irradiation response, rats were euthanized at about 180 days at various dose levels, listed previously. At least 6 rats were euthanized for each dose group or time point. The consistency of histological damage between

different radiations and the correlation between breathing rate increase and histological damage was assessed during both the early and the late response phases. Rats were euthanized with i.p. injection of a lethal dose of pentobarbital. Immediately before the death of the animal, the lung was infused with 10% neutral buffered formaldehyde through the opened trachea and fixed. Two slices of lung, each about 3 mm thickness, were taken from each animal: one at the left lung close to the main bronchus and the other at the lower half of the superior lobe of the right lung. The two slices were embedded in a paraffin block and two sections of 4 μm thickness were cut from the sample and stained with Hematoxylin and Eosin (H&E) and Van Gieson separately. H&E is a routine histological stain while the Van Gieson stain is specialized for elastic fiber.

A scoring system to quantify the lung histology radiation damage was established, similar to what has been used in the literature (11, 20). The presence of the characteristic lesions of the three phases of lung radiation response, early, intermediate, and late (8, 10, 11, 21, 22), was assessed in the lung sections of each animal. The characteristics and lesions of these three phases are listed in Table 5.1. Since the lesions of the three phases may exist simultaneously with varying severity, the presence and severity of each set of lesions in the rat lung was assessed and assigned a score. Therefore, three histological scores (one for each set of lesions) were given to each lung section examined. The percent area of the lung sections occupied by the lesions of a specific criterion was used to quantify the severity of this criterion. The severity scale is described in Table 5.2. In the situation when an integer severity score was

Table 5.1 Histological characteristics and lesions of the three phases of lung radiation responses (11). The three phases were also used as the scoring criteria.

Phase/Criteria	Histological lesion
Early	Patchy areas of pneumonitis with inflammatory cells and intra-alveolar macrophages; perivascular cuffing with mononuclear cell infiltrate; edema
Intermediate	Increased septal cellularity with large foamy cells in the alveoli
Late	Septal fibrosis; pleural fibrosis; pathological organization; alveolar wall epithelialization

Table 5.2 Histological severity scale.

Severity scale	Criterion
0: none	Normal lung
1: mild	Small ($\leq$ 5 alveoli) foci involved
2: moderate	Large (> 5 alveoli) foci involved; not more than 10 large foci involved
3: marked	More than 10 large foci but less than 50% of the section area involved
4: severe	More than 50% of the section area involved

difficult to determine, a half-integer score (e.g., 1.5) was assigned to the slide. During the histological scoring process, the examiner was blinded to the identity of each slide and rat including dose and euthanasia date. All slides were scored within a few days to ensure scoring consistency. The scoring system and some sample slides were examined and the scores of these slides were confirmed by a pathologist, Dr. Prashant Nambiar of the MIT Division of Comparative Medicine (DCM). A Nikon light microscope was used for the histology scoring with magnifications of 20–400x. Examples of some common lesions seen in the radiation damaged lung are shown in Fig. 5.1.

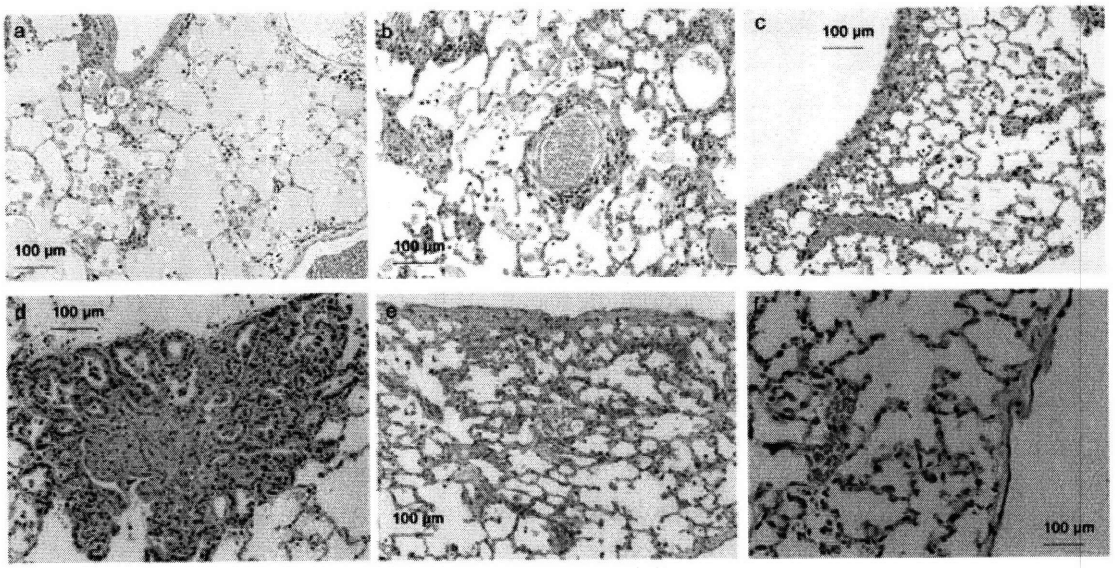

Fig. 5.1 Examples of the histological lesions: a) alveolar edema, b) perivascular cuffing with mononuclear cells exudates; c) mesothelial hyperplasia d) chronic lesion with collagen nodule and epithelialization, e) interstitial and pleural fibrosis, f) pleural fibrosis.

5.3 Results

5.3.1 Time course for lung histological damage from x-ray irradiations

For rats receiving 12 Gy x-rays, the evidence of early phase histological changes (Table 5.1) presented at 20 days post irradiation, peaked at 60 days, and had diminished by 180 days. The early changes were characterized by intra-alveolar macrophages, perivascular cuffing, mononuclear cell infiltrate and edema. The intermediate phase (Table 5.1) started at 60 days, although Type II pneumocyte hyperplasia was seen as early as 20 days post irradiation. The late phase, pulmonary fibrosis (Table 5.1), started at 100 days with organization of inflammatory cells, markedly thickened alveolar wall and epithelialization, although the unusual collagen deposition in the lung parenchyma was continuously observed from 20 days after irradiation. Both the intermediate and late phases lasted through 180 days post irradiation with increasing

severity. At about 180 days, a mix of intermediate and late characteristics was present in the lung. Other lesions occurring less often than the ones listed in Table 5.1 were also observed, including fibrins in blood vessels from 20 days post irradiation, fibrous connective perivascular tissue later than 100 days post irradiation, and osseous metaplasia or calcification in the alveolar space, mostly at 180 days in the late phase. The normal architecture of the lung parenchyma demonstrated more distortion and depletion than in the early phase from the radiation damage. The lesions were not uniformly distributed within the lung and usually more damage occurred close to the bronchioles. The severity of damage could also vary significantly between the different lung sections from the same rat. Similar histological changes have been reported in literature (8, 10, 11, 21, 22) as were observed in this experiment. The group average severity scores versus time for the three specified phases after 12 Gy x-rays are plotted in Fig. 5.2.

5.3.2 Comparison of X-rays, neutrons, and neutron plus BPA at 60 days

For the rats sacrificed at 60 days post irradiation, during the early phase, similar histological damage in terms of lesion characteristics and severity was observed in the rat lungs that received 12 Gy x-rays and 9.7 Gy neutrons. This similarity in histological damage for these two doses of x-rays and neutrons is consistent with the similarity in their functional damage measured with the breathing rate. These two doses produced a 100% response in breathing rate (Fig. 4.3 and Fig. 4.5) and about 10% death rate before 60 days post irradiation, with about 20 animals irradiated in each dose level. Much more severe early phase response was observed with 10.5 Gy of neutrons plus BPA, with significantly more perivascular cuffing of mononuclear cell infiltrates and edematous exudate in the alveolar space, as shown in Fig. 5.1, a-c. Most of the doses higher than 10 Gy of neutrons plus BPA produced a 100% response in breathing rate and a death rate of 90% before 60 days with about 10 animals irradiated at each dose level.

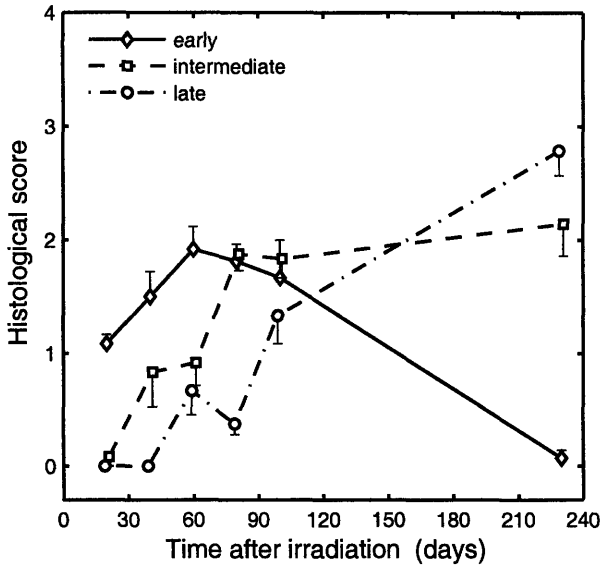

Fig. 5.2 The severity of the histological damage versus time after irradiation of rat lung with 12 Gy of x-rays. The uncertainties plotted in this figure are standard error of the mean (SEM).

Some examples of the histological changes in the pulmonary pneumonitis and fibrosis phases are shown in Fig. 5.3, from rats in different radiation groups during the early and late response phases. A mix of early and intermediate phase characteristics was evident in the lung at about 60 days post irradiation. The typical lung histological changes at this time seemed to be monocyte infiltrates with foamy cells in the alveolar space, with fibrins sometimes seen in blood vessels and alveolar space. Various types of chronic inflammatory and pathological reorganization were observed in addition to fibrosis during the late response phase. Some examples of different lesions present during the late phase are shown in Fig. 5.3, e-f.

5.3.3 Comparison of X-rays, neutrons, and neutron plus BPA at 180 days

At approximately 180 days post irradiation, all the remaining rats were euthanized. Dose response curves of the late lung response assessed functionally or histologically of these rats, are shown in Fig. 5.4. The dose response curves for functional damage measured with the breathing

rate are reproduced from Chapter 4. The sum of the three histological scores (early, intermediate and late) of each rat was used to quantify the overall lung histological damage of the rats. Group means of the total scores of rats at different dose levels are plotted as the responses. From the dose response curves of the lung histological damage, the sum of the histology score appears to increase linearly with dose above a certain threshold value. For doses below the threshold, the histological damage was similar to or slightly above the control (Table 5.3) and remained constant with dose. For neutron only radiation, the threshold was about 7 Gy and for neutrons plus BPA, the threshold was about 5.5 Gy. For the dose response curve of X-rays, the minimum doses delivered were above the threshold but extrapolating the linear fit to lower doses suggests a threshold of approximate 10 Gy. A simple linear regression was used to fit the response data above the threshold dose for each radiation, as shown in Fig. 5.4b. A method was then used to determine the biological weighting factors with this set of response curves, similar to the weighting factors measured functionally. First, a reference endpoint, analogous to the 50% response for breathing rate increase was determined with the responses of histological damage. The doses of neutrons plus BPA covered the entire range of severity of the histological damage well, from below the threshold where the score was low and nearly constant, to above the threshold where the severity increased linearly with dose, to just below the lethal dose range, where the rats mostly died in the early phase. The reference level of histological damage, used as the endpoint in this assessment, was defined as the mid point (4.3) of the response between the threshold score (1.5) and the maximum score observed (7.1) for rats irradiated with neutrons plus BPA. The doses corresponding to this score with the different radiations are listed in Table 5.4, along with the ED_{50}s of the breathing rate responses. The differences between the doses corresponding to the histological damage endpoint, listed in Table 5.4, and the ED_{50} values of the

breathing rate responses are not statistically significant. Using the conventional method of weighting factor determination described in Chapter 4, the RBE for the neutron beam only determined here histologically was 1.22 ± 0.09 (SD), the same as the RBE obtained with the breathing rate assay. The CBE for BPA with histological response estimated here was 1.9 ± 0.2 (SD), and had no statistically significant difference from the CBE measured for late lung functional response, 2.3 ± 0.3. This is because the 95% confidence intervals of the corresponding doses, from which the two CBE factors were derived, overlap (Table 5.4).

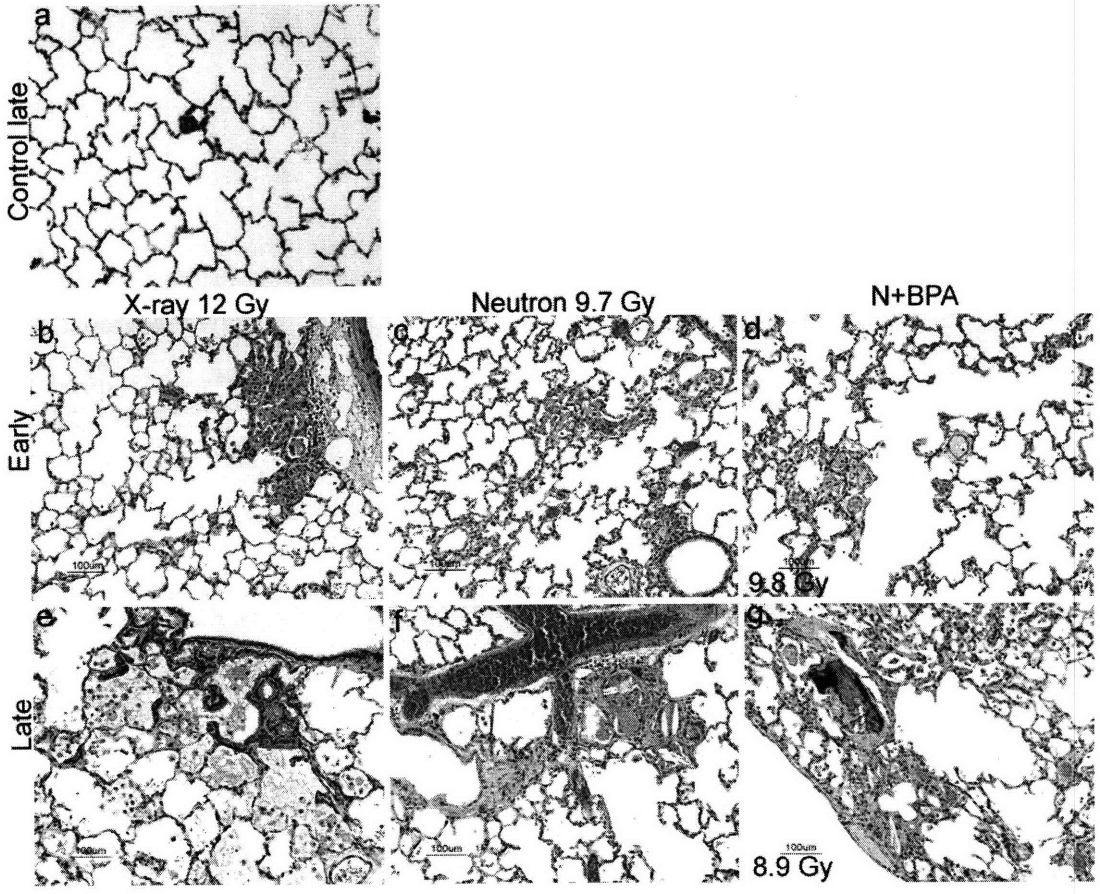

Fig. 5.3 Histological changes of the early and late phase for different radiations. Panels b-d show typical changes at 60 days post irradiation with different radiations. Panels e-g show examples of various lesions during the late pulmonary response phase at about

180 days: epithelialization (e), fat cells deposition (e), cholesterol clefts (23) (f), calcification (g) and muscle hyperplasia (g), in addition to collagen deposition.

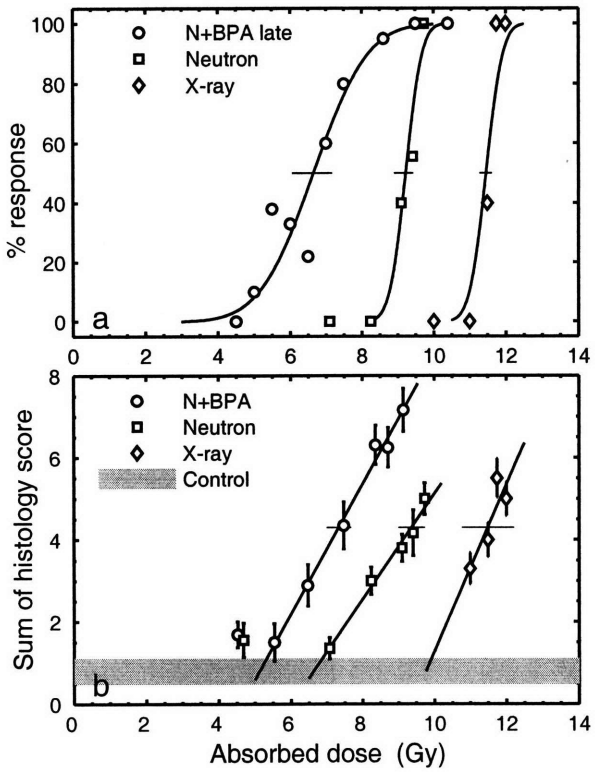

Fig. 5.4 Dose responses and fitted curves with breathing rate increase (a) or histological damage (b) as the biological endpoint at 180 days after the irradiation. The shaded area in panel b represents the control group mean ± one standard deviation of the mean (SEM). The uncertainties plotted for each dose groups in panel (b) are standard errors of the mean (SEM).

Table 5.3 Mean histological scores for different groups during early (around 60 days) and late (around 180 days) response phases.

	Euthanasia	Average histology score			
	Phase	Early	Intermediate	Late	Total
Sham-irradiated controls	late	0.1±0.1	0.3±0.1	0.4±0.1	0.8±0.3
X 11.75 Gy	late	1.2±0.4	2.4±0.2	1.9±0.2	5.5±0.5
N 9.7 Gy	early	1.8±0.1	1.3±0.2	0.6±0.2	3.7±0.2
N 9.7 Gy	late	0.7±0.3	1.9±0.1	2.4±0.2	5.0±0.4
N+BPA 10.5 Gy	early	3.4±0.4	1.3±0.2	1.0±0.3	5.7±0.6
N+BPA 9.1 Gy	late	1.5±0.3	3.0±0.3	2.7±0.3	7.2±0.5

Table 5.4 The doses corresponding to functional and histological endpoints used to determine the weighting factors for the M011 thermal neutron beam and ^{10}B dose component from BPA.

	Dose (Gy) (mean ± SD)			Neutron	CBE for
	X-ray	Neutron	N + BPA	beam RBE	BPA
ED_{50} of BR	11.5 ± 0.4	9.2 ± 0.5	6.7 ± 0.4	1.24 ± 0.08	2.3 ± 0.3
Hist. Score = 4.3	11.5 ± 0.5	9.4 ± 0.6	7.3 ± 0.4	1.22 ± 0.09	1.9 ± 0.2

The correlation between the two assays is demonstrated in a direct way by examining the relationship between histological score and breathing rate response. This is demonstrated in Fig. 5.5, which shows the breathing rate response for rats grouped by histological score. Rats were separated according to their euthanasia date during early (<100 days post irradiation) or late phase (>100 days). Most rats euthanized in the early phase were sacrificed at 60 days and most animals euthanized during the late phase were sacrificed at 180 days. In the breathing rate percent response, the last breathing rate measured before the euthanasia and the maximum breathing rate measured during the early or late phase were assessed separately. During the early phase, differences between the breathing rate response curves using the last breathing rate and maximum breathing rate are statistically significant while during the late phase, the two are similar except at one histology score.

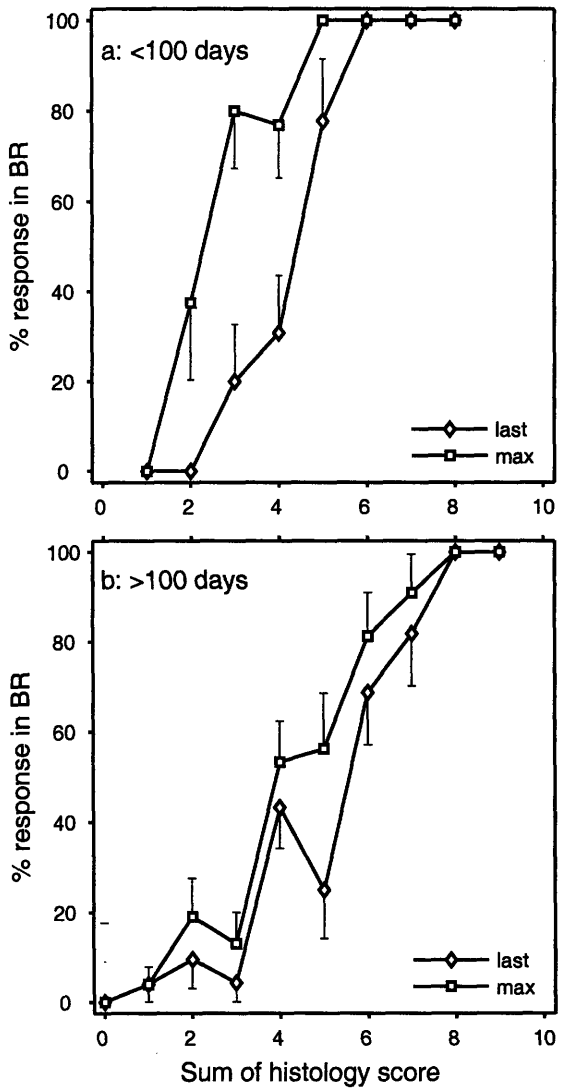

Fig. 5.5 Percent of rats with breathing rate increase for the histological scores for early (a. euthanasia ≤ 100 days) and late (b. euthanasia > 100 days) phases of response. The breathing rate percent response was calculated for both the last breathing rate measured before euthanasia and the maximum breathing rate measured. For the animals euthanized later than 180 days in panel b, maximum breathing rate measured after 100 days was used to calculate the breathing rate percent response.

5.4 Discussion

Using the technique described in this chapter, the time course of the lung histological

changes for rats receiving high LET radiation to the lung were observed similar to those receiving x-rays. For the rats receiving lung irradiations of neutron plus BPA and showing breathing rate elevation only after 100 days post irradiation, histological examination of the lungs demonstrated that the breathing rate elevation was due to pulmonary fibrosis, rather than a delayed pneumonitis.

Another important objective of assessing the radiation lung damage with histological changes was to confirm the assessment of the lung damage with breathing rate. The breathing rate measurement showed a peak elevation in the breathing rate at about 60 days post irradiation, and later decreased, sometimes back to normal, breathing rates until the response of the late phase (Fig. 4.3). A peak in the histological score versus time of lesions of the early phase was also observed at 60-80 days (Fig. 5.2), indicating a peak response of the early phase at this time. The score for the early phase decreased later and the presence of the early phase lesions almost diminished at 180 days post irradiation (Fig. 5.2). From Fig. 5.4 and Table 5.4, consistent weighting factors were obtained using the functional assessment with breathing rate measurement and histological assessment. With functional assessment, dose responses were fitted into sigmoidal curves with binary response of individual animals. With histological assessment, linear dose response curves were obtained with the histological response of each animal estimated with a quantitative score. The consistency of the two assessments was also shown more directly in Fig. 5.5.

In Chapter 4, two explanations were proposed for the phenomenon that most animals receiving lower doses (e.g., 5-9 Gy) of neutrons plus BPA demonstrated the late phase of breathing rate response without first showing the early phase of response. One possibility suggested higher BPA microdistribution in the target cells responsible for the late lung response.

The other involved heart complications. Further investigations are necessary to prove the involvement of the heart in this phenomenon and also to further understand the lung response to BNCT irradiation. First, examination of histological changes during the early phase after 5-9 Gy neutrons plus BPA would be helpful for interpreting the development of the late lung response. Second, examination of heart histological damage at about 180 days during the late lung response phase may answer the question of the heart involvement in this case. If the heart were indeed involved, it would affect the late lung response more, which has also been reported in the literature (24). If the heart were not involved, a more interesting alternative hypothesis is that different target cells may be responsible for the early and late lung responses. The ^{10}B concentration of BPA at cellular level in lung tissue needs to be investigated with ^{10}B microdistribution techniques such as High Resolution Quantitative Autoradiography (HRQAR) (25) or Secondary Ion Mass Spectroscopy (SIMS) (26).

5.5 References

1. Cardozo BL, H. Z, van Bekkum DW, Zurcher C, Hagenbeek A. Lung damage following bone marrow transplantation: I. the contribution of irradiation. International Journal of Radiation Oncology Biology Physics 1985;11:907-914.
2. Torres PY, Bross DS, Lam WC, Wharam MD, Snatos GW, Order SE. Risk factors in interstitial pneumonitis following bone marrow transplantation. International Journal of Radiation Oncology Biology Physics 1982;8:1301-1307.
3. Abratt RP, Morgan GW, Silvestri G, Willcox P. Pulmonary complications of radiation therapy. Clinics in chest medicine 2004;25:167-177.
4. Anscher MS, Kong F, Marks LB, Bentel GC, Jirtle RL. Changes in plasma transforming growth factor beta during radiotherapy and the risk of symptomatic radiation-induced pneumonitis. International Journal of Radiation Oncology Biology Physics 1997;37:253-258.
5. Rubin P, Casarett GW, editors. Respiratory system. Philadelphia: W. B. Saunders Company; 1968.

6. Gross NJ. Pulmonary Effects of Radiation-Therapy. Annals of Internal Medicine 1977;86:81-92.
7. Coggle JE, Lambert BE, Moores SR. Radiation effects in the lung. Environmental health perspectives 1986;70:261-291.
8. Phillips TL. An ultrastructural study of the development of radiation injury in the lung. Radiology 1966;87:49-54.
9. Perez CA, Brady LW. Thoracic radiotherapy: complications and injury to normal tissue. In: Principles and practice of radiation oncology. New York: Lippincott Williams & Wilkins; 2002.
10. Maisin JR. The ultrastructure of the lung of mice exposed to a supra-lethal dose of ionizing radiation on the thorax. Radiation Research 1970;44:545-564.
11. Travis EL. The sequence of histological-changes in mouse lungs after single doses of X-rays. International Journal of Radiation Oncology Biology Physics 1980;6:345-347.
12. Murray JC. Radiation-Induced Fibrosis - the Structure/Function Relationship. Scanning Microscopy 1994;8:79-87.
13. Moosavi H, McDonald S, Rubin P, Cooper R, Stuard D, Penney DP. Early radiation dose-response in lung: an ultrastructural study. International Journal of Radiation Oncology Biology Physics 1977;2:921-931.
14. Siemann DW, Hill RP, Penney DP. Early and Late Pulmonary Toxicity in Mice Evaluated 180 and 420 Days Following Localized Lung Irradiation. Radiation Research 1982;89:396-407.
15. Down JD. The nature and relevance of late lung pathology following localized irradiation of the thorax in mice and rats. Br J Cancer Suppl 1986;7:330-332.
16. Down JD, Nicholas D, Steel GG. Lung damage after hemithoracic irradiation: dependence on mouse strain. Radiother Oncol 1986;6:43-50.
17. Hopewell JW, Rezvani M, Moustafa HF. The pig as a model for the study of radiation effects on the lung. Int J Radiat Biol 2000;76:447-452.
18. Choi J-HR. Development and characterization of an epithermal beam for boron neutron capture therapy at the MITR-II Research Reactor. Nuclear Engineering Department: Massachusetts Institute of Technology; 1991.
19. Choi JR, Clement SD, Harling OK, Zamenhof RG. Neutron capture therapy beams at the MIT Research Reactor. In: J. A. Bernard, Harling OK, Zamenhof RG, editors. Neutron Beam Design, Development, and Performance for Neutron Capture Therapy. Vol 54. New York and London: Plenum Press; 1990. pp. 201-218.
20. Ashcroft A, Simpson JM, Timbrell V. Simple method of estimating severity of pulmonary fibrosis on a numerical scale. Journal of clinical pathology 1988;41:467-470.
21. Lehnert BE, Dethloff LA, Finkelstein JN, Vanderkogel AJ. Temporal Sequence of Early Alterations in Rat Lung Following Thoracic X-Irradiation. Int. J. Radiat. Biol. 1991;60:657 - 675.

22. Pauluhn J, Baumann M, Hirth-Dietrich C, Rosenbruch M. Rat model of lung fibrosis: comparison of functional, biochemical, and histopathological changes 4 months after single irradiation of the right hemithorax. Toxicology 2001;161:153-163.

23. Travis EL, Meistrich ML, Finchneimeyer MV, Watkins TL, Kiss I. Late Functional and Biochemical-Changes in Mouse Lung after Irradiation - Differential-Effects of WR-2721. Radiation Research 1985;103:219-231.

24. Novakova-Jiresova A, van Luijk P, van Goor H, Kampinga HH, Coppes RP. Pulmonary radiation injury: Identification of risk factors associated with regional hypersensitivity. Cancer Research 2005;65:3568-3576.

25. Kiger WS, 3rd, Micca PL, Morris GM, Coderre JA. Boron microquantification in oral muscosa and skin following administration of a neutron capture therapy agent. Radiat Prot Dosimetry 2002;99:409-412.

26. Chandra S, Lorey ID, Smith DR. Quantitative subcellular secondary ion mass spectrometry (SIMS) imaging of boron-10 and boron-11 isotopes in the same cell delivered by two combined BNCT drugs: in vitro studies on human glioblastoma T98G cells. Radiat Res 2002;157:700-710.

CHAPTER SIX

Summary, Conclusions, and Recommendations for Future Work

6.1 Conclusions

This project investigated the radiobiology of the normal rat lung and measured the radiobiological weighting factors required for the weighted lung dose calculation in BNCT. The male F344 rat was used as the experimental animal model. Rat thorax irradiations were carried out with x-rays and neutrons with or without the boron compound p-boronophenylalanine fructose (BPA-F). Functional assay of breathing rate measurement and histological damage scoring were used to assess the lung radiation damage. Dose response curves for the different radiations were constructed using endpoints of breathing rate elevation or histological damage. These dose response curves were analyzed and the radiobiological weighting factors were determined for the high LET dose components in BNCT.

A system for the rat lung neutron irradiation was designed using Monte Carlo radiation transport simulations. The design goal of the rat lung irradiation system was to deliver a uniform thermal neutron dose to the lung region while sparing the adjacent radiosensitive normal tissues. The two neutron beam facilities available for BNCT experiments at the MIT Research Reactor were compared and the M011 thermal neutron beam was found to be the most suitable for the rat lung irradiation. A delimiter was then designed and optimized for the rat lung irradiations as a Li-Poly plate of 1.5 cm thickness with a tapered aperture of 4-3 cm width to expose the lung

section to the beam. The simulation design was validated with in-phantom dose measurements using gold foil activation and the dual ion chamber method. A 10 Gy dose of neutron-only or beam-only irradiation could be delivered to the lung in about 50 minutes beam time with a two-field irradiation. About 20% of the total beam dose is neutron dose mostly from the $^{14}N(n, p)$ capture reactions, and the remaining 80% is from photons. With ^{10}B present from BPA, a 10 Gy total dose was delivered in about 20 minutes and about 50% of the total dose was from the neutron beam and 50% from ^{10}B.

An open-flow whole-body plethysmography with fully automated signal processing programs was developed to non-invasively measure the rat breathing rate after lung irradiation. The apparatus was adapted from a commercially available system for rat breathing signal collection (Respiromax, Columbus Instruments, Columbus, OH). Software was developed to automatically process digital pressure change signals from the plethysmography system and determine breathing frequencies. Three minutes of pressure signal were collected in each rat breathing rate measurement at a data-sampling rate of 200 Hz. Noise discrimination was employed in the time domain against ripple noise (<0.04 s) and large amplitude noise from animal movement. The breathing pressure signals were then analyzed using the Fast Fourier Transform (FFT) with a circular moving block in combination with the bootstrap (1-3) for noise suppression and to allow estimation of the statistical uncertainty (standard deviation) of frequency measurements. The mean standard deviation of all measurements in the data set was 2.4%. As an independent check on the FFT results, a peak-counting method was used to analyze the same set of breathing signal data and determine the Breathing Frequency Density Function (BFDF) of the signal from the periods of all breath cycles. Using this software, more than 4269 stored breathing rate signals were analyzed and 90% of the breathing frequency results from the

FFT and BFDF methods agreed to within 10%. The measured mean breathing rate for the control group (8 animals and 17 measurements each) was 176 ± 13 (7.4%) min^{-1} (mean ± SD) and breathing rates 20% (~ 3 SD) above the control mean were considered abnormal.

Radiobiological studies in the normal lung of rats were performed to measure the radiobiological weighting factors required for the weighted lung dose calculation in BNCT. Rat thorax irradiations of Fisher344 rats were carried out with x-rays, thermal neutrons, and thermal neutrons with BPA-F. The rat breathing rates were measured up to 180 days post-irradiation to assess and quantify functional damage in the lung following irradiation. For the responding rats that received neutrons-only or x-ray radiation, most rats showed a biphasic response in breathing rate elevation, the early phase (≤100 days) and the late phase (>100 days). The response was different for neutrons plus BPA since that at relatively low doses (~ 5-9 Gy), 25 out of 47 animals responded only in the late phase. The dose responses of different irradiation groups were analyzed with probit analysis. The ED_{50} values for x-rays, neutrons only, and neutrons plus BPA during the early response phase, and neutrons plus BPA during the late response phase, were 11.5 ± 0.4 Gy, 9.2 ± 0.5 Gy, 8.7 ± 0.6 Gy and 6.7 ± 0.4 Gy (mean ± SD), respectively. The radiobiological weighting factors for the neutron beam (neutrons and photons) and thermal neutrons only were determined as 1.24 ± 0.08 and 2.2 ± 0.4, respectively. A new algorithm was used to determine the weighting factor for the ^{10}B dose component in neutrons plus BPA irradiation. A potential radiobiologically weighted dose response curve of the neutron plus BPA irradiation was constructed, with probit analysis and the weighted dose estimated with the neutron beam RBE for the beam dose component and a testing CBE for the ^{10}B dose component. A series of CBE values were tested and each produced a weighted dose response curve and a corresponding ED_{50} value. These ED_{50} values were compared to the ED_{50} value of the x-ray

dose response curve. The testing CBE value that produced minimum difference between the two was determined as the weighting factor for the ^{10}B dose component in rat lung irradiation of neutron plus BPA. Thus, the weighting factors for the ^{10}B dose component were measured at 1.4 ± 0.2 during the early response phase and 2.3 ± 0.3 during the late response phase.

The lung damage during the late response phase in the irradiated rats was also evaluated and quantified with a histological scoring system. The lung damage from different irradiations and dose levels was compared in severity and development in time. The dose responses were fitted with a linear response curve for each irradiation. The radiobiological weighting factors for the different dose components were also determined at a degree of lung histological damage corresponding to a median histological score, 4.3, between the baseline (similar to the control) and the maximum. The doses estimated at this histological damage level were 11.5 ± 0.5 Gy, 9.4 ± 0.6 Gy, and 7.3 ± 0.4 Gy, for x-rays, neutrons-only, and neutrons plus BPA at the late response phase. The weighting factors determined at this damage level were 1.22 ± 0.09 for the neutron beam and 1.9 ± 0.2 for the ^{10}B dose component with BPA during the late response phase. The two measured sets of weighting factors for the high-LET dose components of rat lung irradiation in BNCT, with either histological damage or functional damage as the biological endpoint, have no statistically significant difference between each other.

6.2 Clinical implications

One of the major motivations of this study was to investigate whether the lung complications that the three patients developed during the Harvard-MIT BNCT clinical trial in the period between 1994 and 1999 were due to BNCT dose. With the lung dosimetry measured in an anthropomorphic phantom positioned for cranial irradiation in a prone position, the minimum

weighting factors for neutron and ^{10}B dose needed to initiate the lung damage in the patients were estimated to be at least 3.2 and 4, respectively (4). In this study, the RBE measured for thermal neutrons was 2.2 ± 0.4, and the range of the CBE factor for BPA with the early breathing rate response was 1.0 - 2.2, both below the estimated requirements for weighting factors. Using the information provided by the report (4) and the measured biological weighting factors, a maximum weighted dose to the lung apex, using the dose in Table 6.1, is estimated to be 5.3 Gy_w for the patients who developed ARDS. The mean lung dose in these patients would be well below 5.3 Gy_w. With conventional x-ray irradiation, the threshold for radiation pneumonitis in patients treated with whole lung irradiation was 7 Gy of single fraction (5-8). This suggests that the lung complications developed by the patients after BNCT treatment for brain tumors most likely did not result from BNCT irradiation.

Table 6.1 Estimation of maximum dose delivered to the lung apex of the patients treated for brain tumors at the MIT-Harvard BNCT clinical trial in 1994-1999 who later developed ARDS. Lung ^{10}B concentration is assumed at 15 μg/g, the same as measured in blood.

	N_F	N_T	Photon	^{10}B	Weighted dose rate (cGy_w/min)	Beam time (min)	Total weighted dose (Gy_w)
Dose rate (cGy/min)	0.17	0.014	0.66	0.12	1.33	400	5.3
RBE/CBE	2.2	2.2	1	2.2			

The weighting factors in BNCT for normal lung irradiations measured in this project are also helpful for evaluating the feasibility of BNCT for lung cancer (9). With these measured biological weighting factors, a simple treatment plan with two field (anterior and posterior) lung irradiation in the FCB is calculated. The dimensions for this calculation were estimated from a human thorax cross section at lung from the Visible Human Project National Medical Library (10). The thickness of the human body at this region was measured at 26 cm, with 4.5 cm thickness of soft tissue on each side, and 17 cm thickness of lung in the middle. The dose-depth

profile in the lung region of the human cross section was estimated by extrapolating the dose-depth profile for the MIT FCB measured along the central axis of a large rectangular water phantom (40 x 40 x 60 cm^3) (11) by a factor of 4, since the lung density (0.26 g/cm^3) is about a quarter of water density or soft tissue density (1 g/cm^3). The ^{10}B concentration and RBEs used in BNCT brain tumor treatments at Harvard-MIT listed in Table 6.2 are used in calculation of the weighted dose rate for skin and tumor. The CBE for BPA in BNCT rat lung irradiation measured at ED_{10} during the late phase, 3.6, is used in this calculation to ensure minimum lung complication. The soft tissues between the skin and lung mainly include fat, muscle, bone and connective tissues. The weighted dose rate delivered to this region was estimated with the same weighting factors measured for lung in this experiment, as listed in Table 6.2. This is a higher estimate since soft tissues are very likely to be less radiosensitive than lung. The weighted dose rate profile through the human lung is plotted in Fig. 6.1a. The weighted dose rate to skin is plotted at a depth of 0.5 cm. The profile of the posterior field is simply the reverse of the anterior field profile. The weighted dose-depth profile for normal lung tissue and tumor with a two-field neutron irradiation (anterior and posterior) at this cross section is plotted in Fig. 6.1b. In this simulation, the maximum dose to the lung was 8.2 Gy_w (TD_{10}), which is the maximum dose delivered to the normal lung in conventional radiation for bone marrow transplant (5-8). From this figure, the minimum biologically weighted dose that could be delivered to the tumor is about 20 Gy_w and a clear dose separation between normal lung dose and tumor dose is achieved at all depths, mainly as a result of the higher ^{10}B concentration in the tumor. A relatively uniform dose distribution is also achieved on the central axis, due to the good penetration of the epithermal neutrons and the low lung density. The weighted dose to skin is estimated as 6.4 Gy_w and is well below 22 Gy_w, the threshold for skin dose in BNCT irradiation for brain tumors (12).

Table 6.2 Information used to calculate the weighted dose in the hand calculation of lung irradiation (12).

	Weighting factors			^{10}B conc.
	Neutron	^{10}B	Photon	μg/g
Skin	3.2	2.5	1.0	22.5
Normal lung/soft tissue	2.2	3.6*	1.0	15
Tumor	3.2	3.8	1.0	52.5

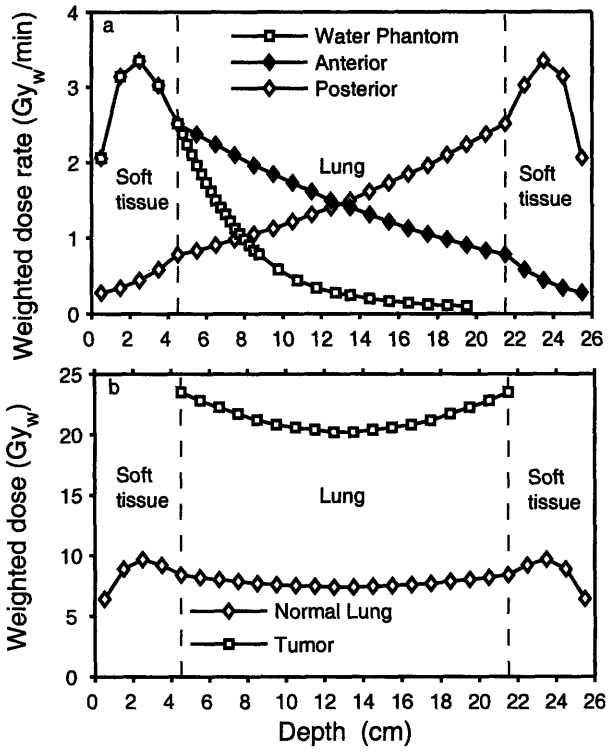

Fig. 6.1 Weighted dose and dose rate profiles for single-field irradiation (a) and two-field (anterior and posterior) irradiation (b) of the lung. The dose depth profile calculated along the central axis in the water phantom (40 x 40 x 60 cm^3) was obtained from Ref (11).

6.3 Future work

In this project, the dose-response curves with early (<100 days) and late (>100 days) breathing rate response as the biological endpoint had different dose ranges for neutron

irradiations with BPA. The ED_{50} for the late response was 6.7 ± 0.4 Gy, smaller than the ED_{50} for the early response, 8.7 ± 0.6 Gy. Most animals receiving lower doses (4-9 Gy) of neutrons plus BPA did not demonstrate the early phase but showed breathing rate elevation during the late phase. Two explanations were proposed for this phenomenon. One hypothesis is that a higher microscopic BPA concentration is in the unknown target cells which are responsible for the late lung response. The other hypothesis is that heart complications were involved in the breathing rate increase in the late phase with neutrons plus BPA irradiation. Further investigations are necessary to investigate the heart involvement and also to further understand the mechanisms of the lung damage in BNCT irradiation.

First, the histological changes during the early phase (~ 60 days post irradiation) of the animals receiving 4-9 Gy neutrons plus BPA should be studied, which will also help to interpret the development of the late lung response. Second, examination of cardiac histological damage at about 180 days during the late lung response phase may answer the question of the heart involvement in this case. If the heart was indeed involved, the late breathing rate response should be considered as a combined radiation effect from both lung and heart damage. Cardiac complication will have to be considered and heart irradiation avoided, should BNCT be used for lung cancer in the future. This will be very helpful for understanding the mechanisms of lung radiation damage that have been studied for about a half century. In order to assess the hypothesis of higher ^{10}B concentration in different cell types, the ^{10}B concentration of BPA at the cellular level in lung tissue needs to be investigated with ^{10}B micro-imaging techniques such as High Resolution Quantitative Autoradiography (HRQAR) (13) or Secondary Ion Mass Spectroscopy (SIMS) (14).

6.4 References

1. Zoubir AM, Iskander DR. Boostrap techniques for signal processing. New York: Cambridge University Press; 2004.
2. Efron B, Tibshirani RJ. An introduction to the Bootstrap. Boston: Chapman & Hall; 1993.
3. Politis DN, Romano JP. A circular block-resampling procedure for stationary data. In: R. L, L. B, editors. Exploring the limits of Bootstrap. New York: John Wiley & Sons; 1992. pp. 263-271.
4. Palmer MR. Measurements and estimates of dose to the lungs during cranial BNCT with the MIT M67 beam. Cambridge: Harvard/MIT BNCT program; 1999.
5. Fryer CJH, Fitzpatrick PJ, Rider WD, Poon P. Radiation pneumonitis: experience following a large single dose of radiation. International Journal of Radiation Oncology Biology Physics 1978;4:931-936.
6. Keane TJ, Van Dyk J, Rider WD. Idiopathic interstitial pneumonia following bone marrow transplantation: the relationship with total body irradiation. International Journal of Radiation Oncology Biology Physics 1981;7:1365-1370.
7. Van Dyk J, Keane TJ, Kan S, Rider WD, Fryer CJ. Radiation pneumonitis following large single dose irradiation: a re-evaluation based on absolute dose to lung. International Journal of Radiation Oncology Biology Physics 1981;7:461-467.
8. McDonald S, Rubin P, Phillips TL, Marks LB. Injury to the lung from cancer therapy: Clinical syndromes, measurable endpoints, and potential scoring systems. Int. J. Radiat. Oncol. Biol. Phys. 1995;31:1187-1203.
9. Imahori Y, Mineura K, Fujii R, Ido T, Ono K. Simulation studies of BNCT for lung cancer [abstract]. The 11th World Congress on Neutron Capture Therapy (ISNCT-11). Waltham, MA; 2004.
10. The Visible Human Project. AnatQuest. U.S. National Library of Medicine; 2004. http://anatquest.nlm.nih.gov/index.html.
11. Riley KJ, Binns PJ, Kiger III WS, Harling OK. Clinical dosimetry of the MIT FCB. In: Sauerwein W, Moss RL, Wittig A, editors. Research and development in Neutron Capture Therapy. Proceedings of The 10th International Congress on Neutron Capture Therapy for Cancer. Essen, Germany: Monduzzi Editore; 2002. pp. 347-351.
12. Kiger III WS, Lu XQ, Harling OK, Riley KJ, Binns PJ, Kaplan J, Patel H, Zamenhof RG, Shibata Y, Kaplan ID, Busse PM, Palmer MR. Preliminary treatment planning and dosimetry for a clinical trial of neutron capture therapy using a fission converter epithermal neutron beam. Appl Radiat Isot 2004;61:1075-1081.
13. Kiger III WS, Micca PL, Morris GM, Coderre JA. Boron microquantification in oral muscosa and skin following administration of a neutron capture therapy agent. Radiat Prot Dosimetry 2002;99:409-412.
14. Chandra S, Lorey ID, Smith DR. Quantitative subcellular secondary ion mass spectrometry (SIMS) imaging of boron-10 and boron-11 isotopes in the same cell delivered by two

combined BNCT drugs: in vitro studies on human glioblastoma T98G cells. Radiat Res 2002;157:700-710.

APPENDIX A

Error Analysis of the Dosimetry and the Dose Uncertainty from Rat Positioning during Irradiations

A.1 Equations for uncertainty estimation

The basic uncertainties used for uncertainty estimation are listed as:

	Uncertainty detected	Uncertainty Used
x-ray (D_x)	2%	3%
Neutron flux (D_x)	6%	7%
Photon dose (D_γ)	6%	7%
BPA	1% (counting)	5%

The detected uncertainty was measured over time during the lung irradiations with x-rays or neutrons. These uncertainties were expanded to 'used' uncertainties, since not all factors were detected. The uncertainties for x-ray, neutron dose, photon dose were beam fluctuations measured over time during rat lung irradiations. The detected uncertainty listed here for BPA, 1%, is the estimate of the counting errors usually obtained for 0.5 ml blood sample with about 20 μg of ^{10}B present in each gram of blood.

The Equations used for error propagations are as the following:

1) Basic equations:

$$Z = \frac{X}{Y}, or, Z = XY;$$

$$\frac{\sigma_Z}{Z} = \sqrt{\left(\frac{\sigma_X}{X}\right)^2 + \left(\frac{\sigma_Y}{Y}\right)^2}; (relative\ error)$$

$$\sigma_Z = Z \times \sqrt{\left(\frac{\sigma_X}{X}\right)^2 + \left(\frac{\sigma_Y}{Y}\right)^2}; (absolute\ error)$$

$$Z = X + Y;$$

$$\sigma_Z = \sqrt{(\sigma_X)^2 + (\sigma_Y)^2}; (absolute\ error)$$

2) Beam dose and the dose of neutron plus BPA, assuming that the beam dose was composed of 20% neutron dose, and 80% photon dose, and the dose of neutron plus BPA was composed of 50% ^{10}B dose, and 50% beam dose.

$$D_{n\_beam} = D_n + D_\gamma;$$

$$\sigma_{n\_beam} = \sqrt{\sigma_n^2 + \sigma_\gamma^2}; (absolute\ error)$$

$$\left(\frac{\sigma_{n\_beam}}{D_{n\_beam}}\right) = \sqrt{\left(\frac{\sigma_n}{D_{n\_beam}}\right)^2 + \left(\frac{\sigma_\gamma}{D_{n\_beam}}\right)^2} = \sqrt{\left(\frac{\sigma_n}{D_n}\right)^2 \left(\frac{D_n}{D_{n\_beam}}\right)^2 + \left(\frac{\sigma_\gamma}{D_\gamma}\right)^2 \left(\frac{D_\gamma}{D_{n\_beam}}\right)^2}$$

$$= \sqrt{\left(\frac{\sigma_n}{D_n}\right)^2 (0.2)^2 + \left(\frac{\sigma_\gamma}{D_\gamma}\right)^2 (0.8)^2} = 6\%; (relative\ error)$$

$$D_B = N \times C_{BPA}; (C_{BPA} : BPA\ concentration)$$

$$\left(\frac{\sigma_B}{D_B}\right) = \sqrt{\left(\frac{\sigma_n}{N}\right)^2 + \left(\frac{\sigma_{BPA}}{C_{BPA}}\right)^2} = 9\%; relative\ error$$

$$D_{N+BPA} = D_{n\_beam} + D_B;$$

$$\left(\frac{\sigma_{N+BPA}}{D_{N+BPA}}\right) = \sqrt{\left(\frac{\sigma_B}{D_{N+BPA}}\right)^2 + \left(\frac{\sigma_{n\_beam}}{D_{N+BPA}}\right)^2} = \sqrt{\left(\frac{\sigma_B}{D_B}\right)^2 \left(\frac{D_B}{D_{N+BPA}}\right)^2 + \left(\frac{\sigma_{n\_beam}}{D_{n\_beam}}\right)^2 \left(\frac{D_{n\_beam}}{D_{N+BPA}}\right)^2}$$

$$= \sqrt{\left(\frac{\sigma_B}{D_B}\right)^2 (0.5)^2 + \left(\frac{\sigma_{n\_beam}}{D_{n\_beam}}\right)^2 (0.5)^2} = 5\%; relative\ error$$

Propagated errors of the ED_{50} (or some other endpoints, e.g., ED_{10}) values using fitting errors and dose errors:

$$\left(\frac{\sigma_{ED50(x-ray)}}{ED_{50(x-ray)}}\right)=\sqrt{\left(\frac{\sigma_{ED50(x-ray\_fitting)}}{ED_{50(x-ray)}}\right)^2+\left(\frac{\sigma_{x-ray}}{D_{x-ray}}\right)^2};\ relative\ error$$

$$\left(\frac{\sigma_{ED50(n\_beam)}}{ED_{50(n\_beam)}}\right)=\sqrt{\left(\frac{\sigma_{ED50(n\_beam\_fitting)}}{ED_{50(n\_beam-fitting)}}\right)^2+\left(\frac{\sigma_{n\_beam}}{D_{n\_beam}}\right)^2};\ relative\ error$$

$$\left(\frac{\sigma_{ED50(N+BPA)}}{ED_{50(N+BPA)}}\right)=\sqrt{\left(\frac{\sigma_{ED50(N+BPA\_fitting)}}{ED_{50(N+BPA\_fitting)}}\right)^2+\left(\frac{\sigma_{N+BPA}}{D_{N+BPA}}\right)^2};\ relative\ error$$

Errors of the ratios of the ED_{50}s:

$$Ratio\ of\ ED_{50(x-ray)}\ to\ ED_{50(n\_beam)}:\sigma_{relative(x-ray/n\_beam)}=\sqrt{\left(\frac{\sigma_{ED50(x-ray)}}{ED_{50(x-ray)}}\right)^2+\left(\frac{\sigma_{ED50(n\_beam)}}{ED_{50(n\_beam)}}\right)^2};$$

$$Ratio\ of\ ED_{50(x-ray)}\ to\ ED_{50(N+BPA)}:\sigma_{relative(x-ray/N+BPA)}=\sqrt{\left(\frac{\sigma_{ED50(x-ray)}}{ED_{50(x-ray)}}\right)^2+\left(\frac{\sigma_{ED50(N+BPA)}}{ED_{50(N+BPA)}}\right)^2};$$

Error of the RBE for neutron beam only (n+γ):

$$\left(\frac{\sigma_{w(n\_beam)}}{W_{n\_beam}}\right)=\sigma_{relative(x-ray/n\_beam)}=\sqrt{\left(\frac{\sigma_{ED50(x-ray)}}{ED_{50(x-ray)}}\right)^2+\left(\frac{\sigma_{ED50(n\_beam)}}{ED_{50(n\_beam)}}\right)^2};$$

Error of the RBE for thermal neutron only:

$$W_n=\frac{\frac{ED_{50(x-ray)}}{ED_{50(n\_beam)}}-0.8}{0.2}=5\times\frac{ED_{50(x-ray)}}{ED_{50(n\_beam)}}-4;$$

$$\sigma_{w\_n}=5\times\sigma_{relative(x-ray/n\_beam)}\times\left(\frac{ED_{50(x-ray)}}{ED_{50(n\_beam)}}\right)$$

$$=5\times\sqrt{\left(\frac{\sigma_{ED50(x-ray)}}{ED_{50(x-ray)}}\right)^2+\left(\frac{\sigma_{ED50(n\_beam)}}{ED_{50(n\_beam)}}\right)^2}\times\left(\frac{ED_{50(x-ray)}}{ED_{50(n\_beam)}}\right);\ absolute\ error$$

Error of the CBE for the BPA (during the early phase or the late phase):

$$W_B = \frac{\frac{ED_{50(x-ray)}}{ED_{50(N+BPA)}} - 0.5 \times W_{n\_beam}}{0.5} = 2 \times \frac{ED_{50(x-ray)}}{ED_{50(N+BPA)}} - W_{n\_beam};$$

$$\sigma_{w\_B} = 2 \times \sigma_{relative(x-ray/N+BPA)} \times \left(\frac{ED_{50(x-ray)}}{ED_{50(N+BPA)}} \right)$$

$$= 2 \times \sqrt{\left(\frac{\sigma_{ED50(x-ray)}}{ED_{50(x-ray)}} \right)^2 + \left(\frac{\sigma_{ED50(N+BPA)}}{ED_{50(N+BPA)}} \right)^2} \times \left(\frac{ED_{50(x-ray)}}{ED_{50(N+BPA)}} \right); \textit{absolute error.}$$

A.2 Results of the uncertainties

Table A.1 Summary of the measured end doses and their standard deviations. (B.R.: breathing rate; Hist.: histology scoring.)

	ED_{50} with B.R. (Gy)		ED_{10} with B.R. (Gy)		ED_{90} with B.R. (Gy)		ED_{50} with Hist. (Gy)	
	Dose	SD	Dose	SD	Dose	SD	Dose	SD
x-ray	11.5	0.4	11.0	0.3	11.9	0.4	11.5	0.5
N beam (n+γ)	9.2	0.5	8.8	0.6	9.7	0.6	9.4	0.6
N+BPA early	8.7	0.6	6.7	0.6	11.0	0.8	-	-
N+BPA late	6.7	0.4	5.1	0.5	8.2	0.6	7.3	0.4

Table A.2 Summary of the measured weighting factors and their standard deviations.

	At ED_{50} with B.R.		At ED_{10} with B.R.		At ED_{90} with B.R.		At ED_{50} with Hist.	
	w	SD	w	SD	w	SD	w	SD
N beam (n+γ)	1.24	0.08	1.25	0.09	1.23	0.09	1.22	0.09
N only	2.2	0.4	2.3	0.5	2.2	0.4	2.1	0.5
N+BPA early	1.4	0.2	2.2	0.3	1.0	0.2	-	-
N+BPA late	2.3	0.3	3.6	0.5	1.7	0.2	1.9	0.2

A.3 Positioning errors

Uncertainties of dose delivered to the lung in the neutron beam only irradiation were estimated in MCNP, with the two rat models positioned 0.5 cm off to different directions, and also with only one rat model in the field. Maximum discrepancies of 23% for local neutron dose

rate and 11% for local beam dose rate were observed from the DVH calculations. However, the maximum discrepancies for mean lung neutron dose rate and for mean lung total dose rate were within 5%. As the mean lung dose was used to predict the rat lung response from radiation damage, the final lung responses of the animal were not significantly influenced by the positioning errors during the lung irradiation. Also since the positioning errors are random errors, they were not propagated in the total error analysis. The calculated DVHs of the rat lung irradiation with different positioning are plotted in Fig. A.1.

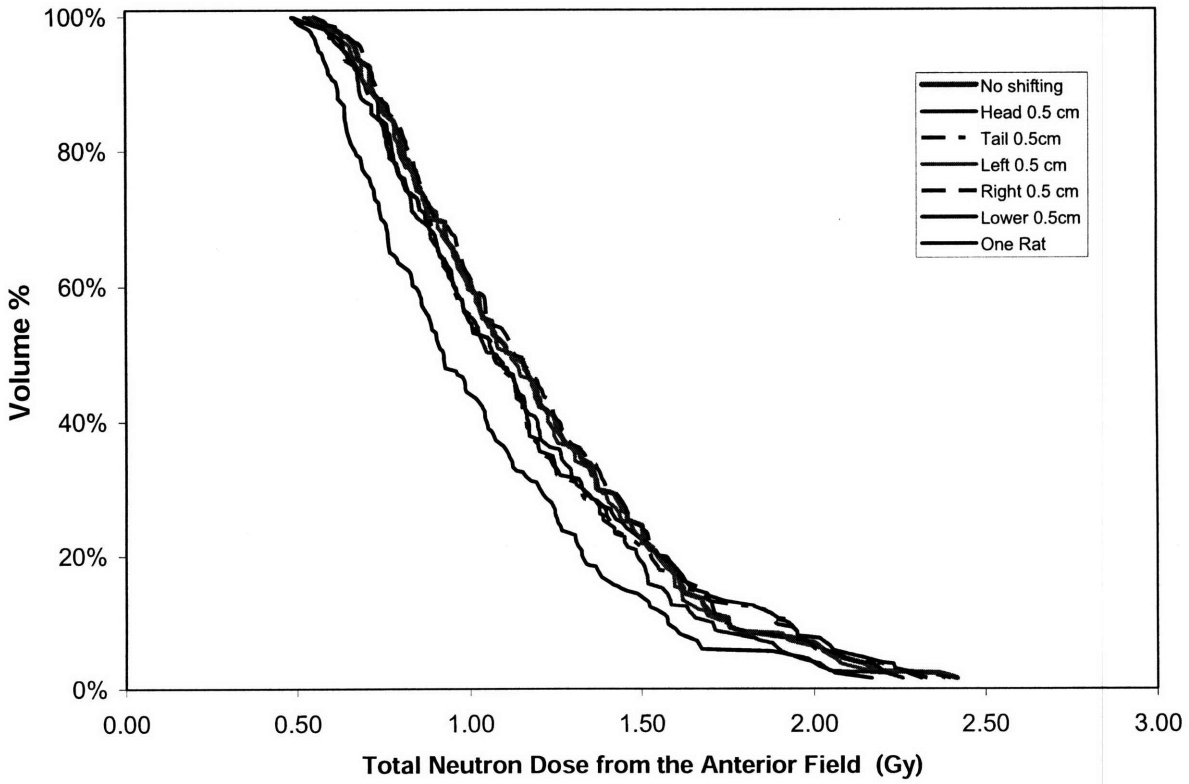

Fig. A.1 The calculated DVHs with different positioning of the rats.

APPENDIX B

Rat Breathing Rate and Weight Measurements after Lung Irradiation

In this appendix, breathing rate and weight measurements of individual rats are plotted. The Y axis in all the figures is used for both breathing rate and weight. Breathing rates are represented with diamonds and the weights are represented with squares. The control mean and 20% above is represented with the shaded area.

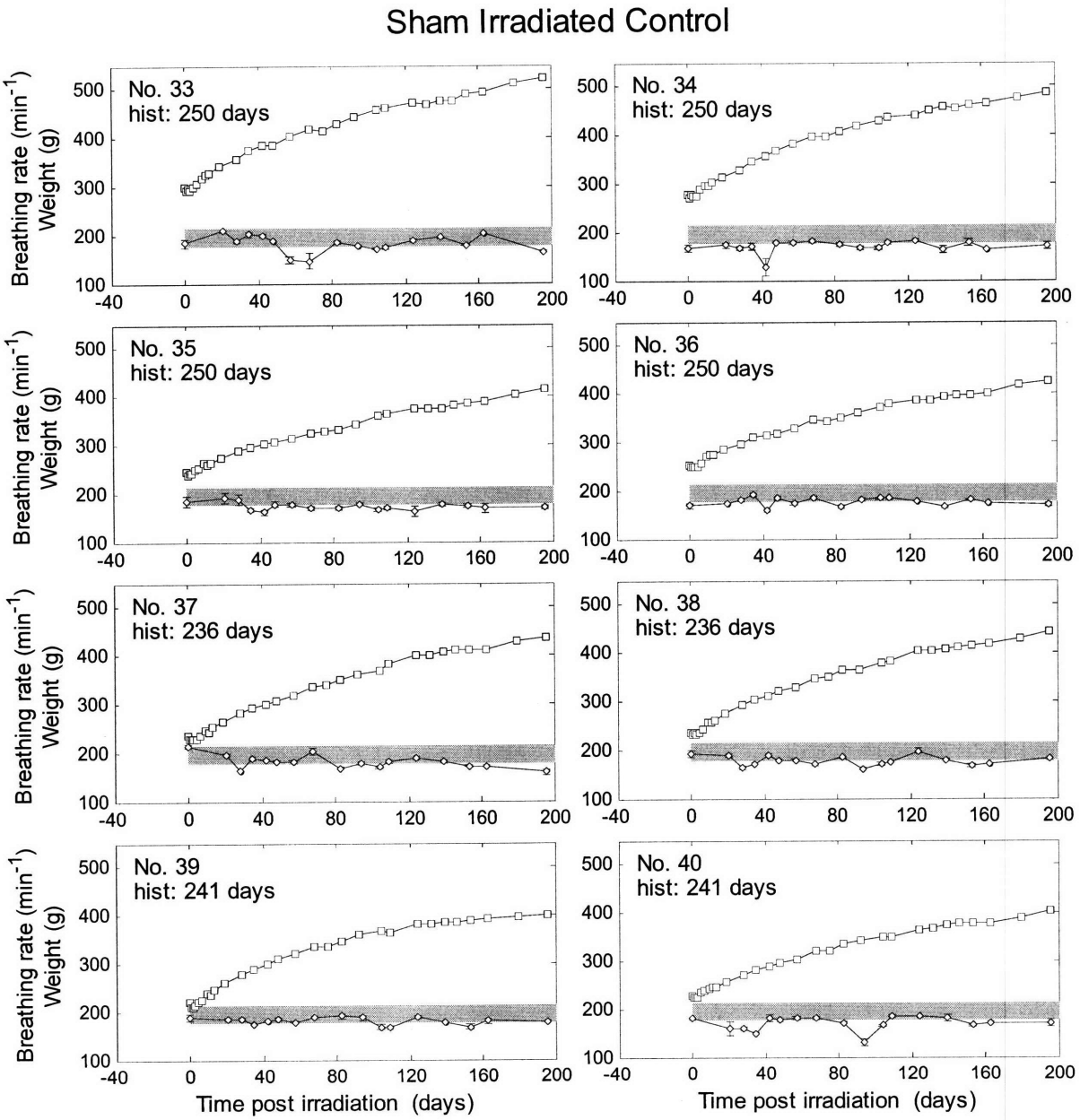

Fig. B.1 Breathing rate and weight of the control group.

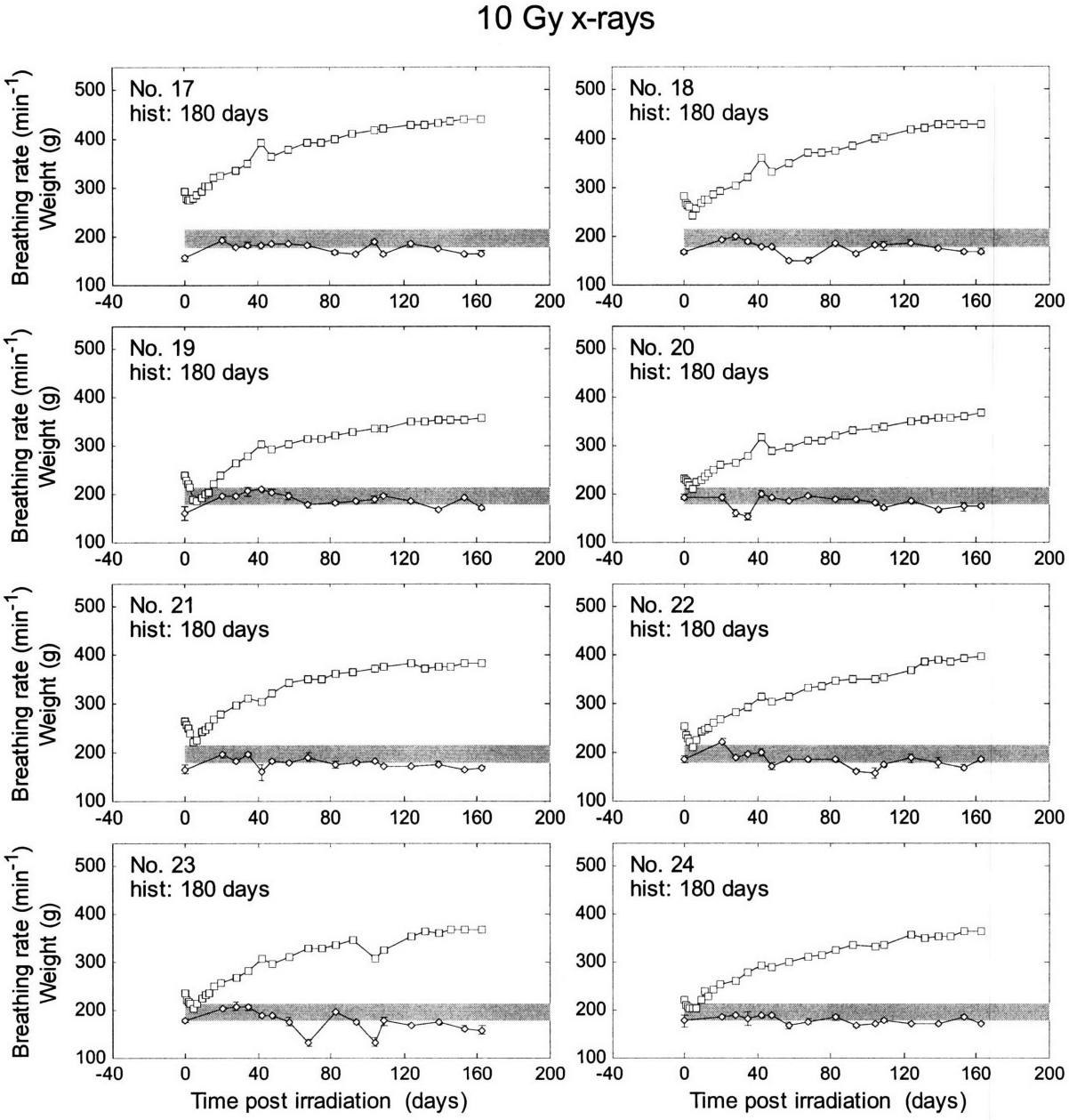

Fig. B.2 Breathing rate and weight after lung irradiation of 10 Gy x-rays.

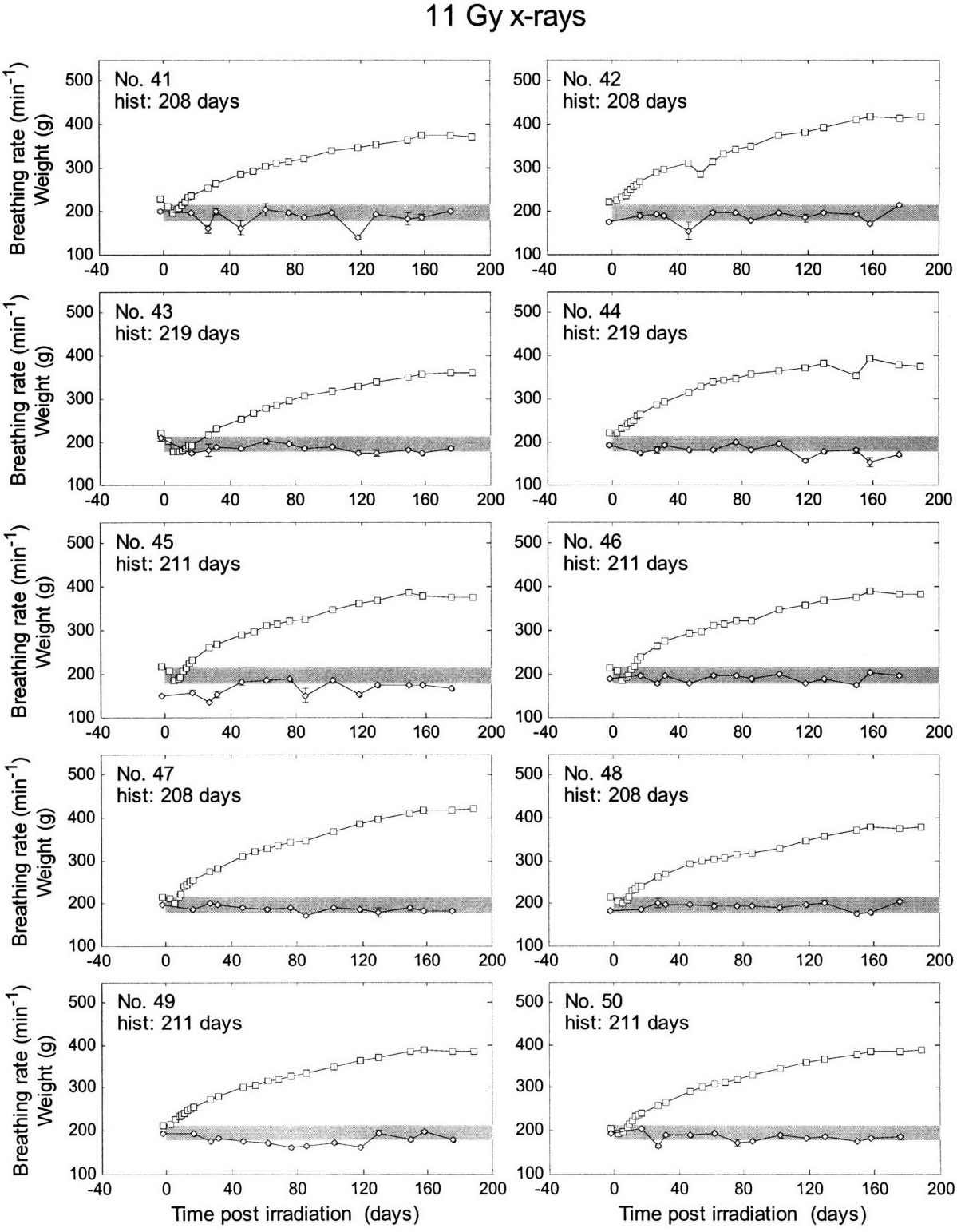

Fig. B.3 Breathing rate and weight after lung irradiation of 11 Gy x-rays.

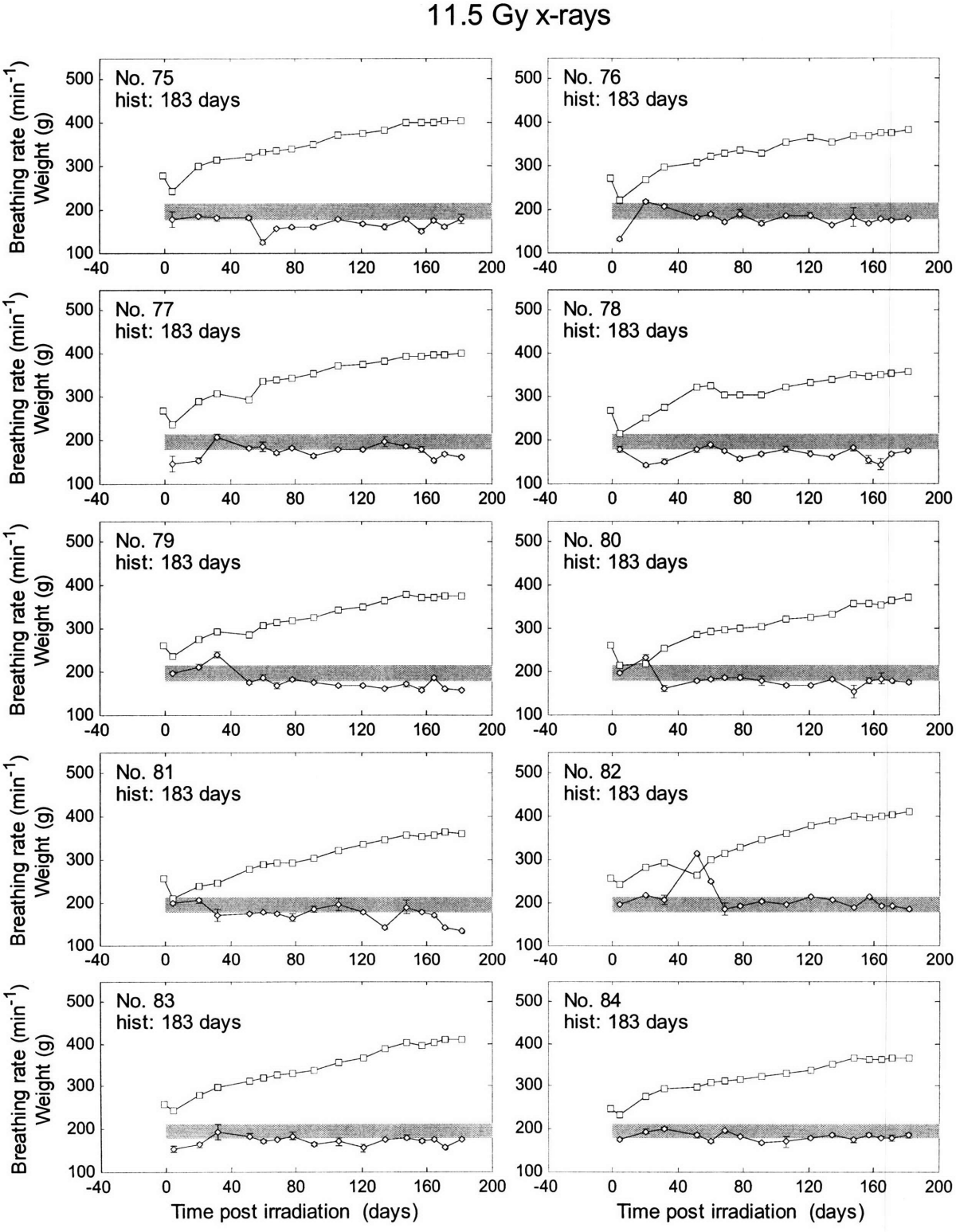

Fig. B.4 Breathing rate and weight after lung irradiation of 11.5 Gy x-rays.

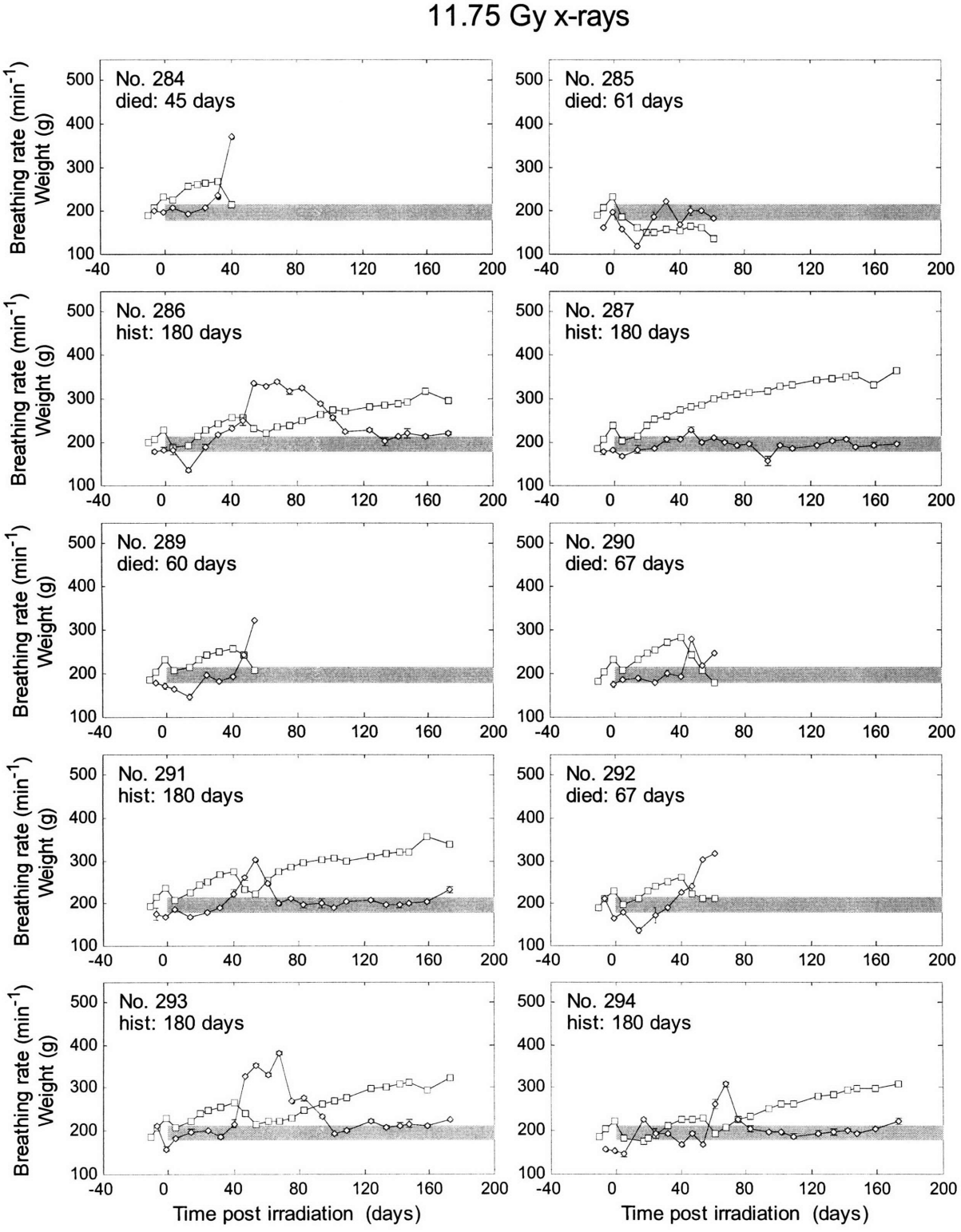

Fig. B.5 Breathing rate and weight after lung irradiation of 11.75 Gy x-rays.

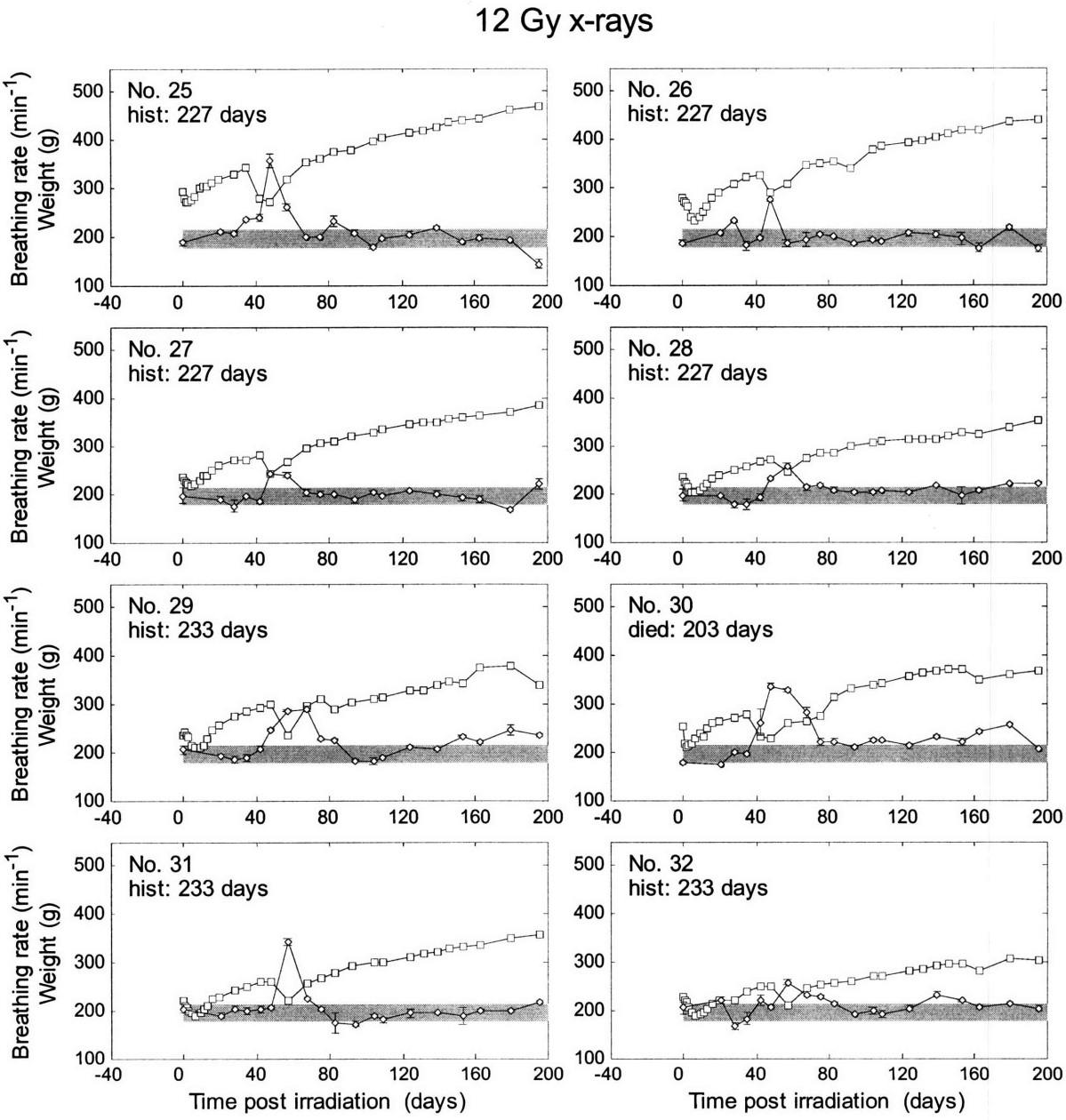

Fig. B.6 Breathing rate and weight after lung irradiation of 12 Gy x-rays.

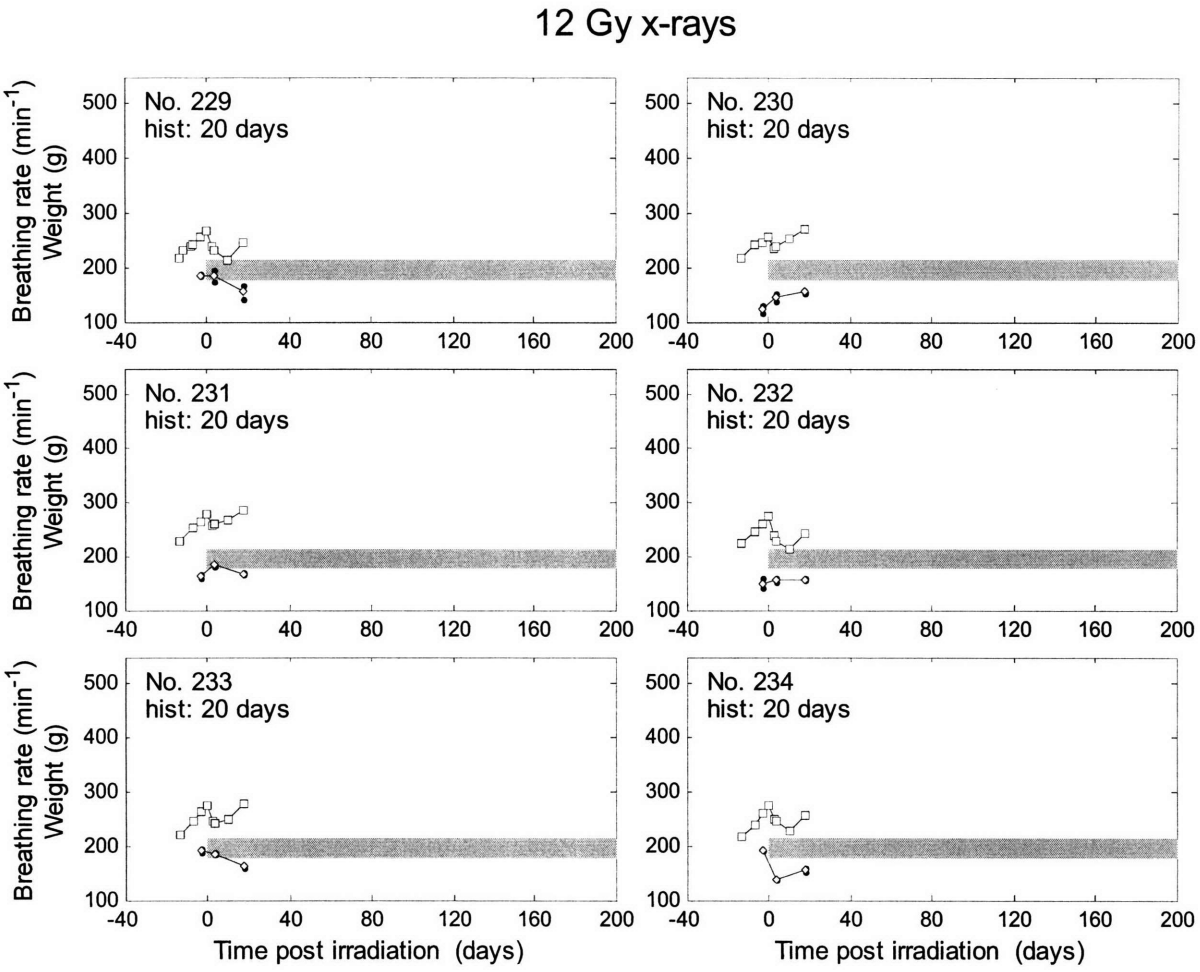

Fig. B.7 Breathing rate and weight after lung irradiation of 12 Gy x-rays.

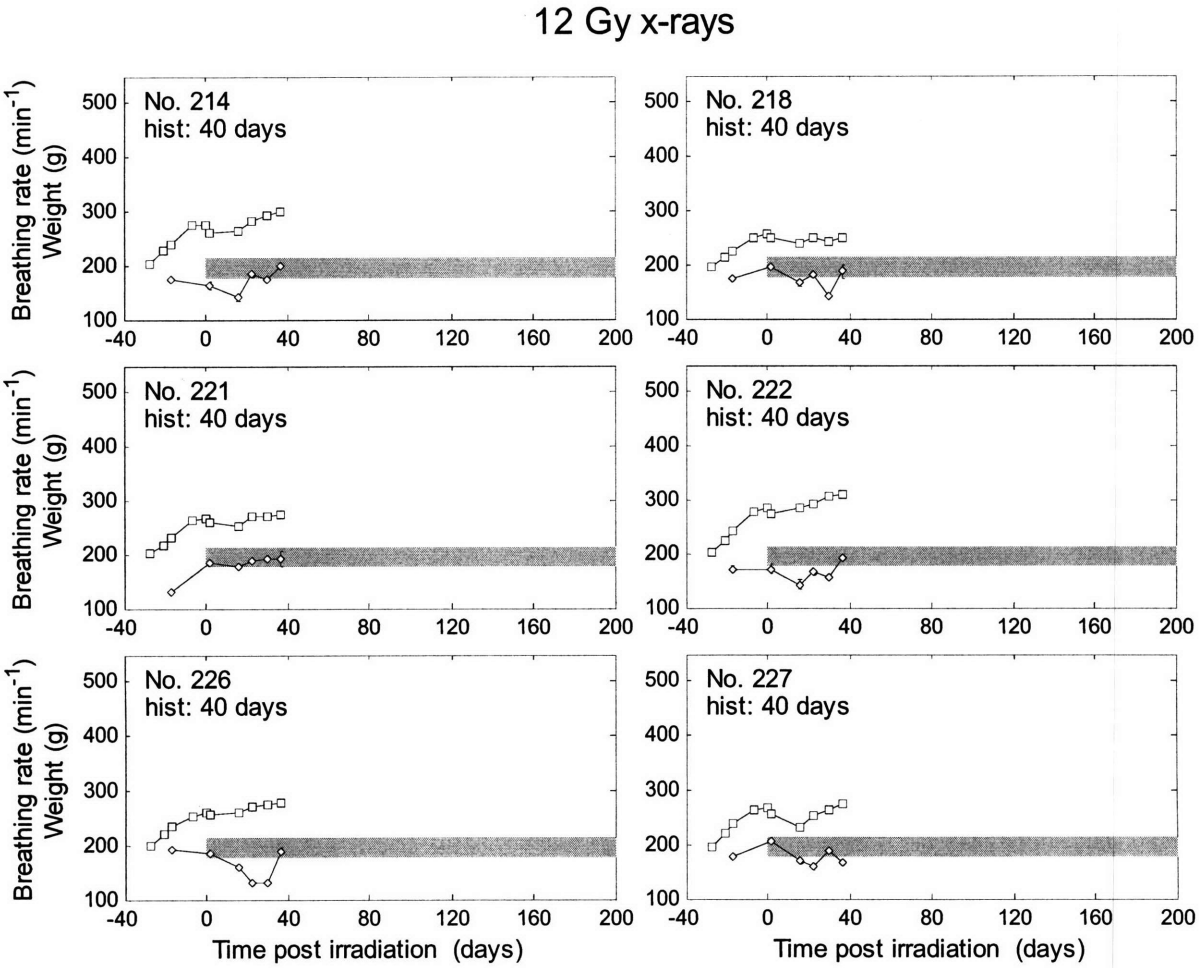

Fig. B.8 Breathing rate and weight after lung irradiation of 12 Gy x-rays.

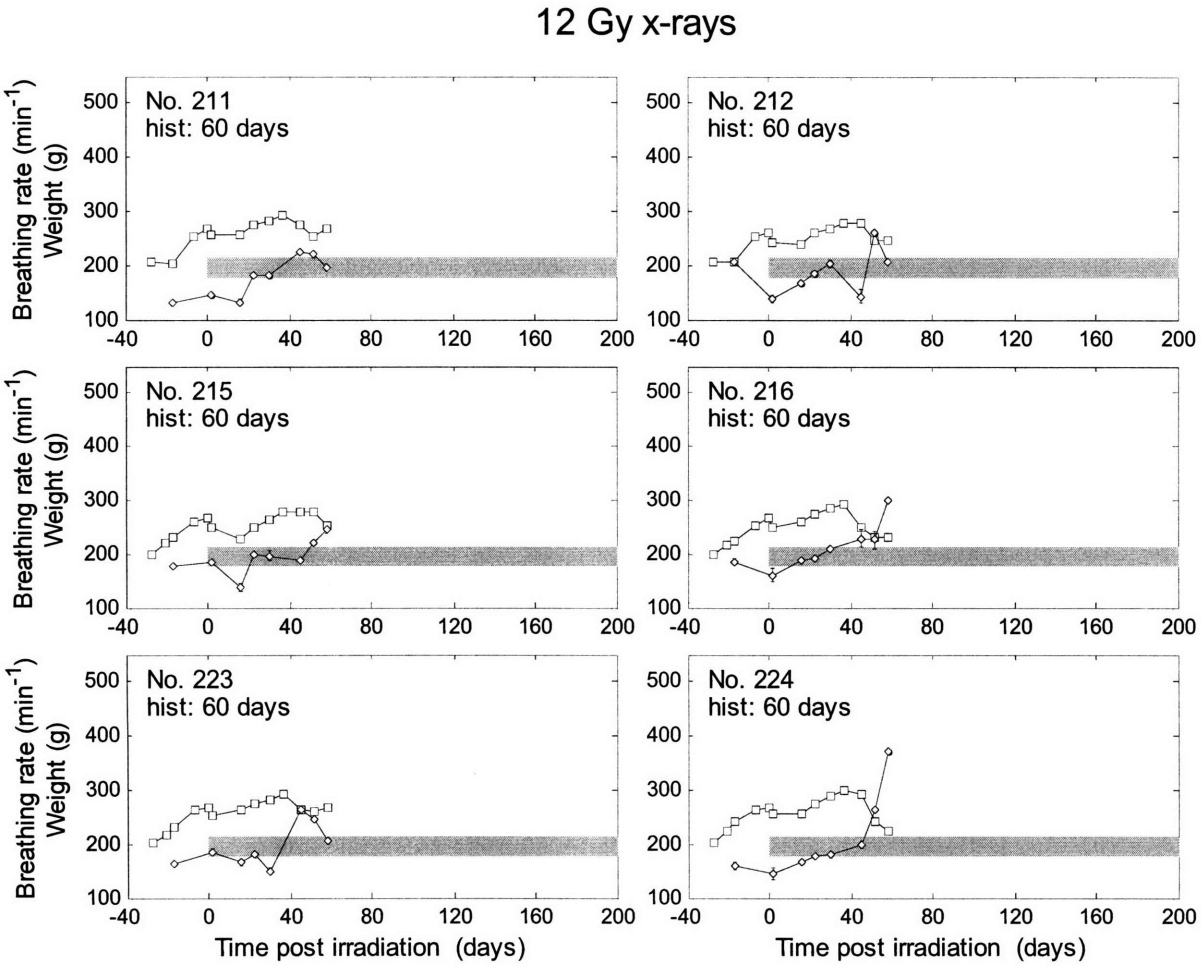

Fig. B.9 Breathing rate and weight after lung irradiation of 12 Gy x-rays.

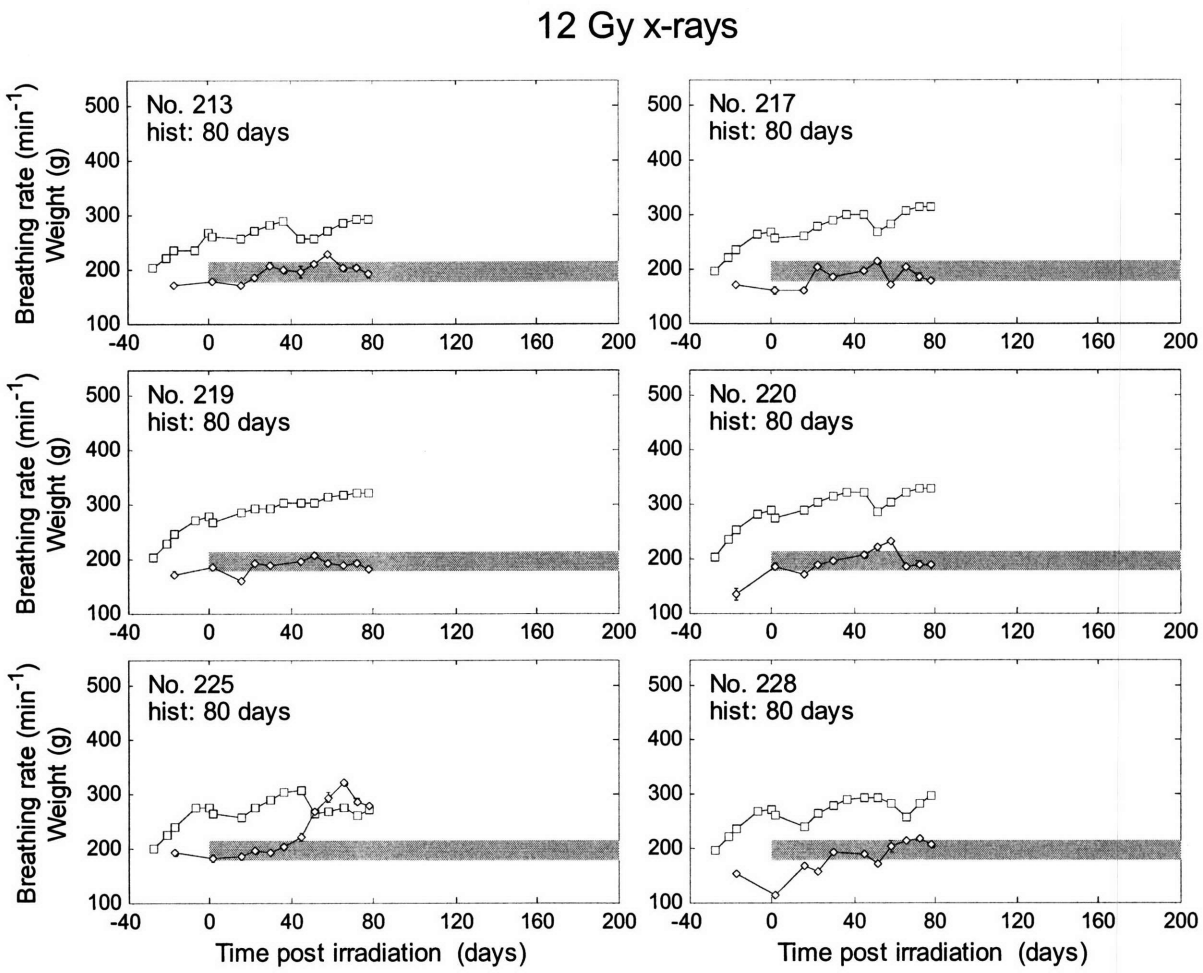

Fig. B.10 Breathing rate and weight after lung irradiation of 12 Gy x-rays.

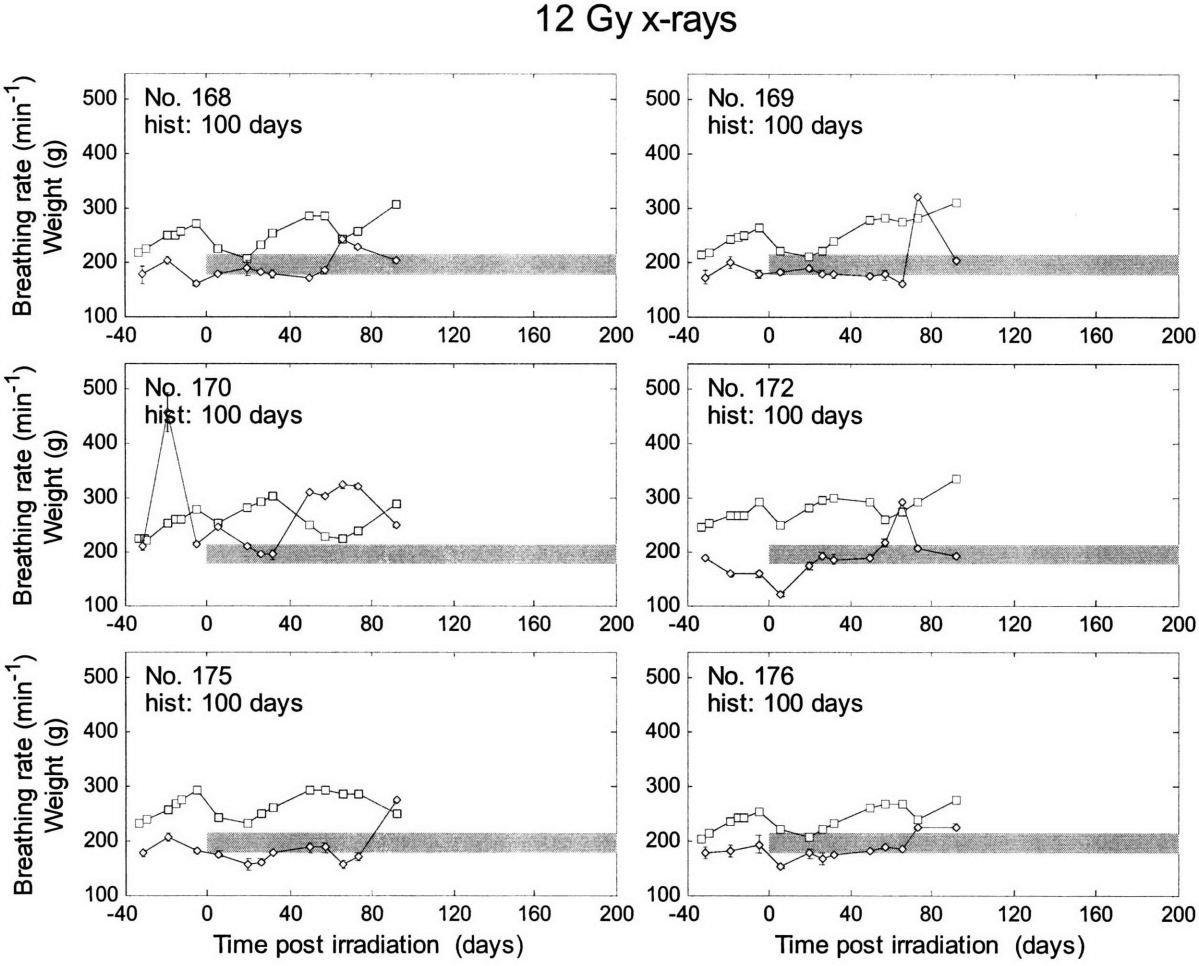

Fig. B.11 Breathing rate and weight after lung irradiation of 12 Gy x-rays.

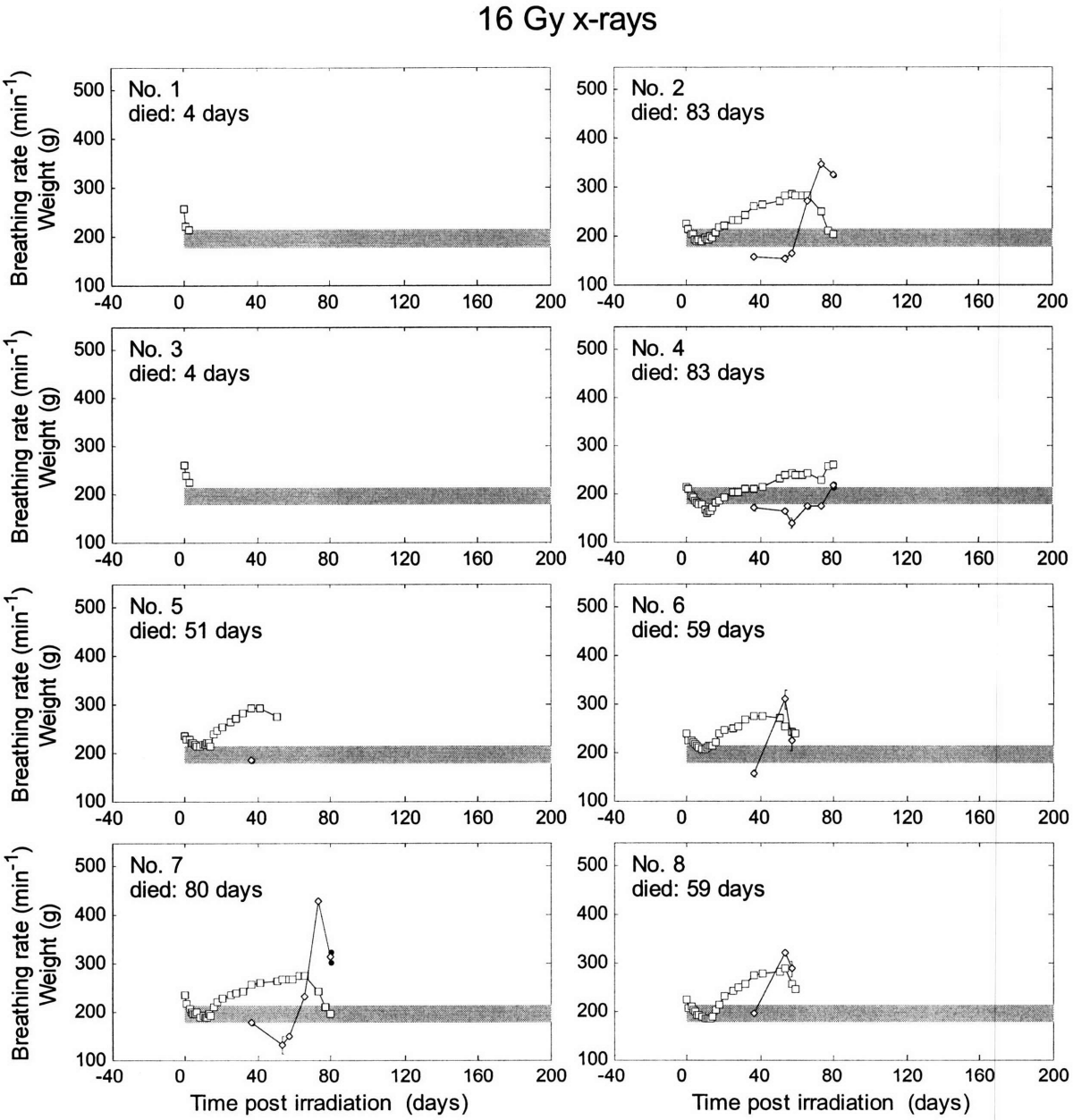

Fig. B.12 Breathing rate and weight after lung irradiation of 16 Gy x-rays.

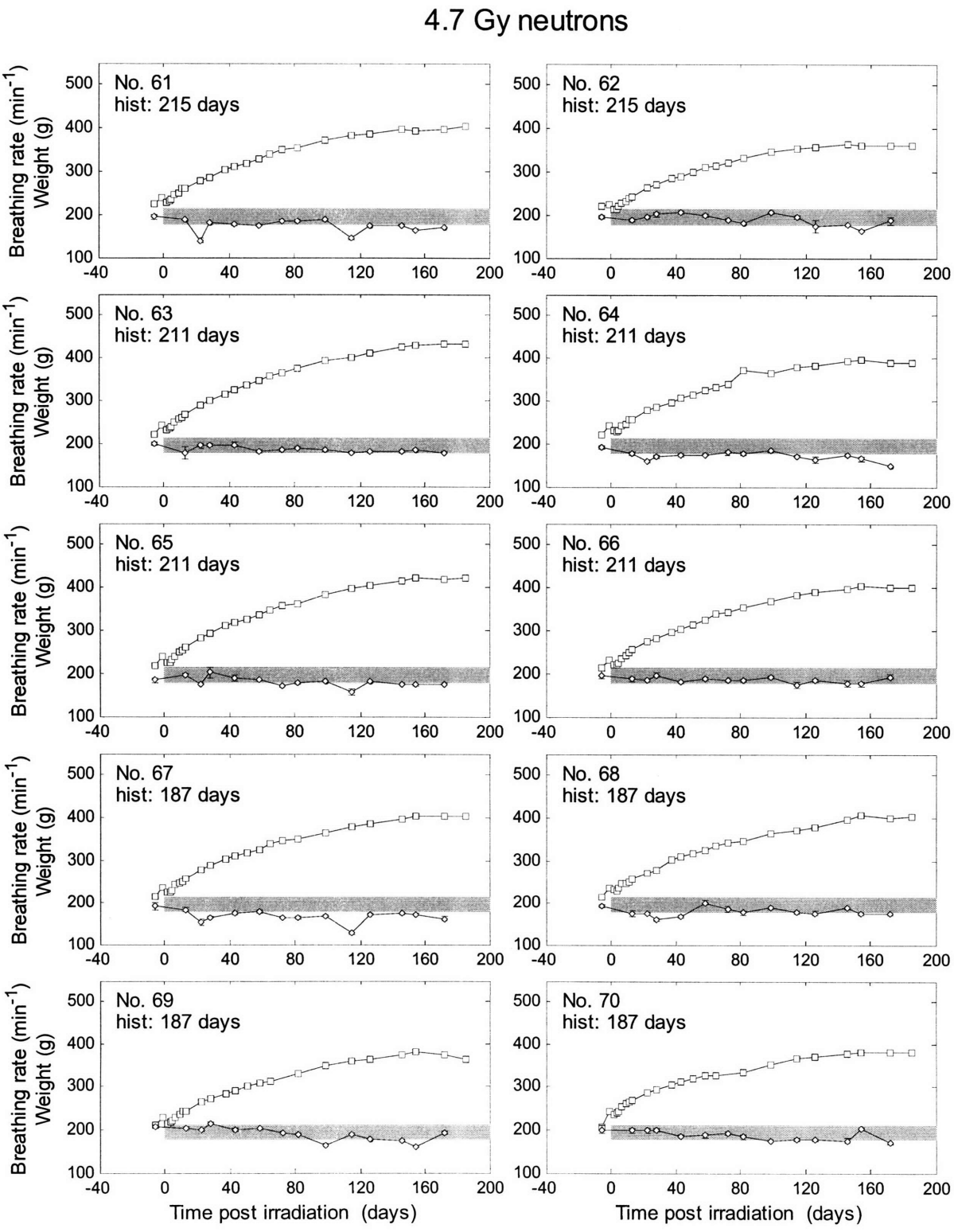

Fig. B.13 Breathing rate and weight after lung irradiation of 4.7 Gy neutrons.

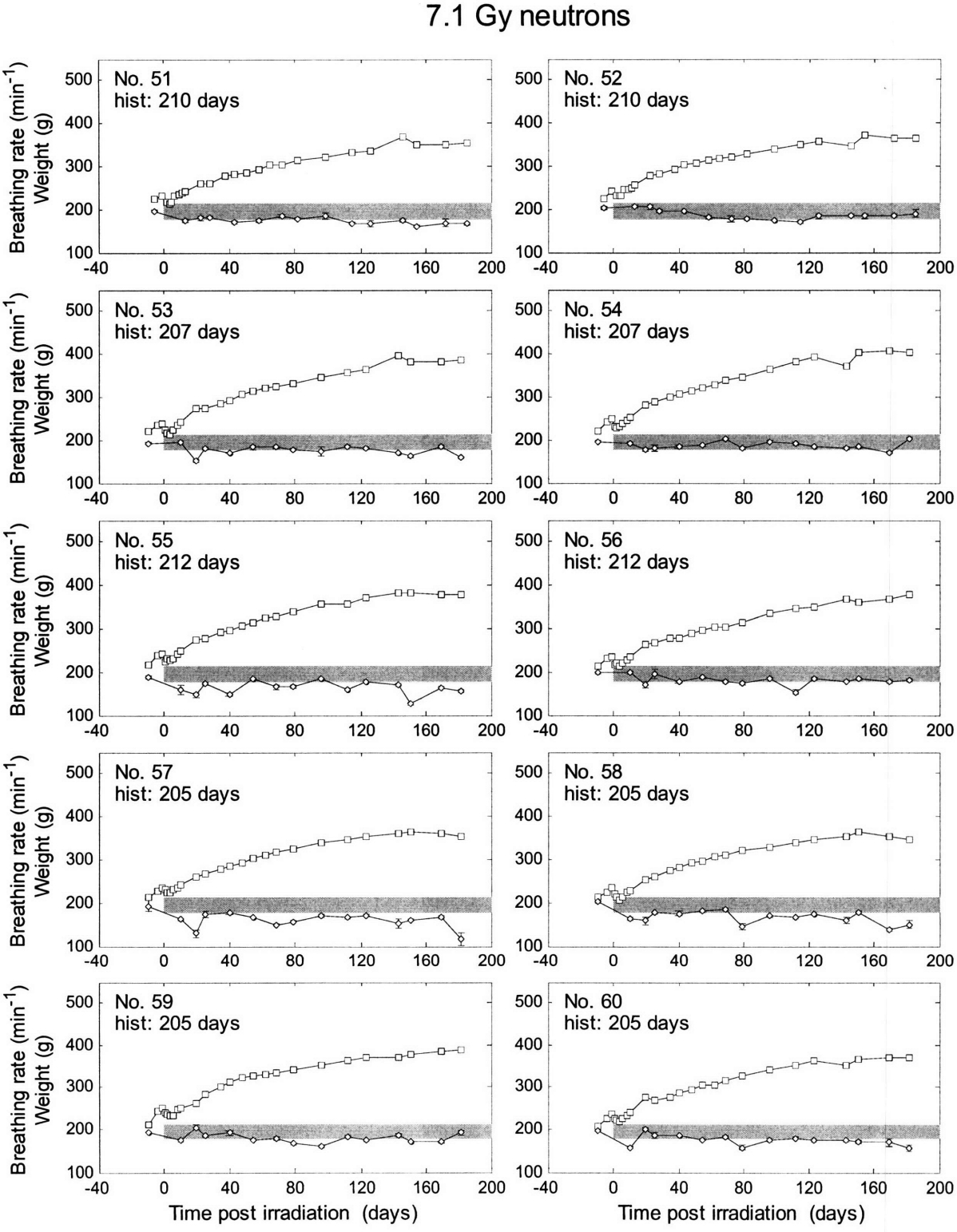

Fig. B.14 Breathing rate and weight after lung irradiation of 7.1 Gy neutrons.

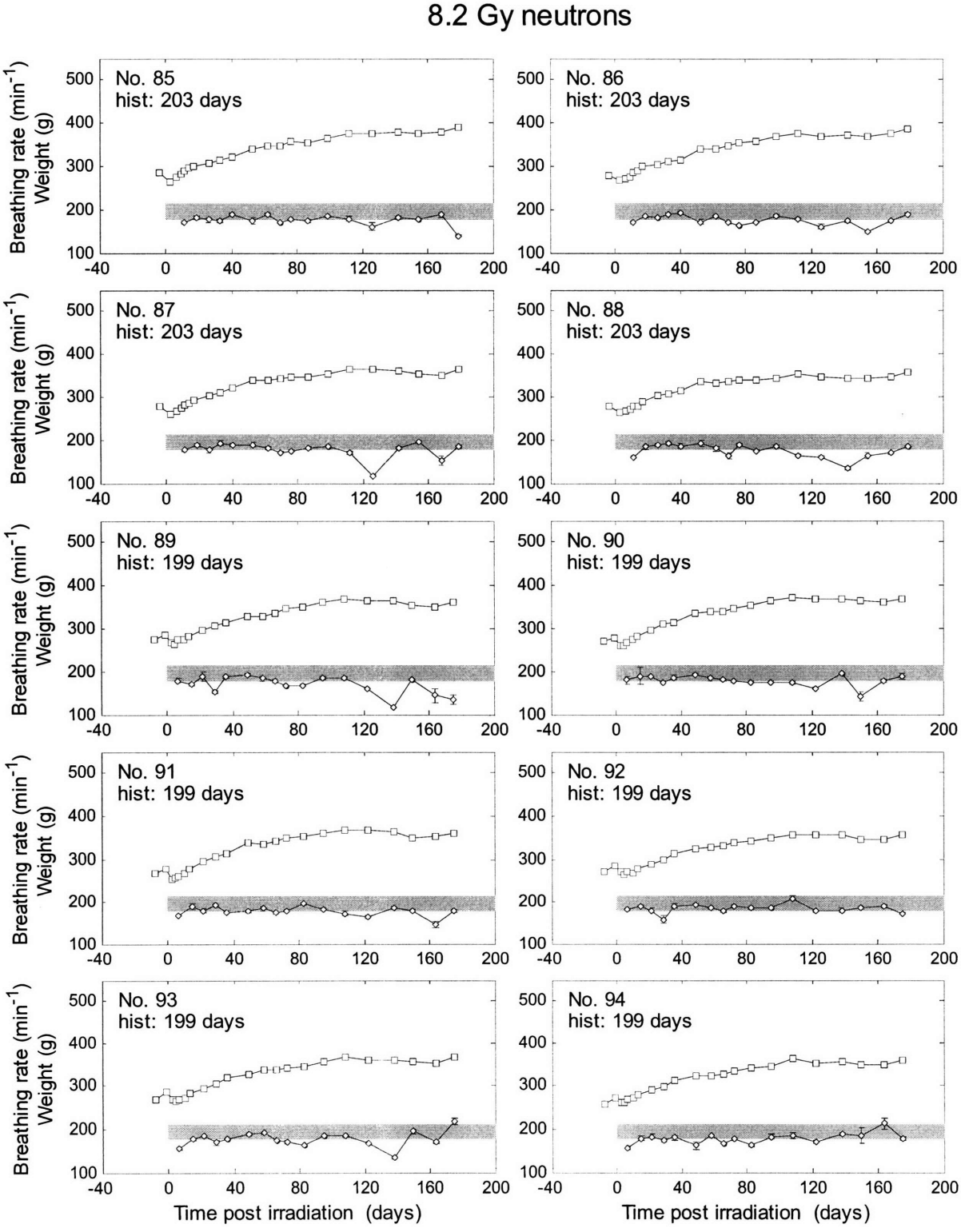

Fig. B.15 Breathing rate and weight after lung irradiation of 8.2 Gy neutrons.

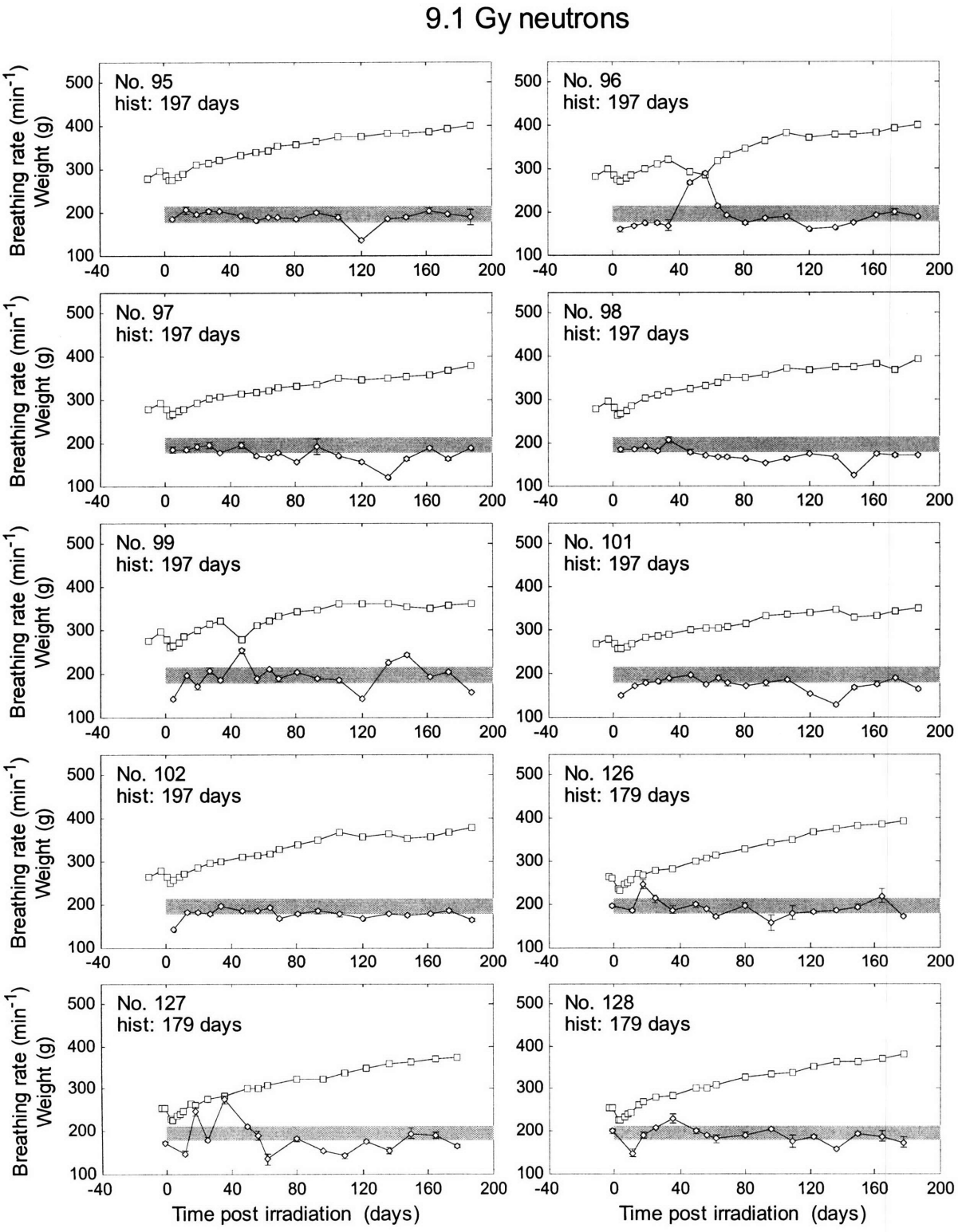

Fig. B.16 Breathing rate and weight after lung irradiation of 9.1 Gy neutrons.

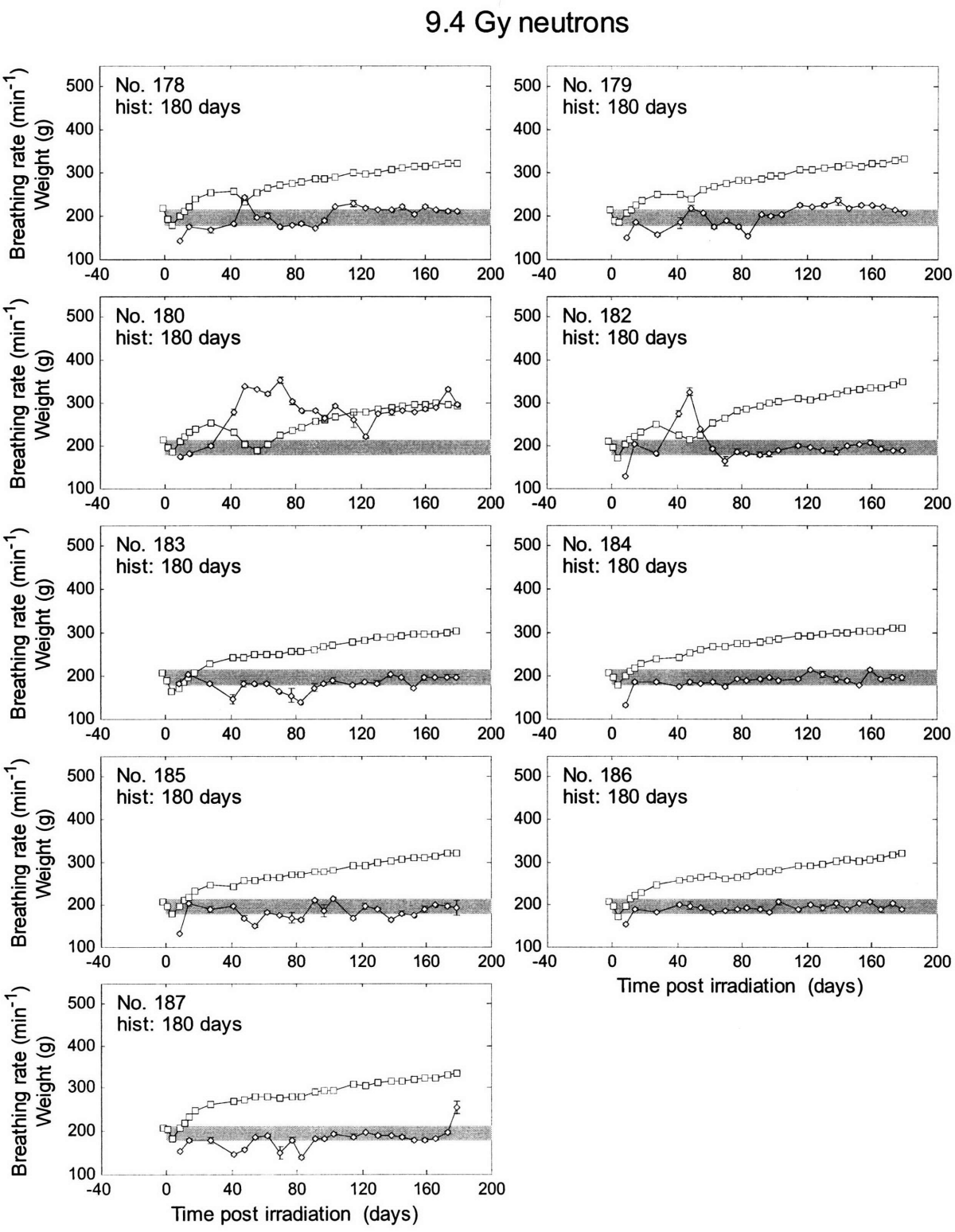

Fig. B.17 Breathing rate and weight after lung irradiation of 9.4 Gy neutrons.

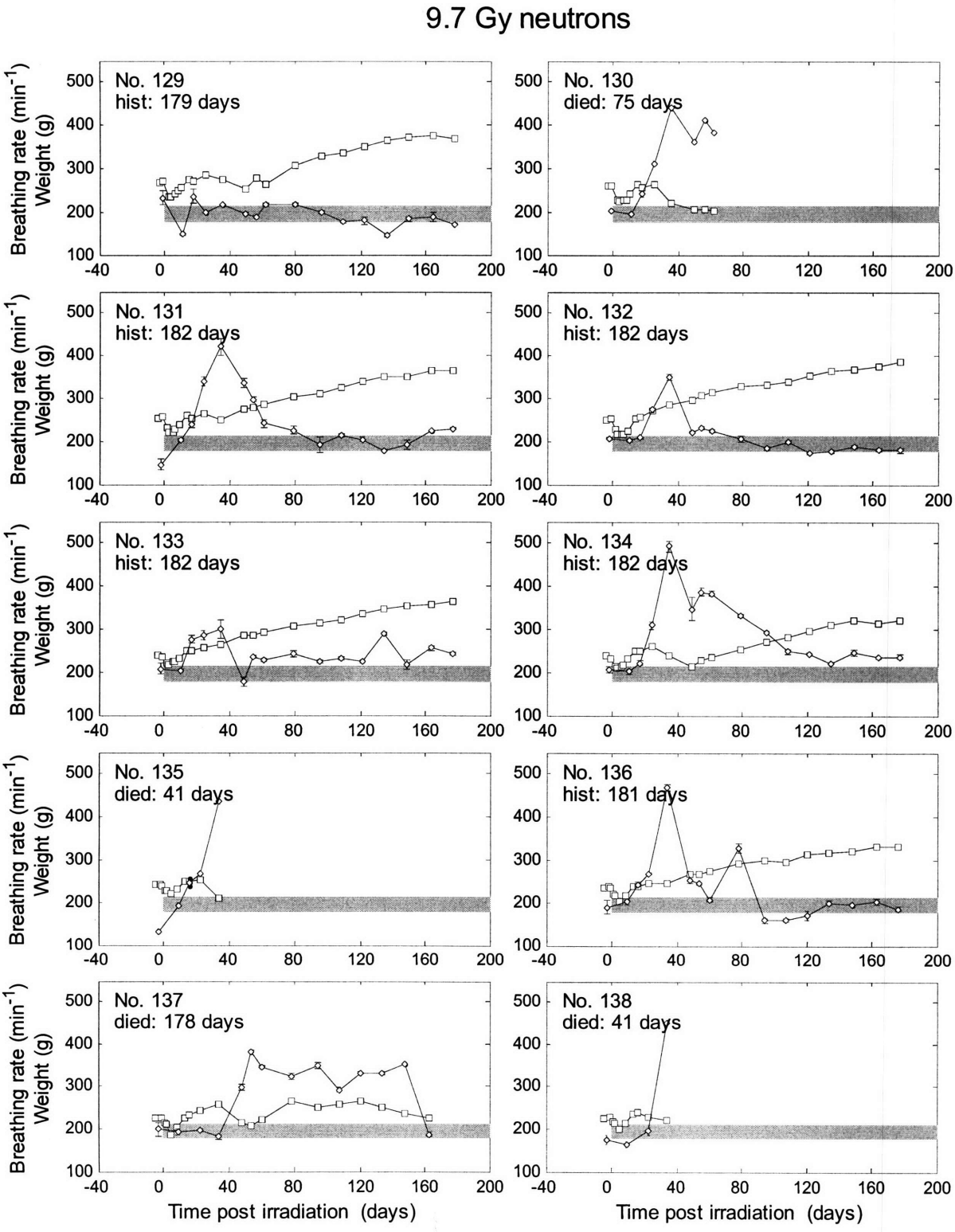

Fig. B.18 Breathing rate and weight after lung irradiation of 9.7 Gy neutrons.

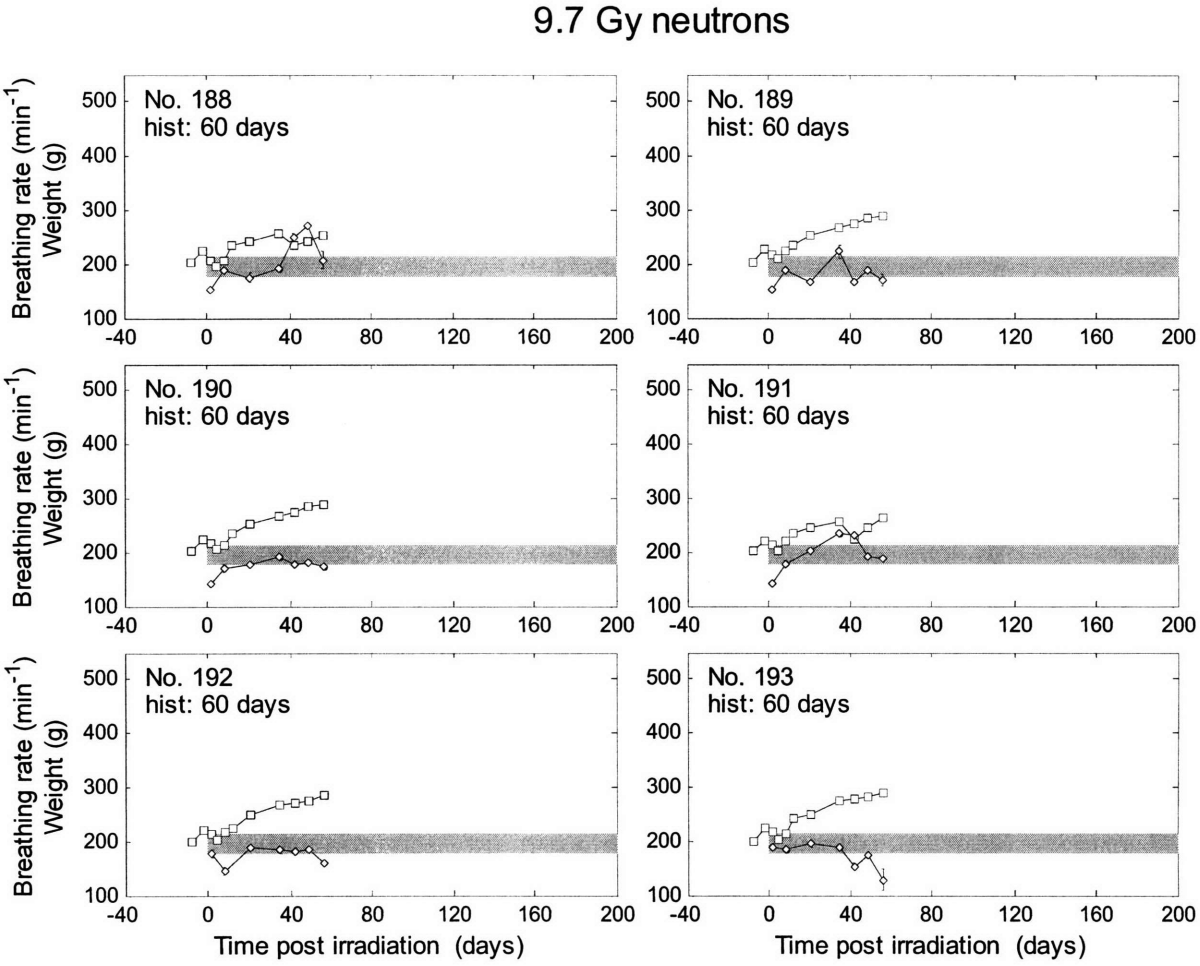

Fig. B.19 Breathing rate and weight after lung irradiation of 9.7 Gy neutrons.

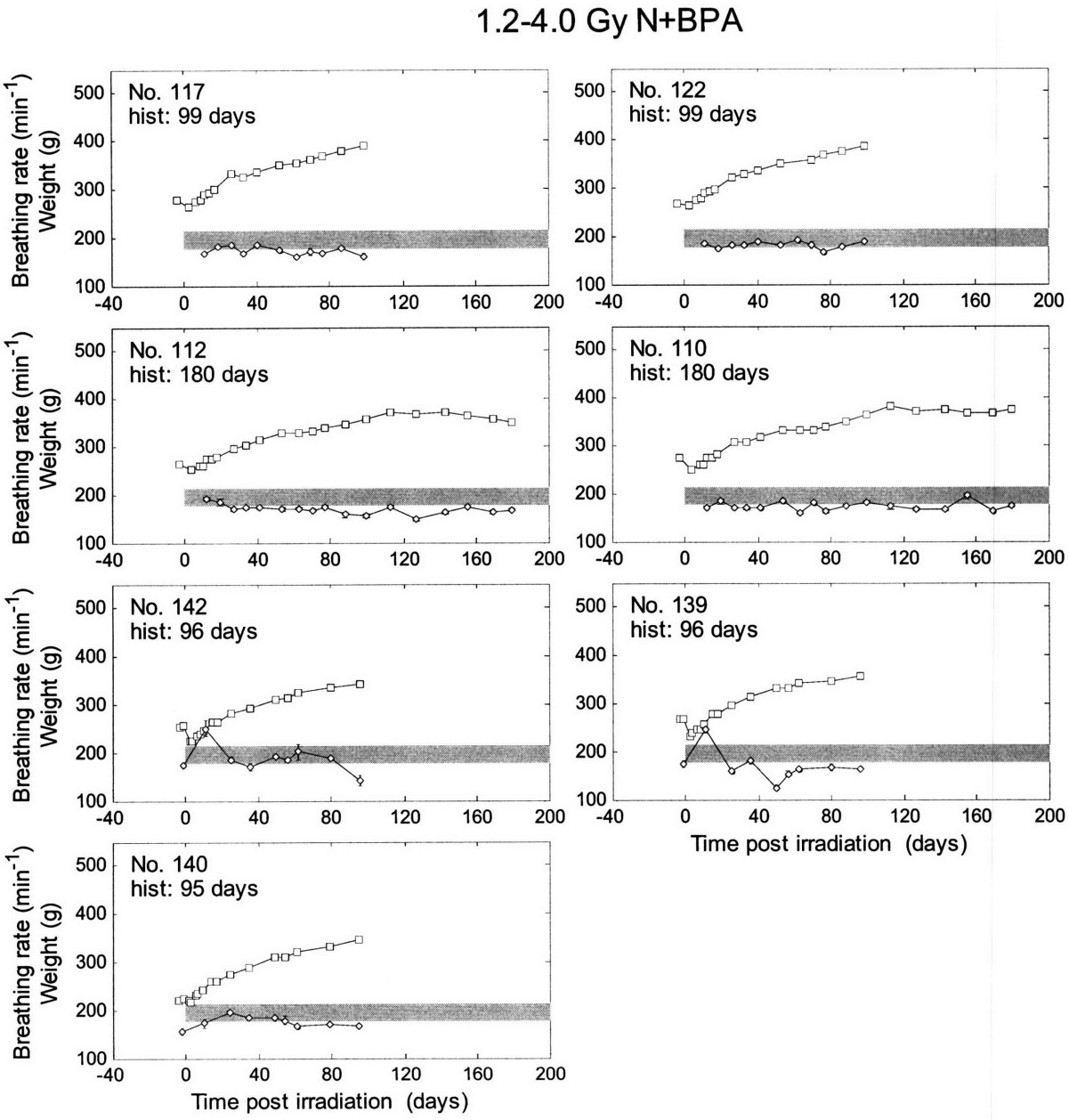

Fig. B.20 Breathing rate and weight after lung irradiation of 1.2-4.0 Gy neutron plus BPA.

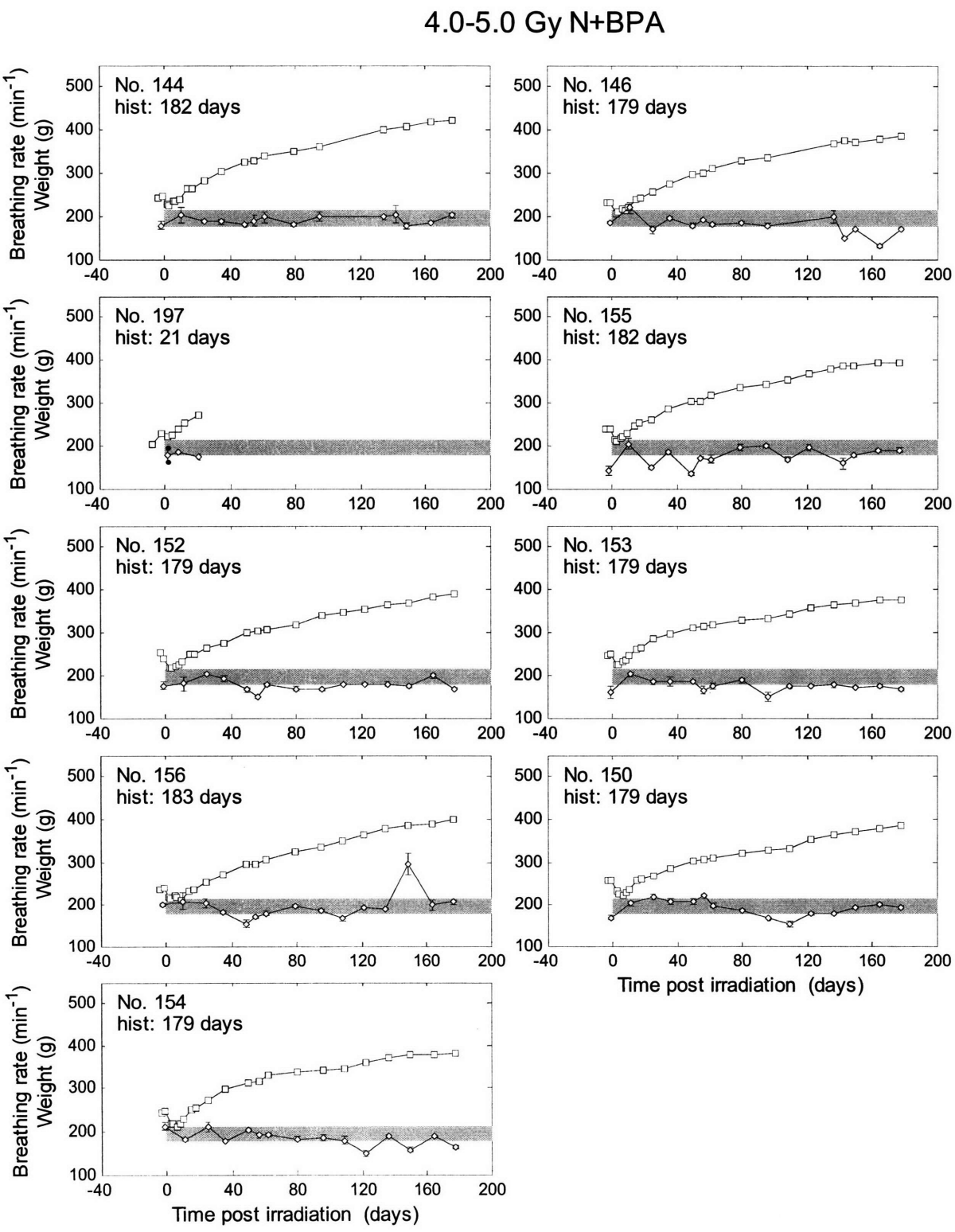

Fig. B.21 Breathing rate and weight after lung irradiation of 4.0-5.0 Gy neutron plus BPA.

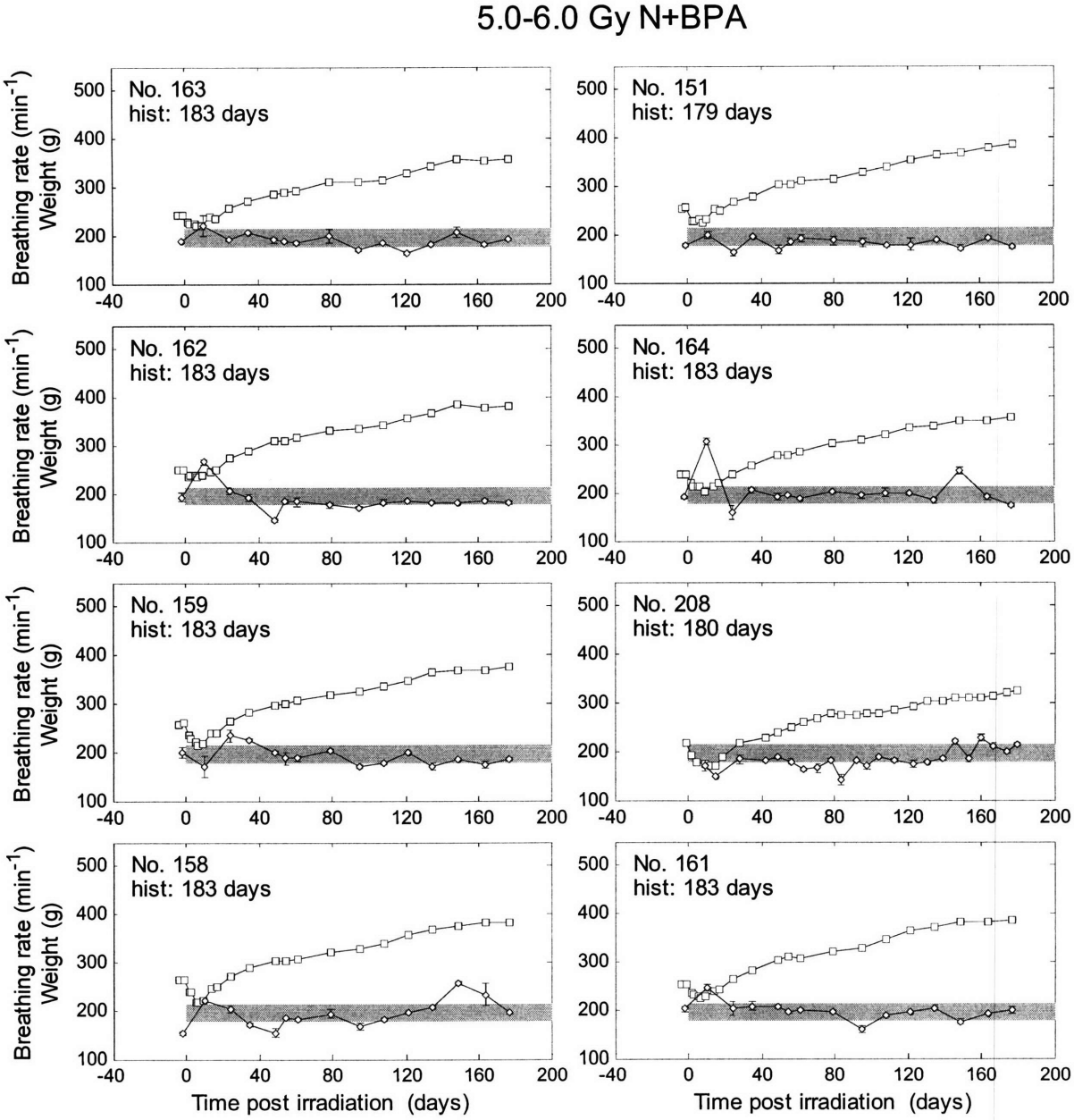

Fig. B.22 Breathing rate and weight after lung irradiation of 5.0-6.0 Gy neutron plus BPA.

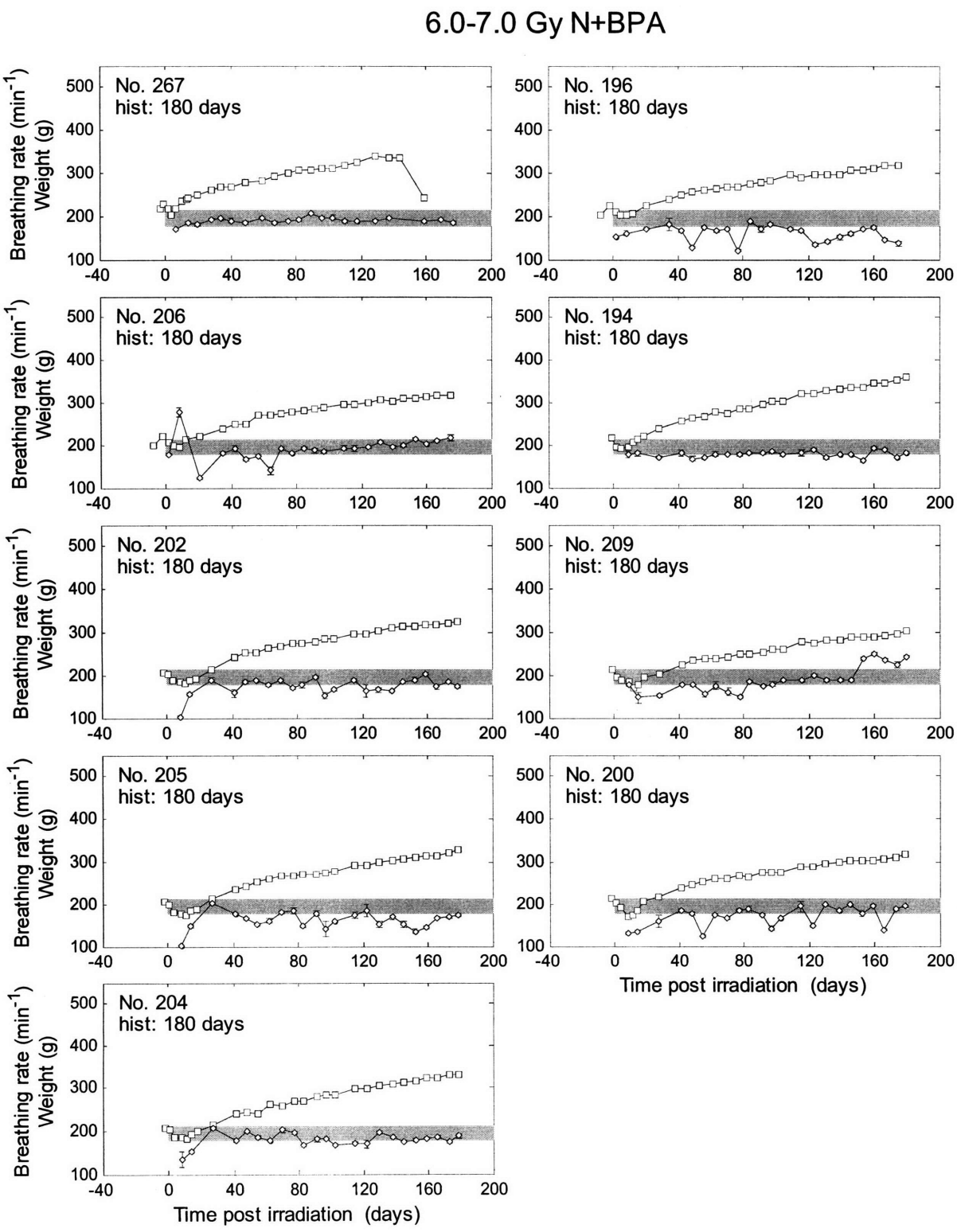

Fig. B.23 Breathing rate and weight after lung irradiation of 6.0-7.0 Gy neutron plus BPA.

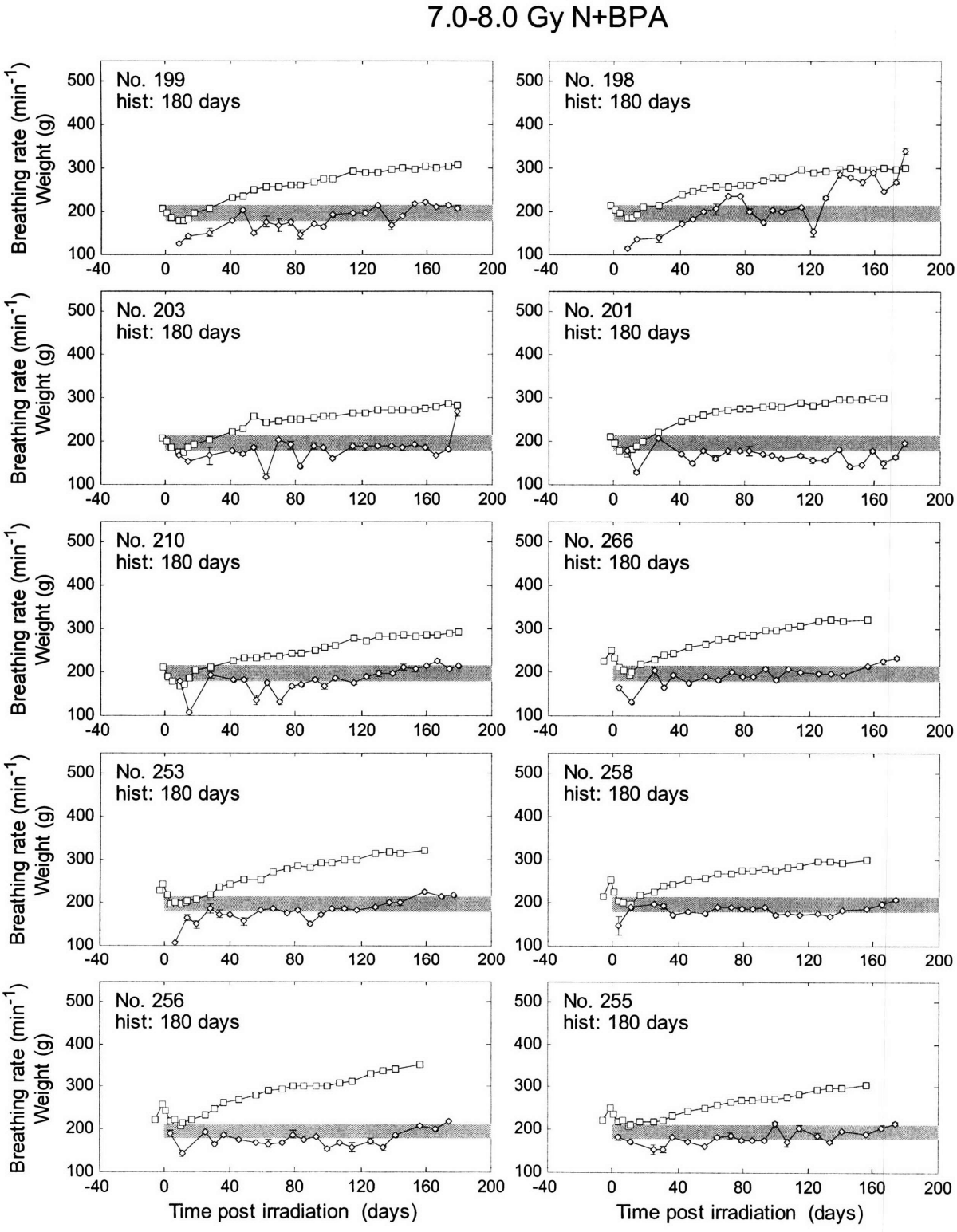

Fig. B.24 Breathing rate and weight after lung irradiation of 7.0-8.0 Gy neutron plus BPA.

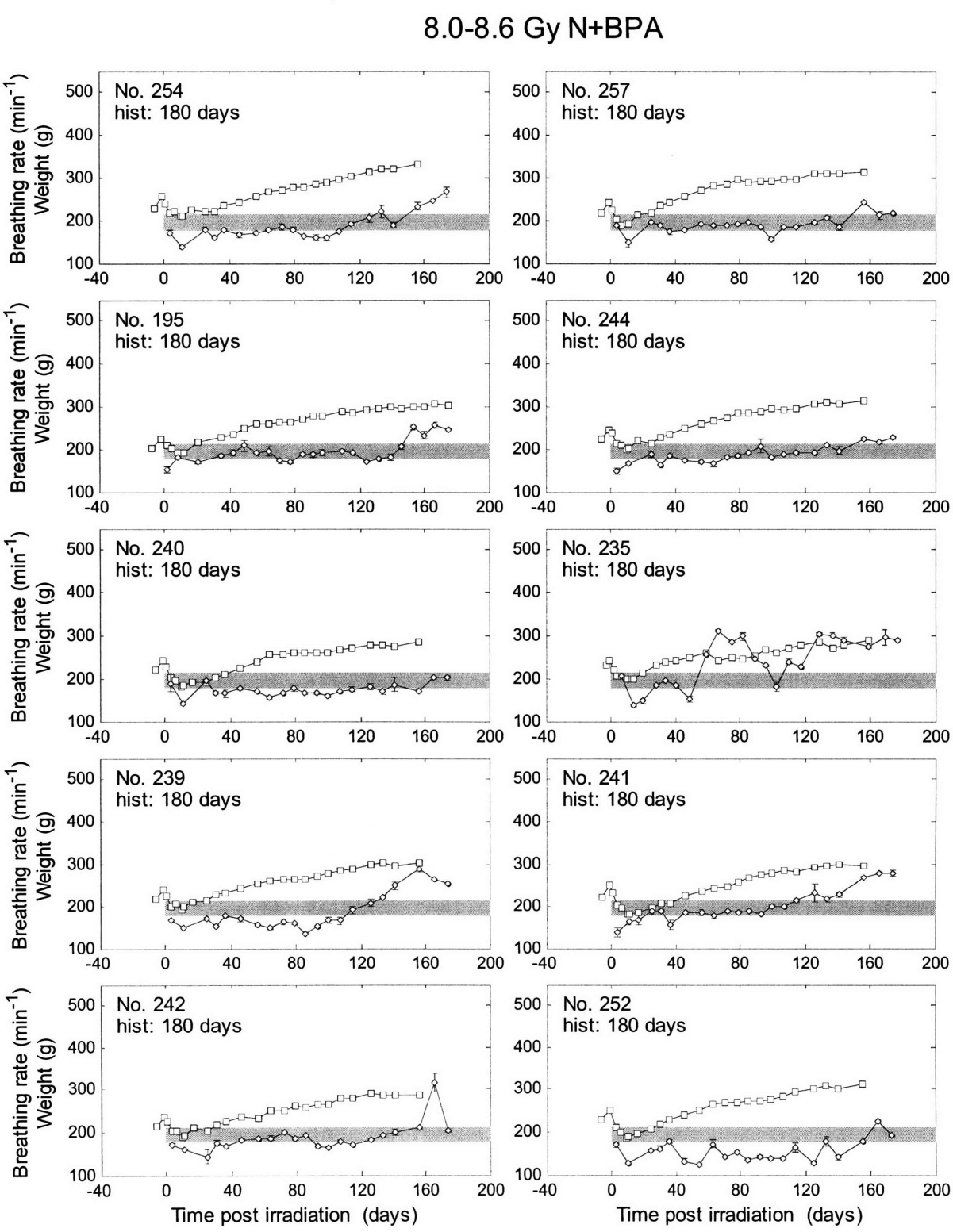

Fig. B.25 Breathing rate and weight after lung irradiation of 8.0-8.6 Gy neutron plus BPA.

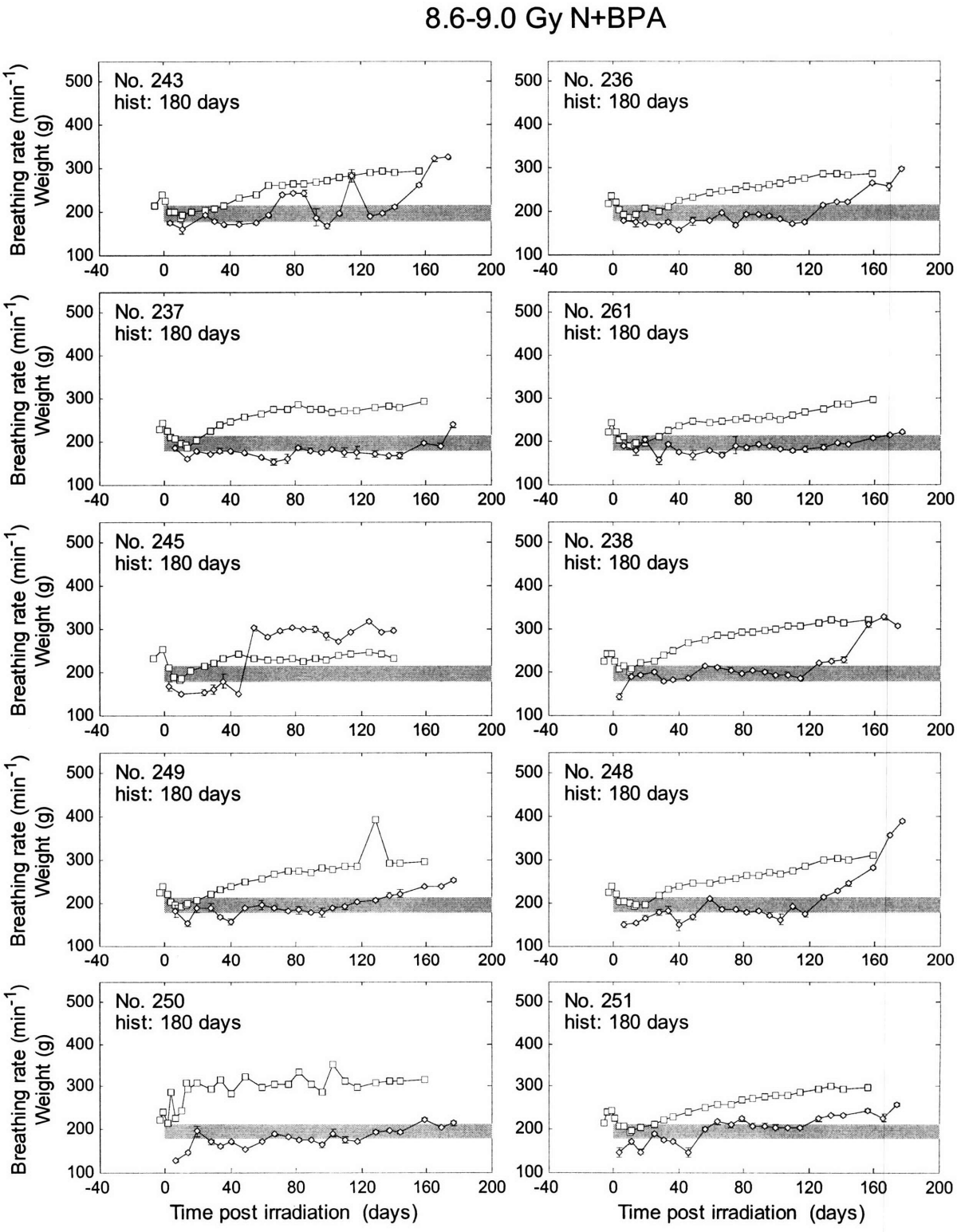

Fig. B.26 Breathing rate and weight after lung irradiation of 8.6-9.0 Gy neutron plus BPA.

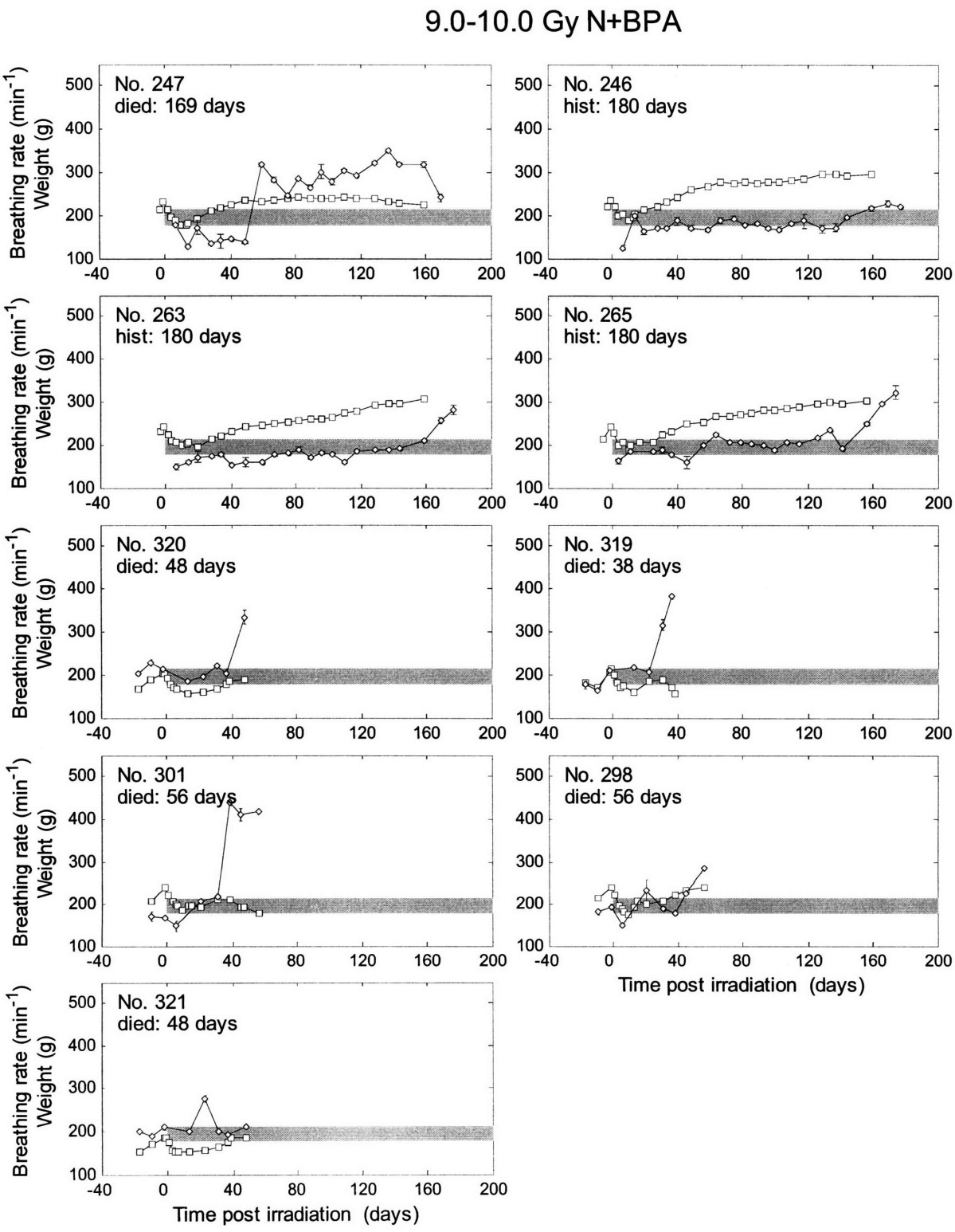

Fig. B.27 Breathing rate and weight after lung irradiation of 9.0-10.0 Gy neutron plus BPA.

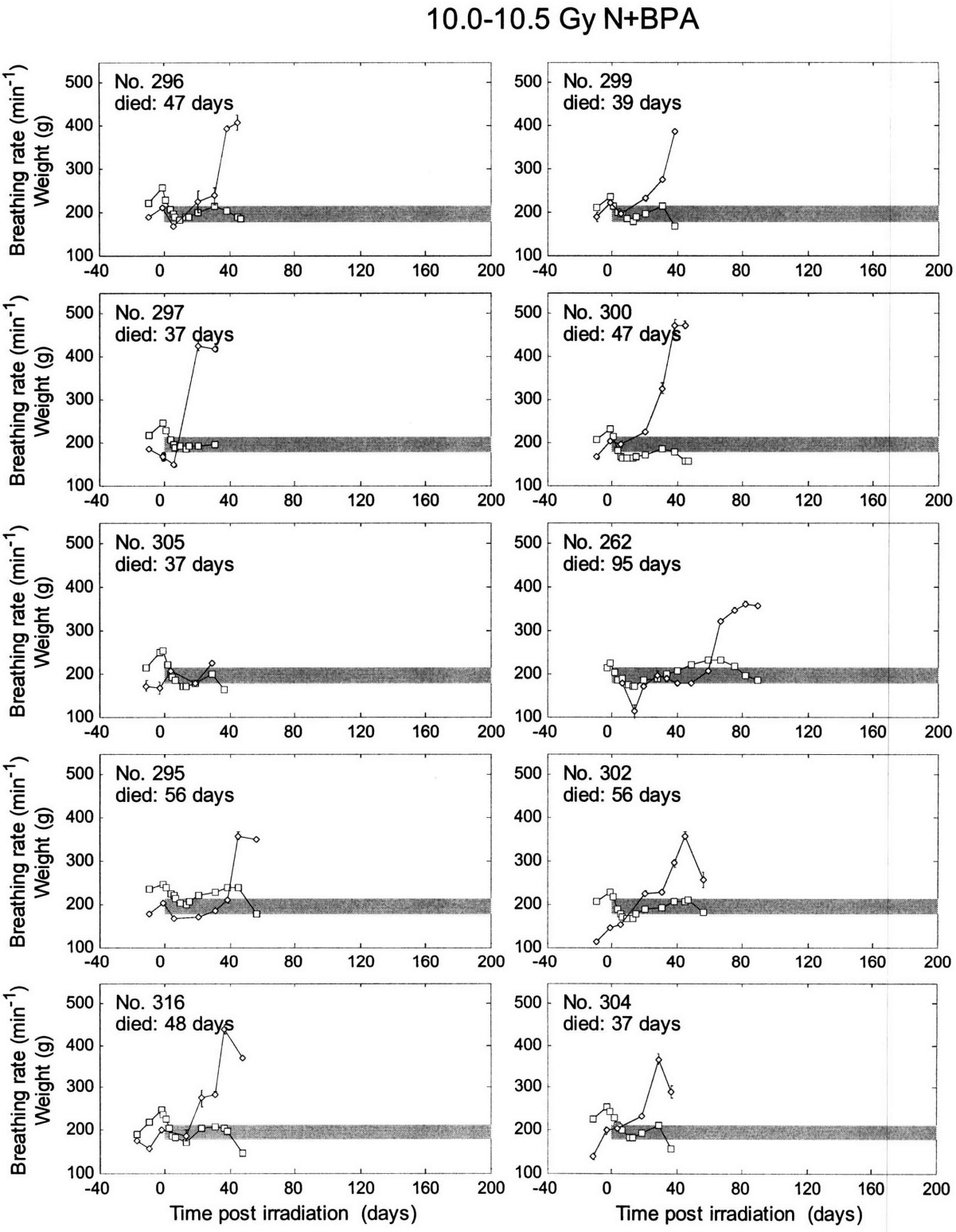

Fig. B.28 Breathing rate nd weight after lung irradiation of 10.0-10.5 Gy neutron plus BPA.

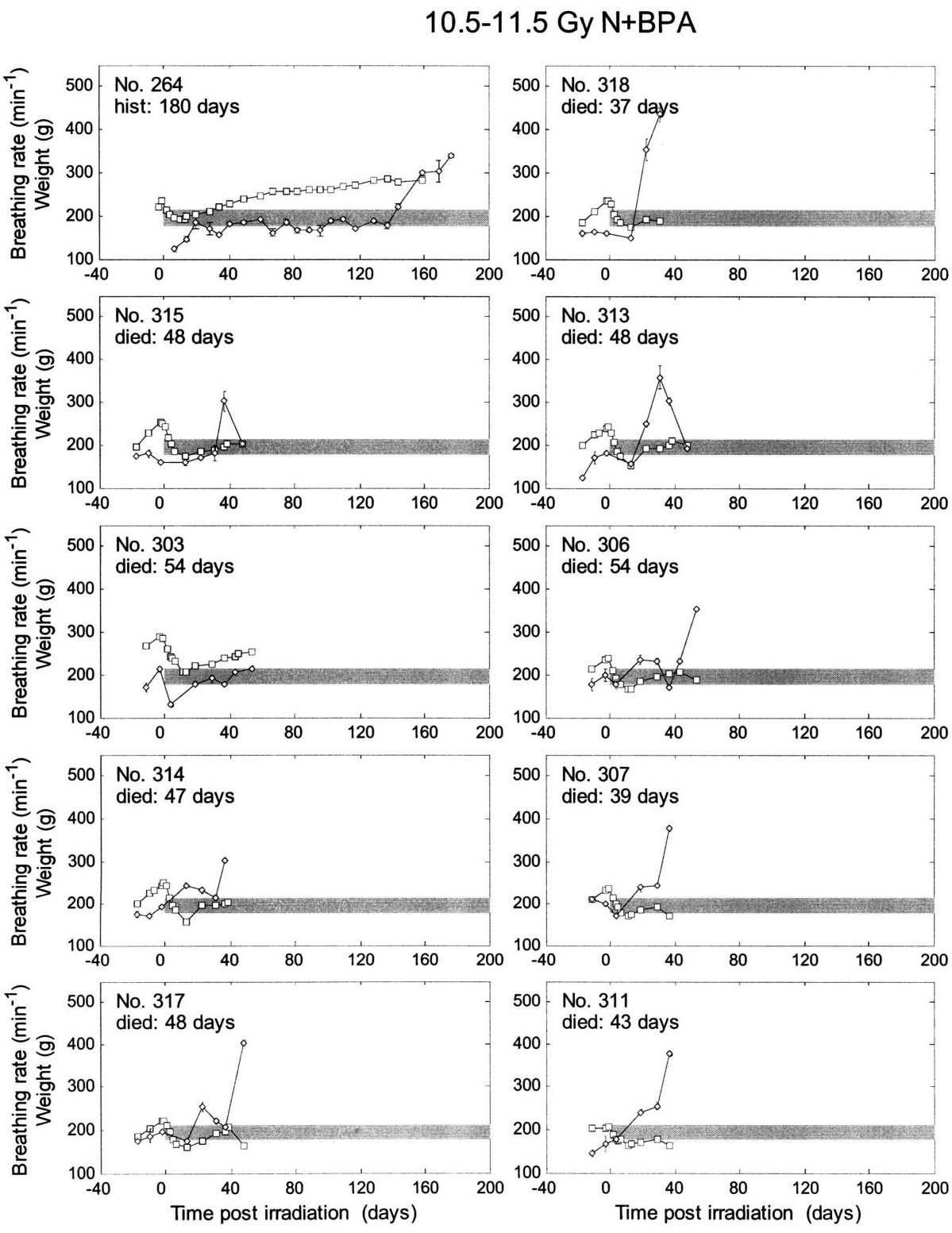

Fig. B.29 Breathing rate and weight after lung irradiation of 10.5-11.5 Gy neutron plus BPA.

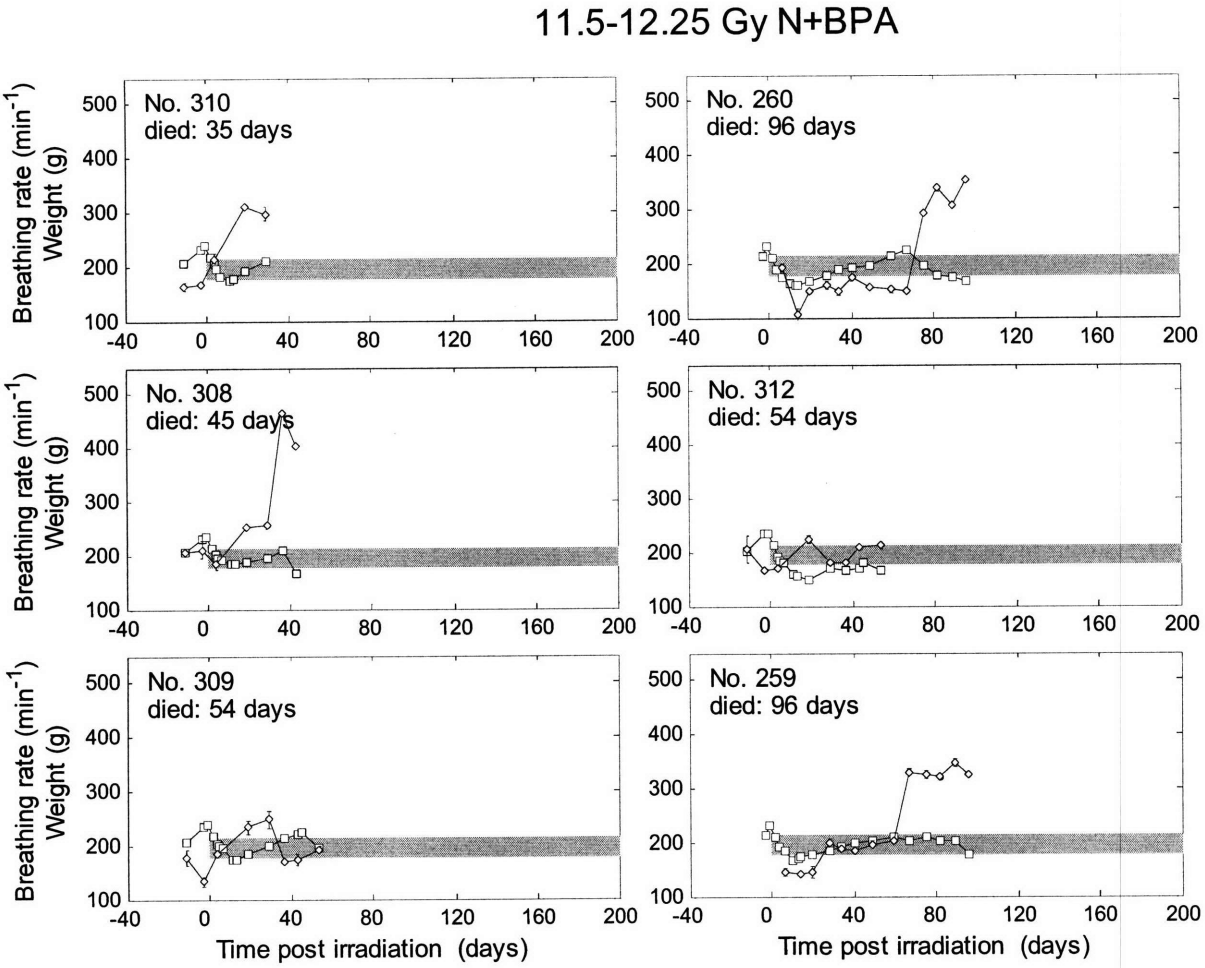

Fig. B.30 Breathing rate and weight after lung irradiation of 11.5-12.25 Gy neutron plus BPA.